Development of new dosimetric standards for low energy X-rays ($\leq$ 50 keV) used in contact radiotherapy

Abdullah Abudra'A

université PARIS-SACLAY

NNT : 2017SACLS489

Thèse de doctorat

Development of new dosimetric standards for low energy X-rays (≤ 50 keV) used in contact radiotherapy

Thèse de doctorat de l'Université Paris-Saclay
préparée à l'université Paris-Sud

École doctorale n°576 : Particules Hadrons Energie et Noyau, Instrumentation, Image, Cosmos et Simulation (PHENIICS)

Spécialité de doctorat : Radio et Hadron-thérapies

Thèse présentée et soutenue à Gif-sur-Yvette, le 11/12/2017, par

Abdullah ABUDRA'A

Composition du Jury :

Marc VERDERI Directeur de recherche, Ecole Polytechnique Laboratoire Leprince-Ringuet (Palaiseau)	**Président**
Aurélie DESBREE Ingénieur chercheur, Institut de Radioprotection et de Sûreté Nucléaire (IRSN) - Laboratoire d'Evaluation de la Dose Interne (Fontenay-aux-Roses)	**Rapporteur**
Régine GSCHWIND Professeur des universités, Université de Franche-Comté Laboratoire Chrono-Environnement UMR (Montbéliard)	**Rapporteur**
Albert LISBONA Physicien médical, Institut de cancérologie de l'Ouest Centre René Gauducheau (Saint Herblain)	**Examinateur**
Ramona ITTI Physicien médical, Hôpital Saint Louis Service de Cancérologie et Radiothérapie (Paris)	**Examinateur**
Isabelle AUBINEAU-LANIECE Professeur, Commissariat à l'énergie atomique et aux énergies alternatives - CEA saclay/LIST/ LNHB (Gif-Sur-Yvette)	**Directeur de thèse**
Christel STIEN Ingénieur chercheur, Commissariat à l'énergie atomique et aux énergies alternatives - CEA saclay/LIST/ LNHB (Gif-Sur-Yvette)	**Invité**

Titre : Développement d'une référence métrologique pour les faisceaux X de basse énergie utilisés en radiothérapie de contact
Mots clés : Radiothérapie de contact, référence primaire, curiethérapie électronique, RX de basses énergies INTRABEAM®
Résumé : La curiethérapie électronique, également appelée radiothérapie de contact, est une technique de traitement du cancer utilisant des rayons X de faible énergie (≤ 50 keV) générés par des tubes à rayons X miniaturisés et positionnés au contact des tissus à irradier. La miniaturisation des générateurs à rayons X a conduit au développement de nouveaux systèmes de traitement, dont le plus répandu dans le monde et le seul utilisé en France est le système INTRABEAM® commercialisé par la société Zeiss. Au-delà du bénéfice médical, les avantages potentiels de la curiethérapie électronique sont une diminution drastique de l'inconfort du patient combinée à un moindre coût de traitement. Ainsi, dans le cadre du cancer du sein qui correspond à l'application principale de l'INTRABEAM, cette technique remplace la trentaine de séances de radiothérapie externe classiquement prescrite suite à l'exérèse du volume tumoral par une seule et unique séance délivrée en 20 à 50 minutes au bloc opératoire directement après l'acte chirurgical alors que la patiente est encore sous anesthésie. Cette radiothérapie peropératoire (RTPO) associe au mini générateur de rayons X des applicateurs qui, en sénologie, correspondent à des sphères de différents diamètres conçues pour épouser au mieux la cavité tumorale résultant de l'exérèse. La dose délivrée en RTPO est classiquement de l'ordre de 20 Gy en surface du lit tumoral et diminue rapidement avec la profondeur afin de préserver les tissus sains voisins (< 1 Gy après quelques cm). En France, le 1er traitement par RTPO a eu lieu à Nantes fin 2011. Aujourd'hui, une dizaine de centres hospitaliers français propose des traitements par RTPO au moyen de la technique INTRABEAM®. Très rapidement, plusieurs physiciens médicaux ont exprimé au laboratoire français de métrologie de la dose (LNHB), leur besoin de raccordement dosimétrique à une référence indépendante du constructeur. Ce besoin a été réaffirmé par la Haute Autorité de Santé (HAS) dans un rapport sur l'évaluation de la RTPO dans le cancer du sein, édité en avril 2016.
Le présent travail vise à renforcer la sécurité d'emploi d'appareils de RTPO par rayons X de basse énergie (< 50 keV). Cependant, afin de répondre aux physiciens médicaux français et du fait de contraintes temporelles, l'étude est ici limitée au système INTRABEAM associé au seul applicateur sphérique de 4 cm de diamètre. Le travail a été articulé autour de trois axes.
Le premier a concerné l'établissement et le transfert d'une référence primaire en termes de dose absorbée dans l'eau à 1 cm de profondeur. La méthodologie a été développée et ensuite appliquée pour le système INTRABEAM® associé à un applicateur sphérique de 4 cm, pour lequel, la référence primaire a été réalisée.
Le deuxième axe a eu pour objet la détermination de la distribution spatiale de dose autour de la source considérée par l'utilisation de gels dosimétriques et par calcul de type Monte Carlo. L'hydrogel à base de Fricke, utilisé ici, est lu par imagerie par résonance magnétique à l'hôpital d'Orsay. Ce gel a été étalonné en dose pour des photons d'énergie inférieure à 50 keV puis utilisé pour déterminer les profils de doses autour de la source INTRABEAM® associée à l'applicateur sphérique de 4 cm de diamètre dans les plans axial et transverse incluant le centre de la source INTRABEAM®.
Quant au dernier axe, il s'est agi de confronter des données dosimétriques fournies par la société Zeiss, concernant l'INTRABEAM® en utilisation à l'hôpital St-Louis à Paris, à celles obtenues au cours de la présente étude pour le même système. Des différences significatives ont été trouvées entre les doses délivrées par Zeiss et celles obtenues dans la présente étude. Une étude indépendante menée par le PTB pour une autre configuration de source INTRABEAM® a conduit à des observations comparables. L'approche adoptée par Zeiss a ainsi été investiguée dans le présent travail et une cause de divergence a été proposée.

Title: Development of new dosimetric standards for low energy X-rays (≤ 50 keV) used in contact radiotherapy
Keywords: Electronic brachytherapy, Primary standards, Low-energy X-rays, INTRABEAM®
Abstract: Electronic Brachytherapy (eBT), also called contact radiotherapy, is a cancer treatment technique using low energy X-Rays (≤ 50 keV) generated by X-Ray tubes which are placed in close contact with the treated lesions. The latest evolutions of miniaturized X-Ray tubes led to the development of new treatment systems, such as the INTRABEAM® system of the ZEISS Company which is the most available eBT system and the only one currently used in France. Beside its medical benefit, the potential major advantages of treatment by eBT are the drastic decrease in patient discomfort and treatment cost. In the case of breast cancer treatment with such technique, the treatment is given in a single session that lasts 20 to 50 minutes where a high dose, in the order of 20 Gy, is delivered to the tumor bed surface in contact with spherical applicators associated to the X-Ray source. The delivered dose decreases rapidly with depth (< 1 Gy after a few centimeters) enabling to preserve neighboring healthy tissues. In France, the first IORT treatment performed was in Nantes in 2011. Today, ten medical centers offer IORT treatment using the INTRABEAM® system. Consequently, several medical physicists addressed to the French national metrology laboratory for ionizing radiation (LNHB) their need for a dosimetric traceability with a reference independent from the manufacturer. This need was reaffirmed by the French Authority for Health (HAS), in their report on the evaluation of the IORT for breast cancer treatment published in April 2016.
This thesis work is a contribution to the metrological work initiated by LNHB for enhancing the safety of employing IORT by eBT systems. It was limited, within the thesis period, to the INTRABEAM® system associated with a 4 cm diameter spherical applicator. The thesis work was oriented towards three main objectives.
The first one concerned the establishment and the transfer of a primary dosimetric standard, in terms of absorbed dose to water at 1 cm depth in water. The methodology was developed and applied on the INTRABEAM® system with 4 cm spherical applicator, for which, the dosimetric reference was established.
The second objective was to use a dosimetric gel and the Monte Carlo method to assess the 3D spatial distribution of the relative absorbed dose delivered by such a system. The dosimetric gel system used was a Fricke-based hydrogel read by Magnetic Resonance Imaging at Service Hospitalier Frédéric Joliot in Orsay (SHFJ). The gel reading was calibrated, in terms of absorbed dose for low energy X-Rays (< 50 keV), and then used to define the relative dose distributions of the INTRABEAM® X-Ray source associated with the 4 cm spherical applicator in the axial and transverse planes of the X-Ray source probe tip.
The last objective was to compare the dosimetric data delivered by Zeiss, for the INTRABEAM® system used at St. Louis hospital in Paris, by the ones obtained in the current study for the same system. Significant discrepancies were found from this comparison between the doses delivered by Zeiss and those obtained in the current study. Discrepancies were also observed in a separate work conducted by the PTB under a different INTRABEAM® configuration. Some reasons of these discrepancies are outlined and discussed in this study.

Acknowledgments

Et voilà, it's the end of this "adventure". An adventure that I was so glad to start yet thrilled to finish. Actually, it's so bizarre this feeling, once you're in, you strive to pop out, and once it's done, you want to jump back in. Well ... in fact, not really!

Several persons have actually participated, in a way or another, to accomplish this work. Words succeed most of time to express gratitude yet falls drastically when comes to certain persons who leaves you out of words. At least, I'll do my best!

I would like to express my appreciation to Valentin BLIDEANU, director of "laboratiore de métrologie de la dose (LMD)", and Loïc LE NOIR DE CARLAN, director of "Henri Becquerel National Laboratory (LNHB)", for giving me the chance to get into this adventure and to be part of the LNHB/LMD team. I'm also so grateful for the cancerology & radiotherapy service at Saint Louis hospital in Paris for giving us an access to their INTRABEAM® system, and more practically, for madam Ramona ITTI for all the help and expertise she provided for this work.

I would like also to express my deep gratitude to Isabelle AUBINEAU-LANIECE, my research supervisor, Marc DENOZIERE and Christel STIEN, my research tutors, for their patient guidance, enthusiastic encouragement and useful critiques on this research work. Also, with a great respect and acknowledgement, I thank the jury members for the time and efforts they conferred to examine this work.

I wish to acknowledge the help and demonstrations provided by Jean and Juan in the field of Monte Carlo simulations, and the rich discussions and guidance led by Johan "Le HdO" in the fields of instrumentations, spectroscopy, and DIY (bricolage); See how beautiful the measurement systems we have developed together!

Know what, they exist, Really! … no, no I don't mean the aliens, even more exceptional! I mean these wise characters who escort you throughout adventures as in fairytales! He's one of them, Bruno CHAUVENET. Actually, without him, this work would not have been accomplished. THANK YOU SO MUCH Bruno.

I want to extend my gratitude to all my colleagues at LMD for their kindness and help, for the work environment they have, and for all the good moments we spent together. I will definitely always remember the funny and warm-hearted Nelly & the "petit" discussions with you Dominique.

The shiny brilliant funny colorful and helpful couple (Fabien & Mélanie). You guys are so adorable. You actually are one of the best things I had through my thesis. Thanks for everything 😊

The Ph.D. title looks cool, huh… in fact what even cooler are the moments you live and the experience you share with your Ph.D. compatriots. I want to thank "le Capitaine" Stéphane, Sybelle and Isabelle with whom I shared the first months of my thesis, Héléna for all the good, and bad, stories we shared together. As well, the whole wonderful international group of "homeless fellas" and especially the kind Monika (keep us impressed with your artistic nail-polish), Li**V**ia (with a **V** this time and not an F), Alessia (el bella italiana), Oscardo, Aninda, Hector, Bianca, Mohcine, Mario, Anshuman and surely my precious buddy Malik Shukeir (it's been 11 years already, and wherever I go, it's a pleasure to find him there!). To the three awesome Post-docs, Nadia & Anne-Laure (les superb Mamies) and Guillaume, who have been always present to share lovely discussions during the coffee-breaks, and beyond 😉 many many thanks.

They say "True friends never apart, maybe in distance but never in heart". I totally agree, and hence, I want to thank my beloved friends: Alaa Al-Najjar, Obada Al-Ali, Mutaz Kalabani, Khamees Al-Jazarah, Nabrawi, Abdullah Darwish, and the trio Hussam and Ayman² for their constant supportive calls and messages. I have particularly appreciated your travel to be present at my defense beautiful Mireeeeen & Pierre, and you priceless Gryffindor gang, thanks for being always around.

I want to thank each one in my Jordanian family here in France: Laith (le parrain), Hazim, Fadous, Hussam, Mutaz, Lara, Tasneem, Malik, Rania, Nassima, Rostum, Wafa (the best storyteller) and my valuable “host-family” Jordan and Malak.

To the special person who accompanied me along this adventure: the fastidious French teacher, the TripAdvisor, the friend and lover… for every part you fill in my life, Merci Alice.

I thought I was the happiest, once I finished this adventure, till I called my parents… The enormous delight they had in their voices recalled me how my life is completely different just because they are always by my side. My treasure: elder brother Mohammed (one of a kind) and Montaha, Ibrahim & Ruba, Ahmed & Tahani, Suad & Mohammed and you our “little” Fatin, I am so lucky for having you all. At last, for sure, I won’t forget the kitties and teddy bears of my big family: Sarah, Tala, Layan, Ahmed (Sultan) and the last, but not the least, the brand-new little angel, P’tit Abdullah.

I might have forgot to thank you, yes you who’s reading these lines, by name in the previous lines, I am really sorry, and believe me, I’ll be so happy to thank you in person!

Remember always « La vie est belle » cuz « c’est bientôt le weekend » 😉

To the heroes fighting against cancer…

anywhere and in any manner, we've never been closer to defeat this intruder… So, never cease, even for a single instant, before winning your battle

Table of contents

INTRODUCTION

Electronic BrachyTherapy (eBT), also called contact radiotherapy, is a cancer treatment technique using low energy X-Rays (≤ 50 keV) generated by X-Ray tubes which are placed in close contact with the treated lesions. The latest evolutions of miniaturized X-Ray tubes led to the development of new treatment systems, such as the INTRABEAM® system manufactured by the Company ZEISS. The INTRABEAM® is the most available eBT system in the world and the only one used in France.

Beside its medical benefit, the potential major advantages of treatment by eBT are the drastic decrease in patient discomfort and treatment cost. In addition, in the case of breast cancer treatment, which is the main application of the INTRABEAM®, the treatment is applied after the lumpectomy, when the patient is still under general anesthesia in the operating room; that is why eBT is considered as an IntraOperative RadioTherapy (IORT) technique. The treatment is given in a single session that lasts 20 to 50 minutes. This is equivalent to the about 30 regular sessions classically prescribed for treatment with an external radiotherapy technique.

In IORT treatment of breast cancer by eBT, spherical applicators of different sizes, intended to fit into the cavity left after tumor excision, are mounted on miniaturized X-Ray generators. A high dose, in the order of 20 Gy, is delivered to the tumor bed surface in contact with the applicator. The dose decreases rapidly with depth (< 1 Gy after a few centimeters) enabling to preserve neighboring healthy tissues. In France, the first IORT treatment performed was in Nantes in 2011, while today, ten medical centers offer IORT treatment using the INTRABEAM® system. Consequently, several medical physicists addressed to the French national metrology laboratory for ionizing radiation (LNHB) their need for a dosimetric traceability with a reference independent from the manufacturer. This need was reaffirmed by the French Authority for Health (HAS), in their report on the evaluation of the IORT for breast cancer treatment published in April 2016.

This work is a contribution to the metrological work initiated by the LNHB for enhancing the safety of employing IORT by eBT systems. However, in order to respond to the need of French medical physicists within the time constraints of a thesis, the study was limited to the INTRABEAM® system associated with a 4-cm in diameter, spherical applicator.

The thesis work was oriented towards three main objectives: the first objective was the establishment and the transfer of a primary dosimetric standard, in terms of absorbed dose to water at 1 cm depth in water, the second objective was to use a dosimetric gel and the Monte Carlo method to assess the 3D spatial distribution of the relative absorbed dose delivered by such a system and the last objective was to compare the dosimetric data delivered by Zeiss, for the INTRABEAM® system used at St. Louis hospital in Paris, with the ones obtained in the current study for the same system.

This manuscript presents the work realized in response to these objectives, it is divided into four main chapters:

- The first chapter, named “Materials and methods”, gives a global view on the IORT technique using eBT systems with a focus on the INTRABEAM®. It reminds the main dosimetric quantities and dosimetry principles related to the kilovoltage X-Ray beams.

The metrology of low energy photons comprising the different available dosimetry protocols, dose traceability and established primary standards for eBT systems are lastly presented.

- The second chapter covers the first objective. It describes the methodology adopted to realize the dosimetric reference for the INTRABEAM® source with spherical applicators. It presents the different steps completed to determine the dosimetric reference for the INTRABEAM® system associated with a 4-cm spherical applicator. The characterization and reproduction of INTRABEAM® photon spectra at LNHB, as well as the development of a MC model of the INTRABEAM® X-Ray source with a 4-cm spherical applicator, are presented in this chapter.

- The third chapter deals with the second objective. The methodology developed to characterize and calibrate the dosimetric gel in the photon low-energy range, and the resulting calibration function are detailed. The calibrated gel was then used to define the relative absorbed dose profiles in gel and water around the INTRABEAM® X-Ray source with a 4-cm spherical applicator.

- The fourth and last chapter addresses the last objective. The dose values obtained according to the manufacturer's procedure for the INTRABEAM® system were compared to those determined by the LNHB primary standard. To complete the confrontation of the dosimetric data delivered by the Zeiss Company, some data involving another comparison performed by the PTB using its primary standard and considering a bare miniaturized X-Ray INTRABEAM source were also considered. On this basis, a further analysis was performed on the "TARGIT" method used originally by ZEISS for the INTRABEAM® dosimetry. Finally, the dose distributions established in the present work with the ones delivered by Zeiss were confronted.

These chapters are followed by a general conclusion and some perspectives concerning the future evolutions and improvements of the current work.

Chapter 1

1. Materials and methods

1.1. Intraoperative radiotherapy by electronic brachytherapy

The clinical applications of radiation therapy have a major role in cancer treatment. Each radiotherapy technique aims at having specific advantages over the others. The treatment cost, period, efficiency and patient's comfort are amongst main goals intended by all techniques. A main challenge of all treatments is to deliver the highest dose to tumor cells while leaving healthy tissues spared.

IntraOperative RadioTherapy (IORT), as the name implies, is a radiotherapy technique where irradiation is delivered during surgery. A high dose, in the order of 10-20 Gy, is delivered in a single session to the surgically exposed internal organ, tumor or tumor bed. The IORT can be applied with other treatment modalities, such as chemotherapy and external beam radiotherapy that are used to shrink the tumor, and hence, simplifying the subsequent surgical resection [1].

Since the first use of IORT in the 1960s [2], different modalities relying on the IORT technique have been developed, such as Intraoperative Electron Radiotherapy, High Dose Rate brachytherapy, Orthovoltage IORT and electronic brachytherapy (low kilovoltage) IORT. Intraoperative radiotherapy using electrons has been the favored approach over orthovoltage beams because of better dose homogeneity, decreased treatment time and less bone absorption attributed to the photoelectric effect. However, orthovoltage IORT has advantages in certain clinical settings and is generally more cost-effective. Recently, electronic brachytherapy devices have become commercially available [3]. This later technique will be discussed in more detail in the next section.

1.1.1. Electronic brachytherapy (contact X-Ray therapy)

Brachytherapy (the Greek prefix "brachy" literally means "short", "close" or "near") techniques were firstly developed in the 1930s using radioactive sources. The name was adopted since the radiation source, used in treatment, is placed in contact, or close to the tissues to be treated. Lately, due to the development of small-sized electronic X-Ray generators, which replaced the radioactive sources, a new name was settled, i.e. electronic BrachyTherapy (eBT) or, as also called, contact X-Ray therapy.

Electronic Brachytherapy (eBT) is a cancer treatment technique, in which, the irradiator material, comprising an X-Ray generator and a variety of applicators (each applicator corresponds to a type of treatment), is placed in direct, or close, contact with the tumor. eBT uses the radiobiological properties of low-energy X-Rays, emitted by an X-Ray generator with a high voltage ($\leq$ 50 kV) to treat cancer.

The latest evolutions of X-Ray tubes rehabilitated the interest of clinicians. It empowered the replacement of radioactive sources used in the treatment of certain types of cancer by brachytherapy techniques. For the last ten years, it has been the subject of clinical studies through which its efficiency was proven for intraoperative treatments of breast cancers [4]. Beside its medical benefit, the potential major advantages of eBT are: less requirements for protective shielding (low energy X-Rays) during the treatment and increased radiobiological

effectiveness [5]. It also allows to drastically decrease patient discomfort, treatment duration and cost [6].

1.1.2. Conventional and miniature X-Ray generators (purpose and principles)

Since their discovery by W. Röntgen in 1895, numerous applications of X-Rays have been demonstrated and implemented. X-Ray generators have also evolved, and are currently used in a variety of domains including medicine.

The concept of X-Ray generators is still almost the same since its development in the late 19th century. An X-Ray tube is a simple vacuum (~10^{-6} mbar) tube that contains a cathode and an anode under an electric potential difference, as described in Figure 1.1 (left). The tube current (expressed in milliamperes [mA]) passes through the cathode filament to produce electrons by thermoelectrical effect (thermionic emission). Under the effect of the electric potential applied to the X-Ray tube, these electrons are accelerated towards the anode, where they decelerate, which leads to the emission of X-Rays and heating up the anode. The high voltage (HV) value determines the quality (penetrability) of the generated X-Rays, and the tube current determines the quantity of emitted X-Rays (photon flux).

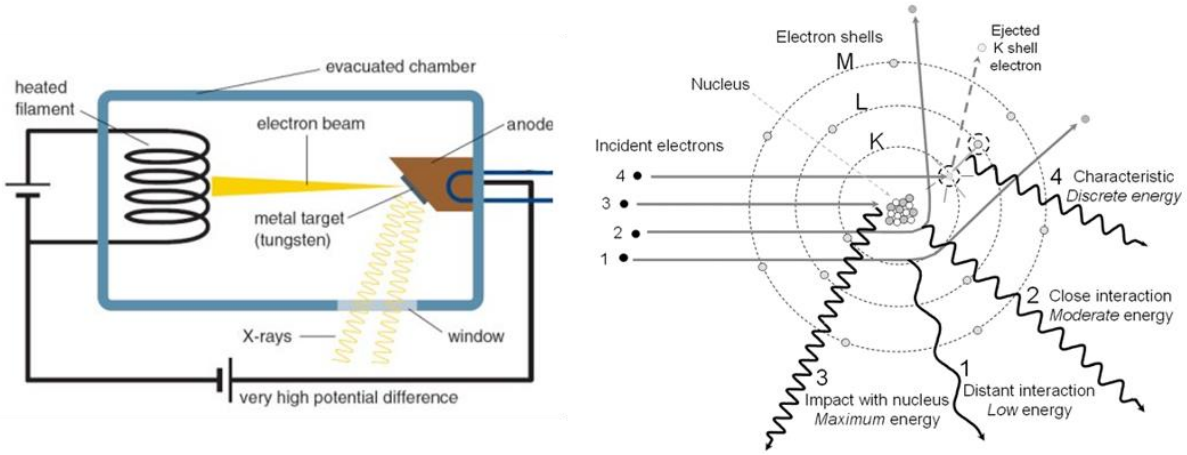

Figure 1.1. Schemes of (left) an X-Ray tube (image extracted from Jacaranda Physics 1 [7]) and (right) a target atom showing the four possible X-Ray production cases: events (1-3) result in bremsstrahlung production with the emission of a continuous energy spectrum of X-Ray photons, event 4 demonstrates characteristic radiation emission [8].

The emitted X-Rays are distributed in energy according to a continuous spectrum with some discrete peaks. When the highly energetic electrons interact with the X-Ray tube anode, they lose their kinetic energy, partially or totally, as demonstrated in Figure 1.1 (right). This loss in energy is caused either by the interaction with the nucleus or an inner-shell electron. The interaction with the nucleus results in the conversion of the kinetic energy into electromagnetic radiation known as bremsstrahlung (or braking radiation). The interaction distance results in different amounts of energy loss (higher close to the nucleus). The emitted X-Ray photons then form a continuous energy spectrum up to a maximum energy corresponding to the initial kinetic energy of the most energetic electrons. The interaction with an inner-shell electron removes it from the atom; this is consequently followed by an atomic electron rearrangement and the emission of discrete-energy X-Ray photons. These photons are characteristic for each element,

and contribute to the X-Ray spectrum in the form of monoenergetic peaks added to the continuous spectrum.

Miniaturized X-Ray Tubes have emerged as a cutting-edge application of nanotechnology, possessing massive potential for use in various important fields, including precision medical therapy. Miniature X-Ray tubes deliver high doses from the closest possible distance. The word “miniature” implies “very small” and refers to the tube size. Some authors define that “miniature” refers to a tube size of less than 10 mm diameter [9].

The operating principle of miniature X-Ray tubes is almost the same as the conventional X-Ray tubes. However, in addition to thermionic emission, cold emission cathodes, based on field-electron (FE) emission technique, are also used. FE emission refers to the extraction of a free electron from a non-insulating solid surface exposed to a high electric field. FE is based on the phenomenon of electron tunneling where an electron penetrates through a potential barrier due to the large applied electric field. Since this process has a weak dependence on the temperature of the emitter, FE is also known as cold emission and subsequently the FE cathodes are called cold cathodes.

The miniaturizing of thermionic emission X-Ray tubes has been achieved by using thermionic dispenser cathodes. The dispenser cathodes have a limited lifetime in non-ultrahigh vacuum at which X-Ray tubes are generally operated. Indeed, this type of electron sources interacts with the residual gas molecules, leading to the deactivation of the emitter and thus to the limitation of its lifetime. The necessary prerequisite for fabricating a miniaturized X-Ray tube able to work for a large number of hours is therefore to employ a cold cathode made of one of the most common materials used as FE X-Ray sources such as carbon nanotubes [10], and other carbon nanomaterials, e.g., carbon nanofibers.

A variety of clinical systems are now available for treatment using eBT, each of them has its own miniature X-Ray generator and corresponding applicators. The next section describes several available eBT systems employing miniature X-Ray generator.

1.1.3. Available systems and sources

Over the past decades, eBT systems have seen a remarkable development. More than 400 systems are now available worldwide. The operating parameters differ from one manufacturer to another. Table 1.1 gives a summary of the existing systems and some of their operational parameters while Figure 1.2 shows their spectral distributions and the radial dose functions of some devices. Information given in this part mostly relies on the review article of D. J Eaton (2015) [11].

eBT devices were barely used until the 1960s when the Philips RT50 (Philips Healthcare, Amsterdam, Netherlands) was produced and made available on the market. This device was intended for endocavitary treatment of rectum and skin cancers. While it was progressively abandoned, the Papillon 50 contact radiotherapy system (Ariane Medical Systems Ltd, Derby, UK), with a collimated X-Ray source, was developed and then released in 2008 to replace the RT50. In the Papillon 50, electrons are accelerated into an evacuated copper tube to hit a rhenium transmission target. Photons are then produced in an approximately isotropic distribution but collimated by cones of increasing diameter to give a fixed aperture angle of 45°. A dose of 90 Gy to the tissue surface in three fractions is delivered by an “internal superficial” method where the applicator end is inserted into the rectum and placed against the lesion.

Seventeen applicators for skin lesions treatment are also available whereas breast IORT is under development.

The Xoft® Axxent® system (iCAD Inac., Nashua, New Hamphire, USA) is a miniature X-Ray tube integrated with a cooling sheath into a multi-lumen catheter, first released in 2006. The position of the source may be stepped along the length of the catheter, as for a high dose rate (HDR) radioactive source. Unlike the INTRABEAM® system described below, Xoft® sources have a limited lifetime of about 3 hours or 10 treatments. However, the dose rate is higher and the depth dose falls off less steeply. Source strength is verified using an internal well chamber before each treatment. Balloon catheters are used to treat early stage breast cancer with IORT. Dose distributions are similar to the MammoSite® balloon catheter (Cytec Industries Inc., Mountain View, California, USA) used with iridium-192 (^{192}Ir) HDR sources. Multiple studies have described the dosimetric characteristics for different applicators [12–14].

The Esteya® eBT system (Elekta AB-Nucletron, Stockholm, Sweden) is a mobile collimated miniature X-Ray source released in late 2013 and designed specifically for treatment of skin lesions. Surface applicators with a flattening filter are used to give a dose distribution similar to the Valencia ^{192}Ir HDR applicator, produced by the same manufacturer. The tube current is varied to give an approximately constant treatment time. The dosimetry of the unit has been described by Garcia-Martinez *et al.* [15]. They found that the flatness and symmetry of the system were within 5 %, along with a sharper penumbra and shallower depth dose than the Valencia or Leipzig HDR applicators (Elekta AB-Nucletron).

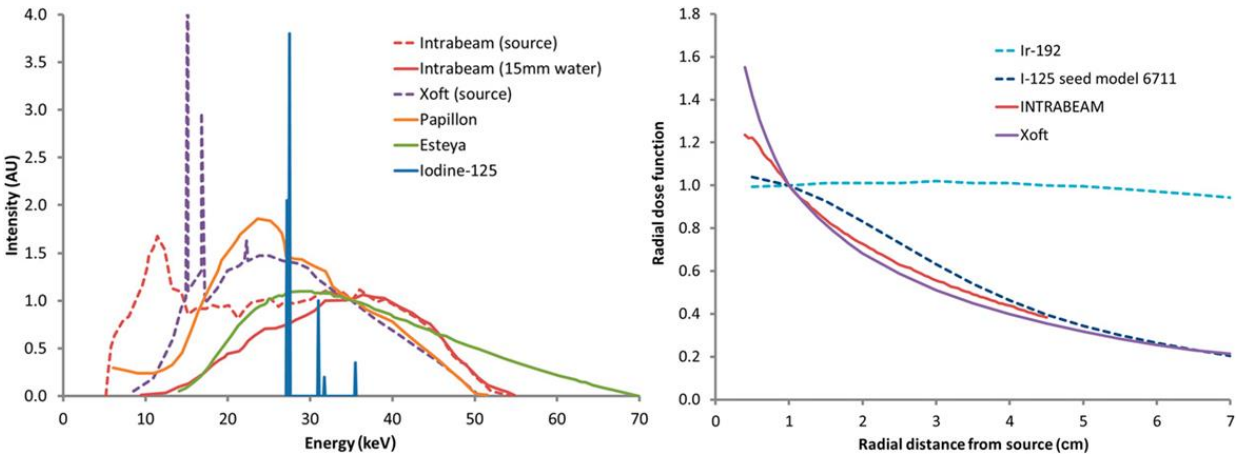

Figure 1.2. (Left) photon energy spectra of different electronic brachytherapy devices normalized to the value at 35 keV (except for iodine-125). (Right) Radial dose functions normalized to the value at 1 cm distance. Data collected from different sources and presented in the review article of D.J Eaton [11].

Photoelectric therapy (Xstrahl Ltd, Camberley, UK) is a new product launched in late 2014, also aimed at treating skin lesions. This system is a compact ultralight mobile unit with built-in cooling, easy-to-shape collimation and flattening filters to give a uniform dose profile.

Finally, the SRT-100™ (Sensus Healthcare, Boca Raton, Florida, USA) is another mobile collimated low-kilovoltage unit specifically aimed at treating skin lesions, but with focus-to-skin distance (FSD) and field sizes comparable to a standard kilovoltage therapy unit, such as the Xstrahl 100 or 150 series. This device is an example of the overlap between conventional superficial units and eBT devices.

Table 1.1. Operating parameters and usage of current eBT systems, clinical applications in bold refer to the primary application of the machine. These data are extracted from D. J Eaton article [11].

Machine name	Approx. # of units worldwide	Clinical applications	Approximate treatment time	Accelerating potential, tube current	Geometry
INTRABEAM®	250	Skin, **Breast**, Intracranial, Kyphoplasty, other	25-40 min (sphere) & 5-30 min (surface) applicators	50 kV, 0.04 mA	Point source (probe tip)
Xoft®	>150	**Skin, Breast**, Vaginal	10-25 min (balloon), 5-10 (surface) and 10-15 min (endocavitary)	50 kV, 0.3 mA	Point source (catheter)
Papillon	11	**Rectum**, Skin, Breast	2 min	50 kV, 2.7 mA	Collimated source
Esteya®	10	**Skin**	2 min	70 kV, 0.5-1.6 mA	Collimated source
Photoelectric therapy	1	**Skin**	1-2 min	80 kV, 1.3 mA	Collimated source
SRT-100™	150	**Skin**	1-2 min	50-100 kV, 8-10 mA	Collimated source

1.1.4. INTRABEAM® system by Carl ZEISS

The ZEISS INTRABEAM® (Carl Zeiss Surgical GmbH, Oberkochen, Germany) system is a compact mobile X-Ray source originally used in the treatment of brain tumors in the early 1990's [16]. It has subsequently been used for other indications, after the development of its applicators, and since 1998 it is primarily used for IORT of breast cancer [2]. It is composed of a miniaturized X-Ray generator (XRS-4), a floor stand ensuring a precise and easy positioning of the irradiation head in the patient's body and a user terminal connected to a control console, to set and monitor treatment parameters and to communicate data, as shown on Figure 1.3. In addition, a quality control equipment are also supplied with the system [17].

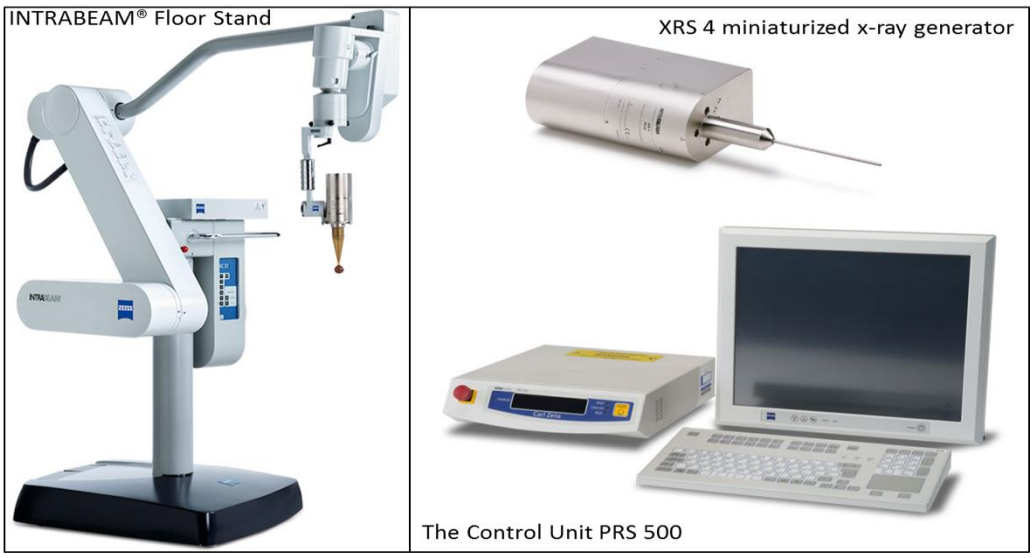

Figure 1.3. (Left) INTRABEAM® Floor stand. (Right, top), X-Ray generator of the INTRABEAM system. (Right, bottom) Control Unit PRS 500 controlling and monitoring the XRS-4 miniaturized linear accelerator (X-Ray generator) during the treatment.

Electrons emitted by a heated cathode wire are accelerated to a potential of 50 kV (40 kV potential is also accessible) and collimated using an electromagnetic deflector. The resulting electron beam is then guided through a 10 cm long probe (external Ø = 3.2 mm) toward a gold target, of a thickness of 1 µm, covering the inner surface of the hemispherical probe tip. Finally, the interactions of electrons with the gold target lead to the production of X-Rays in an approximately 4π distribution, as seen in Figure 1.4.

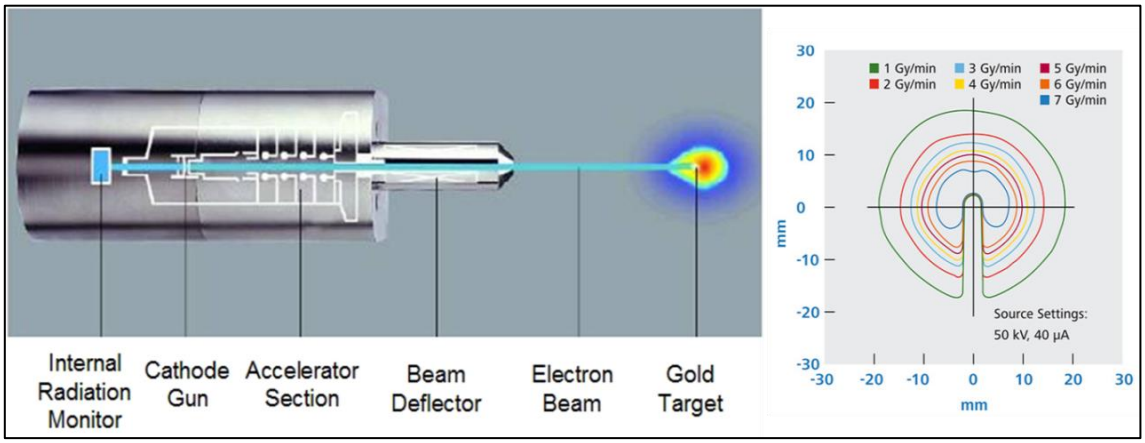

Figure 1.4. (Left) schematic of the INTRABEAM X-Ray miniaturized generator; (right) external dose distributions of the needle applicator in water. (Data taken from zeiss.com)

Different sizes and shapes of applicators allow to treat different types of cancer, i.e. gastrointestinal [18], spinal metastasis [19] and skin [20,21]. The treatment times depend on the chosen applicator size and prescribed dose (10-20 Gy) and vary between 2 to 50 minutes. The dosimetry and quality assurance of the INTRABEAM® system have been reviewed in different publications [17,22,23].

INTRABEAM® spherical applicators are used for breast cancer treatment [4,24]. They are mounted on the X-Ray source, with the probe tip placed at the center of the applicator sphere, to give a homogenous dose at the applicator surface. The applicator is inserted into the tumor cavity after excision to treat the tumor bed. The applicator spheres are made of biocompatible polyetherimide material, trade name Ultem®, whose density ranges from 1.27 to 1.51 g/cm3. To give a good conformance of the applicator surface to the tumor cavity, the outer diameters of spherical applicators range from 1.5 cm to 5 cm, by steps of 0.5 cm. They are solid with an inner cavity (radius equal to 2.8 mm) where the probe is inserted. For the applicators with a diameter smaller than 3 cm, an aluminum "flattening filter" is added into this cavity to produce a spherical flattening field (Figure 1.5). To attach the applicator to the X-Ray source, a metal ring in stainless steel is added to its shank end [2,25].

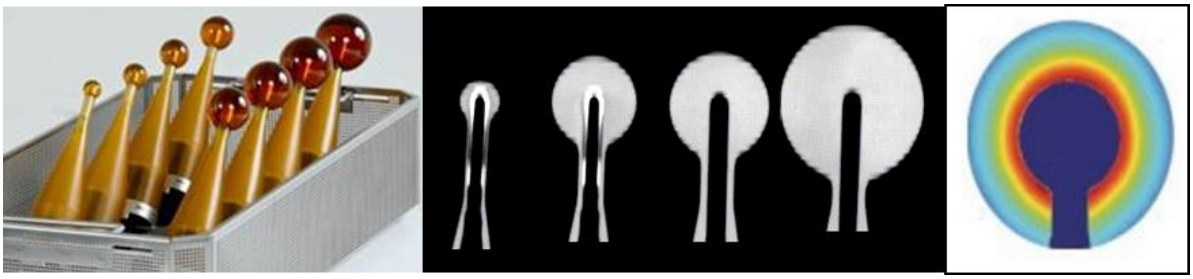

Figure 1.5. (Left) INTRABEAM® spherical applicators, (middle) computed tomography image showing the cross-section of 1.5, 3, 3.5 & 5 cm diameter applicator ends, the brighter part around the inner cavity refers to the internal aluminum filter [26] and (right) homogenous dose distribution around a spherical applicator (zeiss.com)

1.2. Dosimetric quantities

Radiation dosimetry is the science of measurement of ionizing radiation effect on matter. It includes the development and implementation of measuring instruments and methods, including Monte-Carlo simulation codes, that can be used for a quantitative determination, measurements or calculations of the energy deposited in a given medium by directly or indirectly ionizing radiation. The effects of radiation on matter depend on the nature of radiation, its energy, its intensity and the medium nature in which radiation interacts. The dosimetric quantities have been defined to provide a physical measure that can be correlated with the actual or potential effects of radiation. The most commonly used dosimetric quantities for health applications, i.e. air kerma and absorbed dose to water, are described in the following subsections. In general, they can be expressed as the product of a radiometric quantity multiplied by an interaction coefficient [27].

1.2.1. Air kerma (K_{air})

The quantity "kerma" (an acronym for Kinetic Energy Released per unit MAss), *K*, characterizes the energy transferred to a given material by a beam of indirectly ionizing radiation (photons or neutrons). It is the quotient of the sum of the initial kinetic energies, dE_{tr}, of all the charged particles liberated by uncharged particles (photons in our case) into a mass of material, d*m*, (air in our case, and hence comes the name, air kerma, K_{air}). The unit of kerma is J.kg^{-1}, called gray (Gy), where 1 Gy is equal to 1 J.kg^{-1}. The kerma rate, $\dot{K}$, refers to the variation of kerma, d*K*, over a time interval d*t*, and has the unit Gy.s^{-1} [27].

Kerma can be expended in two distinct ways. The first is the collision kerma, K_{col}, which corresponds to the part of the initial energy of the liberated charged particles that is spent through Coulomb interactions with atomic electrons of the medium, leading to ionizations and excitations along their track. The second is called the radiative kerma, K_{rad}, that corresponds to the part of the initial energy of the liberated charged particles that is spent through the production of radiative photons, which carry energy far from their track. Those photons can be bremsstrahlung photons, fluorescence X-Ray photons, emitted after hard (knock-on) collisions, or, after a photon energy transfer through pair production, the part of annihilation-photon energy that corresponds to the kinetic energy of the positron when annihilated. The total kerma is therefore equal to the sum of these two components ($K = K_{\mathrm{col}} + K_{\mathrm{rad}}$) [1].

For photon beams, the total kerma at a point in a medium, *K*, can be related to the energy distribution of photon energy fluence, $\Psi_E(E)$, at the same point, given the corresponding values of mass energy transfer coefficients, (μ_{tr}/ρ), as follows:

$$K = \frac{\mathrm{d}E_{\mathrm{tr}}}{\mathrm{d}m} = \int \Psi_E(E) \left(\frac{\mu_{\mathrm{tr}}}{\rho}(E)\right) \mathrm{d}E$$

Remark

The historical quantity exposure should no longer be used, being presently replaced by air kerma for practical applications. The exposure [27], *X*, is defined as the quotient of d*Q* over d*m*, where d*Q* is the absolute value of the mean total charge of the ions of one sign produced when all the electrons and positrons liberated or created by photons incident on a mass d*m* of dry air are completely stopped in dry air. The unit of exposure is C.kg^{-1}, the older roentgen (R) unit corresponding to 2.58×10^{-4} C.kg^{-1}.

The exposure could be considered as the ionization equivalent of collision kerma for photons in air [1]. To relate these two quantities, *W*, the mean energy expended in air per ion pair formed, divided by the elementary charge, i.e. *W/e*, is introduced. The value of *W*/e for dry air is 33.97 $J.C^{-1}$ [28]. The relation between exposure and collision air kerma can then be written as follows:

$$X = \frac{dQ}{dm}[C.kg^{-1}] = K_{col,air}[J.kg^{-1}] \times \frac{e}{W}[C.J^{-1}]$$

1.2.2. Absorbed dose (*D*)

The quantity "absorbed dose" characterizes the energy imparted to matter. It is defined as the quotient of the mean energy, $d\bar{\varepsilon}$, imparted into a volume of matter by ionization radiation (sum of all deposited energies), by the mass of that volume, d*m* [27]. The absorbed dose has the same unit as kerma, namely gray [J. kg^{-1}]. The absorbed dose rate $\dot{D}$ [$Gy.s^{-1}$] is defined as the variation of the absorbed dose over a period of time d*t*, divided by d*t*.

For photons, the released secondary charged particles deposit some of their kinetic energy along their track into the volume. This energy deposition does not take place at the same location as the transfer of energy described by kerma. However, at some point in the medium, kerma could be used as an approximation of the absorbed dose. At this point, the kerma value approaches that of the absorbed dose, provided that charged-particle equilibrium (explained in the next section) exists and radiative losses are negligible, i.e. kerma and collision kerma can be considered equal.

1.2.3. Relation between kerma and absorbed dose (charged-particle equilibrium)

To attain Charged-Particle Equilibrium (CPE) in a certain volume, the number of charged particles, of a certain type and energy, entering the volume should be equal to that of charged particles leaving it. It can be shown, as demonstrated in Figure 1.6, that for a collimated photon beam impinging a given volume of matter, this situation can be obtained for distances travelled in this volume larger than the maximum charged particle range. Before, the absorbed dose starts from a very low value, and progressively builds up as more and more secondary charged particles deposit energy.

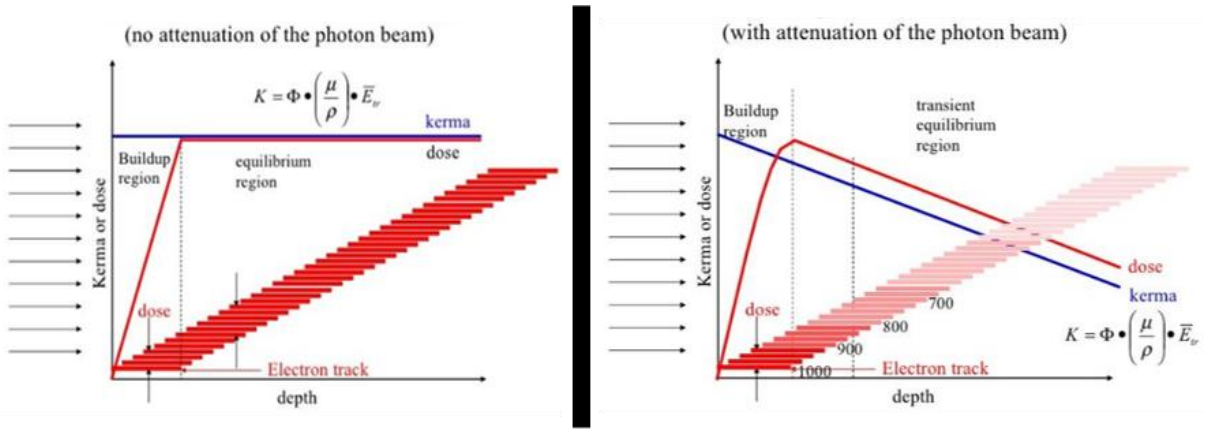

Figure 1.6. Relationship between kerma and absorbed dose, with and without significant attenuation of photon beam in matter as a function of depth in matter. Both graphs are plotted in a logarithmic scale for the kerma or dose axis.

In the volume where CPE exists, absorbed dose becomes strictly equal to collision kerma, and to kerma when radiative losses are negligible [29]. Thus, in the case where CPE is achieved, the absorbed dose, total kerma and collision kerma can be related by the following equation:

$$D = K_{col} = K(1 - \bar{g})$$

where $\bar{g}$, the radiative fraction, is the average fraction of the energy transferred to electrons that is lost through radiative processes. For dosimetric calculations, this relation could be directly related to $\Psi_E(E)$, at the same point, given the corresponding values of mass energy absorption coefficients, (μ_{en}/ρ), as follows:

$$D = K(1 - \bar{g}) = \int \Psi_E(E) \left(\frac{\mu_{\text{tr}}}{\rho}(1 - g)\right) dE = \int \Psi_E(E) \left(\frac{\mu_{\text{en}}}{\rho}\right) dE$$

1.2.4. Low-energy photon specificities (dosimetry of low-energy photons)

The low-energy range of X-Rays refers to X-Ray beams with half-value layers (HVL, presented later in section 2.4.1.2) of up to 3 mm of aluminum and generating potentials of up to 100 kV. The division into low- and medium-energy ranges is intended to reflect the two distinct types of radiation therapy for which kilovoltage X-Rays are used, i.e., 'superficial' and 'deep' ('orthovoltage'). The boundary between the two ranges is not strict and has an overlap between 80 kV, 2 mm Al and 100 kV, 3 mm Al [30].

Low-energy photons have some main specific properties that govern their dosimetry formalism. The photoelectric effect becomes significant and even can be the predominant interaction over the Compton effect. It varies strongly with both photon energy and atomic number. This energy dependence requires a greater knowledge of the photon energy fluence spectrum, $\Psi_E(E)$, and its variation over depth inside the material. Thus, kerma will vary noticeably with changing photon energy (especially for materials with high atomic number).

In this range of energy, bremsstrahlung production is negligible in water and air [31,32] (i.e. $\bar{g} = 0$). This means that, the mass energy transfer coefficient and the mass energy absorption coefficient are equal ($\mu_{\text{en}} = \mu_{\text{tr}}$), and hence, the relation between the kerma and the collision kerma becomes: $K = K_{\text{col}}$.

Photon mean free paths in this energy range are much higher than the ranges of the electrons which they produce. Therefore, charged particle equilibrium is easily established in volumes in which the photon fluence can be considered homogeneous [33]. Thus, with no bremsstrahlung and with CPE established, we can conclude that kerma and absorbed dose are equal after a very short penetration depth (depends on charged particles range) in an irradiated medium.

1.3. Dosimetry of kilovoltage X-Ray beams

For the dosimetry of low-energy photons, two types of dosimeters are discussed in this section. On the one hand, the **primary standard dosimeters**, which refer to instruments of the highest metrological level, provide an absolute value of the quantity to measure and require no calibration in terms of the quantity of interest, and on the other hand, **secondary (as a transfer or relative) dosimeters,** which are used along with the primary standard, are to be calibrated in a reference beam and are then used for measurements in users' practical conditions in institutes and hospitals.

Relative secondary dosimetry is used to determine, in relative terms, the radiation dose at a point (1D), or dose distributions in a plan (2D) or in a volume (3D). To convert the relative value of a relative dosimeter into an absolute dosimetric quantity, a calibration coefficient is to be applied.

The following sections discuss first the instruments used for the primary and transfer measurements of low-energy X-Ray beams. Then, the most widely recognized relative (secondary) dosimeters, used for relative dosimetry (with a focus on the one specifically used in the present study), are presented. At last, a section about Monte Carlo simulation codes that are used as an additional tool to characterize radiation beams in dosimetric terms.

1.3.1. Primary standards for low-energy X-Ray beams

The Free-Air ionization Chamber (FAC) is the reference instrument (primary standard) for air kerma measurement in low-energy X-Ray beams [29,34]. The notion "free-air" is due to the absence of influence, in principle, of the chamber window or walls, and hence, the interactions of photons and secondary electrons are expected to occur almost exclusively in air. FACs essentially allow to measure the quantity exposure, yet the quantity air kerma is mostly used [35]. There are different types of FACs. The model mostly used is the plane-parallel type. In this work, a plane-parallel plate free-air chamber is used. This FAC, named WK07, was developed and characterized at LNHB, in a previous work of W. Ksouri [36], for reference air kerma measurements for low-energy photon beams.

A schematic plan view of a plane-parallel type FAC is shown in Figure 1.7. To measure the air kerma of an X-Ray beam, the diaphragm at the front of the FAC is aligned with the central axis; it delimits the cross section of the photon beam which enters the chamber. Those photons that enter the diaphragm aperture interact with air in the chamber and produce secondary electrons (e.g. $\mathbf{e_1}$, $\mathbf{e_2}$, $\mathbf{e_3}$). In the chamber, a high voltage is applied between two electrodes consisting of parallel plates. The collection electrode, connected to an electrometer, is isolated from the rest of the lower plate establishing the guard electrodes. This defines a region of air, of length l, so-called the collection volume (shaded and marked V'), from which charges are collected and measured as ionization current [29]. The volume V, named the interaction volume, is defined as the intersection of the collection volume V' and the volume occupied by the beam. In order to know V accurately, the electric field lines must be strictly parallel; this is ensured by correcting the electric field distortions by applying adapted voltages to the wires surrounding the volume of air.

While electrons are slowed down, charges are liberated and swept in the electric field between the plates. The parallel plates are equidistant from the X-Ray beam axis. Their distance from the beam is intended to be sufficiently large so that most of the secondary electrons, such as $\mathbf{e_1}$, come to rest within the air of the chamber. The ionizations produced by electrons such as $\mathbf{e_2}$ out of the collection volume, and then lost, must be compensated by charges from other electrons such as $\mathbf{e_3}$. This occurs since the chamber is designed to ensure charged particle equilibrium in this volume; air thickness before and behind the collection volume is larger than the maximum electron range.

With the preceding conditions and after correcting for some phenomena (such as: ion recombination, contribution of scattered photons, electron losses, etc.), the collected charge is equal to the charge liberated by all the secondary electrons set in motion after photon

interactions in the volume *V*. The collected charge is then proportional to the sum of the initial kinetic energies of those electrons, and hence, to the air kerma. The effective center of origin of electrons is the geometric center of *V* and *V'* called *P'*. The reference point *P* at which air kerma is to be determined is placed at the center of the diaphragm aperture. Therefore, a correction factor for attenuation in air between *P'* and *P* allows to get air kerma at this reference point P.

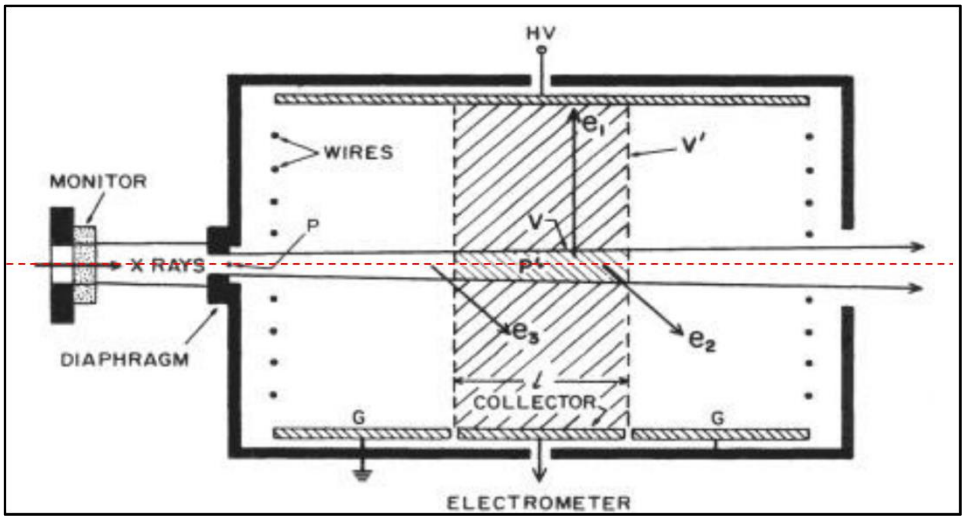

Figure 1.7. Schematic view of a typical standard free-air ionization chamber [29]

The air kerma rate in the reference plane is derived from the following expression:

$$\dot{K}_{\text{air}} = \frac{I}{\rho_{\text{air}} \cdot V} \times \frac{W_{\text{air}}}{e} \times \frac{1}{1-\bar{g}} \times \prod_i k_i \,,$$

where $I/(\rho_{\text{air}} V)$ is the specific ionization current. I is the net ionization current, i.e. the current resulting from the charges created by ionizing radiation in reference atmospheric conditions, i.e. 1013.25 hPa, 293.15 K, and 0 % relative humidity. A product of correction factors, $\prod_i k_i$, is introduced to correct for the limitations of the free-air chamber.

Some correction factors are applied to the measured current to deal with the atmospheric conditions during the measurements (k_p, k_T, and k_H respectiveley for pressure, temperature and humidity), for ion recombination (k_s) and for polarization (k_{pol}).

Further correction factors, listed below, are also applied. These factors depend on the design and operation of the free-air chamber:

- the field distortion correction factor (k_d) dealing with the potential lack of parallelism of the electric field applied between the electrodes which can impact the interaction volume (volume *V* in Figure 1.7);
- the wall transmission correction factor (k_p) dealing with the contribution to the ionization current of the radiation that could cross the walls of the chamber;
- the aperture transmission correction factor (k_l) correcting for the contribution of the radiation crossing the aperture diaphragm of the chamber;
- the scattered radiation correction factor (k_{sc}) correcting for the contribution of the photons that are scattered in the chamber volume;

- the correction factor for electron loss (k_e) dealing with the potential loss of charge due secondary electrons losing part of their initial kinetic energy out of the collection volume (volume *V*' in Figure 1.7) of the chamber (in the walls, in the electrodes);
- the air attenuation correction factor (k_a) correcting for the attenuation of the photon fluence in air between the interaction volume of the chamber and the reference point.

Moreover, the electrometer must be capable of measuring the very small output current which ranges from femto-amperes to pico-amperes, depending on the chamber design, radiation dose rate and applied voltage.

Water calorimetry is also used as a primary standard in radiation dosimetry [37,38]. It is used in LNHB for the primary measurement of absorbed dose to water for medium-energy X-Rays [39] as well as in other laboratories [40], yet the minimum energy voltage covered was of 70 kV.

1.3.2. Secondary dose measurements – transfer chambers

The secondary standard chambers recommended for low-energy X-Rays are the plane-parallel type ionization chambers. The chamber must have an entrance window consisting of a thin membrane of a thickness in the range of 2 to 3 mg/cm². The characteristics of plane-parallel ionization chambers used for X-Ray dosimetry at low energy are given in the TRS 398 [30].

The ionization chamber used in this work is the PTW soft X-Ray ionization chamber type-23342 [41], shown in Figure 1.8-A. Its energy dependence is optimized for the measurements of either kerma free in air or absorbed dose to water in a PMMA phantom. It has a very flat energy response, as shown in Figure 1.8-B, in the range from 10 kV to 100 kV, a vented sensitive volume of 0.02 cm^3, and a very thin flat entrance window of 0.03 mm polyethylene (2.5 mg/cm²).

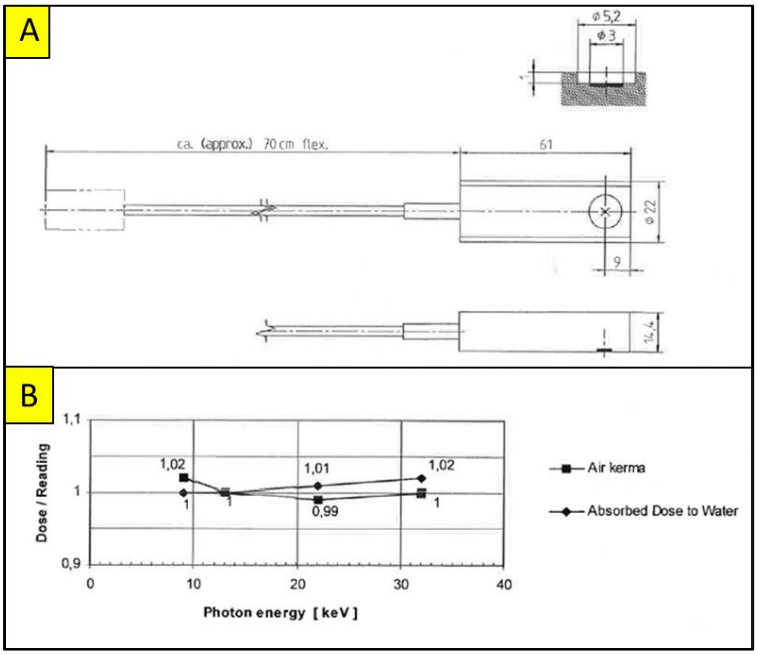

Figure 1.8. (A) Schematic view of the PTW Soft X-Ray chamber 23342. The top image shows the collection volume (Ø=5.2 mm) and the sensitive volume (Ø=3 mm) of the chamber, images at the middle and bottom are top and side views of the chamber, respectively. All dimensions are in mm. (B) Typical energy response values of soft X-Ray chamber type 23342 for air kerma and absorbed dose to water. Data are extracted from the chamber manual provided by the manufacturer [42].

1.3.3. Relative dose measurements (1, 2 or 3D)

Relative dosimetry is used to define, in a relative way, either the dose at a point (1D) or a dose distribution in a plane (2D) or in a bulk geometry (3D). To convert relative doses obtained using a relative dosimeter into absolute dose values, a calibration coefficient, traceable to a primary standard, is to be applied.

The difference, in properties, of radiation dosimeters rules their choice for relative dose measurements. Dosimeters are characterized by their accuracy and precision, dose or dose-rate dependence, energy response, directional dependence and spatial resolution [1]. Since these characteristics are more or less achieved by one dosimeter to another, the choice of the proper dosimeter should take into account the measurement conditions, radiation type and the radiation properties; for example, ionization chambers are recommended for beam calibrations (reference dosimetry as in the previous section) and other dosimeters are particularly suitable for the evaluation of spatial dose distributions or for dose verification.

1.3.3.1. Detectors for 1D and 2D dose measurements

A range of dosimeters are available for relative dose measurements in the domain of low-energy X-Ray beams. Thermoluminescent dosimeters and radiochromic films are among the most widely recognized dosimeters for 1D and 2D measurements, respectively. These two detectors are presented in this section.

ThermoLuminescent Dosimeters (TLDs) are largely used in radiation dosimetry measurements. They are based on the phenomena of thermally activated phosphorescence [1]. They are available in different forms (e.g. ribbons, chips, etc.) and made of different materials such as LiF:Mg,Ti, $Li_2B_4O_7$:Mn and $CaSO_4$:Dy. TLDs have the properties of being small in size, reusable, near tissue equivalent for most beam energies and of high sensitivity. However, many TLDs have a large variation in energy response for low energy X-Ray beams [43,44]; the variation in response is up to 40 % for X-Ray beams in the energy range from (20–250) keV compared to cobalt-60 [45].

TLDs have been used for the dosimetry of kilovoltage X-Ray beams with applications including measurements of skin doses, dosimetric verification within tissue equivalent phantoms, for comparing against planning system (TPS) calculations, and quality assurance testing of kilovoltage X-Ray beams [46]. TLDs have also been used to measure backscatter factors (BSF)s of kilovoltage X-Ray beams [47].

The radiochromic film, used for almost 30 year [48], is a well-known type of film for 2D relative dosimetry determination. The most commonly used one is the GafChromic film. It has a nearly tissue equivalent composition that changes color upon exposure to radiation [1]. Among their several advantages, radiochromic films offer a high spatial resolution suitable for the measurement of steep dose gradients around brachytherapy sources [49].

Radiochromic films have also been used in the photon low-energy range with IORT devices. A study with an INTREABEAM® source has revealed significant changes in the response of several radiochromic film types for small changes in the X-Rays spectrum [50]. This is in contrast to previous studies which have reported smaller or negligible energy dependence for similar film types [51,52]. Another study with “Papillon 50” reported the high heterogeneity of applicator shapes that may prevent the proper use of traditional measurements

such as those from EBT2 films [53]. Thus, although radiochromic films provide a convenient and relatively quick mean to measure relative dose distributions, their use should be considered with caution regarding the different aspects just mentioned.

1.3.3.2. 3D dose measurements

It is possible to perform dosimetric measurements in all three dimensions using several dosimetric methods. Quasi-3D dosimetry was achieved by interpolating points or 2D detectors measurements, such as: TLDs, ion chambers and films [54,55]. However, isotropic and high-resolution 3D dosimetry is not readily achievable with these methods without a prohibitive amount of effort. Gel dosimeters are the only dosimeters capable of providing this high-resolution dose distribution in the three dimensions, without needing inter- or extra-polation, unlike TLD or films.

Gel dosimeters are based on quantifying the effects of radiation-induced chemical changes occurring within some volume of material [56,57]. The amount of the chemical changes must be related to the absorbed dose, these changes must be able to be spatially fixed and localized in the irradiated volume by some imaging technique [58]. Their use for clinic applications requires high reproducibility and stability.

The choice of a relative dosimeter instead of another is based on several criteria, such as spatial resolution, accuracy and precision. Among them, gel dosimeters are those providing the most advantageous properties for measurements in terms of absorbed dose to water around an isotropic source. Actually, it can easily be shaped around the INTRABEAM® source and applicators, and provide a good spatial resolution in all 3 dimensions, as will be seen in this work.

Several gel dosimetry systems are currently used. Three major classes of chemical dosimeters are available: the Fricke-based and Polymer gels, which are mostly investigated, and more recently, the novel radiochromic dosimetry systems. These dosimeters can be associated with one or more readout (imaging) methods to form a 3D dosimetry system. The principles of these three dosimeters and main readout systems are summarized in Table 1.2 and discussed in the following sections.

Table 1.2. **A review of the main classes of 3D chemical dosimeters. It shows the basic mechanisms for interaction and conventional readout mechanisms (with typical dose sensitivity). The dose sensitivities listed are rough ranges only as the sensitivity for a given dosimeter is highly dependent on the system preparation and readout details. More complete summaries detailing these characteristics are available in instructive reviews [56,59,60]. The acronyms for the polymer gel dosimeters follow common convention [56]. Table extracted from L J Schreiner article [58].**

Class	Dosimeter		Readout		
	Basic mechanism	Usual Stabilizing substrate	MRI ($s^{-1}Gy^{-1}$)	Optical CT ($cm^{-1}Gy^{-1}$)	X-ray CT ($HUGy^{-1}$)
Fricke Gels			Δ relaxivity	Δ absorbance	N/A
Fricke	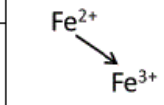	Gelatin or agarose	~0.04 (R1)	~0.01	
Fricke Xylenol			~0.009 (R2)	~0.1	---
Polymer Gels			Δ dynamics and structure	Δ scatter	Δ density
PAG, PAGAT, MAGIC, NIPAM, VIPAR, BANG etc.	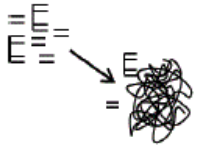	Gelatin or agarose	~0.1 – 1.0	~0.1	~0.25 – 0.85
Novel Radiochromic systems			N/A	Δ absorbance	N/A
Plastic	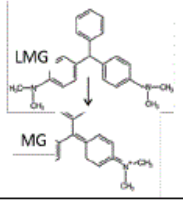	polyurethane	---	~0.01-0.05	---
Silicone		Poly-dimethyl-silocane	---	~0.01	---
Micelle gel	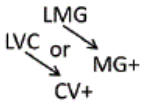	Gelatin +micelles	---	~0.003-.007	---

A. The three-major 3D chemical dosimeters

i. Fricke-based gel dosimetry

3D Fricke (or ferrous sulfate) dosimetry is based on the oxidation of ferrous ions into ferric ones under irradiation by reaction with water radiolysis products. It was first proposed by Gore *et al.* [61] who investigated the Nuclear Magnetic Resonance (NMR) relaxation properties of irradiated Fricke solutions. They showed that radiation-induced changes, where ferrous ions (Fe^{2+}) are turned into ferric ions (Fe^{3+}), could be quantified using NMR measurements, since ferric ions have a greater influence on proton relaxation times than ferrous ions. This work enabled the imaging of 3D dose distributions by Magnetic Resonance Imaging (MRI) after the dispersion of Fricke solutions into a gel matrix [62].

The use of Fricke-based gel dosimeters suffers from the diffusion of Fe^{3+} ions in gel, which restricts the time between irradiation and measurement to one hour, including acquisition time [63,64]. Moreover, this restriction tends to limit the use of Fricke gel dosimeter to entities that have an access to a MRI device.

To overcome these issues, a new generation of Fricke based gel dosimeters had arisen, which can be imaged by cheaper, benchtop optical systems. This was achieved after the addition of a metal ion indicator agents (e.g. xylenol orange) to the Fricke solution, which led to a visible color change in the presence of ferric (Fe^{3+}) ions [65]. For example, Kelly *et al.* [66] demonstrated the feasibility of 3D Optical-Computerized Tomography (OCT) in the dosimetry of Fricke-Benzoic-Xylenol (FBX) gels, where they achieved sub-millimeter spatial resolution and corresponding dose measurement accuracy of within 5 % in the dose range 1 to 10 Gy. Moreover, the addition of these agents improves significantly the stability of the spatial dose information. This happens due to the reduction of diffusion coefficient of the Fe^{+3} ions [67].

To conclude, Fricke gel dosimeters have many attractive features. They are relatively easy to prepare without special facilities, are tissue equivalent over a very large photon energy range, non-toxic, manufactured in a normoxic environment and are readily probed by readout techniques very soon after irradiation [68–70]. However, the diffusion, over time, of ferric ions can lead to errors in the dose distribution measurements if readings cannot be undertaken within a few minutes or hours after irradiation. It is mainly to meet this need that the use of polymer gels has arisen.

ii. Polymer gel dosimetry

Polymer gel dosimeters have been proposed in 1993 as materials that can integrate a radiation dose distribution in three dimensions [71]. This proposal came after successive studies on the effect of ionizing radiation on polymers and associated readout techniques [72]. The first 3D dosimetry work proposed the 'BANG' polymer gel formulation, in which the monomers acrylamide and N,N'- methylene-bis-acrylamide are mixed with a jellifying agent in an aqueous solution [71]. These polyacrylamide gels, or PAG gels, are commercially available as BANG® gels (MGS Research, Inc., Madison, CT).

Since then, many different variations in the gel composition have been tested and used. Their main constituents are water, monomers and a gelling agent. The gelling agent forms a 3D matrix into which the monomers are dispersed.

Under irradiation, water radiolysis generates free radicals and molecular species [69]. Free radicals create reactive monomer ends which bind to neighboring monomer molecules in a polymerizing or cross-linking reaction. Polymer microparticles continue to grow until a termination reaction occurs. Since the polymerization reaction continues well after irradiation has finished, dosimeters are often imaged about (> 12-24 hours) after irradiation, when the gel is relatively stable [58].

Several refinements have been introduced to the polymer gel system material compositions, targeting improvements in main areas such as: decreasing the negative impact of oxygen (MAGIC gel [73]) and increasing the gel radiosensitivity (NIPAM gel [74]). An overview of the improvements and on the compositions of polymer gel dosimeters can be found in several publications [60,75].

Polymer gel dosimeters are radiologically soft-tissue equivalent and exhibit a linear dose response [60]. Some of them are commercially available [58,60]. The 3D radiation dose distribution of polymer gels may be imaged using MRI, OCT, X-Ray CT or ultrasound [60,76]. They present a considerable advantage, by their great stability over time after stabilization that, notably, they solve the problem of reading time which is inherent to Fricke gel dosimeters.

However, polymer gels are more difficult to prepare. They actually contain toxic constituents and usually require anoxic conditions during preparation of oxygen scavengers. It is, thus, more difficult to obtain a reproducible preparation than for Fricke gels.

iii. Novel radiochromic systems

As mentioned earlier, radiochromic materials exhibit a color change when exposed to ionizing radiation. Since the first Fricke gels with metal ion indicator addition, works on new radiochromic 3D dosimeters have come up. This section covers briefly two of them: radiochromic plastic and micelle gel.

A promising system for routine clinical 3D dosimetry is the radiochromic plastic, Presage™ [77]. This system is robust and available for purchase, eliminating the need for a preparation in laboratory. It has passed through continuous improvements in optical quality and tissue equivalence from subsequent formulations. It is characterized by high dose sensitivity, linearity (independent of both photon energy and dose rate) and lack of diffusion.

Jordan and Avvakumov [78] and Babic *et al.* [79] have proposed another approach where the color dye and halogen are dissolved in a gel when embedded in micelles. The advantage of these dosimeters is their tissue equivalence over a wide range of photon energies. In addition, the fabrication procedure is less complicated (than that of polyurethane-based dosimeters as Presage™ for which dedicated equipment is needed) and hence, more practical to implement in a clinical environment [80]. Moreover, the absence of an exothermic reaction during fabrication results in a better optical homogeneity [81]. However, these dosimetric systems can be read by optical techniques only, which may limit their use under certain conditions

B. Readout methods

A dosimetric system, as previously stated, is comprised of a material that exhibits a physical response to radiation that can be quantified, and a readout (imaging) system that can read these changes. Three main readout systems are currently associated with 3D chemical dosimeters, discussed above: Magnetic Resonance Imaging (MRI), Optical Computer Tomography (OCT) and X-Ray CT.

MRI was the first imaging modality utilized for 3D gel dosimetry with Fricke gels [61]. This technique is thoroughly explained in section (2.3.3.3.1). MRI and X-Ray CT techniques were developed primarily for medical applications which then stirred their application as imaging modalities for 3D radiation dosimetry. However, the development of OCT was retarded to the late 1990's where the required technology to perform measurement with such technique commenced to be feasible and efficient [82]. The technique of **OCT**, well explained by is analogous to the more familiar **X-Ray CT**, except using visible light as the imaging radiation. In both optical and X-Ray CT, line integrals of attenuation are acquired at various views through the object to be imaged. The main differences include the methods of production and detection of either the X-Rays or visible light, and also the scanning configurations [68,83].

Both OCT and X-Ray CT methods are potentially susceptible to several artifacts: including stray radiation, beam hardening, attenuation, etc. [84,85]. The primary advantages of OCT, when compared to MRI, are substantially reduced costs, increased accessibility, and potentially higher accuracy and precision in shorter imaging times [83]. However, the constraints on phantom size and reading modality put MRI imaging in favor for this work; this is especially

true for all works using large phantoms with complex forms and/or integrated objects that cannot be removed before reading.

The dosimetric system used in the current study is a Fricke-based gel with MRI readout technique. Elucidation over the gel choice and characteristics with a comprehensive description of the MRI technique are given later in the next section (2.3.3.3).

Still, the main limitations to MRI 3D dosimetry of Fricke gels are the difficulty of generating low-noise images, with high spatial resolution. Then, expertise in MRI was identified to be a prerequisite for accurate 3D dosimetry [86]. While some expertise is necessary, the prospect has been greatly simplified by the recommendations in a recent report of De Deene [87].

In conclusion, 3D radiation dosimetry is an example of an area that requires considerable experience in three separate fields: polymer and/or Fricke chemistry, radiation physics and the quantitative use of a mastered readout technique. There are thus significant pitfalls in sample preparation and handling, in the design of the irradiation and experimental protocols and in the analysis of quantitative data [60]. In particular, as with all chemical dosimeters, the dose response is sensitive to the preparation and can change if the manufacturing conditions are even slightly altered (as a change in chemical suppliers or in timing of a given stage at a given temperature).

1.3.3.3. The gel dosimetry method used for this study

This section presents the dosimetric gel used in the current study and the associated MRI readout technique. This section comprises three parts. The first one covers the gel characteristics and principle. The second one covers the imaging device and process, along with the used MRI readout parameters. The third and last part described the principle used to convert the gel response into a quantity related to the absorbed dose in the gel.

1.3.3.3.1. Gel characteristics and principle

The dosimetric gel used in this work is a Fricke hydrogel, with 80 % of water. It has been developed by the University Paul-Sabatier of Toulouse in collaboration with the CRLCC Jean-Perrin in Clermont-Ferrand and the LNHB. This gel was previously characterized for the high-energy photon range in another study [88].

As mentioned before, the use of the gel as a dosimeter is based on the oxidation of ferrous ions into ferric ions resulting from the reaction with radicals formed under irradiation. The variation of the proton-spin relaxation behavior in the gel, measured by Nuclear Magnetic Resonance (NMR), is dependent on the concentration of paramagnetic ion species (notably Fe^{3+}). These ions have different magnetic susceptibilities and, hence, perturb the relaxation of neighboring water protons differently. Thus, since the concentration of the ferric ions changes under irradiation, the observed variation in NMR relaxation rate is dose dependent.

The used gel has been chosen due to different characteristics: the previous knowledge about the gel, its capability to be shaped in various forms, its nontoxicity and its simplicity to be prepared and used. Furthermore, its density of 1.08 ± 0.01 g/cm^3 makes it a good water equivalent.

However, as said before, Fricke gels are known as being subject to diffusion effects that may induce a loss of spatial information of dose distribution. The stability of the spatial information of the developed dosimetric gel depends basically on the diffusion of the paramagnetic agents which is so governed by several factors. These factors are either connected to the concentration of various gel components or to the preparation and transfer conditions (temperature, exposure to air, knocks, etc.). However, this gel (with a specific composition) showed low diffusion within a few hours after irradiation under stable temperature conditions i.e. 20 °C ± 4 °C (diffusion speed of about 9.10^{-11} $m.s^{-1}$), and a favorable reading practice (MRI machine very close to the irradiation local).

After the irradiation process, the gel response is read using the MRI technique. This readout process is detailed in the next part.

1.3.3.3.2. Magnetic Resonance Imaging (MRI)

MRI was adopted here as the reading method due to the previous usage-knowledge developed alongside with the dosimetric gel, its ability to read phantoms of different sizes and forms, and its accessibility. The basic MRI imaging principles, the device used and the corresponding parameters are presented in this part.

MRI is based on the variation in relaxation behavior of hydrogen nucleus, with one proton, which has the strongest magnetic moment and abundance in organic tissues. In the absence of an external magnetic field, the hydrogen nucleus has a net magnetic moment that is randomly oriented. However, when an external magnetic field, B_0, is applied, it aligns the majority of nuclear spin magnetic moments along the field axis, as seen in Figure 1.9-a. Applying a radiofrequency pulse creates a non-equilibrium state i.e. excitation, due to energy added to the system, inducing a precession of a magnetic moment, and leading to the production of a radiofrequency wave, Figure 1.9-b. This wave is measured, in the transverse (XY) or longitudinal (OZ) planes, while magnetic moments get back to their initial state (relaxation) after the pulse is switched off.

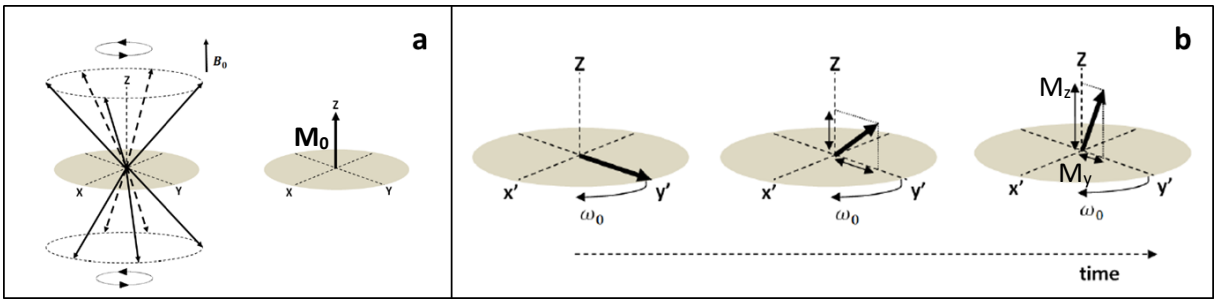

Figure 1.9. (a) Magnetization represented by vectors. (Left) individual magnetization vectors are randomly distributed around a cone with respect to the B_0 (z) axis. The vector sum of all the individual magnetization vectors (Right) is simply a static component in the direction of B_0.

(b) (Left) magnetization vector after a 90° RF pulse about the x-axis. (Center) T_1 and T_2 relaxation times of the magnetization after the pulse has been applied, result in an increased M_z component and reduced M_y component, respectively. (Right) After further time, the M_z and M_y components have almost returned to their equilibrium values of M_0 and zero, respectively [89].

Either transverse (spin-spin, T_2) or longitudinal (spin-lattice, T_1) relaxation times can be measured, and hence, either R_2 or R_1 relaxation rates, respectively, are deduced, as follows:

$$R_2 = 1/T_2 \text{ and } R_1 = 1/T_1$$

Both these relaxation rates depend on the chemical environment of the protons. That is why oxidation-reduction reactions of Fe^{2+} into Fe^{3+}, resulting from radiolysis reactions of water into the gel, induce variations of the measured relaxation rate between before and after an irradiation, and thus, permit 3D dose distribution measurements. Despite the fact that R_1 imaging is faster and has higher dynamic range (low signal-to-noise value) than R_2 imaging [68], the measured value was the R_2 relaxation rate. This choice was due to the knowledge already acquired by LNHB in gel dosimetry with R_2 imaging.

The variation in gel response, ΔR_2 induced by irradiation, is calculated by subtracting the gel response before irradiation from the value obtained after. Thus, with R_2, the gel response for a specific volume element (called "voxel") after irradiation, and $R_{2,0}$ the gel response for the same voxel before irradiation, the variation in gel response can be calculated using the simple following relation:

$$\Delta R_2 = R_2 - R_{2,0}$$

The optimized (in terms of signal-to-noise ratio) sequence used for reading the dosimetric gel is a Multi-Spin Echo (MSE), described in Figure 1.10. In this MSE, the first pulse flips the magnetic moments by 90°, in the XY plane. Subsequently, several pulses of 180° (corresponding to the Number of Echoes, NoE) follow the 90° pulse. These pulses are separated by a time TE (Echo Time), to invert the magnetic moments. The chain of pulses can be launched several times (number of excitations: NSA) with a waiting time between them called repetition time (TR). Finally, to measure the signals (echoes) from the gel phantom, a coil is used. The coil is the piece that makes the pictures. After the radiofrequency is transmitted into the gel phantom, the coil acts as an antenna to receive the radio frequency signal coming out of the gel phantom and transmits that data to a computer which then generates corresponding images.

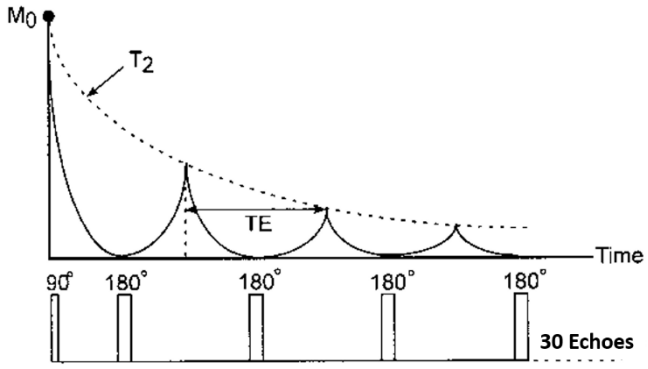

Parameter	Chosen Value
NSA	**2**
NoE	**30**
TR/TE [ms]	**2000/11**

Figure 1.10. A scheme of the MRI Multi-Spin Echo sequence used in this work and its corresponding parameters.

The signal, corresponding to the NoE echoes, is measured within predefined voxels whose dimensions correspond to the measurement spatial resolution and are defined by the user. The smallest voxel size is mainly limited by the strength of the MRI machine magnetic field. The MRI reading process is performed slice by slice, a slice being composed of all the voxels belonging to any defined plane (as shown in Figure 1.11). The thickness of the slice thus corresponds to that of the voxel called here "e".

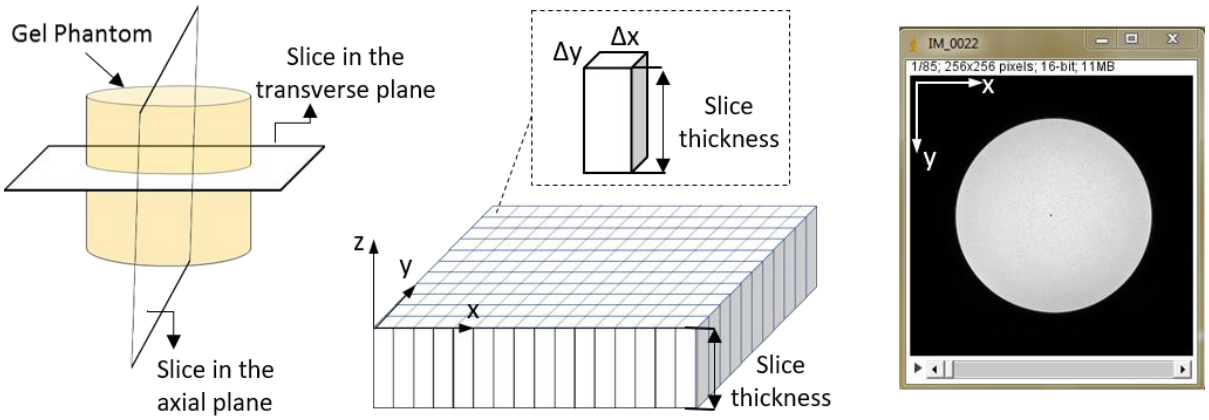

Figure 1.11. Scheme of MRI data acquisition: (left) chosen studied phantom slices, (middle) a slice divided into elemental volumes called voxels and (right) a real acquired slice image depicted using the ImageJ software.

Finally, the signal measured in each voxel is saved into a 2D data matrix, whose indices correspond to the position coordinates of the voxel in the slice (as shown in Figure 1.11). All those data are stored in a standard DICOM image (Digital Imaging and Communications in Medicine).

The DICOM data analysis and the determination of the gel response are presented in the following parts.

1.3.3.3.3. Principle of R_2 determination

The transverse relaxation rate value, R_2, represents the response of the gel to the absorbed dose received in each voxel of the gel and hence is the value to be determined. For the case of MSE sequence, the signal of each voxel is measured NoE times at the corresponding measurement time, t. So, with $S(t)$ the signal measured at time t after the first echo and S_0 the signal measured at $t=0$, the measured signal of each echo satisfies the following equation:

$$S(t) = S_0 e^{-t/T_2}$$

To ease the treatment of the results, the following equation is rather used to obtain the transverse relaxation rate R_2.

$$\mathrm{Ln}(S) = \mathrm{Ln}(S_0) - R_2 \cdot t$$

The linear function, $\mathrm{Ln}(S) = f(t)$, that fits the best all the NoE values of Ln(S), as a function of t, is then defined. The relaxation rate, R_2, corresponds to the slope of this linear function (as shown in Figure 1.12). To study the gel response in a slice, either over a partial region or in the whole slice, the R_2 calculation process, described above, is repeated for each voxel in the slice.

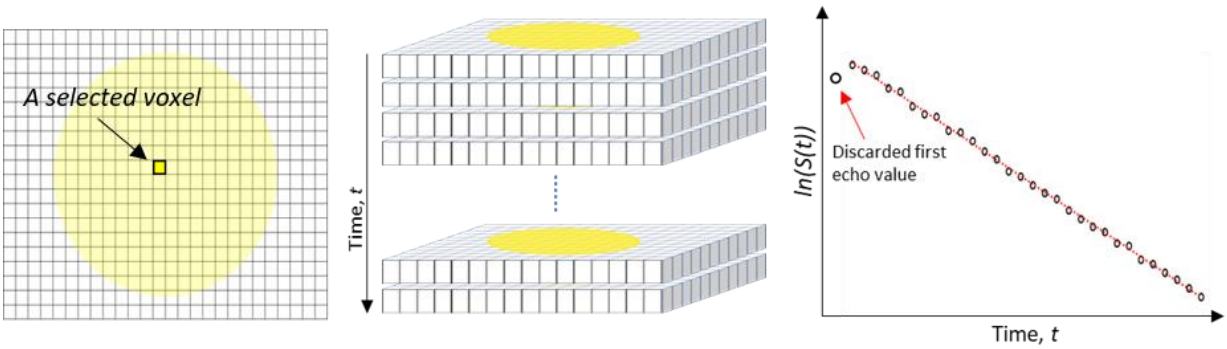

Figure 1.12. Calculation process of R2 value for a specific voxel: (left) scheme for a voxel over the data matrix of one echo, (middle) all data matrices formed for echoes over the sequence time and (right) linear fitting of the corresponding voxel data to define (*t*).

Artifacts inherent to gel dosimetry measurements using MRI can lead to R_2 inaccuracies [1]. Artifacts can be attributed to different sources that can be either machine or object related. Some of them can be handled by working in conditions that limit their impact. This can be, for example, stabilizing the gel at room temperature and using fast sequences to limit the temperature drift while MR imaging, or reading the gel within a limited duration to avoid ionic diffusion inaccuracies. The B_1-field, generated by the radiofrequency reading wave, may also be a source of inaccuracies since it may spatially vary according to its penetration in the object to be imaged, to the coil geometry or to the sequence [1]. This inhomogeneity of the B_1-field can be characterized by imaging the considered object in such conditions that the R_2 distribution is expected to be constant. Such conditions can be obtained by imaging a homogeneous object that is either not or uniformly irradiated. The deviation of the resulted R_2 distribution from a constant (generally considered as equal to the R_2 value measured at the center of the coil) gives the correction factors distribution to apply to correct for the spatial B_1-field inhomogeneity. It has to be noticed that the correction factors distribution can only be applied to images obtained under matching configurations of image acquisition (i.e. MRI sequence parameters, coil type, phantom size and position inside the coil, etc...).

1.3.4. X-Ray beams spectrometry

The accurate determination of the photon energy spectrum, at the point of interest, has a great impact in radiation dosimetry. In the photon low-energy range, it is essential to ensure the beam quality to guarantee a correct traceability and comparison of the delivered doses between dosimetry laboratories and/or end users; any fluctuation in the photon beam energy could have an important impact on the dosimetric quantities, due to the large variation of dosimetric parameters values in this energy range. Moreover, photon energy spectra are also used to calculate many correction factors to assess measured dose values [36,46,90].

Characterizing an X-Ray spectrum enables to define the energy distribution of the energy fluence. This is carried out by either measurements or calculations. In the current study, both approaches were used. Though, the experimental method, by photon spectrometry, was preferred, since it is more reliable. Actually, there is a lack of details about X-Ray tube components and their possible gradual deterioration with time, which can hardly be modelled in calculations.

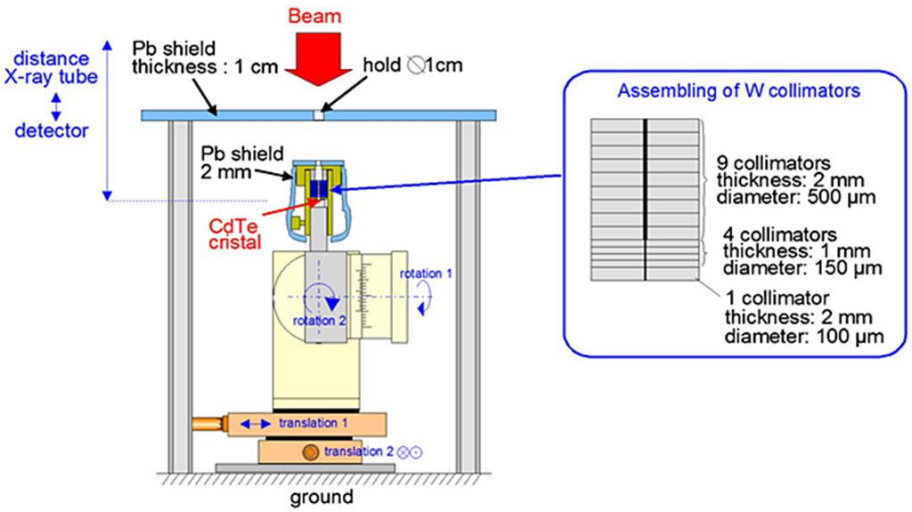

Figure 1.13. Scheme of the CdTe detector used, collimated and mounted on a positioning system. Small collimators used are in tungsten (assembling shown in the zoomed region as an example), and the lead shields were added to eliminate the scattered photons in the vicinity of the detector. Image extracted from J. Plagnard's article [91].

The spectrometry system used in this study has been previously developed and thoroughly described in previous works at LNHB [91,92]. This system, described in Figure 1.13, consists of a cadmium-telluride semiconductor detector (CdTe) connected to the digital signal processing module "LYNX" supplied by Canberra for spectra acquisition. The corrections for distortions of measured spectra, by artifacts associated with the detection processes, i.e. pile-up, fluorescence X-ray photon escape, intrinsic detector efficiency, etc., are achieved by applying several developed correction algorithms. The corrections of fluorescence escape are mainly related to the escape of the K-shell fluorescence X-ray photons of cadmium and tellurium (the minimum energy to create K-shell fluorescence photons is 26.7 keV for cadmium and 31.8 keV for tellurium) emitted after the photo-electric interaction in the CdTe detector. Moreover, in order to limit the high-count rate of incoming photon flux, and hence, limit the pile-up distortion, a very small solid angle (less than 5×10^{-5} sr), resulting from an optimal layout of source-to-detector distance (SDD) and small collimation (in the order of hundredths of micrometers in diameter) is adapted for each measurement. To ensure the good alignment between the collimator and the beam axis, a specific automatic positioning system was developed which includes two automatic rotation stages and a devoted Labview® program. This positioning system enables to find, and then to adjust the detector position, to the point where the detector window faces the highest count rate along the source-detector axis.

1.3.5. Monte Carlo simulations

Monte Carlo (MC) methods rely on computational algorithms based on generation of random samplings to calculate numerical results. In the domain of radiotherapy and dosimetry, the MC method provides a numerical solution to the Boltzmann transport equation that directly employs the fundamental microscopic physical laws of electron-atom and photon-atom interactions [93]. Therefore, a solution is determined by random sampling of the relationships, or the microscopic interactions, until the result converges. Thus, the mechanics of executing a solution involves repetitive actions or calculations [94].

The most commonly used Monte Carlo codes for radiation transport calculations are EGSnrc [95], GEANT4 [96], MCNP(X) [97] and PENELOPE [98]. They are all available at LNHB. Since these codes differ in their calculation algorithms, particle tracks, and cross-

section libraries, significant differences could be observed in results, especially in the domain of low energy X-Rays and in the proximity to the source [99]. Moreover, the use of updated cross-section libraries led to positive effects in reducing these differences [100].

The PENELOPE code was preferred for this study due to several motives. It has been already benchmarked, and its feasibility approved for the study of radiation dosimetry in the region of low-energy X-Rays [99–101]. The accuracy of the PENELOPE code in predicting the X-Ray spectra was also evaluated, by comparison with experimental data and theoretical calculations, and simulation results were shown to be in a close agreement with experimental data [102,103]. In addition, the PENELOPE code has previously been used successfully at LNHB for the simulation of low-energy photons [36,90,92].

PENELOPE was developed at the University of Barcelona by Francesc Salvat, José Maria Fernandez-Varea and Josep Sempau in 1995, initially for the transport of electrons and positrons under the name PENetration and Energy LOss of Positrons and Electrons. Photon transport was later implemented. The version used for this work is the version 2006 [98], which allows the transport of photons and electrons over a range of energy ranging from 50 eV to 1 GeV.

A modified version of the PENELOPE computer code system was used in this study. This specific version [104], based on the Penmain program, includes the integration of several variance reduction techniques and provides the possibility to work in parallel computing by distributing the calculations on 16 to 32 processor units of the calculation cluster. This version is used at LNHB and LM2S (Laboratoire de Modélisation et Simulation des Systèmes, CEA, LIST) laboratories.

The simulation of electron and positron transport is much more difficult than that of photons. This is mainly due to very small average energy loss by electrons and positrons in a single interaction (of the order of a few tens of eV). As a consequence, high-energy electrons suffer a large number of interactions before being effectively absorbed in the medium. In practice, detailed simulation is feasible only when the average number of collisions per track is not too large (say, up to a few hundred). Therefore, multiple-scattering theories, which allow the simulation of the global effect (referred to as “condensed”) of a large number of events in a track segment of a given length (step), are implemented in the simulation code to accelerate the calculations.

In PENELOPE, photon transport is simulated by means of the conventional detailed method. However, the simulation of electron and positron transport is performed by means of a mixed procedure. Hard interactions, with energy loss greater than pre-selected cutoff values are simulated in detail. Soft interactions, with scattering angle or energy loss less than the corresponding cutoffs, are described by means of multiple-scattering approaches.

1.4. Dose metrology of low-energy photon beams

Metrology is the science of measurement, embracing both experimental and theoretical determinations at any level of uncertainty in any field of science and technology [105]. It has a vital importance in assuring the efficient and reliable operation of systems and products of all fields. An international treaty known as the convention of the metre (convention du mètre) was established in 1875 to strive for an international agreement on metrological issues [106]. This

treaty founded the International Bureau of Weights and Measures (Bureau International des Poids et Mesures, BIPM) and remains today the basis of international agreement on units of measurement and international metrological traceability [107]

The ionizing radiation department at the BIPM was established in 1960. The widespread use of ionizing radiation in different fields, especially related to human health and nuclear energy production, led to the importance of establishing such a department to assure international consistency and traceability of ionizing radiation measurements. Its principal activity is to maintain the international reference standards for dosimetry and activity measurements. The Department also undertakes calibrations of national secondary standards for some Member States, and organizes and/or participates in international comparisons under the auspices of the Consultative Committee for Ionizing Radiation (CCRI).

All countries that use ionizing radiation are not directly linked to the BIPM. A worldwide network is established to extend the dissemination of radiation standards as widely as possible; this network is exposed in the next part.

1.4.1. The metrological chain of traceability for dosimetric quantities

1.4.1.1. Different actors

Primary Standard Dosimetry Laboratories (PSDLs) are equipped to realize primary standards, i.e. standards that require no calibration in terms of quantities related to their field of metrology. They validate their standards through international comparisons with other PSDLs, generally carried out under the auspices of the BIPM or of the Regional Metrology Organizations (RMO) such as the EURopean Association of national METrology institutes (EURAMET) in Europe, the Inter-american Metrology System (SIM) in America, or the Asia Pacific Metrology Programme (APMP) in Asia and Pacific. Once the PSDLs have validated their standards, they can transfer them. However, in the field of ionizing radiation dosimetry, there are only about twenty countries with PSDLs, and hence, they cannot calibrate all the dosimeters in use. Therefore, PSDLs usually provide calibrations to Secondary Standard Dosimetry Laboratories (SSDLs), which in turn, calibrate the reference instruments of users (and in some cases directly to end users). Moreover, for the member states of the metre convention that do not hold primary standards, their national standards can be calibrated either by the BIPM or by PSDLs of other countries. Most SSDLs from countries that are not members of the metre convention achieve the traceability of their standards through the International Atomic Energy Agency (IAEA) whose standards are calibrated by the BIPM. In this way, and also with the cooperation of the IAEA through its SSDL Network, the ionizing radiation dosimetric quantities are disseminated as widely as possible [107]. The organization of the radiation metrology network is summarized in Figure 1.14 .

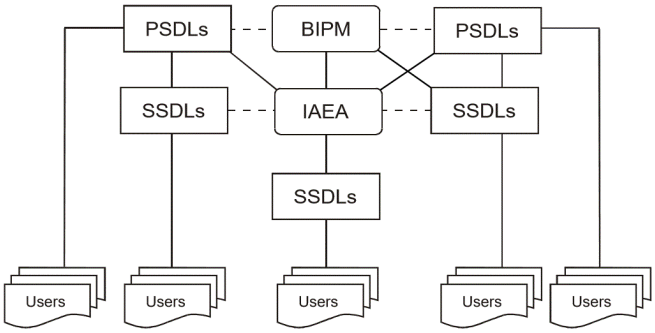

Figure 1.14. The International Measurement System for radiation metrology. The dashed lines indicate inter-comparisons of primary and secondary standards [30].

1.4.1.2. Reference beam qualities and HVLs

The characteristics of photon beams in terms of energy, i.e. their "quality", are defined according to a measurable parameter. This allows realizing "identical" beams in different institutes in order to carry out comparisons and calibrations on an equivalent metrological basis. Various parameters are used as indices for characterizing the beam qualities of low- and medium-energy X-Ray beams, such as the half-value layer (HVL), the nominal accelerating potential, the average or effective energy and others.

The HVL is defined as the thickness of a given material (e.g. aluminum or copper) required to reduce by half the air kerma rate at the calibration distance [1]. It gives little information about the energy distribution of photons in the beam [1]. Therefore, a new beam specifier (parameter) that is more sensitive to variations in the beam distribution was introduced, called the air kerma per unit fluence, corresponding to the air kerma normalized to the beam fluence. The formalism of this parameter is given by:

$$K_{\text{air,norm}} = \frac{\int \Psi_E(E)\left(\frac{\mu_{\text{tr}}(E)}{\rho}\right)_{\text{air}} \mathrm{d}E}{\int \Phi_E(E)\mathrm{d}E}$$

The use of this parameter then requires the knowledge of the photon fluence energy distribution, but it gives a clear indication of the influence of the energy spectrum on the air kerma value.

Table 1.3. Characteristic parameters of used beam qualities

Beam Quality	Filtration [mm]	1st HVL [mm]	HT (kV)	E_{avg}
CCRI50b	1.057 Al	1.018 Al	50	28.9
N20	0.645 Al	0.319 Al	20	16.1
N60	3.99 Al + 0.598 Cu	0.241 Cu	60	48.5

Three beam qualities produced by the conventional X-Ray generator (Gulmay 160), at LNHB were used throughout this study. These beam qualities are namely, the CCRI50b, N20 and N60 beam qualities. The corresponding photon beam spectra and measurement configurations are presented in Figure 1.15, with their characteristics detailed in Table 1.3.

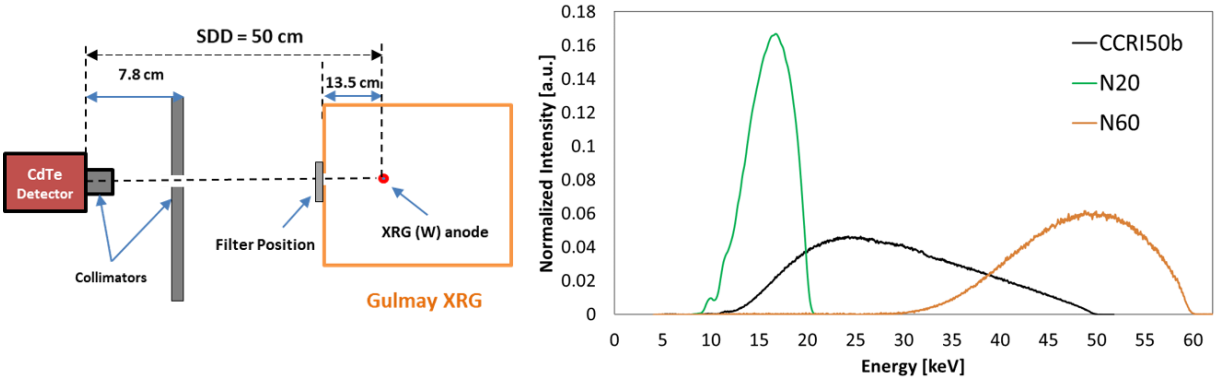

Figure 1.15. From left to right, a scheme (not to scale) of photon spectra measurement configurations and the beam qualities photon distributions

1.4.2. Metrological traceability of IORT beams

Since there is a limited availability of standards of absorbed dose to water in the kilovoltage X-Ray range, it is possible to derive calibration factors in terms of absorbed dose to water from air kerma calibration factors using one of the accepted codes of practice.

This part presents the most commonly used air-kerma calibration protocols as the indirect traceability methods proposed by the AAPM and the IAEA. Then, the current state of two primary standards, developed by NIST (USA) and PTB (Germany) for direct traceability, is presented. Finally, as an application of indirect traceability protocols, the method used by Zeiss for the INTRABEAM® dosimetry is presented.

1.4.2.1. Indirect traceability – Application of existing protocols

1.4.2.3.1. IAEA - TRS 277 & 398

One of the main tasks of the Dosimetry and Medical Radiation Physics Section at the IAEA is the development of codes of practice, or protocols, for the dosimetry of external beams used in radiotherapy. The IAEA published in 1987, and then in 1997 through a second edition updating the dosimetry of mainly kilovoltage x-rays photon beams, an international code of practice, TRS-277 [108], based on in-air kerma calibration to obtain the absorbed dose to water for external beam radiotherapy. This protocol has been followed by several updates and protocols till the issue of the new international code of practice, TRS-398 [30]. This new protocol is based on standards of absorbed dose to water and is applied to a wide range of radiation beams including kilovoltage X-Ray beams.

The formalism given in the TRS-398 to determine the absorbed dose to water, $D_{w,Q}$, at the water surface, for a dosimeter in a low-energy X-Ray beam of quality Q and in the absence of the chamber is:

$$D_{w,Q} = M_Q N_{D,w,Q_0} k_{Q,Q_0},$$

where $\boldsymbol{M_Q}$ is the dosimeter reading corrected to the reference values of influence quantities (air temperature, pressure, humidity, etc.) for which the calibration factor N_{D,w,Q_0} has been defined. $\boldsymbol{N_{D,w,Q_0}}$ is the calibration factor, in terms of absorbed dose to water, of the dosimeter obtained from a standard laboratory in a reference beam quality Q_o. The factor $\boldsymbol{k_{Q,Q_0}}$ corrects for the effects of the difference between the reference beam quality Q_o and the actual user quality Q.

Absorbed dose to water at the surface of water is traditionally derived from the measurement of air kerma, by converting it to absorbed dose to water and applying a correction factor for the backscattering effect. However, the TRS-398 protocol is based on measurements made in a full scatter phantom, using a chamber that has been calibrated directly in terms of absorbed dose to water while mounted in the phantom, and hence, eliminating the need of backscatter correction (previously required for the conventional calibration in terms of air kerma). Nevertheless, according to the TRS-398 protocol, it is still possible to derive calibration factors in terms of absorbed dose to water using air-kerma calibration factors and one of the published air-kerma calibration protocols [46].

1.4.2.3.2. AAPM – TG 43 & 61

The American Association of Physicists in Medicine (AAPM) provided a protocol, developed by the Radiation Therapy Committee Task Group (TG) 61, for reference dosimetry of low- and medium-energy X-Rays (40 kV - 300 kV). The calibration method for low-energy X-Ray beams uses the in-air calibration method, based on air-kerma measurement, to determine the absorbed dose to water at the surface of a water phantom. The following formalism is used [109]:

$$D_{w,z=0} = MN_k B_w P_{stem,air} \left[\left(\frac{\bar{\mu}_{en}}{\rho} \right)_{air}^{w} \right]_{air},$$

where M is the corrected free-in-air chamber reading at the measurement point (z_{ref}=0); N_K is the air-kerma calibration factor for the given beam quality; B_w is the backscattering factor which accounts for the effect of the phantom scatter, $P_{stem,air}$ is the chamber stem correction factor accounting for the change in photon scatter from the chamber stem between the calibration and measurement (mainly due to the change of the field size) and $[(\bar{\mu}_{en}/\rho)_{air}^{w}]_{air}$ is the water-to-air ratio of the mean mass energy absorption coefficients averaged over the incident photon spectrum in air. The $P_{stem,air}$ is taken as unity if, for a given beam quality, the same field size is used in the calibration and the measurement. This methodology used in the TG-61 is similar to that proposed by the IAEA TRS-277.

The AAPM TG-43 report provides the calculation of dose-rate distributions around photon-emitting brachytherapy sources. It was firstly published in 1995. An updated version was published recently including some revisions, corrections and data updates [110,111].

The TG-43 formalism specifies the absorbed dose to water at a reference point of 1 cm from the source, in the transverse-plane, and relates this dose to the air kerma strength[1] at 1 m from the source. However, the TG-43 formalism assumes a full scatter volume of water, so material inhomogeneities should be taken into account [11].

1.4.2.2. Direct traceability (for electronic brachytherapy)

1.4.2.3.1. PTB-CMI calibration method

The German national metrology institute (Physikalisch-Technische Bundesanstalt, PTB) and the Czech Metrology Institute (CMI) are collaborating to develop a primary standard for

[1] Air-kerma strength, S_K, is the air-kerma rate, $\dot{K}_\delta(d)$, in vacuo and due to photons of energy greater than δ, at distance d, multiplied by the square of this distance, d^2, $S_K = \dot{K}_\delta(d) * d^2$. It has units of μGy m^2 h^{-1} and is numerically identical to the quantity Reference Air Kerma Rate recommended by ICRU 60 [112].

eBT. This project is founded in the framework of the European Metrology Research Program (EMRP) [113]. The eBT systems investigated so far are the INTRABEAM® and the AXXENT®. For the development of the primary standard device and investigations of the calibration chain, characterizations of both sources were required: X-Ray emission spectra were measured at various azimuthal and radial angles, relative 3D dose distributions at distances below 3 cm were determined with radiochromic gels [114,115]. Scintillator and X-Ray storage film measurements were used for complementary measurements. –MC simulations were performed to mimic the characteristics of the sources (using the MCNP code), to characterize the utilized measuring devices (using the EGSnrc code) and to calculate conversion and correction factors for the primary standard (using the MCNP code) [116].

The primary standard used is the "Grovex II" chamber, which is an extrapolation chamber in a phantom of water-equivalent material based on the measurement principles of a free-air chamber, as seen in Figure 1.16. This extrapolation chamber is already used at PTB as a primary standard device for I-125 seeds [117]. However, although the photon energy ranges of I-125 and eBT sources are almost the same, the phantom material, RW1, was found less suitable for the radiation fields of eBT systems. This is referred to the higher amount of low energy photons, emitted by eBT systems, which led to a considerable disturbance by the induced low-energy fluorescence-photons of Mg and Ca ingredients of the RW1 material. Thus, the phantom material of the chamber needed to be substituted, and henceforth, recommissioned [116].

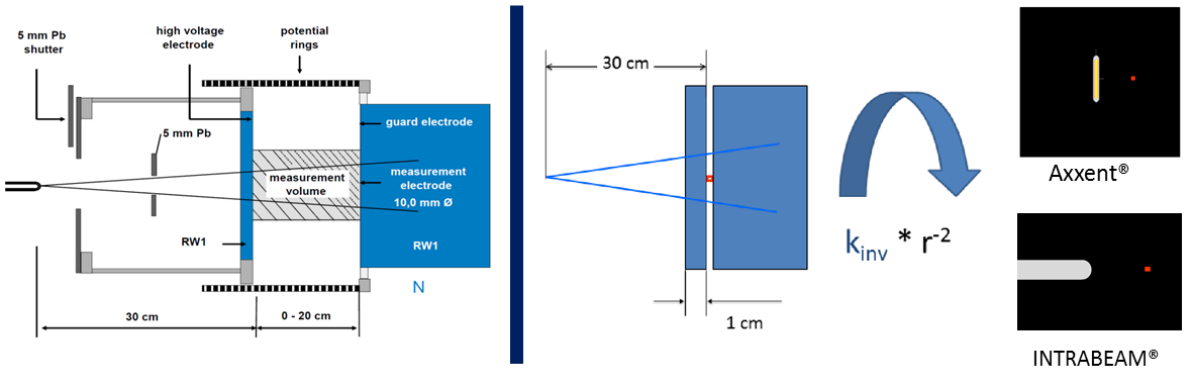

Figure 1.16. (Left) scheme of the extrapolation chamber used by PTB (right) scheme showing the utility of the conversion factor, K_{inv}, to correct for the deviations from the inverse square law of the distance, this law being used to pass from the measurement distance r to the reference one that is at 1 cm from the source in water.

The point of measurement is located at 1 cm depth within the phantom, and the source is located at 30 cm distance from this point, as seen in Figure 1.16. To pass from the measurement conditions to the reference conditions, i.e. absorbed dose to water at 1 cm distance from the source in a phantom of water (considered as 10×10×10 cm^3), the inverse square law accompanied with several correction factors are applied. The equation used to determine the absorbed dose to water at 1 cm in water for eBT sources is the following:

$$D_{\mathrm{w}}(1\ cm) = \frac{W}{e} \cdot \frac{1}{\rho} \cdot \frac{1}{r^2} \cdot k_{\mathrm{inv}} \cdot k_{\mathrm{div}} \cdot \prod_i k_i \cdot C(x_{i+1}, x_i)\left(k_{\mathrm{scat}}(x_{i+1})Q(x_{i+1}) - k_{\mathrm{scat}}(x_i)Q(x_i)\right),$$

with ρ the density of air, r the source-to-measurement point distance, k_{div} the conversion from D_{w} in the measuring area to D_{w} at a point on the beam axis, $Q(x_{i+1})$ and $Q(x_i)$ the ionization charges measured at the two plate separations x_{i+1} and x_i , which must be greater than the range of the secondary electrons, k_{inv} the correction factor for deviations from the inverse square law

of the distance due to stray radiation, absorption and the spatial expansion of the source, $\prod_i k_i$ the product of correction factors k_i that are almost negligible such as k_{sat} to correct for the saturation effect or k_{hold} to correct for the source-holder scatter, and k_{scat} the correction factor for electrons induced by a secondary interaction process, and finally, the conversion factor, $C(x_{i+1}, x_i)$ which is calculated by the MC method to convert the absorbed dose obtained under the conditions of operation of the extrapolation chamber to the one obtained under the conditions of the calibration of the eBT system [118].

1.4.2.3.2. NIST calibration method (for AXXENT)

The NIST has established a new primary standard for low-energy electronic brachytherapy sources. The standard is based on a free-air chamber (FAC) for the realization of the air kerma (as explained in section 1.3.1) produced by the X-Ray beam, at a reference distance of 50 cm, in air. The standard was used with the Axxent S700 source, of Xoft, Inc., to establish the air kerma, as shown in Figure 1.17, and, then, transfer the measurement by calibrating a well-type ionization chamber [119].

The NIST determined the air-kerma rate using their Lamperti free-air ionization chamber [120]. This free-air ionization chamber used for the measurement of air kerma is a validated national standard instrument deemed suitable for the realization of air kerma for these eBT sources. Another FAC dedicated to the calibration of low-energy photon beams was used for comparison and verification of the Lamperti FAC.

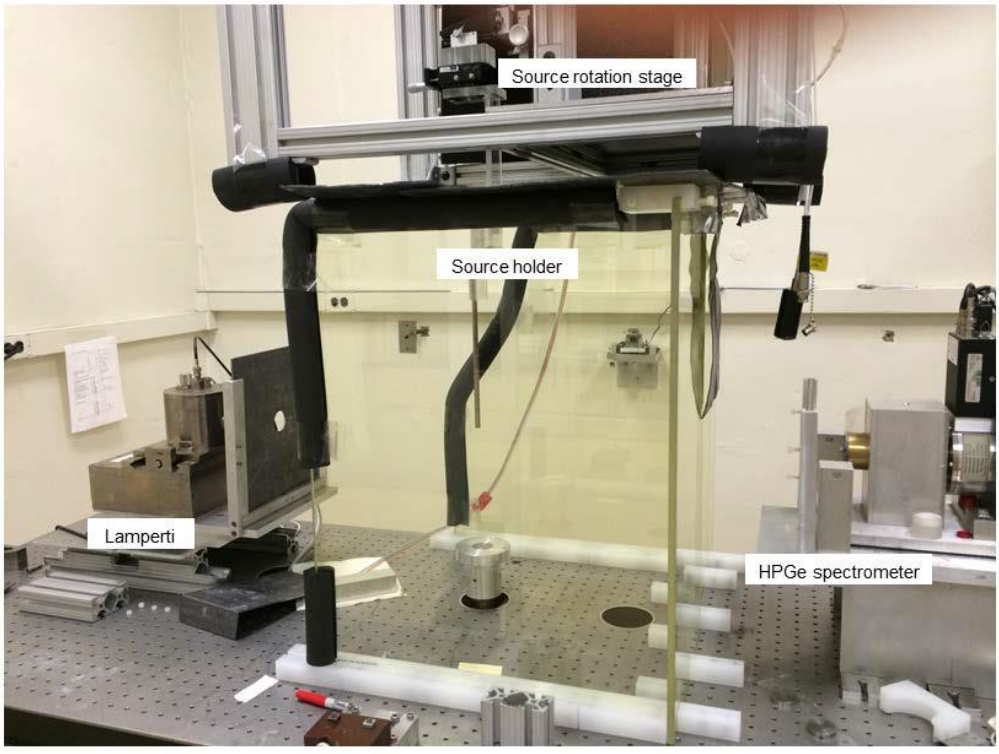

Figure 1.17. Setup of reference air kerma measurement and photon spectrometry at NIST [119]

A well chamber has been evaluated and used as an air-kerma transfer instrument. It has been demonstrated to be an appropriate transfer standard for eBT sources, as well as an efficient mean of determining their stability. The NIST calibration coefficients of the well chamber have units of [Gy. A^{-1} s^{-1}] normalized to reference conditions of 295.15 K and 101.325 kPa.

1.4.2.3. Dosimetry and calibration of the IB-XRS with spherical applicators by Zeiss

The information provided in this section is extracted from the documents delivered by ZEISS for the dosimetry of the system INTRABEAM® [121–123].

Zeiss uses its own INTRABEAM® water phantom accompanied with a PTW-23342 soft X-Ray ionization chamber to determine the Depth Dose Curve (DDC) in water of an IB-XRS. This process is applied during production and recalibration of the XRS. Then, the factory-calibrated system is delivered with the specific depth dose curves and a reference measurement with the ion chamber associated to the system.

The dosimetry of the INTRABEAM® XRS is based on the methodology proposed by the International Commission on Radiation Units in their report-17 (ICRU-17, 1970) [124]. The methodology relies on calibrating the transfer chamber in terms of exposure, X, using a free-air chamber primary standard. Subsequently, using the calibration coefficient and the measured transfer chamber exposure, the conversion to absorbed dose to water is then obtained using the following equation:

$$D_{\mathrm{w}} = \frac{\bar{W}_{\mathrm{air}}}{e} \cdot \left(\frac{\bar{\mu}_{\mathrm{en}}}{\rho}\right)^{\mathrm{w}}_{\mathrm{air}} \cdot X = f \cdot X$$

The roentgen-to-gray conversion factor, f, expressed in Gy.R^{-1}, includes the $(\bar{W}_{\mathrm{air}}/e)$ expressed in J.C^{-1}, the ratio of mass energy absorption coefficients in water and air for the photon energy spectrum of interest, and the conversion factor from the old unit R (roentgen) to the SI unit of exposure [C.kg^{-1}] (1 R = 2.58 10^{-4} C.kg^{-1}). This factor is tabulated for certain photon energies.

The dosimetry of INTRABEAM® and the calibration process passes through three main steps: the determination of the DDC of the XRS, the isotropy measurement of the XRS, and finally the determination of the applicator transfer function and isotropy.

To ensure the alignment of the XRS and the ionization chamber, for the DDC and isotropy measurements, the position and movement of both the XRS and ionization chamber are assured by two independent systems: a positioning unit, shown in Figure 1.18 –a, and the water phantom with all its associated parts, shown in Figure 1.18-b.

In this setup, the ionization chamber current is measured for distances z such as 3 mm < z < 45 mm (with Δz = 0.5 mm), using the XRS tube current of 40 µA and a tube voltage of either 40 or 50 kV. The measured ionization chamber current, corrected to the reference conditions of p_0 = 760 torr and T_0 = 295.2 K, is converted into an absolute rate of absorbed dose to water $\dot{D}_w(z)$ [Gy.min^{-1}], for different water depths, using the exposure calibration coefficient N_S [R.C^{-1}] and multiplying it by the conversion factor f:

$$\dot{D}_{\mathrm{w}}(z)\left[\frac{\mathrm{Gy}}{\mathrm{min}}\right] = I_{T,p}(z)[A] \cdot N_{\mathrm{s}}\left[\frac{\mathrm{R}}{\mathrm{C}}\right] \cdot k_{\mathrm{Q}} \cdot f\left[\frac{\mathrm{Gy}}{\mathrm{R}}\right] \cdot 60\left[\frac{\mathrm{s}}{\mathrm{min}}\right]$$

The determination of the factors f, N_{s} and k_{Q}, depends on the effective energy (or the HVL in mm Al) of the XRS. The HVL measurements, and the resulting effective energies, are conducted at a **water depth of 10 mm** provided the values shown in Table 1.4, for different accelerating voltages.

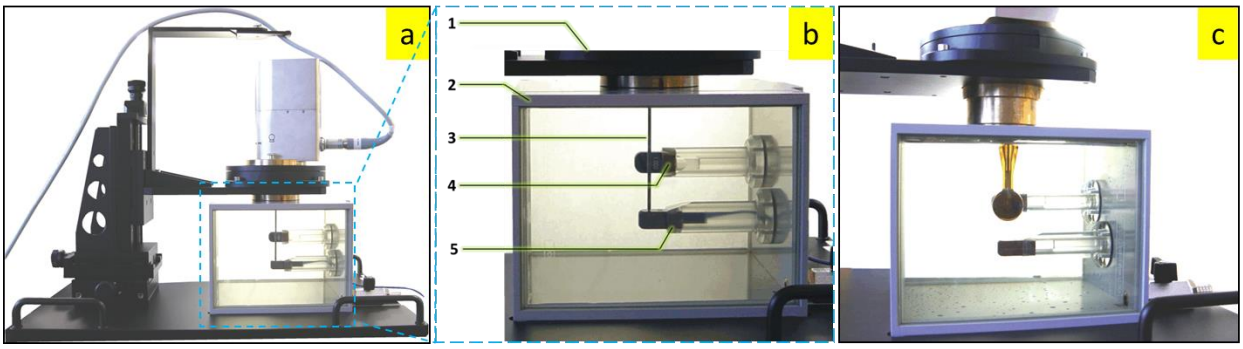

Figure 1.18: Zeiss INTRABEAM® water Phantom system for depth dose determination of an XRS. The fisrt image (a) shows the INTRABEAL XRS mounted on the positioning unit (in black) where the XRS is inserted in the water phantom enlarged in (b) where, 1: 360° rotation platform for isotropy measurements, 2: the water phantom (W: 400 mm x H: 520 mm x L: 580 mm), 3: The XRS probe, 4: a solid water holder for isotropy measurements with PTW-34013 IC and 5: a PTW-23342 IC in a solid water holder (1 mm thickness) for DDC measurements. Image (c) shows a measurement configuration with a spherical applicator for the transfer function determination.

At the energy of 20 keV, the conversion factor f has a value of 8.81 mGy.R^{-1} (value is extracted from the ICRU Report-17). The beam quality correction factor k_Q, that corrects the calibration factor for the difference in beam quality between the calibration and the measurement, is considered as unity for the T30 and T50 beam qualities.

An analytical function is used for fitting the depth dose values to determine the values at the surface of the XRS or applicators. This is due to the thickness of the solid water ionization chamber holder which prevents direct contact of the chamber to the XRS tip or applicator. The fit function of the depth dose curve comprises a combination of three exponential functions (each based on the Lambert-Beer absorption law) and the function of the quadratic distance law.

Table 1.4: Comparison of the HVL of a type 4 XRS at different accelerating voltages in a water depth of 10 mm

Accelerating voltage [kV]	XRS HVL [mm Alu]	Effective energy [keV]	Beam Quality [PTW]
50	0.64	**20.4**	Between T30 & T50
40	0.48	19.1	≈ T30
30	0.41	17.3	≈ T30

The isotropy of an XRS is measured at different points on an imaginary sphere surface with the XRS isocenter as its center. The measuring setup for XRS isotropy measurements corresponds to that described above, the only difference being that a PTW-34013 ionization chamber is used for measurement.

The applicator transfer function is measured for each applicator using a standard XRS in the water phantom as seen in Figure 1.18-c. In this process, the depth dose curve of the XRS is successively measured with and without the applicator. The influence of the applicator on the depth dose curve without applicator is determined by dividing the two depth dose curves obtained, which provides the raw data of the transfer function for this applicator. Again, an analytical function is therefore used to fit the applicator's transfer function between beyond the z measured values (at z = 0 which corresponds to the applicator surface).

In the same way as for the applicator DDC, the isotropy of the XRS with the applicator is measured at a distance of 1 cm from the applicator surface. Since the isotropy of the standard

XRS is known from previous measurements, the isotropy of an applicator can be calculated by subtracting the two values.

To verify the depth dose curves by the end users, Zeiss provide water phantoms with the corresponding PTW ionization chambers to perform dose measurements in the same configurations as explained above (called TARGIT method). Recently, Zeiss has developed new water phantom, similar to that just presented in Figure 1.18, adapted for measurements with the PTW 34013 ionization chamber [125], along the probe axis, instead of the previously used PTW 23342 one.

The dose distributions determined using the new water phantom and the PTW 34013 ionization chamber are based on a new adopted methodology (called the Non-TARGIT method). In this method, the PTW 34013 is first calibrated in terms of air kerma (instead of exposure used by the TARGIT method). Then, to convert the measured air kerma into absorbed dose to water, a $\boldsymbol{K}_{\boldsymbol{K_{air} \rightarrow D_w}}$ conversion factor, determined by the PTW during the calibration process of the ionization chamber, is applied. A constant value of 1.036 is provided for this conversion factor.

The correlation between the two dose distributions obtained by the two methods (TARGIT to Non-TARGIT) is realized by multiplication with a conversion factor. This factor depends on the SDD and has values ranges from 0.51 at 3 mm (distance from the bare probe) to 0.893 at 45 mm. It has a maximum standard error of 5.1 % (stated by Zeiss). The reasons of this difference between the two methods as declared by Zeiss, and the details concerning the adoption of the new methodology are published by Zeiss in a note over the INTRABEAM® dosimetry given in APPENDIX-A.

Chapter 2

2. Establishment and transfer of a dosimetric reference in terms of absorbed dose to water at 1 cm in water $D_{w,1cm}$

Absorbed dose to water at 1 cm in water is the recommended [126] dosimetric quantity for electronic brachytherapy sources used in IORT. As discussed in section 1.1.3, the INTRABEAM® system is the most available eBT system in the world as well as in France (10 systems) [126] and it is mainly used for breast cancer treatment. Therefore, the establishment of the dosimetric reference in this study was focused, as a first stage, on IB systems mounted with spherical applicators (used for breast cancer treatment).

The method adopted to realize the dosimetric reference for the INTRABEAM® X-Ray source (IB-XRS) resulted partly from some practical constraints. First, the LNHB is neither equipped with such a system and nor it is possible to displace the hospital's system to the laboratory, due to its high occupation by patients. Second, the primary appropriate standard instruments of LNHB are not transportable and thus cannot be used for in-situ primary measurements in hospitals.

Collaboration was established between the LNHB and Saint Louis hospital in Paris. It provided to LNHB an access to an IB system to perform the required measurements for the dosimetric reference. The measurements performed relied on the expertise of the Saint Louis radiotherapy service in the IB system (i.e. quality assurance measurements before each measurement, the control of delivered doses and irradiation times and the definition of end-users need in terms of calibration).

Accordingly, the developed methodology is based on reproducing identical photon spectra of the IB system with spherical applicators by a conventional X-Ray Generator, available at LNHB. A primary standard free-air ionization chamber was used to characterize, in terms of air kerma, the reproduced spectra at LNHB. To characterize the INTRABEAM® photon beams in-situ, a transfer dosimeter, calibrated in air kerma in the reference reproduced photon beam at LNHB, was used. At last, MC method was implemented to calculate a conversion factor from air kerma, calculated by modeling measurement conditions, to the absorbed dose to water under reference conditions, i.e. at 1 cm distance from the considered IB spherical applicator surface along the IB-XRS probe axis. This methodology was applied on the IB with a 4 cm spherical applicator, for which, the absorbed dose at a 1 cm depth in water, $D_{w,1cm}$, was established.

This chapter is divided into four main sections. The first one details the adopted methodology. The second one deals with the characterization and reproduction of IB photon spectra at LNHB. Then, the modeling of the IB-XRS with a 4 cm spherical applicator is presented in the third section, and finally in the last part, the methodology to establish the dosimetric reference for the IB-XRS with a 4 cm spherical applicator is applied.

2.1. Methodology adopted to realize the dosimetric reference, $D_{w,\,1cm}$, for the INTRABEAM® source with spherical applicators

This section details the methodology adopted to establish the $D_{w,1cm}$ dosimetric reference for IB system with spherical applicators. The methodology starts by the reproduction of equivalent photon spectra of IB. The "reproduction" term refers to the production of X-Ray beam spectra, at the reference point, identical to those emitted by the IB source with spherical applicators mounted.

The production of IB photon beams relies on two aspects: first, the photon spectra characterization, either by calculation or measurement, of the IB-XRS mounted with spherical applicators, and second, the possibility to produce equivalent photon spectra to those of IB-XRS, using the conventional XRG at LNHB, at the 1 cm reference distance, in water.

The photon beams are further characterized in terms of air kerma rate. The primary standard free-air ionization chamber is used to characterize, in terms of air kerma, the reproduced spectra at LNHB. The calibrated reproduced beam is employed next to calibrate a secondary (or as also called, transfer) ionization chambers. These calibrated chambers are then used to characterize, in air kerma, the emitted photon beams of IB-XRS with spherical applicators. In addition, Monte Carlo method is implemented to calculate correction factors, for the primary standard measurement, and conversion factors, from air kerma to absorbed dose to water under reference conditions, i.e. at 1 cm distance from the considered IB spherical applicator surface along the IB-XRS probe axis.

In other words, the method can be decomposed into the following steps:

1) Characterization of the photon energy spectrum, of the considered IB source configuration, after photons have crossed 1 cm water-equivalent depth along the IB-XRS probe axis. The CdTe semiconductor detector, demonstrated in section 1.3.4, is used to measure the energy distribution of emitted photons after crossing a depth of material equivalent to 1 cm of water. The measured photon spectrum is then corrected for 'measurement' artifacts using algorithms developed in previous works at LNHB [91,92].

2) Reproduction, at LNHB, of the photon energy spectrum emitted by the IB source in the considered configurations. This spectrum is reproduced using the conventional X-Ray generator, Gulmay 160, at LNHB (this generator is already used at LNHB for X-Ray dosimetric references with adapted high-voltage settings and filters).

3) Establishment of a primary standard, in terms of air kerma rate, for the beam reproduced at LNHB. This standard is based on ionometric measurements using a conventional free-in-air ionization chamber (namely the WK07, of LNHB [36]). Appropriate correction factors, consistent with the reproduced spectrum, are calculated by Monte Carlo methods either as a product of several correction factors (as in the conventional method [36]) or as a single/global correction factor (as in a previous study [90]) as described in Figure 2.1

(overlaid green and blue boxes). The air kerma rate is then obtained according to the following formula:

$$\dot{K}_{\mathrm{air,ref}} = \frac{\bar{W}_{air}}{e} \cdot \frac{I_{\mathrm{FAC}}}{\rho_{\mathrm{air}} V} \cdot \frac{1}{1-g_{\mathrm{air}}} \cdot \prod_i k_i \qquad (1)$$

where,

$\bar{W}_{air}$ is the mean energy expended in air per ion pair formed;
e is the charge of the electron;
V is the reference volume of the free-air chamber;
ρ_{air} is the density of air in the reference atmospheric conditions (1013.25 hPa, 20 °C, 0% humidity);
g_{air} is the fraction of energy lost in radiative form by the electrons released in air;
$\boldsymbol{I_{\mathrm{FAC}}}$ is the net ionization current measured with the free-air chamber in the reference beam, corrected for background noise, temperature, pressure and humidity, at a reference distance d_{ref} along the beam axis;
$\prod_i k_i$ is a product of factors that correct for the presence of the free-air ionization chamber in the reference beam.

4) Calibration of a transfer ionization chamber in terms of air kerma, relying on the primary reference described before. The transfer chamber used is a PTW 23342 (described in section 1.3.2). The corresponding calibration coefficient is obtained according to the following formula:

$$N_{\mathrm{K_{air,ref}}} = \frac{\dot{K}_{\mathrm{air,ref}}}{I_{\mathrm{TC,ref}}} = \frac{\bar{W}_{air}}{e} \cdot \frac{I_{\mathrm{FAC}}}{\rho_{\mathrm{air}} V} \cdot \frac{1}{1-g_{\mathrm{air}}} \cdot \prod_i k_i \cdot \frac{1}{I_{\mathrm{TC,ref}}}$$

where $\boldsymbol{I_{\mathrm{TC,ref}}}$ is the net ionization current, of the secondary ionization chamber, measured in the reference beam at a reference distance d_{ref}, in air, along the beam axis. This current is corrected for background noise, temperature, pressure and humidity.

5) Measurement of the air kerma rate of the photon beam emitted by the considered IB source, after crossing a depth of material equivalent to 1 cm of water. This measurement is conducted at a reference measurement distance d_{mes} in air along the probe axis. It has to be noted that the photons emitted by the IB source are collimated, in order to eliminate the potential contribution to the measurement of photons that would be scattered by the surrounding elements. The corresponding formula is:

$$\dot{K}_{\mathrm{air,IB}} = N_{\mathrm{K_{air,ref}}} \cdot I_{\mathrm{TC,IB}} = \frac{\bar{W}_{air}}{e} \cdot \frac{I_{\mathrm{FAC}}}{\rho_{\mathrm{air}} V} \cdot \frac{1}{1-g_{\mathrm{air}}} \cdot \prod_i k_i \cdot \frac{I_{\mathrm{TC,IB}}}{I_{\mathrm{TC,ref}}}$$

where $\boldsymbol{I_{\mathrm{TC,IB}}}$ is the net ionization current of the secondary ionization chamber, measured along the IB-XRS beam axis at the reference measurement distance d_{mes} in air, corrected for background noise, temperature, pressure and humidity.

6) Calculation, by MC method, of the conversion factor to pass from the air kerma rate, determined in step 5, into an absorbed dose to water rate in the reference conditions (at

1 cm distance from the applicator surface, along the probe axis, in a full scatter water phantom).

Consequently, with the calculated conversion factor $F_{(K_{air,IB} \text{ to } D_{w,\,1\,cm})}$, the absorbed dose to water rate, at 1 cm in water under reference conditions, can be determined using the following equation:

$$\dot{D}_{w,\,1\,cm} = \frac{\bar{W}_{air}}{e} \cdot \frac{I_{FAC}}{\rho_{air} V} \cdot \frac{1}{1 - g_{air}} \cdot \prod_i k_i \cdot \frac{I_{TC,IB}}{I_{TC,ref}} \cdot F_{(K_{air,IB} \text{ to } D_{w,\,1\,cm})}$$

All the steps, including measurements or calculations, are illustrated in Figure 2.1. The framed schemes represent the experimental conditions in which Monte Carlo calculations or measurements are carried out to obtain the quantities written beneath them.

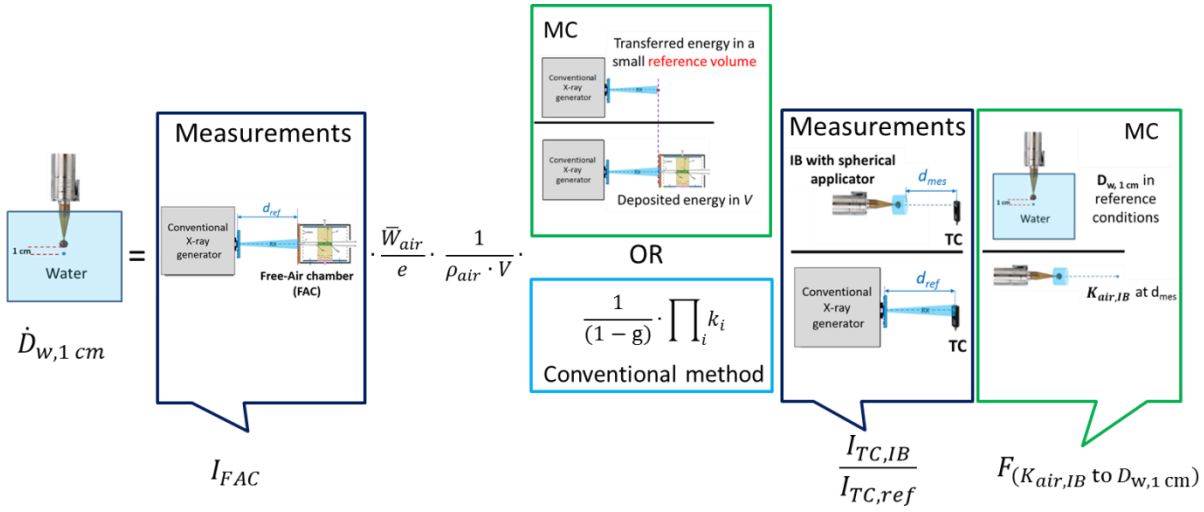

Figure 2.1. Illustration of the formula used to obtain the $\dot{D}_{w,\,1\,cm}$ standard for the IB source associated to a given spherical applicator. The schemes show the series of successive measurements and/or calculations performed. The scheme at the left represents the INTRABEAM in a water phantom in the reference conditions. Dark blue frames indicate steps realized by ionization chambers measurements, while green ones indicate those performed by MC calculations. The light blue frame indicates the correction factors as determined by the conventional method used for low-energy X-Ray air kerma references [36]. The blue volume around the IB applicator represents the additional layer of material equivalent to 1 cm of water.

2.2. Characterization & reproduction of IB spectra at LNHB

This section is divided into three parts: the first part is about the characterization of some emitted IB photon spectra, the second part deals with the reproduction of these spectra, at LNHB, using the conventional X-Ray generator, and the last part covers the comparison and evaluation of the equivalence between the spectra obtained in the two preceding parts.

2.2.1. Measurements of IB photon energy spectra

All photon spectra measurements of the IB-XRS were realized at Saint Louis hospital in Paris. They were all measured in air with a 50 kV potential and a 40 µA current. The CdTe semiconductor detector was used for all measurements. The source-to-detector distance, SDD, refers here to the distance between the IB-XRS probe tip and the detector window. However, spherical applicators of 3 and 4 cm, in diameter, were the only available spherical applicators

for measurement in the current study. Thus, the study at the current state was limited to their corresponding emitted photon energy spectra.

2.2.1.1. Measurement setups

The IB-XRS photon energy spectra, with or without spherical applicators, were measured through two distinct setups. The first setup was used earlier in this study to measure the energy distributions of IB-XRS with and without spherical applicators in air. However, due to the need of measuring the energy distributions after different depths in water along the IB-XRS probe axis, we have developed an appropriate system to perform such measurements. In this part, the two measurement setups, and the performed photon spectra measurements are presented.

Table 2.*2.1*. Tungsten collimators used in measurement setups

	Total number of collimators used	
	1st configuration	2nd configuration
$Ø_{external}$= 16 mm, $Ø_{hole}$ = 2 mm, Thickness = 2 mm	-	1
$Ø_{external}$= 16 mm, $Ø_{hole}$ = 500 µm, Thickness = 2 mm	9	10
$Ø_{external}$= 16 mm, $Ø_{hole}$ = 150 µm, Thickness = 1 mm	4	-
$Ø_{external}$= 16 mm, $Ø_{hole}$ = 100 µm, Thickness = 2 mm	1	-
Total collimation thickness	24 mm	22 mm

The first system setup is shown in Figure 2.2. In this configuration, the photon energy spectra were measured in the transverse plane at three different SDD i.e. 15 cm, 40 cm and 50 cm. The measurements were realized for the bare IB-XRS probe, as well as with the 3 cm and 4 cm spherical applicators mounted. The detector collimation was of 100 µm diameter, see Table 2.*2.1*. Moreover, the photon energy spectrum for the IB-XRS bare probe was also measured along the probe axis, at 15 cm SDD, under the same configurations (by laying the IB-XRS on its side so that the probe axis directs toward the CdTe detector window).

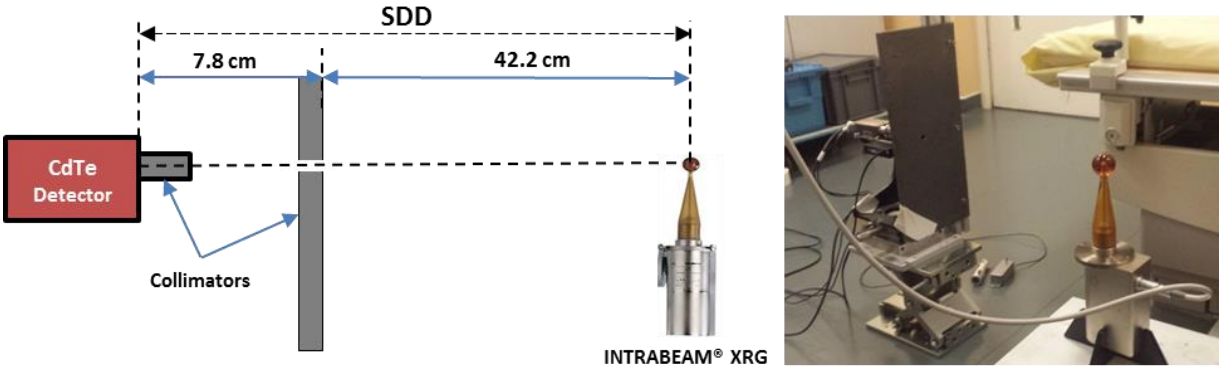

Figure 2.2. The first setup configuration. On the left, scheme (not to scale) of spectral measurements, in the transverse plane, of the IB-XRS with a spherical applicator mounted at 50 cm SDD, and on the right, picture of the real experiment conducted at Saint Louis hospital.

The second measurement setup, shown in Figure 2.3, was developed to measure the photon energy spectra, along the probe axis with the 4 cm spherical applicator, at different depths in water. To this end, new elements were added to the CdTe detection system defined previously to make such measurements possible: a cylindrical container in Plexiglas ($Ø_{interior}$ = 60 mm, H = 100 mm & 2 mm thick) filled with water and micrometric positioning systems (translation

stages providing 10 µm steps); additional to those of the CdTe positioning system (previously presented in section 1.3.4). The container provided the required water thickness (denoted by *t* in Figure 2.3) for attenuation of emitted photons, by the IB-XRS with the 4 cm applicator, at different depths in water (taking also into account the equivalent water attenuation in the container wall). The right depth and position, of the IB XRS and mounted applicator, in the container were adjusted using the translation stages and a micrometric sliding caliper. An optical laser was also used to ease the alignment of the XRS isocenter with the detector window.

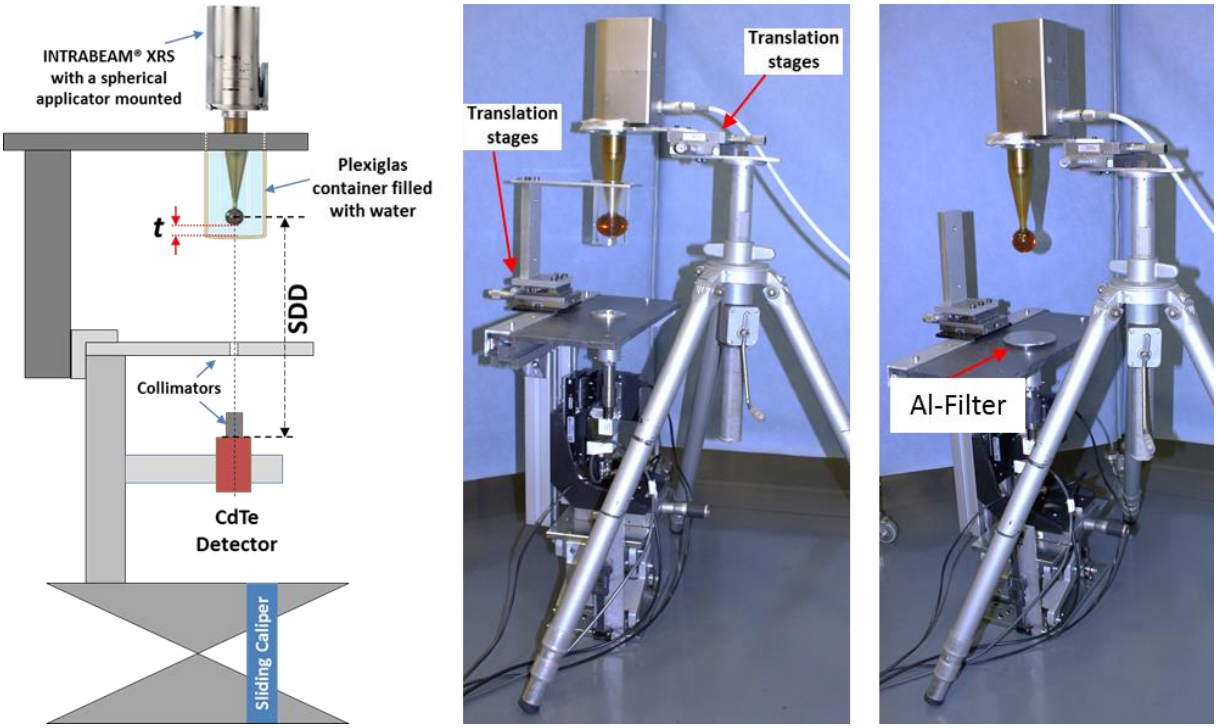

Figure 2.3. The second setup configuration. (left) scheme (not to scale) of the developed system with Plexiglas container configuration (the sliding micrometric caliper was used here to measure the thickness *t*), (middle) picture of the real system used for photon spectra measurements, and (right) same measurement system where the Plexiglas container is replaced by an Al-filter of adequate thickness.

Further measurements were performed using Al-filters to attain 1 cm water-equivalent attenuation. This was performed in order to study the possibility to use aluminum filters to replace the Plexiglas water-filled container. The use of Al-filters has several advantages: it eases the measurement process, avoids the uncertainty associated to the container base thickness and also evades the difficulty to attain the exact distance, *t*, between the applicator sphere surface and the container bottom.

The second measurement setup was used to measure the emitted photon spectra, of IB-XRS with 4 cm applicator, with and without filtrations. An aluminum filter of 0.7 mm is found equivalent to 1 cm water attenuation (in the ≤ 50 keV photons energy range). The measured spectra, with filtrations, were at equivalent water depths of 5 mm to 40 mm, by steps of 5 mm (using both water-filled containers and Al filters). These photon energy spectra, in addition to the ones measured under the first setup, are presented in the next section. A collimation of 500

µm, in diameter, was used in all measurements of the second configuration; the corresponding collimators used are presented in Table 2.*2.1*.

2.2.1.2. Photon energy spectra

Only the photon energy spectra that will be used in the progression of the current study are presented here. Nevertheless, the rest of the results, acquired after measurements carried out in the previous section, can be found in the APPENDIX-B.

Photon energy distributions, measured in the previous section, were corrected for measurement artifacts by applying the developed algorithms, discussed in section 1.3.4. An example is given in Figure 2.4 of the corrections made by comparing the energy distributions of a measured photon energy spectrum, before and after corrections. The discontinuities observed in the uncorrected photon spectrum are due to the escape phenomena of cadmium (Cd) and tellurium (Te) K-shell fluorescence photons. Moreover, the three peaks to the left of the spectra correspond to the L-shell fluorescence photons of the gold anode target of the IB-XRS. This comparison between the two spectra shows the significant role of the spectrometry systems used, and of the associated correction algorithms, to characterize the emitted photon energy spectra in the low energy photon range. Consequently, all photon energy spectra presented from now on are corrected for measurement artifacts.

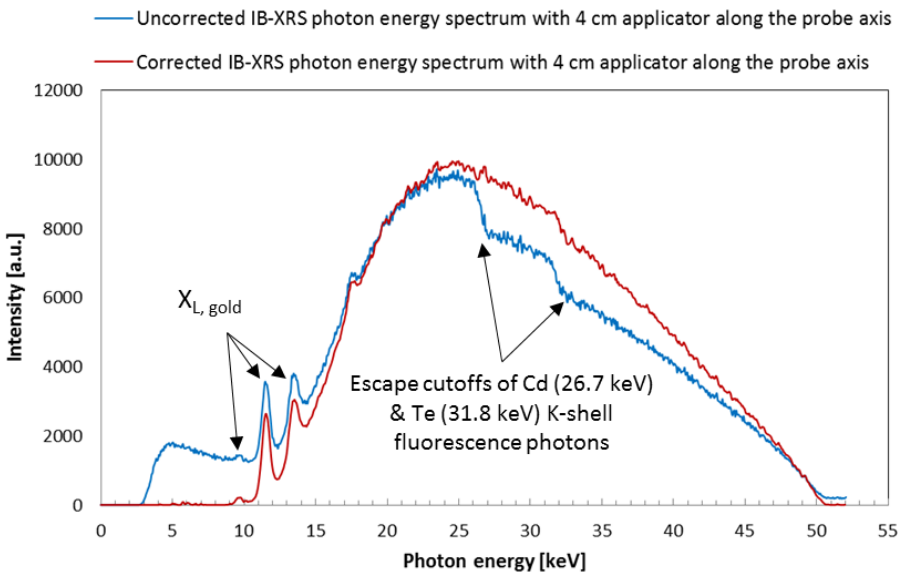

Figure 2.4. Comparison between two photon energy spectra, before and after applying the correction algorithm developed at LNHB.

Several comparisons were conducted between measured photon spectra. In order to make these comparisons possible, all photon spectra were normalized over the total photon fluence. The photon spectra measured for the bare IB-XRS probe in the two planes (axial and transverse planes) are in good agreement with a slight difference, due to less attenuation of the photon spectrum along the probe axis as seen in Figure 2.5-a). Indeed, the effect of attenuation is to harden the spectrum, i.e. to decrease its lower-energy part and to strengthen its higher-energy part. The measured spectrum of the 3 cm spherical applicator, along the transverse plane, is noticeably more attenuated than the spectrum measured with the 4 cm spherical applicator in

the same plane as seen in Figure 2.5-b). This is related to the internal aluminum filter inside the sphere cavity of the 3 cm applicator, discussed previously in section 1.1.4. It is also worth to remark that, the gold L-shell fluorescence photon peaks are almost totally attenuated for the 3 cm applicator while they still exist in the photon spectrum of the 4 cm applicator. The two photon spectra in Figure 2.5-c) are those measured for the 4 cm spherical applicator along the IB axis and in the transverse plane. The photon spectrum is slightly less attenuated (as seen previously for the bare probe) along the IB axis than in the transverse plane.

To compare the effect of this variation in the two photon spectra in a quantitative manner, the air kerma normalized over the photon fluence is calculated for each spectrum. The formula giving this quantity is as follows:

$$K_{\text{air,norm}} = \frac{\int_{Emin}^{Emax} \left(\frac{\mu_{tr}(E)}{\rho}\right)_{\text{air}} E\, \Phi_E(E)\mathrm{d}E}{\int_{Emin}^{Emax} \Phi_E(E)\ \mathrm{d}E}$$

where, Φ_E is the energy distribution of the photon fluence, and $(\mu_{tr}/\rho)_{air}$ is the air mass energy transfer coefficient.

The calculated normalized air kerma ratio ($K_{\text{air,norm}}$ (axial)/ $K_{\text{air,norm}}$ (transverse)) results is 1.037. This value means that the less attenuated spectrum measured along the axial plane leads to a higher air kerma value, for the same number of photons, at the reference points of measurement. The reason of this difference will be discussed in section 2.2.3. Finally, the use of Al filter configuration, for measuring photon energy spectra at different depths in water, is clearly feasible since the two photon spectra measured under the second configuration are perfectly compatible as shown in Figure 2.5-d). This compatibility was confirmed for all photon spectra measured at different equivalent depths in water, and hence, this configuration was adopted for any following measurements.

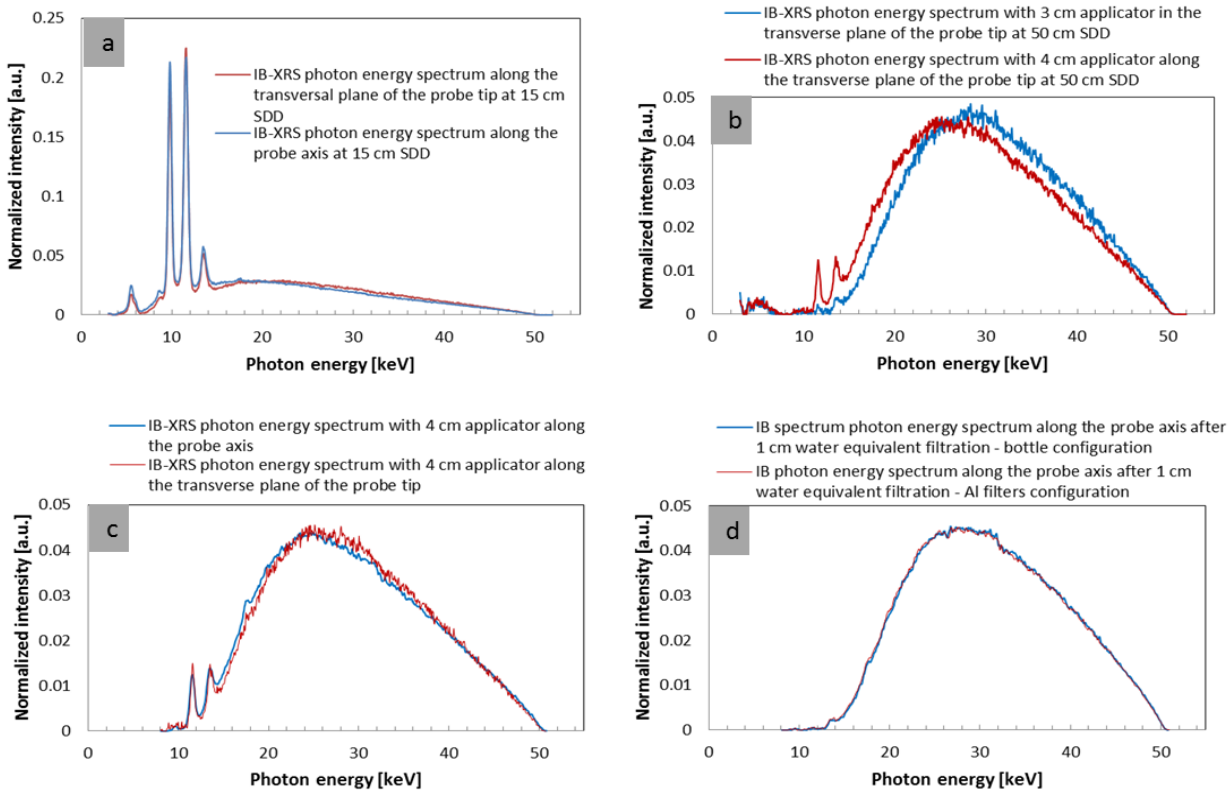

Figure 2.5. Comparison of measured photon energy spectra emitted by IB-XRS (a) bare probe along the axial and transverse planes (b) with 3 cm & 4 cm spherical applicators (c) with a 4 cm spherical applicator along the transverse and axial planes and (d) with a 4 cm spherical applicator after 1 cm of equivalent-water materials in the axial plane, using the Al and container filtration methods.

Therefore, after the characterization of the various photon energy spectra of the IB system, the next part is dedicated to attempt to reproduce equivalent photon spectra at LNHB using the conventional X-Ray generator available.

2.2.2. Reproduction of the IB spectra by the conventional XRG at LNHB

The LNHB has already developed the capability to reproduce photon energy beam qualities using its conventional XRG. The XRG Gulmay (160 kV) available at LNHB was used for the reproduction of photon energy spectra of the IB-XRS. However, the anode of the Gulmay XRG is made of tungsten whereas that of the IB-XRS is made of gold. This difference, in anode materials, led to fluorescence photon peaks placed at different energies along the photon energy spectra, as seen in Figure 2.6. Thus, the reproduction of the bare probe photon energy spectra of IB-XRS is not possible using the Gulmay XRG. But, since the photon energy spectra of the IB-XRS, with spherical applicators mounted, lead to significant attenuation of gold fluorescence photon peaks, an adequate attenuation can also lead to the same result over tungsten fluorescence photon peaks, and then, by the elimination of these peaks, the reproduction of photon energy spectra of the IB-XRS, with the applicators mounted, becomes possible with the Gulmay XRG.

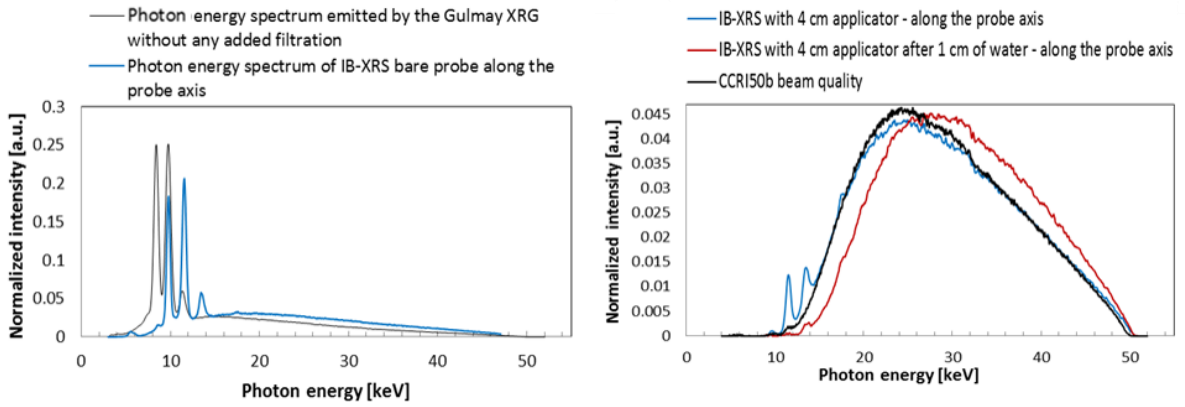

Figure 2.6. On the left, comparison of photon spectra of IB-XRS bare probe and Gulmay XRG. On the right, comparison of CCRI50b beam quality produced by Gulmay XRG to some INTRABEAM® measured photon spectra.

To have an idea on the type and amount of filtration needed, photon energy spectra emitted by the IB-XRS with 3 & 4 cm spherical applicators were compared to the CCRI50b beam quality already reproduced at LNHB. The CCRI50b was chosen for this comparison since it falls in the same energy range and has the same maximum photon energy of the IB-XRS photon spectra. As seen on the right of the Figure 2.6 (spectra CCRI50b, IB 4 cm, IB 4 cm with 1 cm), the spectrum of the CCRI50b beam (produced with a 1.057 mm Al filter) has a good similarity to those of the IB-XRS. The calculation of adequate filtration and the reproduction of the IB beams are successively presented in the following sub-sections.

2.2.2.1. Choice and calculations of adequate filters for each spectrum

The calculation of the photon attenuation needed for the Gulmay XRG, to reproduce IB photon spectra, is based on the Beer-Lambert law [127]. Filters in aluminum, of different thicknesses, were used to attenuate photons emitted by the XRG. All photon attenuation data, i.e., mass attenuation coefficients, mass energy absorption coefficients and materials densities, were extracted from the XMuDat program of NIST [128]. In addition, the air kerma quantity, normalized over the photon fluence, using the formula discussed in section 2.2.1.2, was also calculated for measured spectra (both original spectra of IB-XRS and those reproduced by the Gulmay XRG). This calculation was performed to give a quantitative indication, alongside with the similarity of photon spectra shape, on the reproduction proficiency.

Since gold fluorescence peaks are not totally attenuated in the photon energy spectrum of the IB-XRS with 4 cm applicator, attempts were made to reproduce these fluorescence peaks by introducing gold sheets (~ 4 µm total thickness) into the Al filtration. However, this trial did not lead to any remarkable production of gold fluorescence, due to the low photon-electron interaction probability when compared to the electron-electron interaction one. The result of this trial is also presented in the next section.

2.2.2.2. Measurement of reproduced spectra

The spectrometry system, presented in section 1.3.4, was used for the measurement of the reproduced spectra by the XRG. The measurement configuration is described in Figure 2.7. This configuration was used to measure all reproduced spectra. The operating parameters used for the XRG were a potential of 50 kV (similar to that used for IB-XRS) and a current of 0.5 mA

(to decrease the photon intensity and then the pile-up effect in the measured spectra). The 50 cm SDD corresponds to the distance between the detector window and the tungsten anode of the XRG. The collimation, right at the entrance of the CdTe, is in tungsten with 150 µm in diameter. Finally, the correction algorithms were applied over all measured XRG spectra, as done previously for those emitted by the IB source.

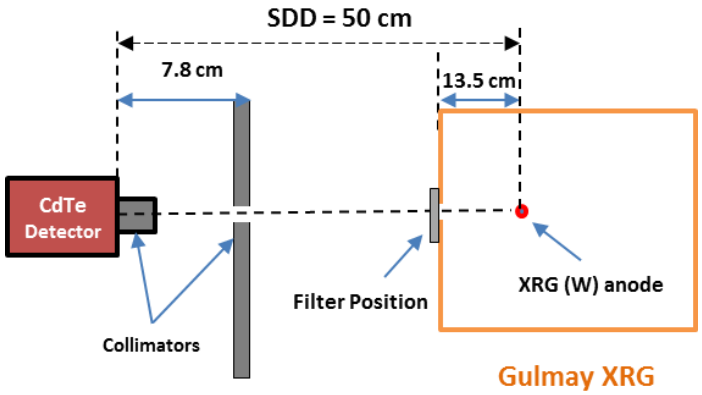

Figure 2.7. Scheme (not to scale) of the measurement configuration of the photon spectra reproduced by the XRG.

Five of the IB photon spectra were reproduced by the XRG at the current state of this study. The reproduced spectra are those of IB-XRS: with a 3 cm spherical applicator in the transverse plane at the surface of the applicator, with a 3 cm spherical applicator in the transverse plane after an equivalent thickness of 1 cm of water, with a 4 cm spherical applicator in the transverse plane at the surface of the applicator and with a 4 cm spherical applicator, in the two planes (axial and transverse), after an equivalent attenuation of 1 cm in water. The comparison, and equivalence, of these reproduced spectra to the original ones emitted by the IB system are presented and discussed in the next section.

2.2.3. Comparison and equivalence of reproduced spectra to those of IB

The comparison and equivalence of the photon spectra reproduced by XRG to those emitted by the IB-XRS are presented in this part. The comparison of photon spectra shapes is shown in Figure 2.8, while related characteristic parameters, i.e. filtration thickness, average energy of the fluence spectrum, measured HVLs and fluence normalized air kerma ratio of IB photon spectra to the corresponding ones reproduced by the XRG are presented in Table 2.2.2.

Table 2.2.2. Characteristic patameters of the IB-XRS and reproduced photon spectra

		3 cm	3 cm after 1 cm water	4 cm	4 cm after 1 cm water	
					Transverse plane	Axial plane
Filter thickness [mm Al]		1.746	2.484	1.18	1.862	1.715
Fluence average energy [keV]	IB	30.685	32.100	29.170	31.045	30.893
	XRG	30.565	32.082	29.344	30.939	30.727
HVL (mm Al)		1.395	1.712	1.096	1.463	1.369
$K_{air,norm}$ ratio: (IB/XRG)		1.007	1.001	1.047	1.000	0.996

We can conclude, for all reproduced photon spectra (except for the 4 cm applicator without attenuation by 1 cm of water), that the continuous part of each photon spectrum was successfully reproduced. This is also confirmed by the tiny difference (< 0.7 %) of the normalized air kerma ratios. However, the inability to produce the gold fluorescence peaks in

the 4 cm applicator photon spectrum, for the reasons clarified in the previous two sections, led to a significant difference (of about 5 %) in the normalized air kerma value, compared to that of the original IB photon spectrum. This difference is due to the significant change in the mass energy transfer coefficient values in the energy region where the peaks appear, as shown in Figure 2.8-c). While this issue could impact the establishment of a dosimetric reference, at the applicator surface, based on a reproduced spectrum, the fact that the reference is established at 1 cm in water eliminates this problem, due to the attenuation of these gold fluorescence peaks by the 1 cm water thickness separating the applicator surface from the reference point. As a consequence, the establishment of the current dosimetric reference, at 1 cm in water, based on a spectrum reproduced by the XRG is eligible.

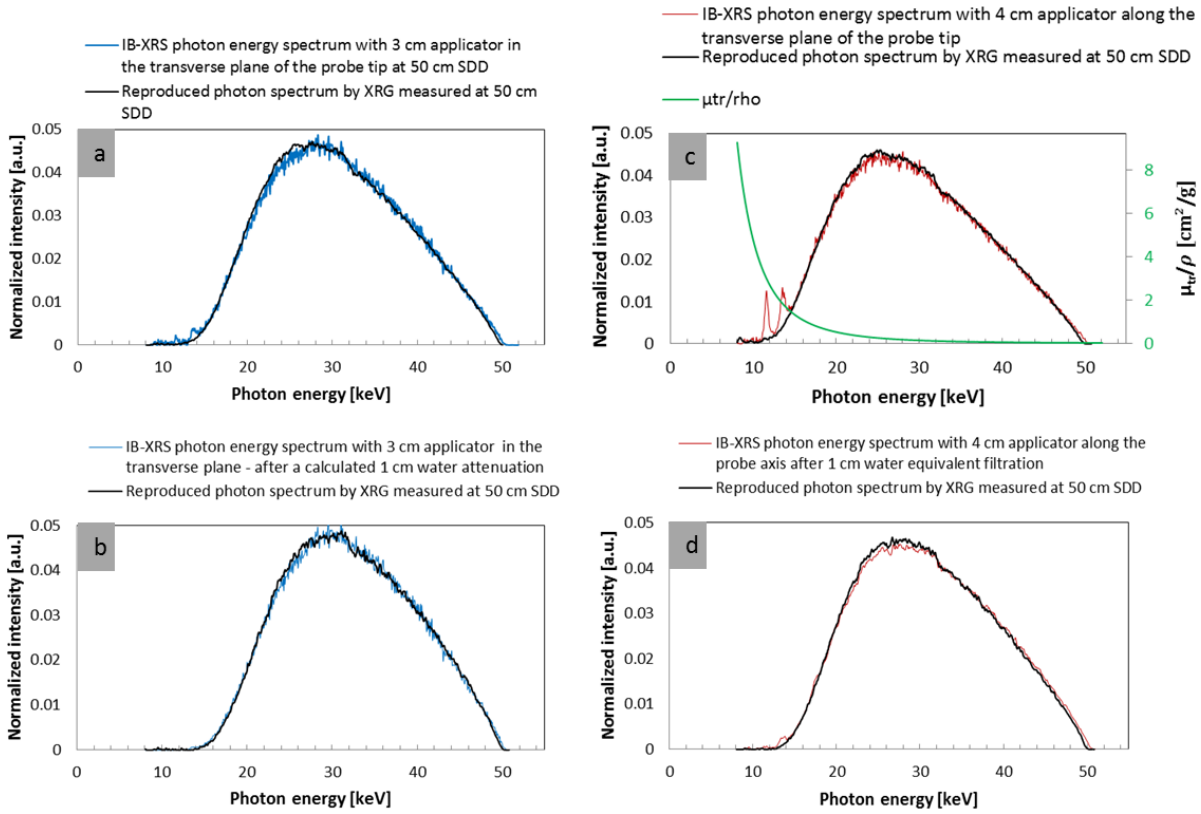

Figure 2.8. Comparisons of reproduced photon spectra by XRG to those of IB-XRS with (a) a 3 cm spherical applicator in the transverse plane (b) a 3 cm spherical applicator after 1 cm of water in the transverse plane (c) a 4 cm spherical applicator in the transverse plane and (d) a 4 cm applicator at 1 cm equivalent of water in the axial plane.

Due to time constraint, the further development of the dosimetric reference has been limited to the emitted photon spectrum of IB-XRS with 4 cm applicator at 1 cm depth in water, shown in Figure 2.8-d).

2.3. Developing a MC model of the IB-XRS with a spherical applicator of 4 cm in diameter

The MC model was developed for the IB-XRS with the 4 cm applicator mounted. It was used further in this chapter, in section 2.4.4, to calculate the conversion and correction factors needed to establish the dosimetric reference. The model was developed using the MC code

PENELOPE, described in section 1.3.5. The model relies on data either delivered by ZEISS, found in publications, or measured in the current study.

The first part of this section describes the modeling parameters of the IB-XRS and the spherical applicator of 4 cm in diameter. To validate the developed model, the second part is dedicated to calculate the photon spectra, emitted according to the developed model, and then, to their comparison to the original photon spectra measured for the IB-XRS with a 4 cm spherical applicator. The last part of this section deals with the creation of a database aimed at reducing the time needed for further calculations with this MC model. This database records the position, energy and angle of a statistically representative sample of photons when leaving the 4 cm applicator surface (PSF file, described in APPENDIX-C).

2.3.1. Modeling of the IB-XRS and of the 4 cm applicator

Only the IB-XRS-4 (section 1.1.4) probe was considered into the MC model. The main probe dimensions and materials are shown in Figure 2.9. The probe shaft is primarily made of µ-metal (a nickel-iron alloy [129]) to provide shielding against magnetic fields and rigidity, except for the last 2 cm made of beryllium working as a transparent X-Ray window. The entire probe is also coated by several thin layers of materials to provide chemical compatibility with the body and physical durability. However, the coating materials nature and thickness, as well as the gold target thickness, are contested from one publication to another [130–134]. The electron beam hitting the gold target is reported to be approximately Gaussian, oscillated around the central axis in order to optimize the isotropy of the radiation field [131,133]; this oscillation results in 16 focal bremsstrahlung emission points, with circular shape and equidistant positions over the probe tip. Regarding the 4 cm spherical applicator, its dimensions were obtained by calculations based on radiography images of the applicator, and its material is mainly polyetherimide (PEI) with relative densities given in section 1.1.4.

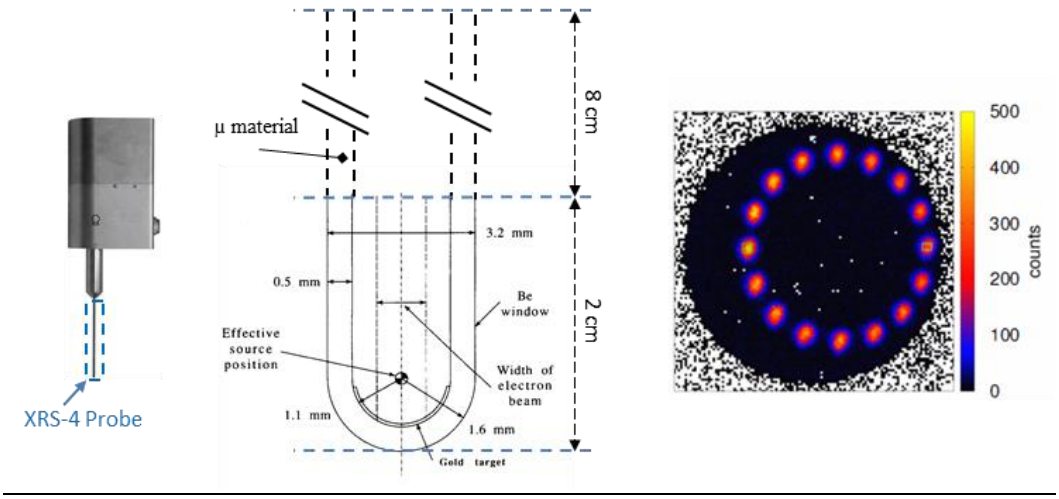

Figure 2.9. (Left) the XRS-4 of the IB with (middle) a zoom-in (not to scale) on the probe tip showing the different dimensions and materials used to make the probe (reconstructed from J. Beatty et al [131]) and (right) the 16 focal spots of the IB-XRS measured using a pinhole camera [135].

2.3.1.1. Geometries and materials

The geometrical models of the IB-XRS and of the 4 cm applicator are presented in this part. Since the data presented in publications vary more or less from one to another, the developed

MC models selected in this study rely on the data optimized over available data. Different models were tested to examine the effect of variations in parameters over the resulting photon spectrum. The models presented here are the final versions considered in this study.

The model of the XRS probe and its corresponding dimensions and materials are presented in Figure 2.10. The probe has a cylindrical shape with a hemispherical tip. The reference center point corresponds to the center of the hemispheres at the probe tip. Electrons emitted from points located at the probe base hit onto a gold target to generate photons. The gold target is of 1 µm thickness, as taken in J. Beatty *et al.* [131], and it covers the inner side of the hemispherical probe tip. This thickness is optimized to permit maximum deposition of electron energy while keeping the target transparent to photons, especially above the clinically relevant penetration energy value (~10 keV) [130]. Nickel alone, with 0.5 mm thickness, is used for the probe shaft (µ-metal is composed of at least 75% of nickel), for the sake of simplicity since aspects such as magnetic shielding and rigidity are not involved in MC simulations. The last 2 cm of the probe are made of beryllium with 0.5 mm thickness. Finally, the biocompatibility and durability layers were also considered into the model, they consist of three layers of 2.5 µm each covering the whole probe, made of NiO, Ni and CrN as considered by O. Nwanko *et al.* [134]. The developed MC model of the probe, as depicted by the geometry viewer of PENELOPE, is also shown in the same figure, with the right dimension scale between the different parts.

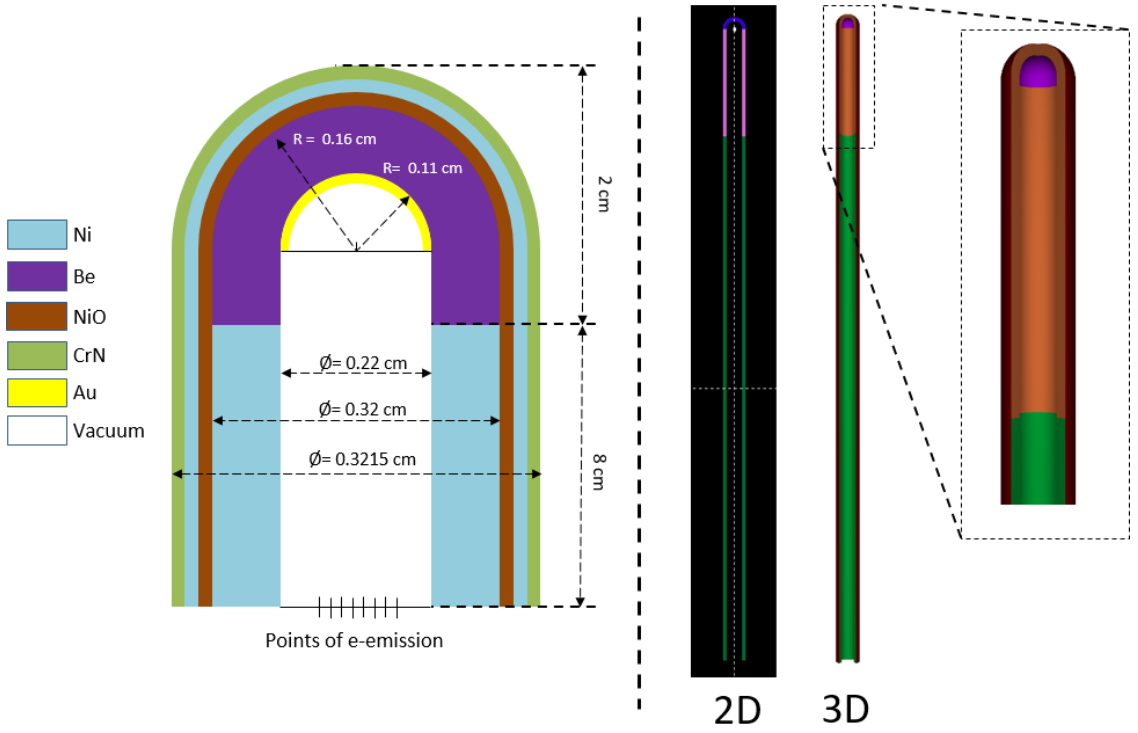

Figure 2.10. (Left) Scheme, not to scale, with dimensions and materials of the IB-XRS as modeled in this study, and (right) corresponding model, in 2D (material mode) & 3D, obtained by the geometry viewer tool of PENELOPE.

A detailed model of the 4 cm applicator was developed for the MC model as seen in Figure 2.11. This model is built on the probe model developed just before. Both the spherical applicator and the probe tip have the same center point. The detailed dimensions of the applicator were obtained by calculations based on radiography images of the applicator and manual measurements of accessible parts. The most interesting dimensions, for simulation purpose, concern the spherical part of the applicator. Inside the sphere is a cylindrical cavity, of 5.8 mm in diameter topped with a truncated cone of a 2 mm height, where the probe is inserted. To optimize the developed model and accelerate the calculations, based on aspects related to the calculation algorithms of the PENELOPE code, the applicator model was divided into different sections as can be remarked in the image of the bodies view mode in Figure 2.11.

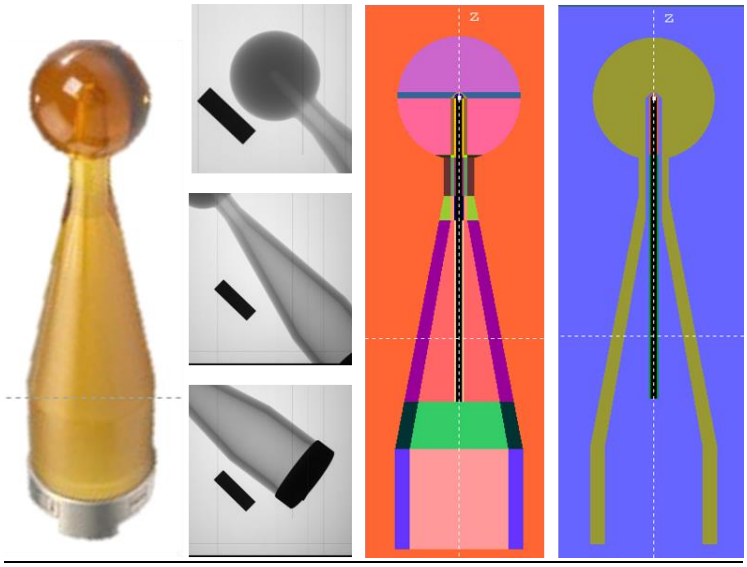

Figure 2.11. (from left to right) 4 cm spherical applicator of the IB-XRS; three radiography images of the 4 cm applicator with a scaling piece used for applicator dimensions calculations; developed geometry of the entire applicator (with metallic ring discarded) together with the XRS probe, in bodies view mode & materials view mode, both along the axial plane.

The applicator is made of polyetherimide biocompatible material. The internal cavity of the applicator is filled with air (represented in blue in the right-most image of Figure 2.11) which also surrounds the probe inside the applicator. Forthcoming MC calculations used this geometrical model, assembling the 4 cm spherical applicator and the XRS probe. However, the corresponding physical parameters, for different materials and particles, should be formerly defined for the calculations to be possible. These parameters are defined in the following part.

2.3.1.2. Materials and simulation parameters

To model the oscillating electron source and the generated 16 focal spots, 16 disk-shape electron sources were modeled. These sources were located on the base of the modeled XRS probe as seen previously in Figure 2.10. The electrons were supposed to be emitted uniformly from each disk source, with a Gaussian energetic distribution, and directed along the probe towards the gold target. The final dimensions and characteristics of the electron sources adopted are shown in Figure 2.12. This electron-source configuration was adopted after the comparison in-between photon energy spectra, measured previously for the IB-XRS with a 4 cm applicator and calculated by this model. This adopted structure, although it could be different from that of the IB-XRS, is practically supposed to give almost the same results.

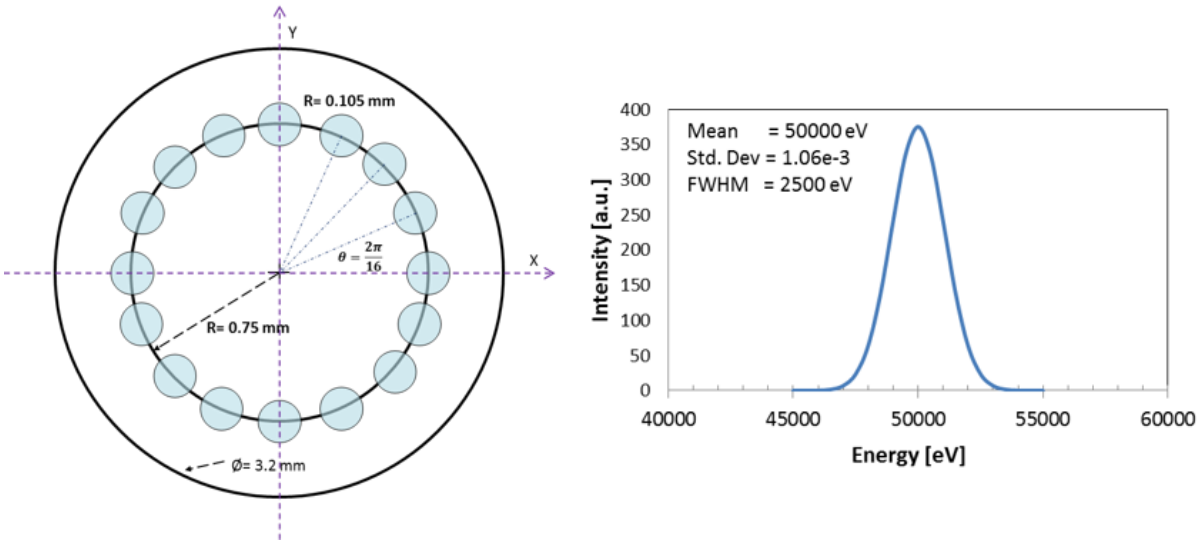

Figure 2.12. (Left) scheme (not to scale) of the 16 disk-shape electron sources used in the MC model and (right) Gaussian energetic distribution of electron beams emitted and their characteristics.

In order to get appropriate results, and control the speed and accuracy of particle simulation, PENELOPE provides a set of simulation parameters and recommendations to use with each material in the simulated structure as described in APPENDIX-C. The assigned values of all simulation parameters, in each material of the developed MC model, are summarized in Table 2.2.3.

Table 2.2.3. Values of simulation parameters assigned to each material used in the developed MC model

E_{abs} (1) [eV]	E_{abs} (2) [eV]	E_{abs} (3) [eV]	C_1	C_2	W_{CC} [eV]	W_{CR} [eV]	*DSMAX(KB)*
1.0E+03	1.0E+03	1.0E+03	0.05	0.05	1.0E+03	1.0E+03	$1/10^{th}$

The materials data used in the model are based on the PENELOPE-pendbase materials database. They were either directly obtained, by the material reference number in the database, or composed, relying on their chemical formula. The reference material numbers along with their corresponding densities are summarized in Table 2.2.4.

Table 2.2.4. Corresponding parameters of materials used in the MC model.

Material	Au	Be	NiO	Ni	CrN	Dry Air	PEI
Reference # in pendbase	79	4	-	28	-	104	-
Density [g/cm^3]	19.32	1.848	6.67	8.902	5.9	1.20479e-3	1.4

The MC model, developed and used in this study, is based on the geometries, materials and simulation parameters mentioned above. The reliability and validation of this model is the subject of the following section. It has to be noted here that variance reduction techniques were not used in any calculation.

2.3.2. Validation of the MC model

This section discusses the validation of the MC model developed in the previous section. It is divided into two parts: the first one concerns the calculations of the photon spectra emitted by the MC model, at the surface of the 4 cm applicator and after 1 cm in water; the second one is dedicated to the comparisons of the spectra calculated in the first part to those measured previously for the IB-XRS.

2.3.2.1. Calculations of beams at surface and after 1 cm of water

The calculation of the photon spectra emitted according to the developed model was performed by impact detectors, described in APPENDIX-C.

Impact detectors were used to calculate the photon distribution, at the surface of the applicator and after 1 cm of water, along the IB axis and in the transverse plane. Since impact detectors are defined for geometrical bodies (volumes), two bodies were defined for each configuration, as shown in Figure 2.13. In both cases, the axial detectors volumes were enclosed between the applicator sphere surface and a cylinder. The cylinder diameter is equal to the outside diameter of the XRS probe (3.2 mm), and its base is at 1 mm apart from the sphere surface. Detectors in the transverse planes are ring-shaped, and they are enclosed between spheres (1 mm thickness), and horizontal planes (2 mm height). For the calculations of the photon distribution after 1 cm of water, a spherical water volume of 1 cm thickness is added, in the second configuration. Moreover, all detectors were filled with air, and the energy window chosen for each detector was (1-51) keV, with 510 energy bins.

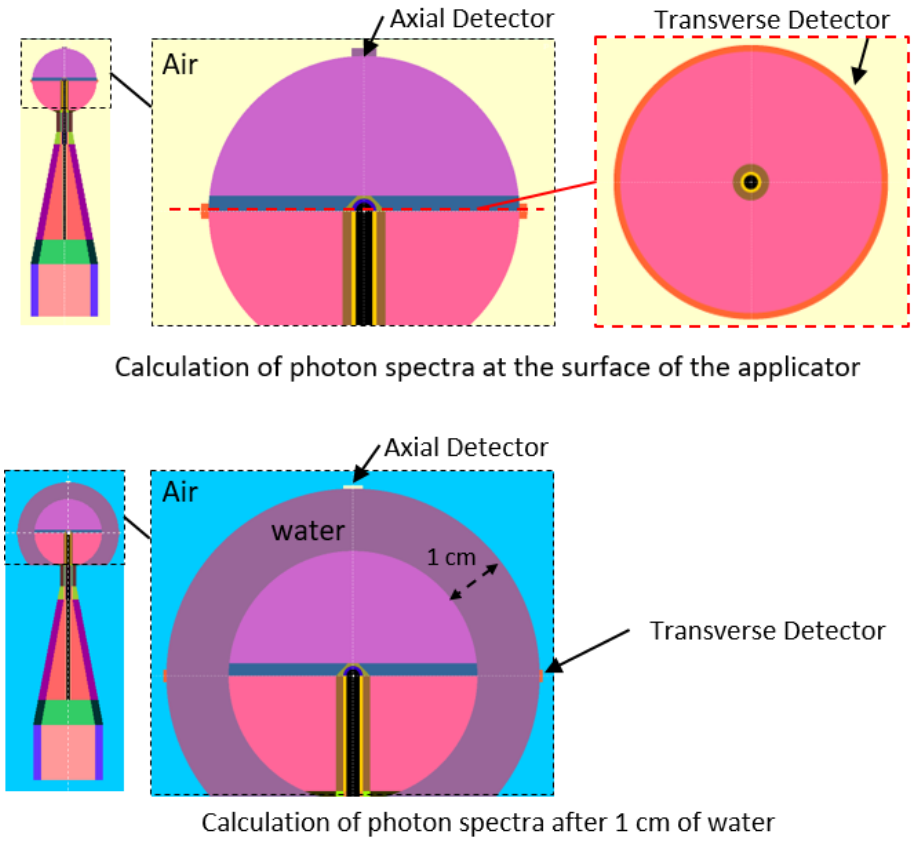

Figure 2.13. Bodies shape and position of the impact detectors modeled to calculate the photon spectra at the applicator surface and after 1 cm of water using the developed MC model. Images obtained by PENELOPE GVIEW2D program.

The calculated photon distributions, in the two configurations, and the comparison with measured photon spectra are presented in the next part.

2.3.2.2. Comparison of the MC calculated to the measured IB spectra

To validate the developed MC model for the further calculations of the conversion factor, the MC calculated photon spectra were analyzed in the same way as done before for the reproduced photon spectra by the XRG.

The photon spectra resulted from the MC model were compared to those measured for the IB-XRS, as shown in Figure 2.14. Their average energies and $K_{air,\,norm}$ ratios to the measured IB-XRS photon spectra were calculated, as summarized in Table 2.2.5. These results were obtained after several adjustments in the model geometry and physical parameters. The main modifications involved the gold target thickness, the density of the PEI (applicator material) and the electron beam Gaussian function (the final dimensions being the ones presented in section 2.3.1.1). The last parameters adopted for this model were due to the compatibility of the photon spectra obtained by the model to those of INTRABEAM especially after 1 cm of water along the probe axis (the reference point of measurements).

Three regions, based on the behavior of the calculated spectra profile compared to that of measured spectra, can be recognized: the first region (up to 23 keV) where both profiles are similar, the second region (from ~23 keV to 36 keV) where the calculated spectra are higher than the measured ones and the last region (above 36 keV) where the calculated spectra are

lower than the measured ones. However, the average energies and the $K_{air,\,norm}$ ratios are quite similar, and the impact of these differences on the calculated conversion factor will be discussed later in section 2.4.4.

Table 2.2.5. Characteristic patameters of the photon spectra measured, reproduced and calculated for the IB-XRS with 4 cm applicator

		At applicator's surface		After 1 cm of water	
		Axial plane	Transverse plane	Axial plane	Transverse plane
Fluence average energy [keV]	IB-XRS	28.251	29.170	30.893	31.045
	XRG	-	29.344	30.727	30.939
	MC calculated	28.981	29.350	30.764	30.941
$K_{air,norm}$ ratio: (IB/MC)		1.05	1.05	1.003	1.013

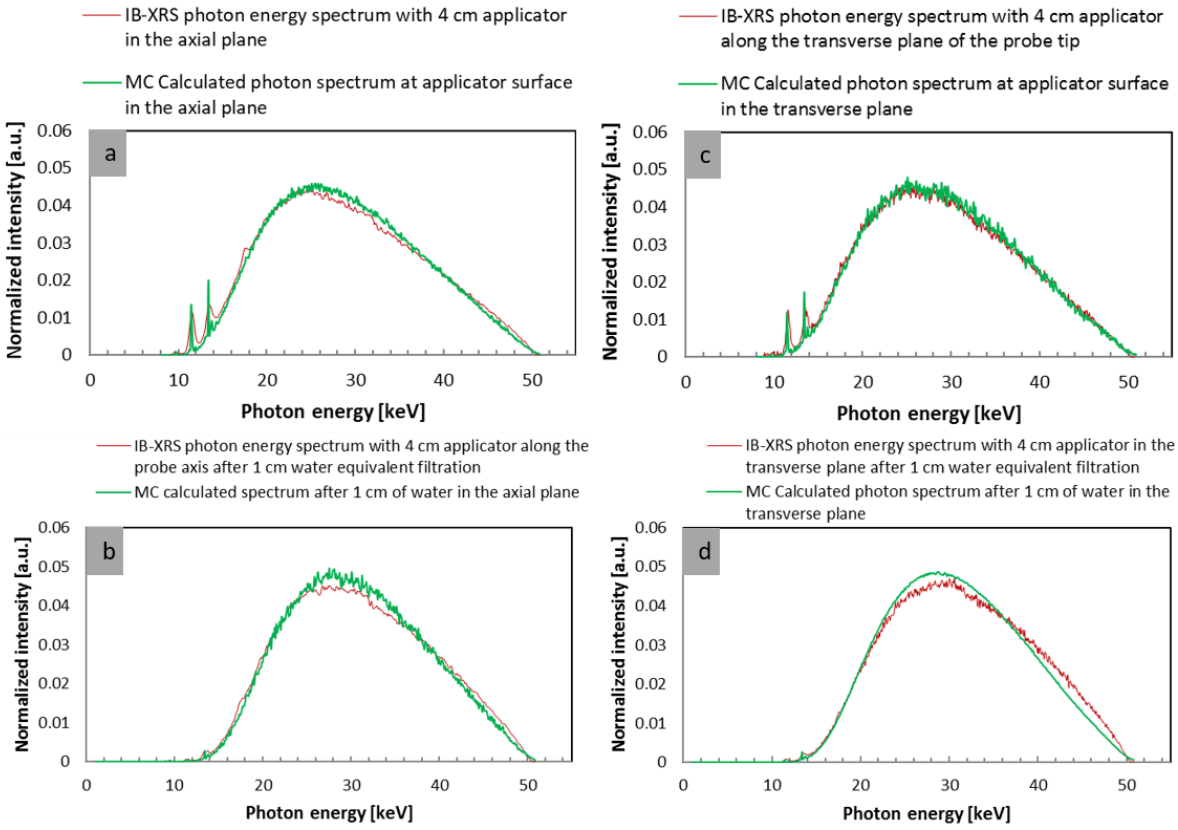

Figure 2.14. Comparisons of calculated photon spectra using the MC model under the configurations in Figure 2.13 to those measured for the IB-XRS with 4 cm applicator. All photon spectra are normalized over the total fluence. All spectra are for the IB with 4 cm applicator in the axial plane (a) at the applicator surface and (b) after 1 cm water attenuation, and in the transverse plane at (c) the applicator surface and (d) after 1 cm water attenuation.

After the adoption of the last parameters of the MC model, the next step was to create PSF files recording the characteristics of the photons at given positions. This is mainly done to reduce the time needed for further calculations with this MC model. The creation of the PSF files is presented in the following part.

2.3.3. PSF creation

Several PSF files (notion described in APPENDIX-C) were generated to reduce the high calculation time. This was performed due to the use of an electron source to generate photons without variance reduction techniques and the level of statistical uncertainty required for the primary reference.

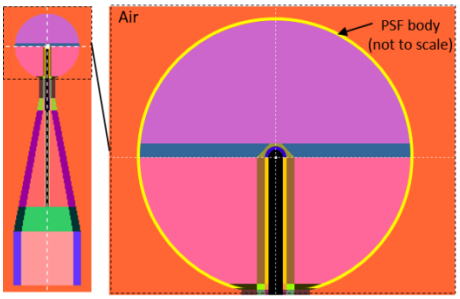

Figure 2.15. Location of the body used for the PSF files creation

To generate a PSF file, a spherical shell volume of 10 µm thickness, surrounding the applicator's spherical surface is used as detector, as seen in Figure 2.15. Six PSF files were generated under the same configuration, but with different initial seed, reaching a total size of 120 Giga-Bytes. These files were further used to calculate the conversion factor, in the process to determine the reference value of absorbed dose to water at 1 cm in water, as presented in the next section.

2.4. Determination of $\dot{D}_{w,1cm}$ for IB with 4 cm spherical applicator

After successive reproduction of photon spectra and development of MC model in sections 2.2 and 2.3, this section is dedicated to the set of calculations and measurements required to establish the primary reference in term of absorbed dose rate to water at 1 cm in water according to the methodology detailed in section 2.1 As shown previously in Figure 2.1, this methodology can be decomposed into six main steps, including the two that had just been presented. Each of the four remaining steps is covered here in a separate section. After the completion of these four steps, the implementation of their results to determine the dose rate value is performed in the fifth section. The last section covers the uncertainty budget associated with the primary reference in terms of absorbed dose rate to water at 1 cm in water.

2.4.1. Determination of the reference air kerma rate, $\dot{K}_{\mathrm{air,ref}}$

This part discusses the measurement of the $\dot{K}_{\mathrm{air,ref}}$ quantity. The reference air kerma rate was measured using the WK07 free-air ionization chamber, described in section 1.3.1. The conventional measurement configuration, used to measure the reference air kerma rate for low energy photon beams, was adopted, as shown in Figure 2.16.

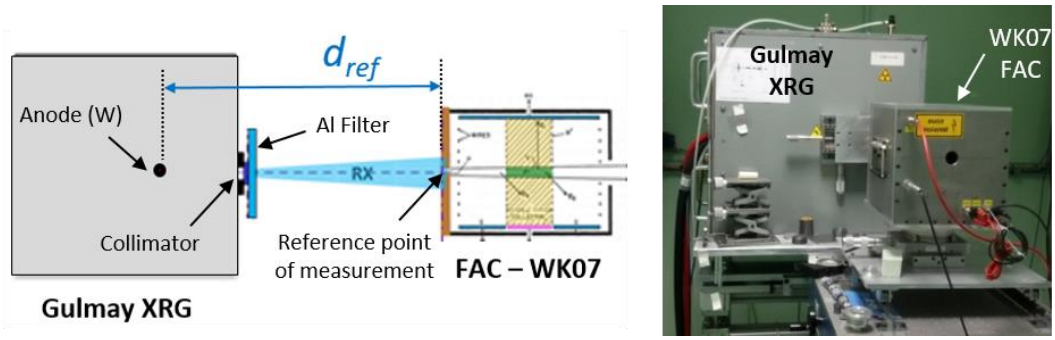

Figure 2.16. Reference air kerma rate measurement configuration, (left) measurement scheme (not to scale) and (right) real measurement.

The reference SDD, so-called d_{ref} in the scheme of figure 16, corresponds to the distance between the XRG anode and the reference point of the WK07 chamber. The current delivered by the FAC, I_{FAC} (as denominated in the aforementioned equation 1 in section 2.1), to establish the primary reference of the XRG reproduced beam was measured with the following parameters values. SSD was taken equal to 50 cm. The beam size, at the reference point, was almost 4.5 cm in diameter and the tube current used was of 15 mA. Finally, the adequate Al filter, calculated previously to reproduce the equivalent photon spectrum of IB-XRS with a 4 cm applicator after 1 cm of water along the probe axis, was introduced after the XRG collimator and corresponded to a total Al width of 1.715 mm.

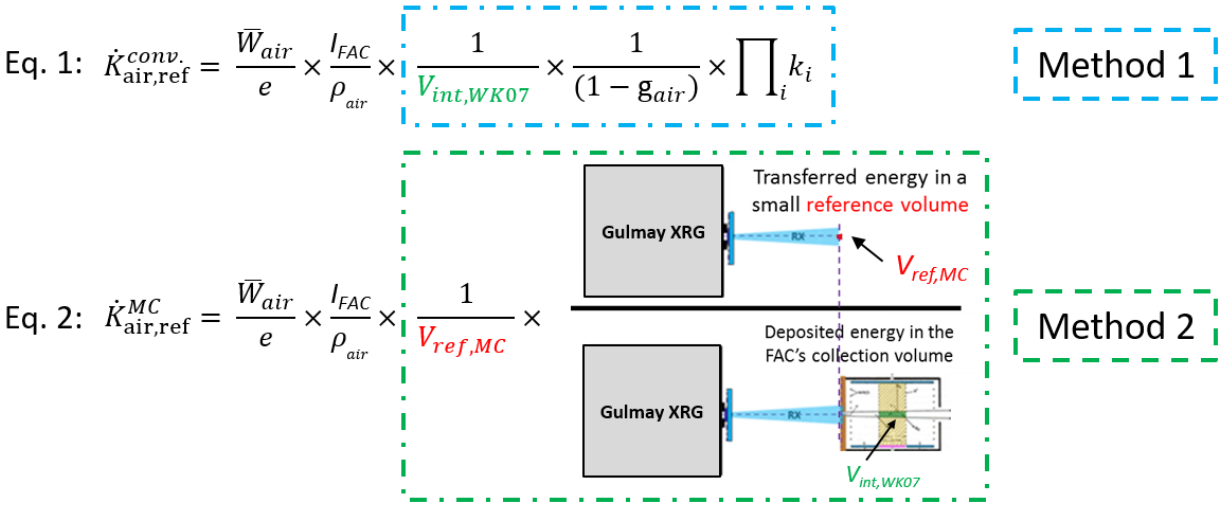

Figure 2.17. Determination of reference air kerma based on two methods to calculate the WK07 correction factors.

The reference air kerma value was determined by applying the equations in Figure 2.17, described before in section 1.3.1. Correction factors were applied to the measured current to deal with the atmospheric conditions (k_P, k_T, and k_H) and ion recombination (k_s). However, the polarization (k_{pol}) and field distortion (k_d) correction factors are unity in this energy range.

The rest on correction factors, i.e. the wall transmission (k_p), the aperture transmission (k_l), the scattered radiation (k_{sc}), the electron loss (k_e) and air attenuation (k_a) correction factors, depend on the photon energy spectrum in addition to the dependence on the design and operation of the free-air chamber. Two methods were used, in this study, to determine these factors for the reproduced INTRABEAM® photon spectra. The first method, the conventional

one, determines each correction factor separately either by means of measurements or MC calculations. The second method relies only on MC calculations to calculate a global correction factor that computes for these factors all at once.

The second method is introduced to show the feasibility to use MC technique to replace the conventional method. It also provides a mean to verify the validity of different developed methodologies in use at the laboratory and the MC model of the FAC, used in the next chapter, to calibrate the dosimetric gel. The application of the two methods is presented in the next two parts.

2.4.1.1. Using correction factors determined with the conventional method

The correction factors defined for the free-air chamber WK07 are presented in Table 2.2.6. These correction factors were already defined in a previous work of W. Ksouri [36]. However, in the energy range covered in the current study (≤50 keV), the value of some correction factors varies, depending on the form of the photon spectrum, while others keep the same value. Thus, only three factors, i.e., k_{sc}, k_a and k_l were recalculated, the others being taken as measured by W. Ksouri since their values were unchanged in the considered energy range. These three factors were calculated by the MC method, in the previous study, for monoenergetic photons over a wide range of energies, and curves were plotted to define their response with energy. To calculate these factors for the reproduced photon spectra of the INTRABEAM, summations weighted by the spectrum shape were performed over the previously calculated curves.

Table 2.2.6. Correction factors defined for the WK07 free-air chamber, all factors are determined by measurements except for those in blue, determined by MC calculations.

Correction factors	Symbol	
Humidity	k_H	**0.9980**
Ion recombination	k_s	**1.0007**
Polarization	k_{pol}	**1.0000**
Field distortion	k_d	**1.0000**
Wall transmission	k_p	**1.0000**
Electron loss	k_e	**1.0000**
Aperture transmission	k_l	**0.9977**
Scattered radiation	k_{sc}	**0.9957**
Air attenuation	k_a	**1.0049**

2.4.1.2. Using a global correction factor calculated by MC simulations

The global correction factor calculates the ratio between two energy quantities as seen in Figure 2.17. The first quantity, represented in the numerator, is the energy transferred in a small reference volume of air, $V_{ref,MC}$, in the reference conditions. This transferred energy divided by the mass of air ($\rho_{air}V_{ref,MC}$) represents the mean air kerma in this volume. Whereas, the second quantity, presented in the denominator, calculates a quantity proportional to the measured current, i.e. the energy deposited in the interaction volume of the chamber in the measurement conditions. Thus, this ratio permits, as a first role, to correct for measurement artifacts due to the free-air chamber, and as well, permits to pass from the measurement conditions to the

reference ones, i.e., a point, at the reference distance in air, in the absence of the free-air chamber and in the reference atmospheric conditions.

The two energy quantities were calculated under the configurations shown in Figure 2.18. These configurations imitate the real measurement configurations at LNHB. The XRG was represented by a point photon source. The emitted beam is the one measured for the IB-XRS with a 4 cm applicator, after 1 cm in water, along the probe axis. This beam was collimated, so that it has a cross section of 4.5 cm, in diameter, at the reference point of measurement, at a distance of 50 cm in air from the point source. Moreover, the surrounding environment in the two configurations was filled with air, and the two energy quantities were then calculated using the forthcoming configurations.

The reference volume $V_{ref,MC}$ was chosen to be a cone truncated by 2 spheres of 8 mm radius difference. Its center was located at the reference distance of measurement, d_{ref}, of 50 cm from the point source, with a cross-section, at this distance, of the same diameter as that of the inner diaphragm of the WK07 FAC. To calculate the transferred energy in this reference volume, the physical parameters were slightly modified from those defined in Table 2.2.3. The absorption energy threshold parameters, E_{abs}(KPAR), for electrons and positrons (even though positrons are not generated at this energy range) were set to 50 keV (almost maximum emitted photon energy). Consequently, once an electron is ionized through the interaction of a photon, its energy is fully absorbed locally at the interaction point, hence making the calculated deposited energy equal to the transferred energy.

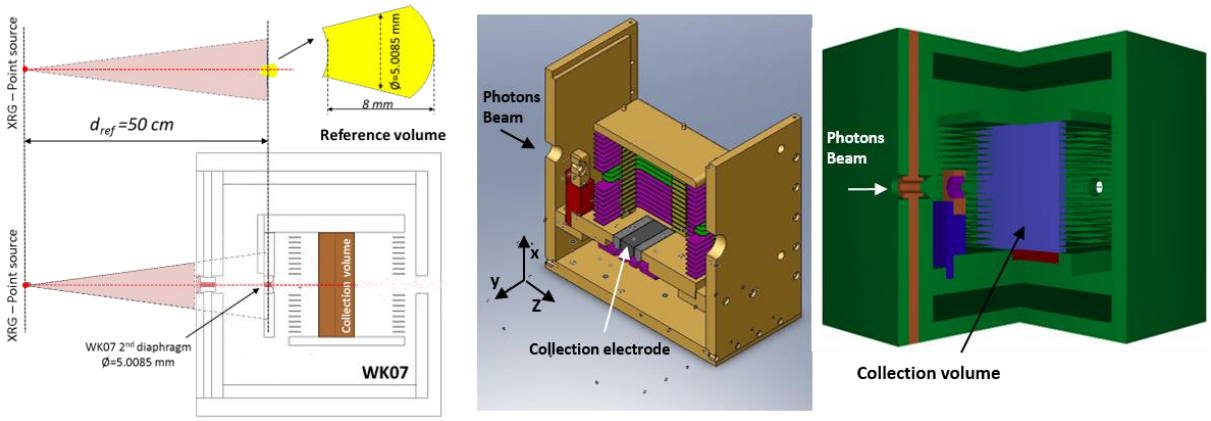

Figure 2.18. (Left) Schemes (not to scale) of the two configurations used to calculate the global correction factor for the WK07, (middle) a cut onto a 3D model representation of the WK07 showing some of its internal parts and (right) a 3D view, obtained using the PENELOPE GVIEW3D tool, of the developed model of the WK07 showing the collection volume

The second energy quantity was obtained by calculating the deposited energy in the collection volume of the WK07 free-air chamber. To this end, a detailed model of the WK07 chamber was used. This model was previously developed at LNHB by J. Gouriou [136] in the PENELOPE Monte Carlo code. For a matter of precision, some dimensions adjustments were performed on this model.

The same point source, as used in calculations of the first quantity, was again used in this second configuration. The reference point of the WK07 free-air chamber (at the second diaphragm) is located at 50 cm from the source along the beam axis. The simulation parameters

used for different materials are summarized in Table 2.2.7. We can remark that the absorption thresholds, in air, for this calculation were set to 1 keV for all types of particles, providing a quite correct tracking of charged particles, and hence, a good estimation of the deposited energy value in the collection volume. However, due to the complex geometry of the chamber, and in order to accelerate the calculations, the threshold values of charged particles in all the other materials of the WK07 chamber were set to 50 keV, resulting in a direct absorption of charged particles once ionized. This is a fair assumption in this energy range due to the high stopping power values of the WK07 chamber materials (primarily lead, tungsten and aluminum). Moreover, the DSMAX value was set to a value of the order of one tenth of the corresponding body thickness.

Table 2.2.7. Values of simulation parameters assigned to each material used in the developed WK07 MC model

	$E_{abs}(1)$ [eV]	$E_{abs}(2)$ [eV]	$E_{abs}(3)$ [eV]	C_1	C_2	W_{CC} [eV]	W_{CR} [eV]
Air	1.0E+03	1.0E+03	1.0E+03	0.05	0.05	1.0E+03	1.0E+03
Other Materials	50E+03	1.0E+03	50E+03	0.2	0.2	1.0E+03	1.0E+03

The comparison between the results obtained by the two methods to determine the WK07 FAC's correction factors are presented in the next part.

2.4.1.3. Results and comparison

The results obtained for the correction factors and the corresponding air kerma rates are presented in Table 2.2.8. The net current, I_{FAC}, corrected for background noise and for atmospheric differences with reference conditions, refers to the net ionization current measured by the WK07 free-air chamber under the configuration in Figure 2.16. To calculate the corresponding reference air kerma rate value, the two formulas defined in Figure 2.17 were solved using the corresponding parameters defined in Table 2.2.8.

The air kerma rate value calculated using the global correction factor, obtained by the MC approach, showed a good agreement with that obtained following the conventional method. An air kerma rate ratio of 1.003 ± 0.002 was attained (ratio of global factor method by MC to the conventional method). A rigorous study was realized on the MC method by evaluating the effect of different parameters used in the MC simulations. The results showed that extensive attention should be paid on dimensions, physical parameters and volume calculations when modeling the free-air chamber and the reference volume. The data adjustment applied on the previous model of the WK07, as mentioned earlier, was a result of this study. In addition, the conventional method of determining the correction factors was also questioned. The international comparison, of the reference air kerma values in the low energy range, showed that the results obtained at LNHB by the WK07 free-air chamber tend to be slightly underestimated of about 0.2%. This difference, of the same order of magnitude of that noticed in the aforementioned ratio, also contributes to validate the agreement between the two methods.

Table 2.2.8. Introduced parameters and results of the reference air kerma rate with the WK07 using the two methods. Values in bold refer to results obtained either by calculations or measurements in this study.

PARAMETER	SYMBOL	UNIT	VALUE	UNCERTAINTY (%) AT (K=1)	
				Type A	Type B
FAC net measured current (corrected by k_T, k_P, k_h, k_s k_{pol}, k_d and noise)	I_{net}	A	**4.784E-11**	0.09	**0.22**
Interaction volume	$\boldsymbol{V_{\mathrm{int,WK07}}}$	m^{-3}	4.03E-07	-	0.05
Air density (20°C, 1 atm.)	ρ_0	$kg.m^{-3}$	1.20479	-	0.01
Avg. energy expended in air per ion pair formed divided by the elementary charge	$\frac{\overline{W}_{\mathrm{air}}}{e}$	$J.C^{-1}$	33.97	-	0.35
Radiative loss correction	$1-\overline{g}_{\mathrm{air}}$	-	1	-	0.01
Correction					
Conventional method – Method 1					
Product of the rest of correction factors	$\prod_i k_i$	-	**0.9983**	-	0.15
Air kerma rate	$\dot{K}^{\mathrm{conv}}_{\mathrm{air,ref}}$	$Gy.\ s^{-1}$	**3.343E-03**	0.09	0.45
				0.46	
MC method – Method 2					
Transferred energy in the reference volume	$\boldsymbol{E_{\mathrm{tr}}}$	eV/PP	**0.06321**	0.06	1
Deposited energy in the WK07 collection volume	$\boldsymbol{E_{\mathrm{dep}}}$	eV/PP	**0.16135**	0.02	1
Reference volume	$\boldsymbol{V_{\mathrm{ref,MC}}}$	m^{-3}	**1.576E-07**	-	-
Air kerma rate	$\dot{K}^{\mathrm{MC}}_{\mathrm{air,ref}}$	$Gy.\ s^{-1}$	**3.353E-03**	0.11	1.48
				1.48	

Subsequently, the air kerma rate value obtained using the global correction factor, by the MC approach, was used in the following sections and in the final determinations of the reference value of absorbed dose to water.

2.4.2. Calibration of transfer ionization chambers under reproduced INTRABEAM beams

To determine by transfer, in the next section 2.4.3, the air kerma rate of the IB-XR beam, $\dot{K}_{air,\mathrm{IB}}$, a secondary ionization chamber was calibrated in the reference beam, that is the one reproduced at the LNHB; this calibration process is described in this section.

As mentioned earlier, a PTW-23342 plane parallel ionization chamber was chosen as transfer chamber. It was calibrated, in terms of $\dot{K}_{air,\mathrm{ref}}$, for the INTRABEAM® photon spectrum along the probe axis after 1 cm of water. To do so, the ionization current of the transfer chamber, $\mathrm{I}_{TC,\mathrm{ref}}$, was measured under the configuration shown in Figure 2.19. This is the same configuration as the one used in the previous section to measure the ionization current of the WK07 free-air chamber, and hence, with the same air kerma rate as the primary reference $\dot{K}_{air,\mathrm{ref}}$. This configuration includes the tube current, the high voltage potential, the reference distance, the photon beam collimation and the Al filtration which were kept all the same.

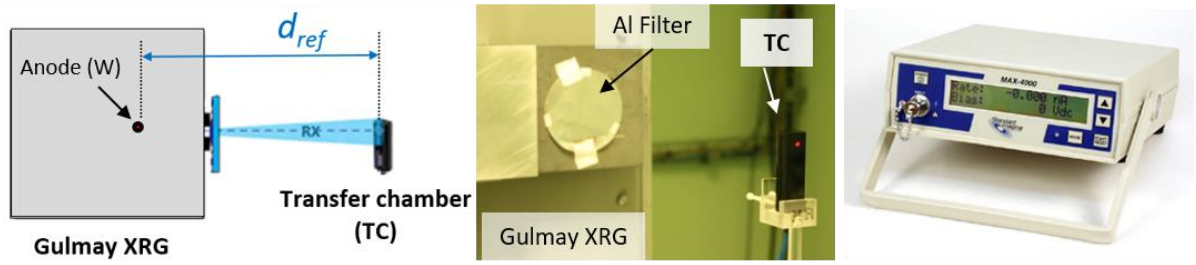

Figure 2.19. Measurements of ionization current delivered by the PTW-23342 transfer chamber when irradiated by the reference beam: (left) measurement scheme (not to scale), (middle) a picture of the real measurement and (right) a picture of the MAX-4000 electrometer used for the ionization current measurement.

The ionization current was measured using a MAX-4000 electrometer [137] (Standard Imaging Inc., Middleton, WI). This electrometer is a broadly used device for such measurements [138–140]. The same MAX-4000 electrometer was used later to measure the ionization current of the IB-XRS, as will be seen in the next section.

The measurement of the calibration coefficient of the transfer chamber $N_{\dot{K}_{air,\mathrm{ref}}}$, was preceded by several steps, to guaranty precise measurements of its ionization current. Since the chamber is vented (exposed to ambient air conditions in the measurement room), it was installed in the measurement room one day before the measurements were performed; to stabilize the air temperature and humidity inside the chamber air cavity to the measurement room air conditions. Besides, as soon as the chamber was installed in the room measurement, it was connected to a high voltage of 300 kV using the MAX-4000 electrometer. At last, preceding the current measurements, the transfer chamber was irradiated following the instructions recommended by the manufacturer.

The charge collection mode of the MAX-4000 electrometer, since more precise than its current mode, was used for the measurement of the ionization current. The latter was deduced from a series of charge measurements over time. For a single measurement, the collected

charges over a specific period of time (fixed to 60 seconds) were corrected for the background noise and reference atmospheric conditions (reference temperature and pressure). Then, to deduce the corresponding ionization current, the total corrected charges were divided by the collection time. This process was repeated at least 15 times, for the same chamber and measurement conditions. Thus, an average net ionization current value, $I_{TC,ref}$, was calculated over the number of measurements.

Two different PTW-23342 chambers were used for ionization current measurements at LNHB. These measurements of the ionization current, with the two chambers, were realized before and after the ionization current measurements performed with the IB-XRS system, discussed in section 2.4.3. The reason of such a procedure is to verify the stability and proper functioning of all parts in the measurement system. Finally, the calibration coefficients, $N_{\dot{K}_{air,\mathrm{ref}}}$, were calculated by dividing the $\dot{K}_{air,\mathrm{ref}}$ value, as obtained in the previous section and completed at each measurement session, by the net current measured by each transfer chamber. Net measured ionization currents, $I_{TC,ref}$ and calibration coefficients, $N_{\dot{K}_{air,\mathrm{ref}}}$ obtained from the previous measurements are summarized in Table 2.2.9.

Table 2.2.9. Net ionization currents and calibration coefficients measured for the two PTW-23342 transfer chambers

	First PTW-23342 chamber	**Second PTW-23342 chamber**
Average net current $I_{TC,ref}$ [A]	**2.872E-12**	**2.424E-12**
Std. deviation (k = 1)	3.187E-15	1.037E-15
Relative uncertainty (%)	**0.19**	**0.16**
Calibration coefficient $N_{\dot{K}_{air,\mathrm{ref}}}$ [Gy. s^{-1}A^{-1}]	1.164E+09	1.379E+09
$\mathbf{u}(N_{\dot{K}_{air,\mathrm{ref}}})$	**0.50**	**0.48**

Moreover, to study the impact of the photon energy distribution on the calibration coefficient, the first chamber was calibrated in three other reference beams spectra as seen in Figure 2.20. For each considered spectrum, the reference air kerma rate, $\dot{K}_{air,\mathrm{ref}}$, was established using correction factors determined by the conventional method as described before under the same configurations.

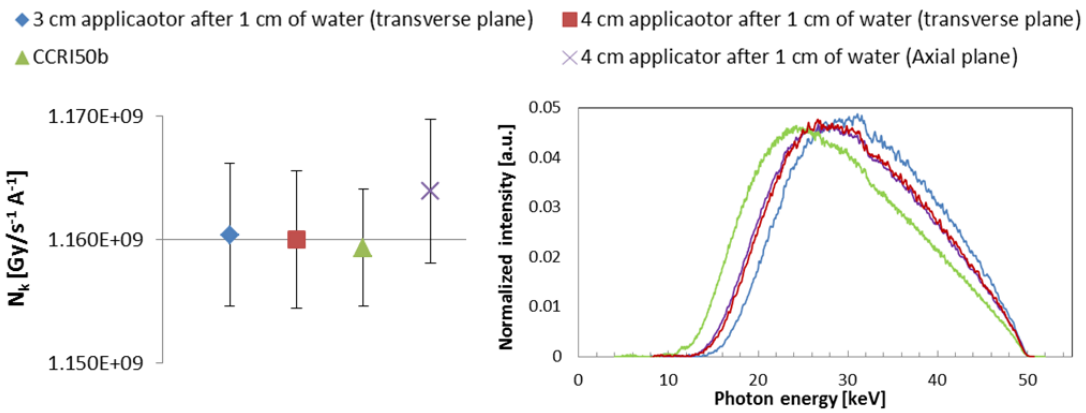

Figure 2.20. Comparison of the calibration coefficients obtained for the first PTW-23342 chamber for different photon energy *spectra*

The calibration coefficients, determined for different energy photon distributions, were similar within the corresponding uncertainty bars. Accordingly, we concluded that the response of the PTW-23342 transfer chamber, over the considered photon energy range, does not significantly depend on the photon energy distribution. Consequently, the PTW-23342 chamber, calibrated using any of these photon energy spectra, can be used for further air kerma measurements of the IB-XRS with 3-cm and 4-cm spherical applicators. This conclusion, subject to further investigations over the rest of IB applicators, could be generalized. In other words, if this conclusion is verified, the PTW-23342 transfer chamber calibrated under an adequate reference beam quality, say CCRI50b, due to its resemblance to the IB photon spectra, may be used to characterize the IB-XRS mounted with any applicator in terms of air kerma rate (as proposed in the next section 2.4.3).

So, as the calibration coefficient was determined in this section, the next step was to measure the $\dot{K}_{air,\mathrm{IB}}$ of the IB-XRS mounted with a 4-cm applicator after 1 cm of water in the axial plane. This issue is treated in the following sections.

2.4.3. Measurements of INTRABEAM $\dot{K}_{\mathrm{air,IB}}^{measured}$

The measurement of the $\dot{K}_{\mathrm{air,IB}}^{measured}$ of the IB-XRS was performed at Saint Louis hospital in Paris. The calibration coefficient determined in the previous section, for the reproduced spectrum of the IB-XRS with a 4-cm spherical applicator after 1 cm of water along the probe axis, was used. The measurement was performed using a home-made system developed especially for this measurement. The measurement system, configurations, results and other aspects, concerning the $\dot{K}_{air,\mathrm{IB}}$ determination, are discussed in this section.

Several issues had to be considered when developing the measurement system: the alignment of the detector on the source axis, a precise measurement of the SDD, the filtration to get the spectrum after an equivalent attenuation of 1 cm in water, the photon scattering from surroundings, and first of all, the transportability and easy handling of the system since measurements were to be realized at the hospital.

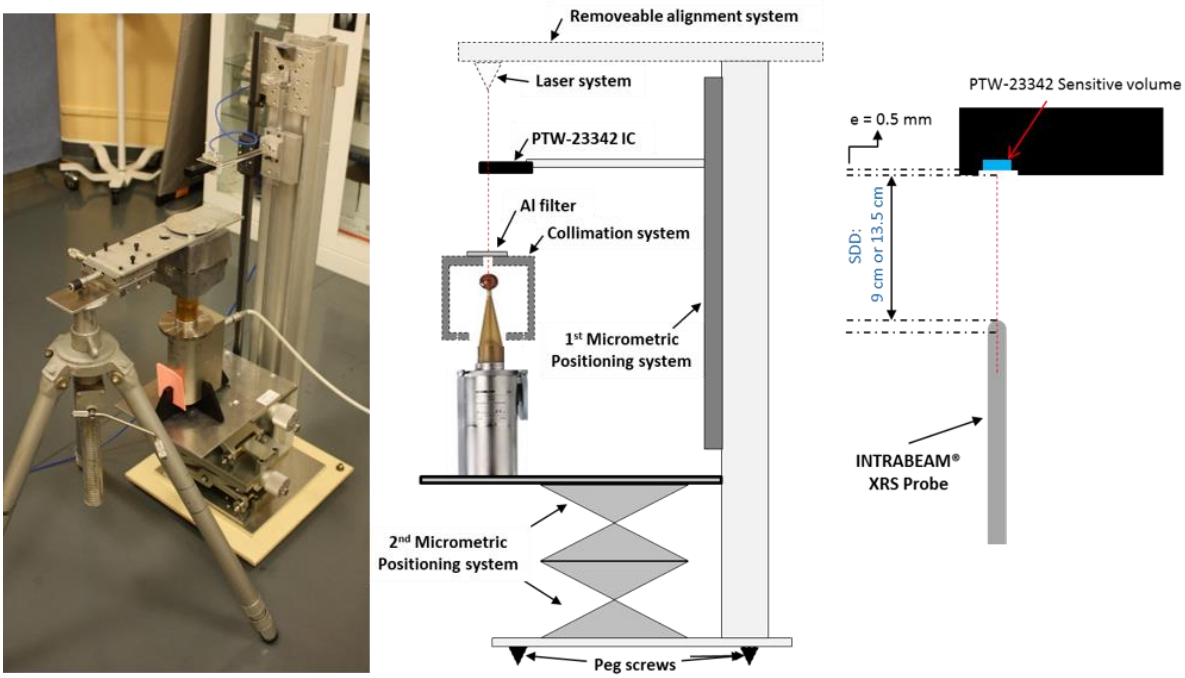

Figure 2.21. Measurements of the ionization current delivered by a PTW-23342 chamber when irradiated by the IB-XRS: (left) picture of the real measurement conducted at St. Louis hospital; (middle) scheme of the measurement system (not to scale); and (right) scheme showing the points of reference for SDD measurements

The developed system is shown in Figure 2.21. The tripod and peg screws were used to account for the irregularity of the measurement room's floor. A laser system was installed to align the detector with the source axis. However, this alignment laser system was removed during measurement to avoid backscattering of photons into the ionization chamber. Two micrometric positioning systems were integrated to control the movements of the ionization chamber and the IB-XRS; they control the movement only in the vertical direction. The first micrometric system offers a displacement of the ionization chamber along a fixed axis, so the chamber can be kept aligned when displaced. Finally, since the IB-XRS emits photons in all directions (4π solid angle), a collimation system was also added to avoid backscattered photons into the ionization chamber from the surrounding parts. Thereby, the conditions of measurement at the hospital using the transfer chamber were kept similar to the ones encountered at LNHB (where the XRG beam is also collimated).

After the alignment, of the ionization chamber sensitive volume center on the beam axis, the SDD was determined from the IB-XRS probe's tip to the PTW-23342 ionization chamber body as shown on the right scheme in Figure 2.21. When the required SDD is set, using the two micrometric positioning systems, the 4-cm spherical applicator was mounted on the IB-XRS and the collimation system was introduced. The collimator dimensions and position were defined as shown in Figure 2.22. The collimator is held over a tripod system to guaranty its flatness. A lead (Pb) shield envelops the collimator to eliminates backscattering into the ionization chamber. The configuration with a 1-cm diameter collimator and a 1-cm separation distance (this distance is attained by the second positioning system while keeping the SDD unchanged) from the applicator surface was optimized. This configuration approaches the point

source conditions with a beam size sufficiently large to fully irradiate the chamber sensitive volume and walls (without interacting with surrounding parts).

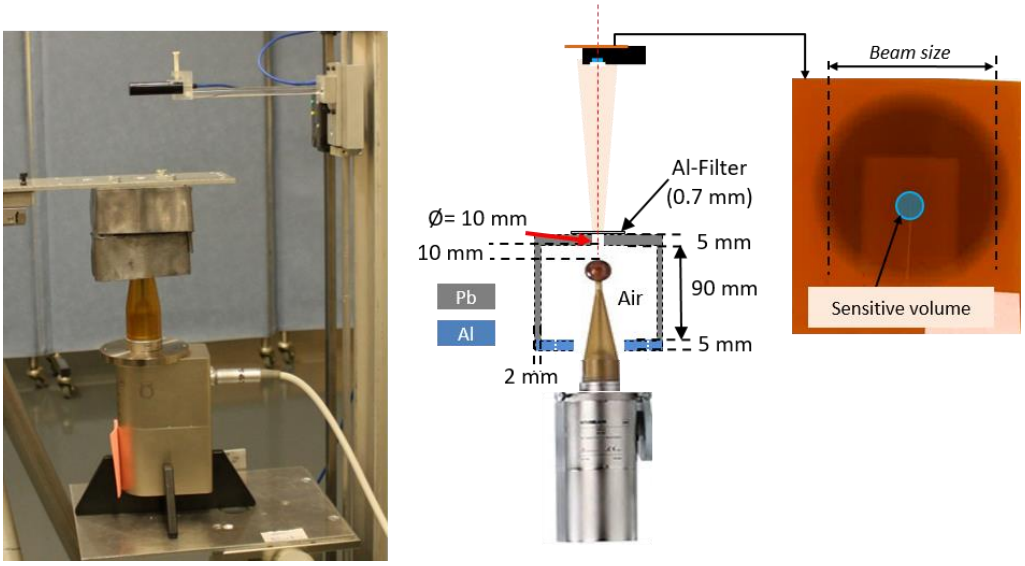

Figure 2.22. Verification of the beam size and the centering of the PTW-23342 along the beam axis: (left) zoom-in on the real measurement shown in Figure 2.21, and (right) scheme showing collimator dimensions and the Gafchromic film used.

To verify for the beam size and sensitive volume position (source-detector alignment), measurements with Gafchromic films were performed. Before each measurement, a Gafchromic film was placed over the ionization chamber as seen in Figure 2.22. Such a measurement has the advantage of giving direct results (without any further treatment) in a very short time (couple of minutes for the considered SDD with the IB-XRS). The films helped to check the system alignment and the collimator position by direct analysis of the form and size of the outlined beam on the film.

Table 2.2.10. Corresponding parameters and results obtained for the two PTW-23342 ionization chambers at the two SDDs

Measurements SDD [cm]	**13.5 cm**		**9 cm**
Chamber number	First chamber	Second chamber	Second chamber
Calibration coefficient $N_{\dot{K}_{air,\mathrm{ref}}}$ [Gy. s^{-1}. A^{-1}]	1.164E+09	1.379E+09	1.379E+09
Average net current $I_{TC,IB}$ [A]	1.122E-13	9.507E-14	2.216E-13
Std. deviation (k=1)	5.227E-16	2.773E-16	5.628E-16
Relative uncertainty (%)	0.47	0.29	0.25
$\dot{K}_{air,IB}^{measured}$ [Gy. s^{-1}]	**1.304E-04**	**1.310E-04**	**3.053E-04**
$u(\dot{K}_{\mathrm{air,IB}}^{measured})$	0.70	0.59	0.57

With all the former steps considered, measurements of the PTW-23342 ionization currents (or $\dot{K}_{\mathrm{air,IB}}^{measured}$ if the calibration factor is applied) were realized at two SDDs: 9 cm and 13.5 cm. The SDD was intended to be large, to decrease the corresponding relative uncertainty. However, since the ionization chamber reading was found to drop dramatically with increasing SDD, and hence, the noise-to-signal ratio increases, the chosen SDDs were a compromise between these

two factors. The choice of two SDDs was to have results at two points, so it provides a tool for comparison for the final dose rate results; as well, it gives an indication of the deviation of the readings from the inverse square law along the measurement axis.

Three measurements, in total, were performed: two at 13.5 cm with the two ionization chambers, and one at 9 cm only with the second chamber (we were short in time due to working conditions in a hospital). The same MAX-4000 electrometer used previously for the chamber calibration measurements was reused here. Moreover, the chambers were set to stabilize for measurement room atmospheric conditions over night. They were connected to the same high voltage value as the one used for calibration (300 kV) and sufficiently pre-irradiated before the measurements.

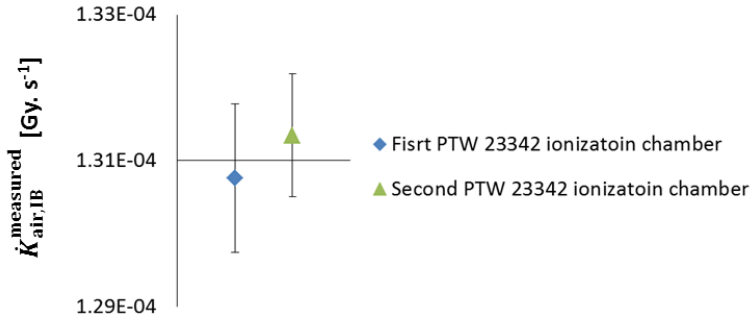

Figure 2.23. Comparison of the IB-XRS air kerma rate values $\dot{K}^{measured}_{air,IB}$, measured with the two PTW-23342 ionization chambers at a SDD of 13.5 cm.

The results obtained from the three measurements are presented in Table 2.2.10. The $\dot{K}^{\text{measured}}_{\text{air,IB}}$ values measured at 13.5 cm SDD with the two chambers agree within the uncertainty bars as seen in Figure 2.23. Nonetheless, even though the number of measurement is statistically low, the accordance observed between the results is on the right way to confirm the values obtained and the system reproducibility. Regarding the single measurement of $\dot{K}^{measured}_{\text{air,IB}}$ at 9 cm SDD, the ratio of the measured value at this point to that measured at 13.5 cm, with the same chamber, was compared to the ratio of the inverse squared value of their corresponding distances. The value obtained was 1.04 (measurement ratio to inverse squared distance ratio). In other words, the measured air kerma rate value gives a 4 % higher value than the expected one relying on the inverse square law. However, it is worthy here to remember, that as the SDD decreases, the point source conditions are less valid and the relative uncertainty over the distance also increases.

To conclude here, $\dot{K}^{measured}_{\text{air,IB}}$ values of the IB-XRS under the prescribed conditions were obtained. The agreement between the two $\dot{K}^{measured}_{\text{air,IB}}$ values, measured at the 13.5 cm SDD, is a good indication on the reliability of the results. The value measured at the 9 cm SDD can confirm the measurements at the 13.5 cm SDD, taking into account the relative uncertainty on the SDD and the deviation from the inverse square law. Henceforth, to convert this air kerma rate value, $\dot{K}^{measured}_{\text{air,IB}}$, into the desired absorbed dose to water rate value, $\dot{D}_{w,1cm}$, MC calculations were used to calculate a conversion factor $F_{(K\ to\ D)_{w,\,1\,cm}}$, as presented in the next section.

2.4.4. MC calculations of the conversion factor, $F_{(K_{\text{air,IB}} \text{ to } D_{\text{w, 1 cm}})}$

The calculation of the conversion factor from $\dot{K}_{\text{air,IB}}^{measured}$ to $\dot{D}_{w,1cm}$ is presented in this section. This factor permits to pass from the measured quantity, as seen in the previous section, to the quantity of interest in reference conditions, the absorbed dose to water at a distance of 1 cm from the applicator surface, along the source axis, in a full scatter water phantom. The calculations were based on the MC model of the IB-XRS with a 4 cm spherical applicator developed previously. The reliability of this model for such calculations is built on the $K_{\text{air,norm}}$ ratio, presented in section 2.3.2.2, which showed a negligible difference (1.003) between the photon energy spectrum determined by this model to that measured for the INTRABEAM® after 1 cm in water (distance at which the conversion factor is determined in water). PSF files were used as sources in all the following calculations.

2.4.4.1. Calculation of $K_{\text{air,IB}}^{\text{MC}}$ under measurement conditions

The calculations of air kerma, in unit of dose (eV.g^{-1}) per history or primary particle (i.e. eV.g^{-1}.pp^{-1}), were performed with a simplified model of the real measurement configurations shown in Figure 2.21. Only the collimation and Al-filter were added to the previously developed MC model of the IB-XRS with the 4 cm spherical applicator. This simplification is quite reasonable due to the lead collimation that limits the interactions of emitted photons with the surrounding system parts, and hence, almost completely eliminates the contribution of scattered photons from the measurement system, into the calculated air kerma at the chamber position.

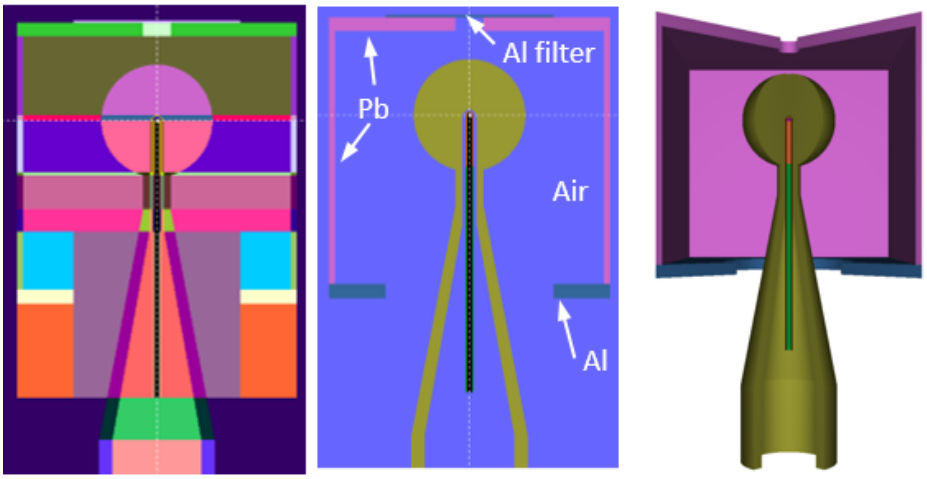

Figure 2.24. MC model for air kerma calculations: (left & middle) bodies and materials cross-section views, respectively, as shown in GVIEW2D and (right) cross-section of a 3D representation, without Al filter, obtained by GVIEW3D.

The developed PENELOPE model is shown in Figure 2.24. The dimensions, materials and configurations considered are as in Figure 2.22. The PSF files, generated previously in section 2.3.3, were used as particle source files. The simulation parameters of lead and aluminum are given in Table 2.2.11. Default values were considered for the rest of parameters (C_1=C_2=0.05, W_{CC}=W_{CR}= 1 keV and 1/10th of the body thickness for DSMAX). The rest of simulation parameters of the previously developed model for the IB-XRS with a spherical applicator of 4-cm in diameter were kept the same (as in Table 2.2.3).

Table 2.2.11. Simulation parameters of lead and aluminum used in the air kerma calculation model

Material	Reference # in pendbase	Density [g/cm^3]	E_{abs}(1) [eV]	E_{abs}(2) [eV]	E_{abs}(3) [eV]
Al	13	2.6989	1.0E+03	1.0E+03	1.0E+03
Pb	82	11.35	50E+03	1.0E+03	50E+03

In parallel to aforementioned measurements using Gafchromic films, MC calculations of the beam form, size and profile were performed at the two reference measurement points, i.e., at SDDs of 9 cm and 13.5 cm. To this end, two air-filled disk detectors, each of 6 cm in diameter and 1 mm thick, were modeled at the two reference points of measurement, perpendicular to the beam axis. The MC model and the results obtained are shown in Figure 2.25. Two main regions can be defined for the beam shape at each distance (see the two top right graphs in Figure 2.25). The outer less dense regions represent regions of low number of photons in comparison to the inner regions; this can also be deduced from their corresponding photon intensity profiles outlined along the x plane (see the corresponding two right bottom graphs in Figure 2.25). The same two regions shape were also identifiable with the Gafchromic films shown on the right of Figure 2.25. The reason of this shape is that the IB-XRS is not a point source as mentioned earlier. However, for the two measurement distances, the inner region beams sizes (almost 3 cm and 4.4 cm at 9 cm and 13.5 cm SDDs, respectively) are largely sufficient to irradiate the sensitive volume (5 mm diameter) and walls of the PTW-23342 ionization chambers.

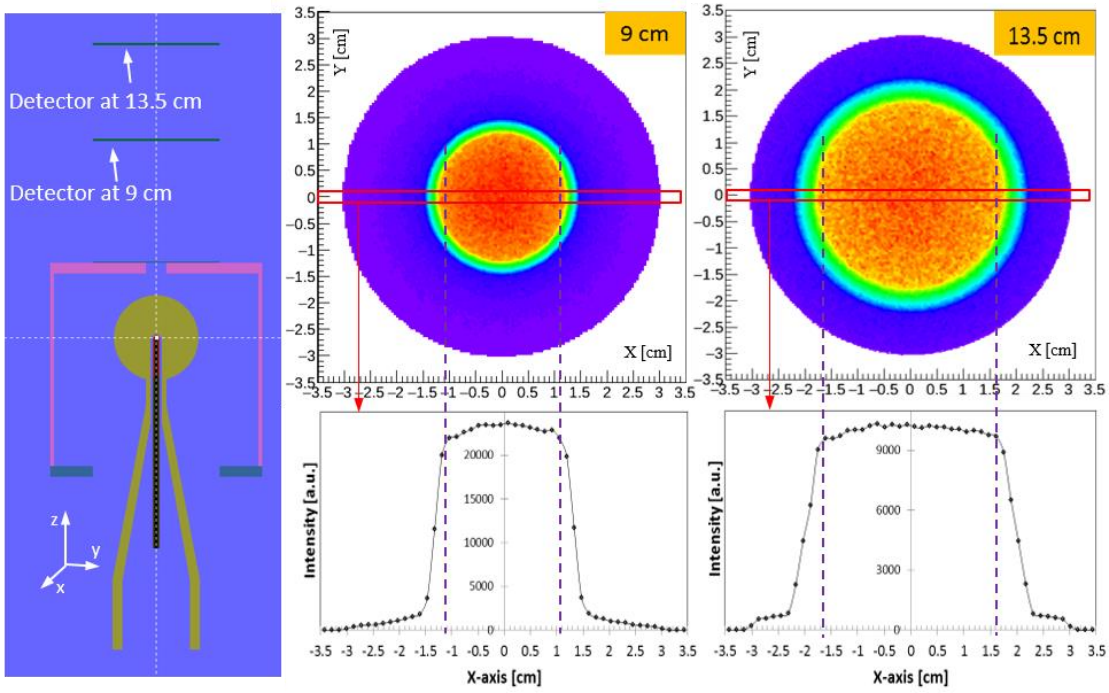

Figure 2.25. On the left, the MC model mimicking the measurements made using Gafchromic films, with detectors are disks filled with air; on the right, MC calculated results in terms of beam sizes (top) and profiles (bottom) at the two considered SDDs.

The configuration shown in Figure 2.26 was used to calculate the air kerma values, $K_{\mathrm{air,IB}}^{MC}$, at the two considered SDDs. The PTW-23342 ionization chamber was modeled, at both SDDs at once (in one calculation model), by small detection volumes filled with air (each representing the chamber sensitive volume). The two detectors were enclosed between concentric spheres of 1 mm difference in radius (detector thickness) and a cone of 10° total angle. These volume shapes and sizes were optimized (instead of cylindrical chamber volume shown in the same figure) to profit the isotropy of the model, and hence, decrease the statistical uncertainty (as discussed in the next paragraph). The values taken for the SDDs correspond here to the distance between the probe tip (outer surface) to the PTW-23342 entrance window of the sensitive volume (the added 0.5 mm distance refers to the air gap between outer surface of the ionization chamber and the entrance window as shown in Figure 2.26). The Al-filter was placed over the collimator in the same configuration as in measurements. The filter was modeled as a disk of 0.7 mm (equivalent to 1 cm water attenuation, see section 2.2.1.1) in thickness and 6 cm in diameter, equivalent to the filter added previously to get an equivalent attenuation of 1 cm of water.

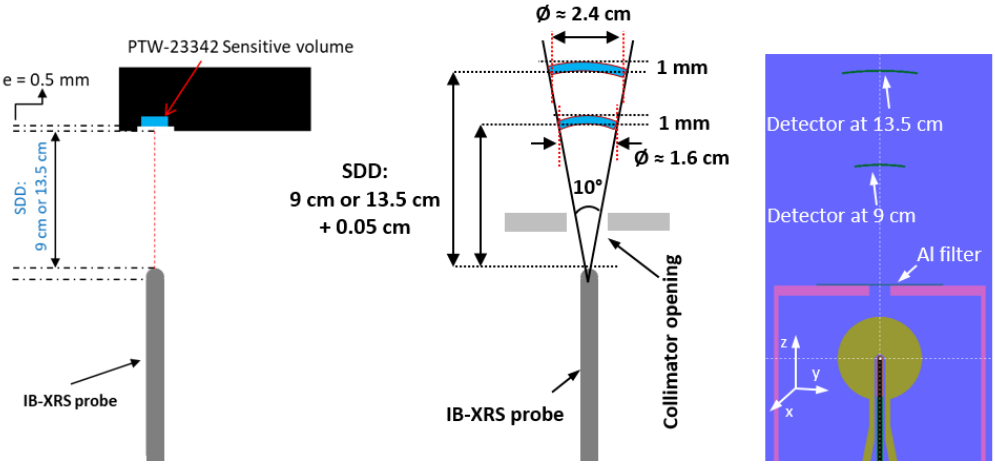

Figure 2.26. Configuration used to calculate the air kerma values, $K_{air,IB}^{MC}$, at the two considered SDDs: (left) scheme (not to scale) of the original reference distances considered to measure the $K_{air,IB}^{measured}$ with the PTW-23342 chamber, (middle) scheme (not to scale) showing the configuration and detectors chosen for air kerma calculations, and (right) a 2D view of the MC model in GVIEW2D

Despite the large size of the used PSF files, the calculated air kerma values in the considered detectors had large relative uncertainties (more than 20 %). These high statistical uncertainties are due to the 4π angular distribution of the photon source combined to the low probability for a photon to be emitted in the considered solid angle (that results from the relatively large SDD and small detection volumes). Moreover, to achieve reasonable uncertainties (in the range of < 0.5 %) using this approach, very large calculation time (at least one year) and storage space (hundreds of gigabytes) are required, keeping in mind that no variance reduction technique is applied. Therefore, since such calculation times and storage space are not available, at least for this study, a second approach was adopted to calculate the air kerma at the reference SDDs.

The second approach relies on analytical calculations of the air kerma value, based on a calculated energy distribution of the photon fluence. Photon energy fluence distributions were calculated at each measurement distance using photon impact detectors (described before in

APPENDIX-C). The used energy window ranged from 1 keV to 52 keV with 204 channels and a constant energy bin (ΔE). Impact detectors give the probability density distribution, per primary particle and energy, E, to enter the detection volume of cross section area A. After division by A, this gives an evaluation of the energy distribution of photon fluence $\Phi(E)$ per primary particle at the point of interest. Thus, the air kerma values, in the two detectors, were calculated using the following equation, using tabulated values of the mass energy transfer coefficient of air [141]:

$$\boldsymbol{K}_{\mathbf{air,IB}}^{\boldsymbol{MC}} = \sum_{E} E \cdot \Delta E \cdot \Phi(E) \cdot \left(\frac{\mu_{tr}}{\rho}\right)_{\text{air}} (E)$$

The calculated air kerma values, $\boldsymbol{K}_{\mathbf{air,IB}}^{\boldsymbol{MC}}$, in the two detectors using the above equation are presented in Table 2.2.12. To verify the reliability of using this approach for air kerma calculations, the air kerma in the WK07 free-air chamber reference volume, presented in section 2.4.1.2, was calculated using both the calculation of transferred energy (based on Table 2.2.8) and the calculation of the photon energy fluence distribution. The comparison between the two *air kerma* values resulted into a relative difference in the order of 0.3 %. This boosts the consistency of using the second approach for air kerma calculations.

Table 2.2.12. Air kerma values calculated at the two reference SDDs using the analytical calculations, and the air kerma values calculated for the $V_{ref,MC}$ using both energy transfer and photon fluence energy distribution methods

	$\boldsymbol{K}_{\mathbf{air,IB}}^{\boldsymbol{MC}}$ **at SDDs [cm]**			$\boldsymbol{K}_{\mathbf{air,ref}}^{\boldsymbol{MC}}$ **in** $\boldsymbol{V}_{\mathbf{ref,MC}}$ (section 2.4.1.2)	
Calculation method	$\Phi(E)$			$\Phi(E)$	$E_{tr}/(\rho.V_{ref,MC})$
Reference detector	13.5 cm	9 cm		$V_{ref,MC}$	$V_{ref,MC}$
Air kerma **[eV. g^{-1} pp^{-1}]**	0.002585	0.005917		**331.76**	**332.89**
***u*(*air kerma*) (%)**	1.28	1.2		1.04	0.06

After the calculation of $\boldsymbol{K}_{\mathbf{air,IB}}^{\boldsymbol{MC}}$ values determined at the two measurement SDDs in this part, the calculation of the absorbed dose to water $D_{\mathrm{w,1cm}}^{MC}$ in the reference conditions is needed to obtain the conversion factor $F_{(K\ to\ D)_{w,\,1\ cm}}$. This calculation is presented in the next part.

2.4.4.2. Calculation of $D_{\mathrm{w,1cm}}^{MC}$ along the probe axis

The calculation of the reference absorbed dose to water value at 1 cm in water, $D_{\mathrm{w,1cm}}^{MC}$, is presented in this part. The $D_{\mathrm{w,1cm}}^{MC}$ value has to be calculated under the reference conditions, i.e., absorbed dose to water in an infinitesimal volume of water in a full scatter water phantom at 1 cm distance from the applicator surface.

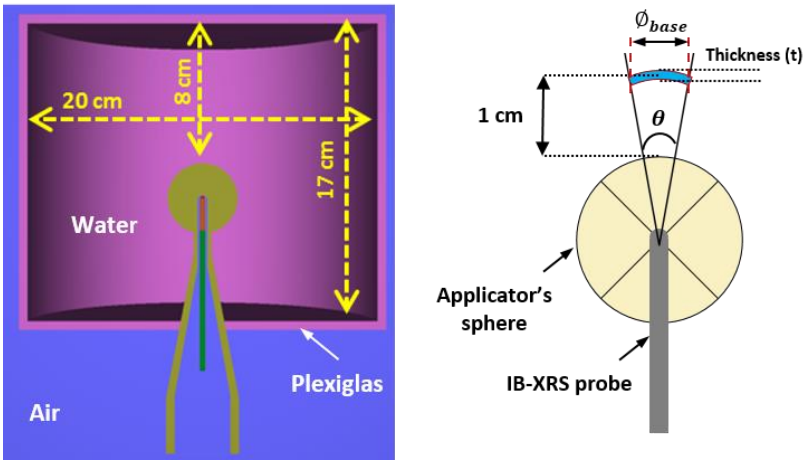

Figure 2.27. (Left) 3D model with dimensions, obtained by GVIEW3D, of the MC model used for $D_{w,1cm}^{MC}$ calculation, and (right) scheme (not to scale) describing the configuration used to define the reference calculation volume of $D_{w,1cm}^{MC}$.

The PSF files associated with the IB-XRS with the 4-cm applicator model developed previously were used (section 2.3.3). The water phantom, added to the previously developed model, and the reference volume description are shown in Figure 2.27. The water phantom has a cylindrical shape. The dimensions of the phantom are large enough to deliver a full scatter phantom at the (≤ 50 keV) photon energy range. The Plexiglas walls were added but had no significant role in our configuration. The water detection volume used for the calculation of the absorbed dose, $D_{\mathrm{w,1cm}}^{MC}$, was placed along the probe axis at 1 cm distance. This 1 cm represents the normal distance between the external applicator sphere surface and the center of the detection volume.

The energy deposition in this water volume was used to derive the $D_{\mathrm{w,1cm}}^{MC}$value. The water and Plexiglas materials were defined using their reference number in the PENELOPE materials database (Pendbase #: 278 for water and 224 for Plexiglas), with corresponding densities, in [g.cm^{-3}], of 1.0 and 1.19 for water (at 4 °C) and Plexiglas, respectively. Physical simulation parameters were similar to those described in Table 2.2.3.

Several forms of detection volume were tested for the reliability of the $D_{\mathrm{w,1cm}}^{MC}$ calculation as shown in Figure 2.28. The first configuration, a spherical reference volume of 1 mm in diameter, was considered since it mostly represents a "point" reference volume, and so, it has the closest analogy to the reference conditions. However, the corresponding statistical uncertainty of $D_{\mathrm{w,1cm}}^{MC}$was much higher than the acceptable limit (2.6% >> 0.5 %). Thus, five more volume configurations were explored, the idea being to take profit of the model symmetry, along the probe axis, to decrease the relative statistical uncertainty, and then find an optimal reference volume configuration. Moreover, all reference volumes, in the number 2 to 6 configurations, were defined as described in the Figure 2.27 scheme with their corresponding parameters summarized in Table 2.2.13.

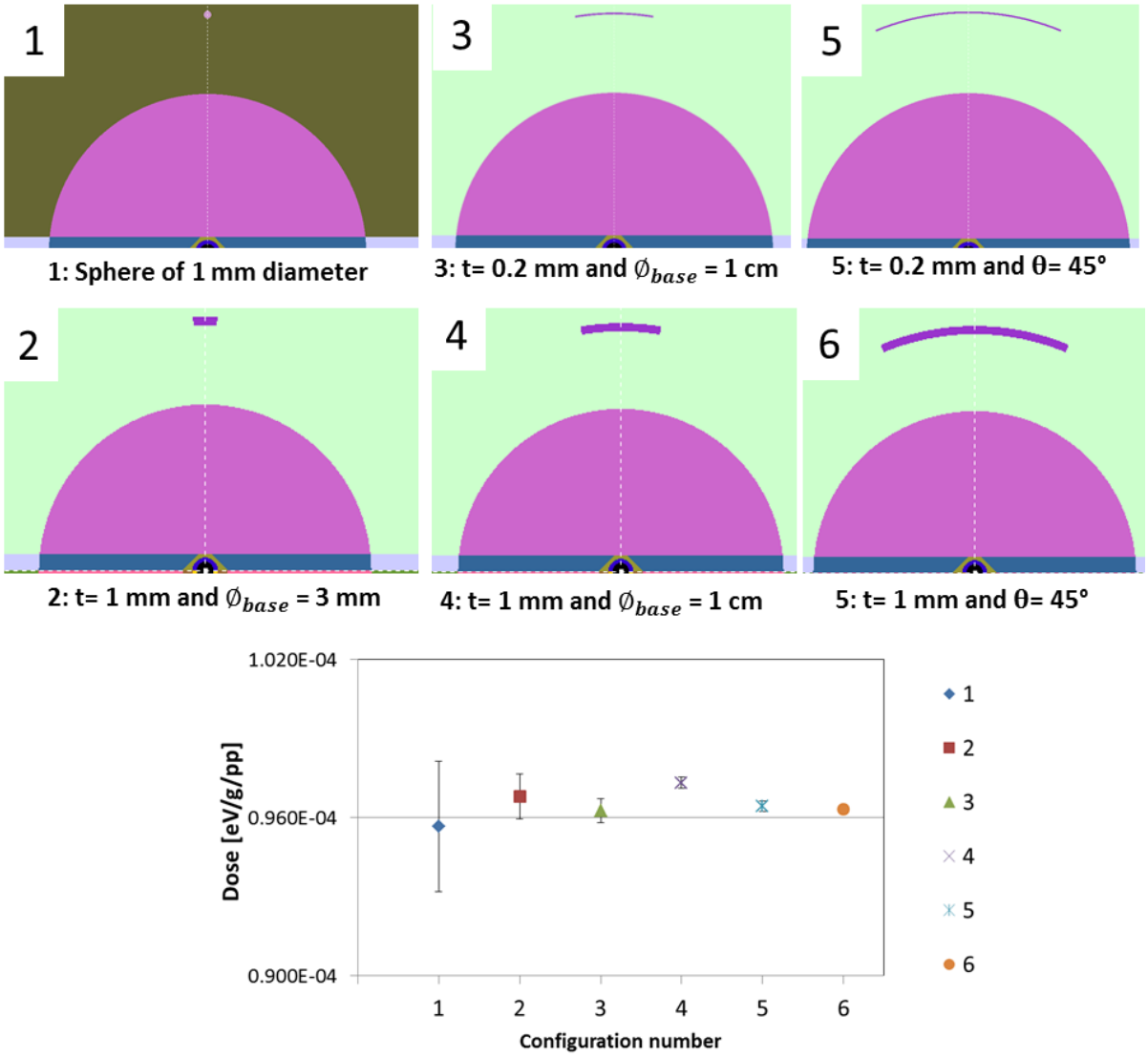

Figure 2.28. (Top) bodies-representations numbered from 1 to 6, obtained by GVIEW2D and showing the 6 detection volumes considered in this study; they zoom in on the upper half of the applicator sphere; (bottom) comparison of the $D_{w,1cm}^{MC}$ values obtained for the 6 different configurations with parameters as defined in the left scheme of Figure 2.27.

The comparison between the $D_{\mathrm{w,1cm}}^{MC}$values, for all configurations, is shown in the bottom part of Figure 2.28, and the detailed data are summarized in Table 2.2.13. The second configuration was omitted due to its high statistical uncertainty which was over the acceptable limit (0.5 %). Regarding the last two configurations (5 and 6), the corresponding $D_{\mathrm{w,1cm}}^{MC}$ value of the sixth configuration deviated from the value obtained in the fourth configuration (out of uncertainty bars with 3k). Thus, since their larger angle involved more demanding conditions, in terms of isotropy of the particle fluence, their values were also discarded. Finally, the third and fourth configurations agreed within their associated uncertainties. However, the fourth configuration was eventually chosen, due to its lower uncertainty, to calculate the absorbed dose to water value used in the calculation of the conversion factor $F_{(K_{\mathrm{air,IB}} \text{ to } D_{\mathrm{w,\,1\,cm}})}$.

Table 2.2.13. Corresponding parameters and calculation results for the six reference volumes described in Figure 2.28.

Configuration #		**1**	**2**	**3**	**4**	**5**	**6**
Angle (θ) [degrees]		Sphere of 1 mm diameter	5.724	18.924	18.924	45	45
Thickness (t) [mm]			1	0.2	1	0.2	1
$\emptyset_{base}$ [mm]			3	10	10	24.86	24.86
E_{dep} [eV. pp^{-1}]		5.009E-05	6.831E-04	1.481E-03	7.488E-03	8.303E-03	4.147E-02
Volume [cm^3]		5.236E-04	7.056E-03	1.539E-02	7.694E-02	8.609E-02	4.305E-01
$D^{MC}_{w,1cm}$ [eV. g^{-1} pp^{-1}]		9.6E-02	9.7E-02	9.6E-02	9.7E-02	9.6E-02	9.6E-02
$u(D^{MC}_{w,1cm})$ (%)	Type A	2.6	0.88	0.47	0.21	0.21	0.09
	Type B	1.41	1.41	1.41	1.41	1.41	1.41

Finally, with the $K^{MC}_{air,IB}$ and $D^{MC}_{w,1cm}$defined in this section, the values of the $F_{(K_{air,IB} \text{ to } D_{w,\,1\,cm})}$ conversion factor at the two reference distances, 9 and 13.5 cm, are summarized in Table 2.2.14. Thus, all the quantities needed for the determination of the dosimetric reference $\dot{D}_{w,1cm}$ are now obtained. The use of all these values to determine the dosimetric reference value $\dot{D}_{w,1cm}$, is presented in the next section.

Table 2.2.14. The calculated conversion factor $F_{(K_{air,IB}\ to\ D_{w,\,1\,cm})}$ for the two reference points of measurements

Reference detector	**13.5 cm**	**9 cm**
$F_{(K_{air,IB} \text{ to } D_{w,\,1\,cm})}$	37.52	16.39
$u(F_{(K_{air,IB} \text{ to } D_{w,\,1\,cm})})$ (%)	1.91	1.86

2.4.5. Calculation of the absorbed dose rate to water at 1 cm

The value of the dosimetric reference quantity $\dot{D}_{w,1cm}$, for the IB-XRS with the 4 cm spherical applicator along the probe axis is calculated in this section. The correction factors considered for the free-air chamber are those calculated by the global correction factor approach, based on MC calculations.

The two configurations, defined previously in section 2.4.3, provided two set of values to calculate the reference absorbed dose to water rate value $\dot{D}_{w,1cm}$. The equation and parameters, presented in Table 2.2.15, used were extracted from the values determined in the previous sections of this chapter.

The $\dot{D}_{w,1cm}$ value, resulted from the source to detector distance of 9 cm configuration parameters, was almost 2 % higher than the $\dot{D}_{w,1cm}$ calculated with the other 13.5 cm configuration. However, this difference is covered within the associated uncertainties, which are in the order of 2.4 % and 2.45 % for the 9 mc and 13.5 cm reference distances, respectively. Hence, the two values are considered compatible taking into account their associated

uncertainties. Moreover, these uncertainties are aptly located in the uncertainty limit of (< 5 %) acceptable in radiotherapy treatments.

Table 2.2.15. Corresponding values for all parameters used to calculate the dosimetric reference value, $\dot{D}_{w,\,1\,cm}$

$$\dot{D}_{w,\,1\,cm} = \frac{I_{FAC}}{\rho_{air}} \cdot \frac{\overline{W}_{air}}{e} \cdot \frac{1}{V_{ref,MC}} \cdot \frac{E_{tr}}{E_{dep}} \cdot \frac{I_{TC,IB}}{I_{TC,ref}} \cdot \frac{D_{w,1cm}}{K^{MC}_{\text{air,IB}}}$$

Parameter	Symbol	Unit	Value	Reference
FAC net measured current (corrected by k_T, k_P, k_h, k_s k_{pol}, k_d and noise)	I_{FAC}	A	**4.784E-11**	Table 2.2.8
Air Density (20°C, 1 atm.)	ρ_{air}	kg.m^{-3}	**1.20479**	
Avg. Energy expended in air per ion-pair formed	$\frac{\overline{W}_{air}}{e}$	J.C^{-1}	**33.97**	
Reference Volume	$V_{ref,MC}$	m^{-3}	**1.576E-07**	
Transferred energy in reference volume	E_{tr}	[eV. pp^{-1}]	**0.06321**	
Deposited energy in the WK07 collection volume	E_{dep}	[eV. pp^{-1}]	**0.16135**	
Net Transfer chamber (TC) current measured at LNHB with the XRG	$I_{TC,ref}$	[A]	**2.424E-12**	2nd chamber Table 2.2.9
Water absorbed dose in reference conditions	$D^{MC}_{w,1cm}$	[eV. g^{-1} pp^{-1}]	**9.7E-02**	Table 2.2.13
Corresponding Parameters for 9 cm SDD				
Calculated air kerma in measurement conditions	$K^{MC}_{\text{air,IB}}$	[eV. g^{-1} pp^{-1}]	**0.005917**	Table 2.2.12
Net TC current measured with the INTRABEAM®	$I_{TC,IB}$	[A]	**2.216E-13**	2nd chamber Table 2.2.10
Absorbed dose to water rate at reference conditions	$\dot{D}_{w,\,1\,cm}$	Gy. s^{-1}	**5.041E-03**	**± 2.40 %**
Corresponding Parameters for 13.5 cm SDD				
Calculated air kerma in measurement conditions	$K^{MC}_{\text{air,IB}}$	[eV. g^{-1} pp^{-1}]	**0.002585**	Table 2.2.12
Net TC current measured with the INTRABEAM®	$I_{TC,IB}$	[A]	**9.507E-14**	2nd chamber Table 2.2.10
Absorbed dose to water rate at reference conditions	$\dot{D}_{w,\,1\,cm}$	Gy. s^{-1}	**4.951E-03**	**± 2.45 %**

Finally, the discussion and comparison of the calculated dose rate $\dot{D}_{w,1cm}$ in this study to the values given by ZEISS are presented in chapter 4.

Summary

A methodology to establish a primary dosimetric reference for electronic brachytherapy sources was developed. The primary reference was provided in terms of absorbed dose to water at 1 cm depth in water from the eBT source, which is the recommended dosimetric quantity for such systems. The methodology was then applied on the INTRABEAM® X-Ray source associated with a 4-cm spherical applicator, for which the dosimetric reference was established on the source probe axis at 1 cm depth in water.

The possibility to get photon energy distributions equivalent to those emitted by the INTRABEAM® X-Ray source associated with spherical applicatorswas demonstrated using conventional X-Ray generators. The attenuation of the emitted beams (through the applicator material or water) was found to enhance the quality of this reproduction by eliminating the induced fluorescence photons peaks of the X-Ray source anode material. The photon energy distributions of the INTRABEAM® X-Ray source with 3 and 4 cm spherical applicators were reproduced at the surface of the applicator and after an equivalent attenuation of 1 cm of water.

Monte Carlo calculations had a main role in the methodology to establish the dosimetric standard. It provides a mean to calculate a conversion factor, from the quantity accessible by measurements i.e. the air kerma, to the practically inaccessible (by direct measurement) dosimetric reference quantity i.e. the absorbed dose to water at 1 cm from the eBT source. Thus, the developed model of the INTRABEAM® X-Ray source associated with the 4-cm applicator required significant efforts to define the right combination between materials, physical parameters, source configurations and dimensions. The model was validated by comparing the resulting photon spectra to those measured for the INTRABEAM® under equivalent conditions. After validation, the conversion factor was calculated.

Moreover, the Monte Carlo method was proved to be valid to determine theglobal perturbation correction factor of the primary standard free-air ionization chamber. This global factor was compared and found compatible to the one obtained using the conventional method (based on measurements and calculations of separate factors). However, detailed Monte Carlo models are essential to obtain such results.

The response of the transfer cavity ionization chamber, PTW-23342, used to calibrate the INTRABEAM source was found stable for photon beams distributed over the considered energy range. The same calibration coefficient, in terms of air kerma, was determined for this chamber under varying photon energy distributions. Therefore, calibration coefficients based on photon beams similar to those emitted by eBT systems are valid for air kerma measurements using this chamber.

Chapter 3

3. Determination of the absorbed dose profiles around the IB-XRS using a dosimetric gel

This chapter deals with the determination of dose profiles around the IB-XRS using a dosimetric gel. The process to determine the dose distribution with the dosimetric gel has already been explained in section 1.3.3.3, it is here briefly summed up in Figure 3.1. When the radiosensitive dosimetric gel is irradiated, the radiation induces chemical reactions inside the gel. These chemical reactions induce the production of species that lead to modifications of the gel properties. These modifications can then be quantified and spatially localized by 3D readout techniques (MRI imaging for our gel). Finally, to translate the measured quantity, into the corresponding absorbed dose to gel, a calibration is to be applied.

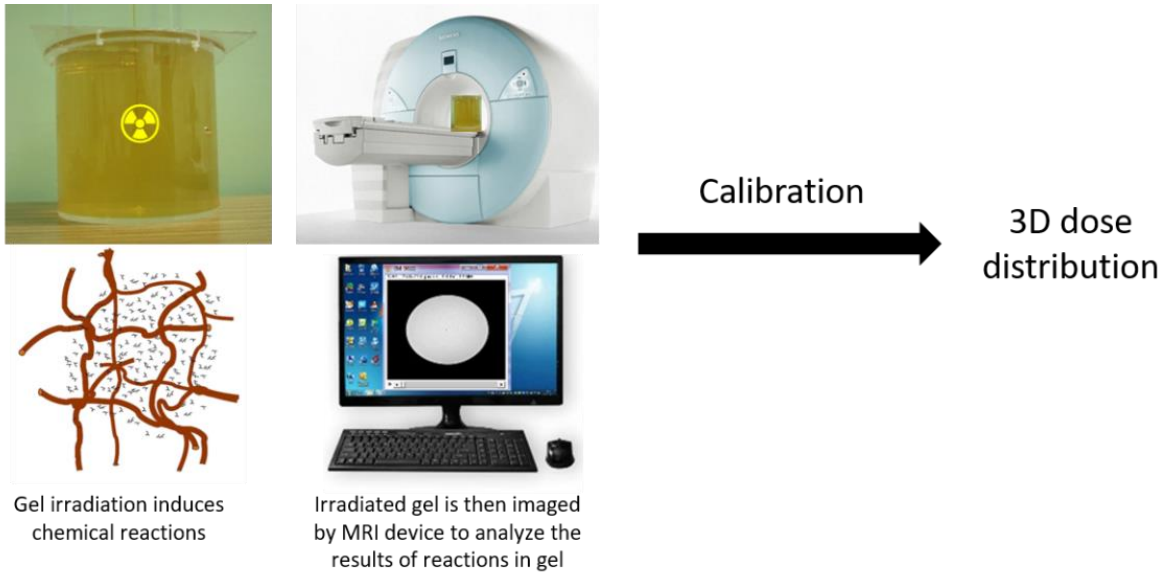

Figure 3.1. The process of 3D dose determination by the dosimetric gel used in this study.

So, in this chapter, the response of the used dosimetric gel is first calibrated in terms of absorbed dose to gel in the low-energy photon range (≤ 50 keV). This gel is then used to determine the absorbed dose distributions in gel according to two different axes around the IB-XRS associated with a 4 cm spherical applicator. Yet, since the absorbed dose to water is the conventional quantity in radiotherapy, MC calculations are finally implemented to convert the absorbed dose profiles in gel, defined by the dosimetric gel, into absorbed dose profiles in water.

3.1. Calibration of the dosimetric gel

The dosimetric gel is to be calibrated in the low-energy photons range (≤ 50 keV) in terms of absorbed dose to gel and energy dependence. The calibration process aims at defining the relation between the gel response, induced by the irradiation, and the actual absorbed dose in the gel. The dosimetric gel, when calibrated, can be used to measure the absorbed-dose-to-gel distributions around any source emitting photons in the considered energy range. To this end, a calibration methodology that relies on terms determined either by measurements or MC simulation was developed. Consequently, the first part of this section describes the adopted methodology, while the second part presents the experimental conditions designed for its

application. The third and fourth parts deal with the realization of the different steps of the developed methodology. Finally, with all the terms defined, the fifth part presents the calibration relation obtained, that links the MRI variation in gel response to the absorbed dose to gel.

3.1.1. Calibration methodology

The calibration aims at defining, for any voxel of a dosimetric gel phantom irradiated by photons of energy E, the relation between the resulting absorbed dose in gel, D_{gel}, and the induced relaxation rate variation, ΔR_2 ($\Delta R_2 = R_2 - R_{2,0}$).

However, the beams delivered by the conventional XRG available at LNHB are not mono-energetic but correspond to continuous energy spectra. Thus, to establish the required calibration, the absorbed dose to gel in a given voxel must be related to the variation in gel response, ΔR_2, in the considered voxel for the average fluence energy of the photon beam incident on that voxel, such that:

$$D_{gel} = f(\Delta R_2, \bar{E}) \qquad \text{with} \quad \bar{E} = \frac{\int E.\Phi(E).dE}{\int \Phi(E).dE}$$

Considering a given photon beam quality, the photon fluence energy varies with depth in the phantom gel. Thus, to study the impact of the photon beam fluence energy on such calibration relation, both the incident beam quality and the depth of the considered voxel within the gel phantom were varied. In other words, let z be the depth of a considered voxel of a given dosimetric gel phantom, and $\bar{E}_0$ the energy of the photon fluence incident on that gel phantom (i.e. $\bar{E}_0 = \bar{E}_{z=0}$), the mean fluence energy, $\bar{E}$, depends on those two parameters as follows:

$$\bar{E} = f(\bar{E}_0, z)$$

So, by considering different photon beam qualities to irradiate a dosimetric gel phantom and different depths, z, within that gel phantom, it is possible to obtain a database of correlated values of $D_{gel}(\bar{E}_0, z), \Delta R_2(\bar{E}_0, z)$ and $\bar{E}(\bar{E}_0, z)$. For a given photon beam quality, the dependence of the database parameters may be reduced to $D_{gel}(z)$, $\Delta R_2(z)$ and $\bar{E}(z)$, as illustrated on Figure 3.2.

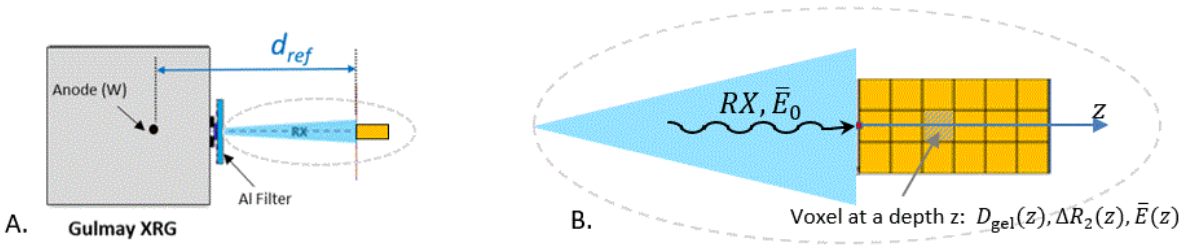

Figure 3.2. Irradiation of a dosimetric gel by a given XR beam of incident average fluence energy, $\bar{E}_0$, as shown on the left scheme (A). Zoom in of the irradiated dosimetric gel: the gel voxel at depth z is irradiated by photons of average fluence energy $\bar{E}(z)$, it receives the absorbed dose to gel $D_{gel}(z)$, and experiments during the MRI readout the variation of the relaxation rate $\Delta R_2(z)$.

In order to establish the calibration relation, such irradiation experiments were performed using XR reference beams characterized in terms of air kerma (see sections 1.2.1 and 1.3.1). Hence, it was convenient to determine the dose absorbed by the gel voxel at depth z, $D_{\mathrm{gel}}(z)$, as follows:

$$D_{\mathrm{gel}}(z) = \left(\frac{D_{\mathrm{gel}}(z)}{K_{\mathrm{air}}}\right)_{\mathrm{MC}} \cdot \dot{K}_{\mathrm{air,WK07}} \cdot t$$

where $\dot{K}_{\mathrm{air,WK07}}$ is the air kerma rate of the reference X-Ray beam measured in gray per second [Gy.s^{-1}] using the primary ionization chamber WK07 (described in section 1.3.1); $(K_{\mathrm{air}})_{\mathrm{MC}}$ is the corresponding air kerma value obtained by MC calculation in eV per primary particle per unit mass [eV.pp^{-1}.g^{-1}], under the same measurement conditions as those of $\dot{K}_{air,WK07}$. $\left(D_{\mathrm{gel}}(z)\right)_{\mathrm{MC}}$ is the dose absorbed by the gel voxel at a depth z calculated by MC simulation whose model reproduces the gel phantom irradiation, also expressed in unit of per unit mass [eV.pp^{-1}.g^{-1}]; t is the irradiation duration of the dosimetric gel phantom expressed in second [s]. The resulting absorbed dose to gel at a voxel depth z, $D_{\mathrm{gel}}(z)$, is consequently expressed in gray [Gy]. The determination of the absorbed dose to gel, at a voxel depth z, is illustrated on the top of Figure 3.3.

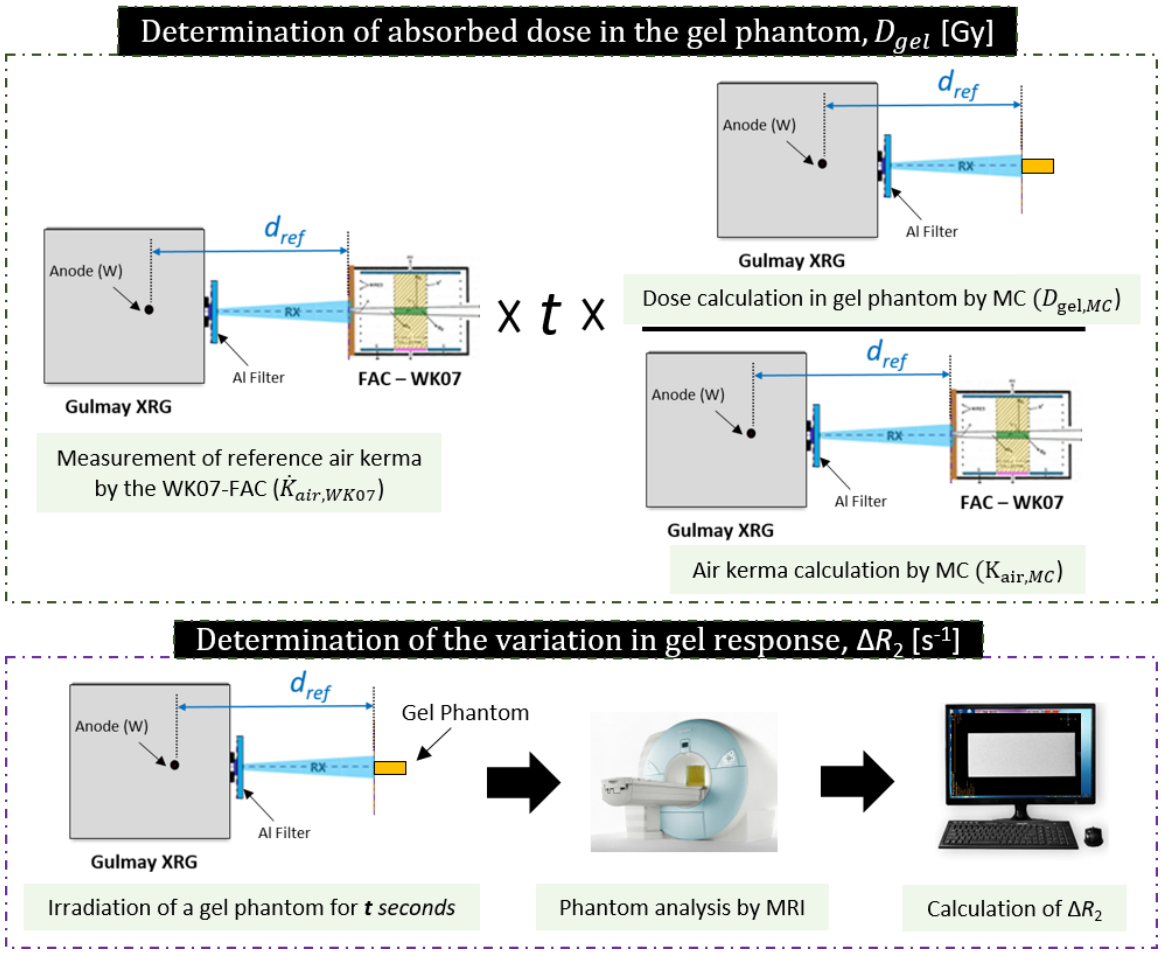

Figure 3.3. Schemes (not to scale) of the methodology developed to determine the relation between the absorbed dose to gel and the corresponding induced gel response: (top) process needed to determine the absorbed dose to gel in [Gy], and (bottom) process to measure, then calculate, the variation in gel response after irradiation.

The variation of the gel relaxation rate, $\Delta R_2(z)$, can be measured in [s^{-1}] as explained in chapter 1 (see section 1.3.3.3) and as described on the bottom of Figure 3.3. Finally, the average fluence energy, $\bar{E}(z)$, was also obtained by MC calculation under the same irradiation conditions as those of $\Delta R_2(z)$.

3.1.2. Experimental design

The experimental design to apply the calibration methodology, described in the previous section, is presented hereafter. This section comprises three parts: the two first are dedicated to the choice of beam qualities used for irradiation and to the primary measurement of the corresponding reference beams in terms of air kerma rate. The irradiation conditions of the gel are also defined in those two parts. The third one deals with the design of the gel phantoms.

3.1.2.1. Choice of beam qualities

Monoenergetic photon beams would have been very convenient for the calibration process, but they do not exist in the energy range of interest. Consequently, several photon beam qualities, generated by the Gulmay XRG, were considered for the dosimetric gel calibration. These photon beams were identified as the N20, N60 and CCRI50b previously characterized in Chapter 1 (see section 1.4.1.2). The beam qualities were generated by modifying the XRG high-voltage value and adding the corresponding filtration (as presented in Table 1.3).

The spectra of the three selected photon beams are shown and compared with the one the IB-XRS with a 4 cm applicator in Figure 3.4. The CCRI50b beam quality was selected since it resembles to the photon beam emitted by the IB-XRS with a 4-cm applicator, and it extends over the region of interest (≤ 50 keV). The N20 and N60 beam qualities were chosen since they cover the energetic boundaries of the region of interest (with almost respectively 16 keV and 48 keV fluence-averaged energies).

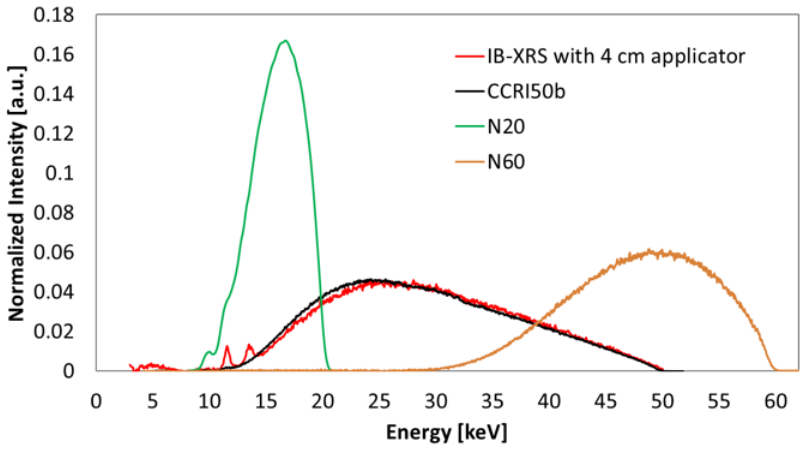

Figure 3.4. Energy spectra of the selected photon beam qualities compared to that of the beam emitted by the IB-XRS with a 4-cm applicator.

3.1.2.2. Air kerma rate of the chosen beams

Based on the developed methodology, the three aforementioned beam qualities were considered to assess the calibration relation. The irradiation times were calculated relying on

the measured reference air kerma rate, $\dot{K}_{\mathrm{air}}$, in order to attain an absorbed dose at the gel surface comprised between 5 and 20 Gy. To this end, the XRG currents were also set at the highest possible values to optimize the $\dot{K}_{\mathrm{air}}$ values. The WK07 FAC primary standard was used to measure the reference air kerma rate for each considered beam quality. The $\dot{K}_{\mathrm{air}}$ values measured at the conventional 50 cm distance were found to be low, especially for the N60 beam. Actually, a compromise has to be found between a delivered dose high enough for MRI measurements and a sufficiently low irradiation time to avoid ion diffusion in gel. Therefore, the reference irradiation distance considered was set at 42 cm, since it is the shortest attainable one between the XRG and the WK07 FAC (from a mechanical point of view). Finally, a collimator in tungsten of 1 cm diameter was used, providing a beam size of 8.5 cm diameter at the reference distance, large enough to irradiate the whole gel phantoms in a homogeneous way at the reference distance. The measured reference air kerma values at 42 cm, $\dot{K}_{\mathrm{air,42\ cm}}$, are presented in Table 3.1. As can be seen on this table, the air kerma rate of the N60 beam is so low that an irradiation time of almost 10 hours would have been required to attain a dose of 10 Gy at the gel phantom surface. So, because of ionic diffusion, the N60 beam was not used to calibrate the dosimetric gel.

Table 3.1: Air kerma rates, at the 42 cm reference distance, measured for the considered photon beam qualities.

Beam Quality	**CCRI50b**	**N20**	**N60**
Anode current [mA]	15	20	30
$\dot{K}_{\mathrm{air,WK07}}$ **[Gy. s^{-1}]**	**7.942E-03**	**1.124E-03**	**2.883E-04**
$u(\dot{K}_{\mathrm{air,WK07}})$ **(%)**	0.29	0.34	0.44

Gel phantoms were next irradiated under the selected beam qualities and irradiation conditions. The design of these phantoms is presented in the next section.

3.1.2.3. Gel phantoms design

Cylindrical-shaped phantoms in Plexiglas were designed for the dosimetric gel calibration. Their dimensions are shown on Figure 3.5. The irradiation of phantoms was done along their axial plane to exploit symmetry with photon beams of circular form. The 100 mm length provides a gel thickness sufficient to absorb almost all photons. Finally, the phantom front wall thickness, indicated by ***e*** in Figure 3.5 was intended to be as small as possible to decrease the attenuation in Plexiglas, and hence, attain higher energy deposition in gel especially for low-energy photons.

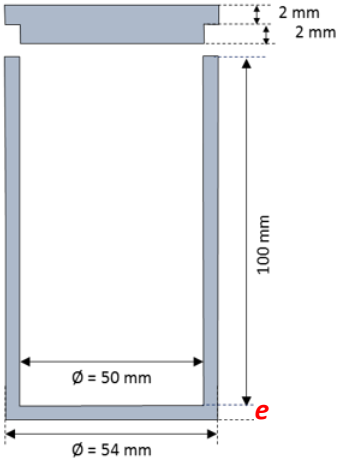

Figure 3.5. 2D scheme (not to scale), with dimensions, of the cylindrical phantom as designed for dosimetric gel calibration.

Following the irradiation of the gel phantoms under the conditions previously described, the next section covers the determination of the gel relaxation rate.

3.1.3. Determination of $R_2(z)$

The determination of the gel relaxation rate, $R_2(z)$, is presented in this section. Following the procedure presented previously in Figure 3.3, this section is divided into three parts: the first deals with the preparation and irradiation processes of gel phantoms, the second covers the readout of the irradiated phantoms by MRI, and finally, the treatment of the resulting MRI images to deduce $R_2(z)$ within each phantom is covered in the last part.

3.1.3.1. Preparation and irradiation of gel phantoms

The gel used in this work was prepared at LNHB a few days before irradiation. The components were mixed and homogenized at almost 40 °C to keep the solution in the liquid form. The gel was then poured into phantoms. Five gel phantoms, with the dimensions previously described, were prepared. To avoid any variation in gel response associated to the proportions of gel components or preparation conditions, the same gel was poured into all gel phantoms. The gel phantoms were kept into a fridge to jellify for at least four hours at 4 °C. Finally, around ten hours before irradiation, the phantoms were removed from the fridge and placed in the irradiation room to attain the room temperature.

All phantoms were irradiated with their front surface at a 42 cm distance from the XRG anode, as illustrated on Figure 3.6. Phantom front walls were facing the photon beams with their centers located on the beams axis. Moreover, polystyrene blocks were used to hold the phantoms during irradiation, to almost eliminate photon scattering into the phantom from the holder.

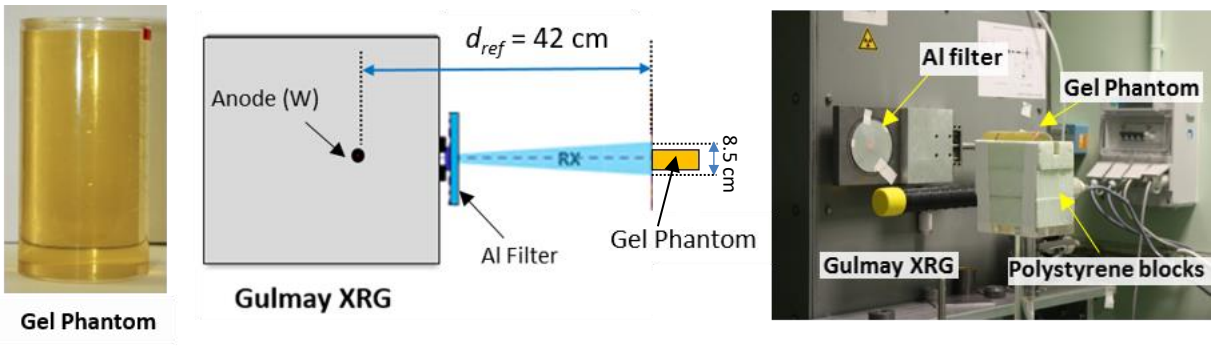

Figure 3.6. Irradiation configuration of gel phantoms: (left) picture of the gel phantom, (middle) a scheme (not to scale) of the irradiation configurations and (right) real picture of a phantom irradiation.

The five phantoms were irradiated under the arrangement detailed in Table 3.2. Four gel phantoms were irradiated with the CCRI50b beam. The corresponding irradiation times were chosen to study the gel response with the delivered dose increasing in the following way: D_{gel}, 2xD_{gel}, 3xD_{gel} and 4xD_{gel}. The fifth gel phantom was irradiated with the N20 beam.

Table 3.2. Beam qualities and times considered to irradiate each gel phantom.

Beam Quality	Phantom reference number	Phantom front wall of thickness, *e* [mm]	Irradiation time [min]	Irradiation day
CCRI50b	1	0.896	12.82	Day 2
	2	0.893	25.65	
	3	0.890	38.47	
	4	0.883	51.30	
N20	5	0.857	173.52	Day 4

After the irradiation, each gel phantom was analyzed by MRI to measure the induced variations in its response. The MRI reading process is presented in the next part.

3.1.3.2. Phantoms reading by MRI

Since no MRI device is available at LNHB, the Intra Achieva Philips imager 1.5 T MRI platform (CNRS, Université Paris-Sud, CEA) located at the Service Hospitalier Frédéric-Joliot (SHFJ) was used with the head coil SENSE (Figure 3.7).

Figure 3.7. (Left) the imaging room of the SHFJ with the MRI Philips imager inside and (right) the head coil.

The gel phantoms were read by MRI within one to two hours after irradiation to avoid diffusion artifacts. In order to place the phantoms in the center of the coil, and to ensure a reproducible position from a phantom to another, a positioning tray (shown on the left image of Figure 3.8) was specifically designed in Plexiglas with polystyrene blocks; since these two materials are non-paramagnetic.

Figure 3.8. Gel phantom analysis by MRI with the head coil: (left) irradiated gel phantom on the positioning Plexiglas tray and the polystyrene blocks; (right) placement of the phantom and positioning tray inside the head coil where the system of coordinates indicates the final position for reading.

For each phantom, the analyzed region (slice) was taken along the axial plane of the gel phantom as shown in Figure 3.9. The sequence parameters used are also given in the same figure. The slice considered was 4 mm thick and covered the whole phantom along the (APHF) plane (corresponding to the region along the irradiation beam axis).

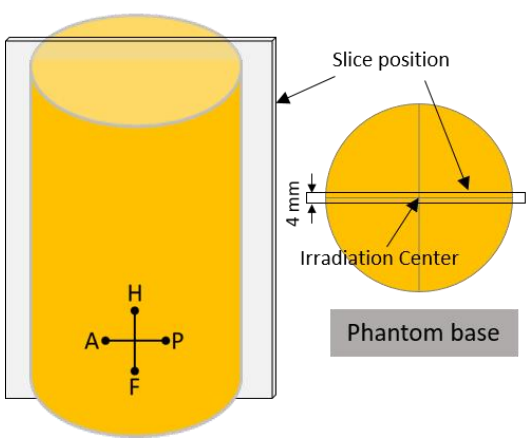

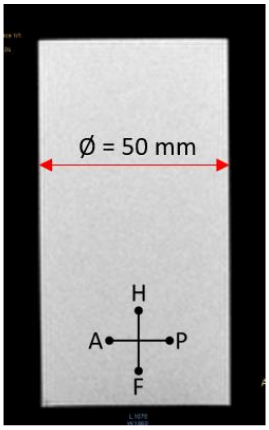

MRI sequence parameters	
NoE	30
TR [ms]	2000
TE [ms]	11
Matrix [pixels]	256 × 256
Slice thickness [mm]	4
Voxel size [mm³]	0.6 × 0.6 × 4
Total acquisition time	9 min 2 sec

Figure 3.9. (Left and middle) schemes showing the position of the analyzed slice and (right) corresponding MRI image parameters of the first echo shown by ImageJ. The system of coordinates corresponds to the reading position presented in Figure 3.8.

As no spatial uncertainty was provided with the reconstruction matrix, the voxel dimension was calculated. A simple calculation was performed by dividing the phantom diameter, in mm, by the corresponding number of voxels. To increase the statistical information, this calculation was repeated over the MRI images of all phantoms by considering different positions on each image. The resulting calculated pixel size was (0.587×0.587) mm^2.

In addition, several phantoms were also analyzed before being irradiated (for blank values). The same MRI analysis configurations were used as for the irradiated phantoms. The results

obtained for these phantoms, as well as for the irradiated ones, are presented and discussed in the following part.

3.1.3.3. Calculations of $R_2(z)$

The analysis of DICOM images to calculate the gel response, R_2, following or not an irradiation, is performed using an image analysis software called ImageJ [142]. Since the dose varies with depth, there are as many R_2 values as voxel positions along z. Therefore, to ease and accelerate the calculation and treatment of the values R_2 corresponding to each considered position z, as described in section 1.3.3.3.3, two home-made programs were developed in Excel® Visual Basic (VB). Those two VB programs are detailed in APPENDIX-D. The data analysis and the determination of the gel response R_2 as a function of z are presented in the following parts.

Uniformly irradiated rectangular ROIs, of fifteen voxels width (8.805 mm) and one voxel depth, were selected over the R_2 matrix along the reference beam axis as shown in Figure 3.10. The calculated $\overline{R_{2_i}}$ values in the selected ROI correspond to the gel response after irradiation at the corresponding ROI position.

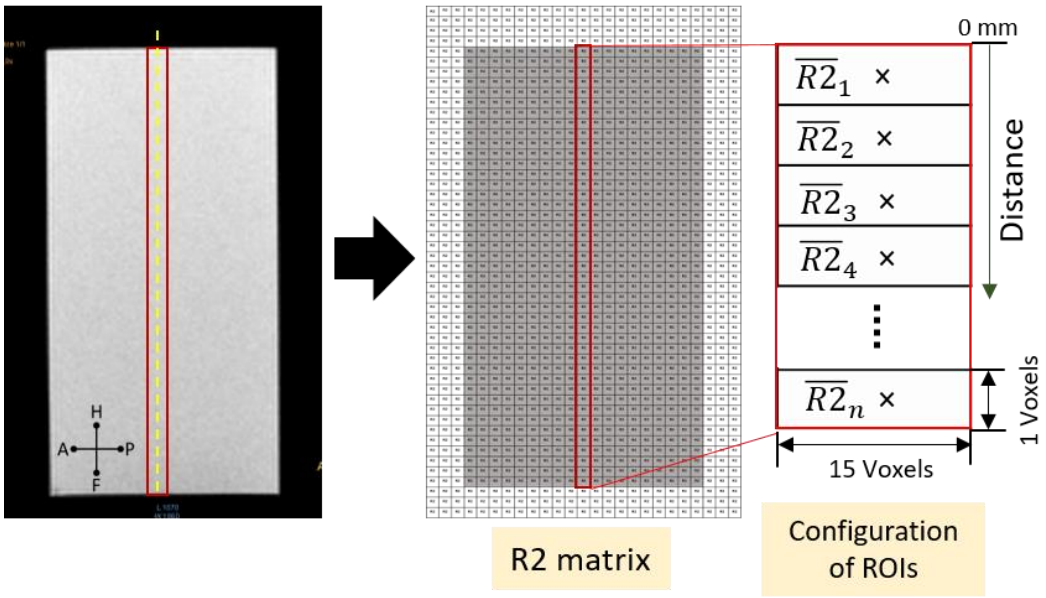

Figure 3.10. MRI image analysis to define the gel response profile, in the chosen region marked by a red rectangle, along the irradiation beam axis (marked by a yellow dashed line).

Before analyzing the irradiated phantoms, the inhomogeneity of R_2 response in the studied volume was evaluated using the homogeneous non-irradiated gel phantoms. The flatness of the resulted R_2 distributions, observed in these homogeneous gels as shown on Figure 3.11, leads to the conclusion that there is no inhomogeneity to be corrected for over the selected ROI along the HF axis.

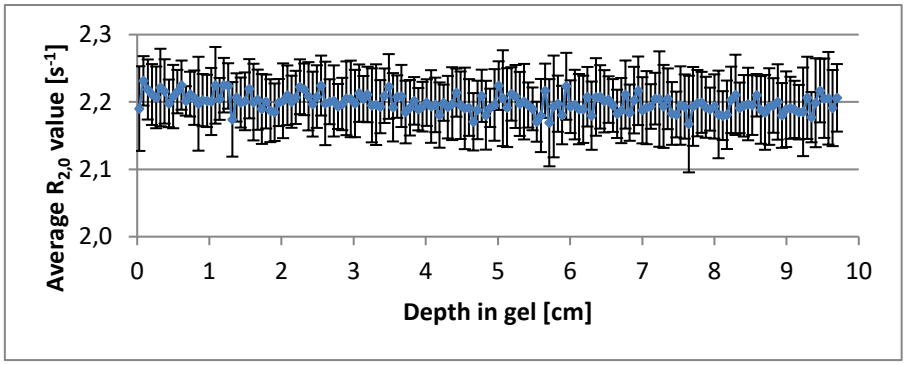

Figure 3.11. Average $R_{2,0}$ values distribution calculated over the selected ROI along HF axis, as demonstrated in Figure 3.10, for a non-irradiated phantom.

Figure 3.12 presents the $\overline{R_2}$ profiles obtained in the axial direction of the irradiated phantoms. Some of those profiles show discrepancies in the first one or two values at the beginning and/or the end of the curve. These discrepancies are related to a measurement artifact of the MRI technique, which occurs at the interface between two materials (gel and Plexiglas in our case). Therefore, the affected points, in each curve, will be omitted in the further analysis.

The distribution curves give an idea over the $R_2/R_{2,0}$ ratio which is quite significantly low. Thus, the determination of the $R_{2,0}$ value plays a major role in evaluating the variation in gel response, ΔR_2. Besides, the gel response of the non-irradiated gel was found to increase with time after jellifying, even without any irradiation, as seen in Figure 3.13, certainly due to natural oxidation of ferrous ions over time.

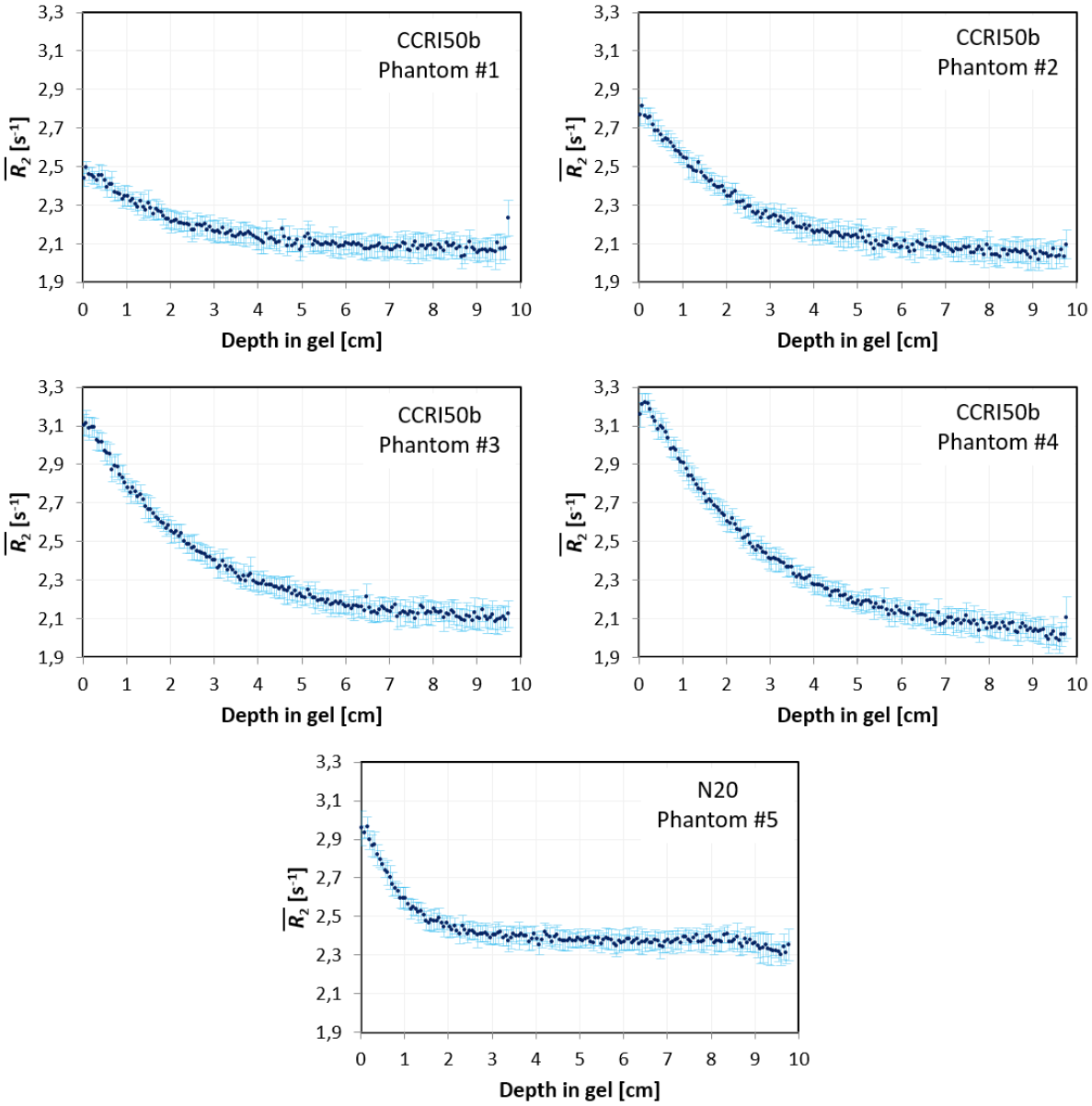

Figure 3.12. Average gel response distributions, $\overline{R_2}$, calculated over the selected ROI along the beams axis, as demonstrated in Figure 3.10, for the five irradiated gel phantoms stated in Table 3.2. The uncertainty, $u(\overline{R_2})$, attached to each point corresponds to the experimental standard deviation over each 15 voxels ROI.

In order to rely on a more robust method, another approach was finally adopted. The $R_{2,0}$ was obtained by plotting the curve $\overline{R_2} = a.D_{gel}^2 + b.D_{gel} + R_{2,0}$, $R_{2,0}$ being the signal for $D_{gel} = 0$. This method, alongside with resulting ΔR_2 values, will be discussed later (in section 3.1.5.) with the establishment of the calibration curve.

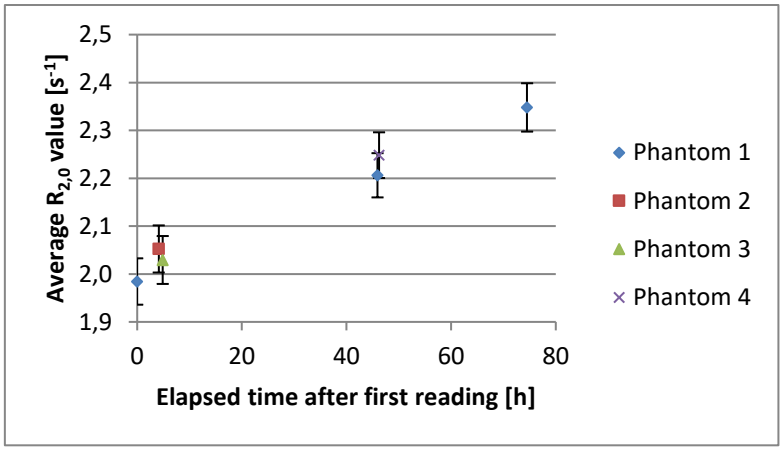

Figure 3.13. Evolution of the non-irradiated gel response over time in the four different gel phantoms before irradiation.

Therefore, the corresponding gel doses, D_{gel}, calculated for the establishment of the calibration, are also used for the determination of the $R_{2,0}$ values.

3.1.4. Determination of the absorbed dose profiles $D_{\mathrm{gel}}(z)$ in gel phantoms

The calculation of the absorbed dose profiles in the gel phantoms, irradiated in the previous section, is presented here. The calculation procedure, formerly presented in Figure 3.3, was applied to calculate the absorbed dose in each selected ROI. Thus, with the reference air kerma rate values and the corresponding irradiation times (given earlier in Table 3.1 and Table 3.2, respectively), only the ratio of absorbed dose in each ROI to air kerma under reference conditions is left to be calculated by the MC method.

Consequently, this section is divided into three parts. The first and second parts present the MC calculations (in unit of [$eV.g^{-1}.pp^{-1}$]) respectively of the absorbed doses to gel and average photon fluence energies in each considered ROI and of the air kerma values. Finally, the absorbed doses to gel (in [Gy]) in each ROI, for all the gel phantoms irradiated under the two beam qualities, are determined in the last part.

3.1.4.1. MC calculation of $D_{\mathrm{gel,MC}}(z)$ and $\bar{E}(z)$

MC calculations of the absorbed doses to gel and average fluence energies as a function of depth for the two photon beam qualities are described in this part. All calculations were performed using the PENELOPE MC code, presented in chapter 1. A consistent model was developed in PENELOPE for the gel phantoms and corresponding beam qualities.

An exact geometrical model, with the corresponding dimensions and materials, was developed for each gel phantom as shown in Figure 3.14. The materials data used in the model were based on the PENELOPE-pendbase materials database. Air and Plexiglas were defined by their reference pendbase-number, i.e. 104 and 224, respectively. The gel material was defined relying on its elemental composition and corresponding mass density (1.08 ± 0.01 g/cm^3). The gel composition being patented, it is not given here.

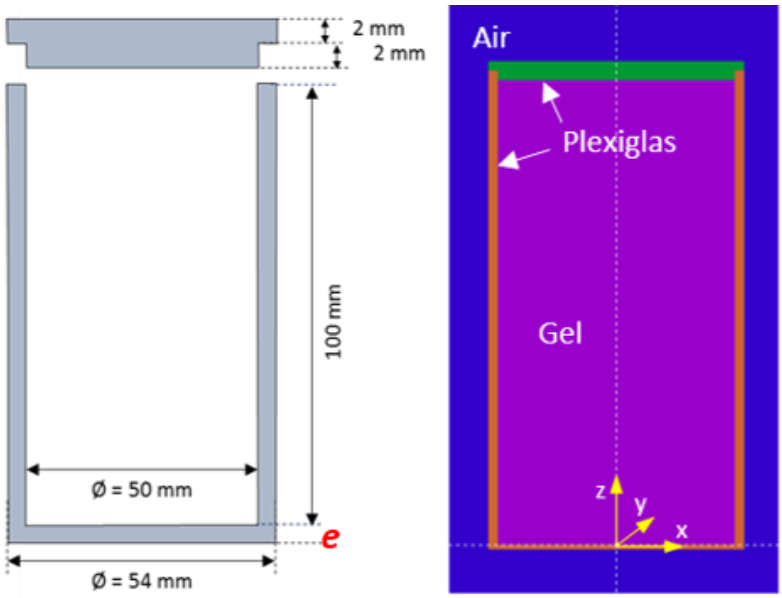

Figure 3.14. The left drawing gives the dimensions of the gel containers. The right picture as presented by PENELOPE GVIEW2D shows the geometric and material modeling of the gel phantoms.

The simulation parameters assigned for each material of the developed MC model are summarized in Table 3.3. The DSMAX parameter value is of the order of one tenth of the corresponding body thickness, as recommended in the PENELOPE manual.

A collimated point-source was used to model the beam qualities generated by the conventional XRG. This approximation is still valid under the reference irradiation configurations (42.0 cm shortest SDD, and collimator of 2.8 cm in diameter placed at 13.5 cm from the source). The photon energy spectra of the measured beams, presented previously in Figure 3.4, were used in our models. At last, the suitable aperture angle was selected to get a beam size of 8.5 cm at the reference irradiation distance, in conformity with the actual irradiation conditions.

Table 3.3. Values of simulation parameters assigned to all materials in the developed MC model.

	$E_{abs}(1)$ [eV]	$E_{abs}(2)$ [eV]	$E_{abs}(3)$ [eV]	C_1	C_2	W_{CC} [eV]	W_{CR} [eV]
All materials	1.0E+03	1.0E+03	1.0E+03	0.05	0.05	1.0E+03	1.0E+03

In order to trace the evolution of each photon beam spectrum, a series of 8 detectors were placed along the beam axis, using the photon impact detector tool in PENELOPE. The modeled configurations of each phantom irradiations and detectors positions are presented in Figure 3.15, where all detectors are pointed with an arrow. Following the recommendations of the PENELOPE developers to reduce the calculation time, the introduction of the 8 detectors led to the implementation of several other integrated modules or bodies, as shown on the body representation of one of the gel phantoms in Figure 3.15. The first detector was in air just before the phantom, the second one was in the Plexiglas front wall, and the six other detectors were placed at different depths in gel. All detectors had a cylindrical shape, 1 mm thick with a diameter of 3 mm (except for the Plexiglas detector thickness which was adapted regarding the phantom front wall thickness *e*).

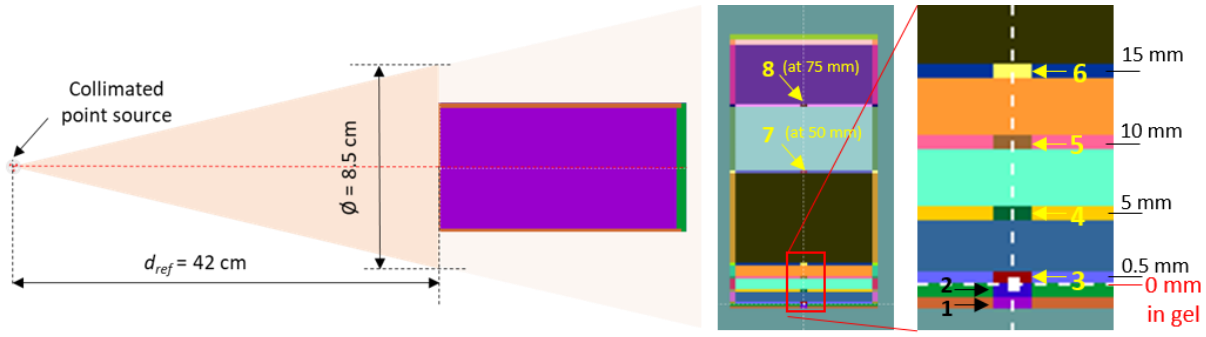

Figure 3.15. (Left) scheme (not to scale) of the simulated configurations for gel irradiations, and (right) locations of the detectors used to trace the evolution of the photon spectra before and within the gel phantoms.

The evolution of the two photon beam energy spectra recorded by the eight detectors is shown in Figure 3.16. The N20 beam is almost totally attenuated at a 50 mm distance in the gel. This attenuation is related to the higher total attenuation coefficient for lower energy photons. The corresponding fluence-averaged energy varies by 2.5 keV in this region, over 50 mm, with the main variation taking place in at least the first 15 mm. The CCRI50b beam spectrum varies slightly, with its low-energy photons almost totally attenuated in the energy region below 20 keV. Finally, the fluence-averaged energies vary respectively of 15 % and 18 % for the N20 and CCRI50b beams, respectively.

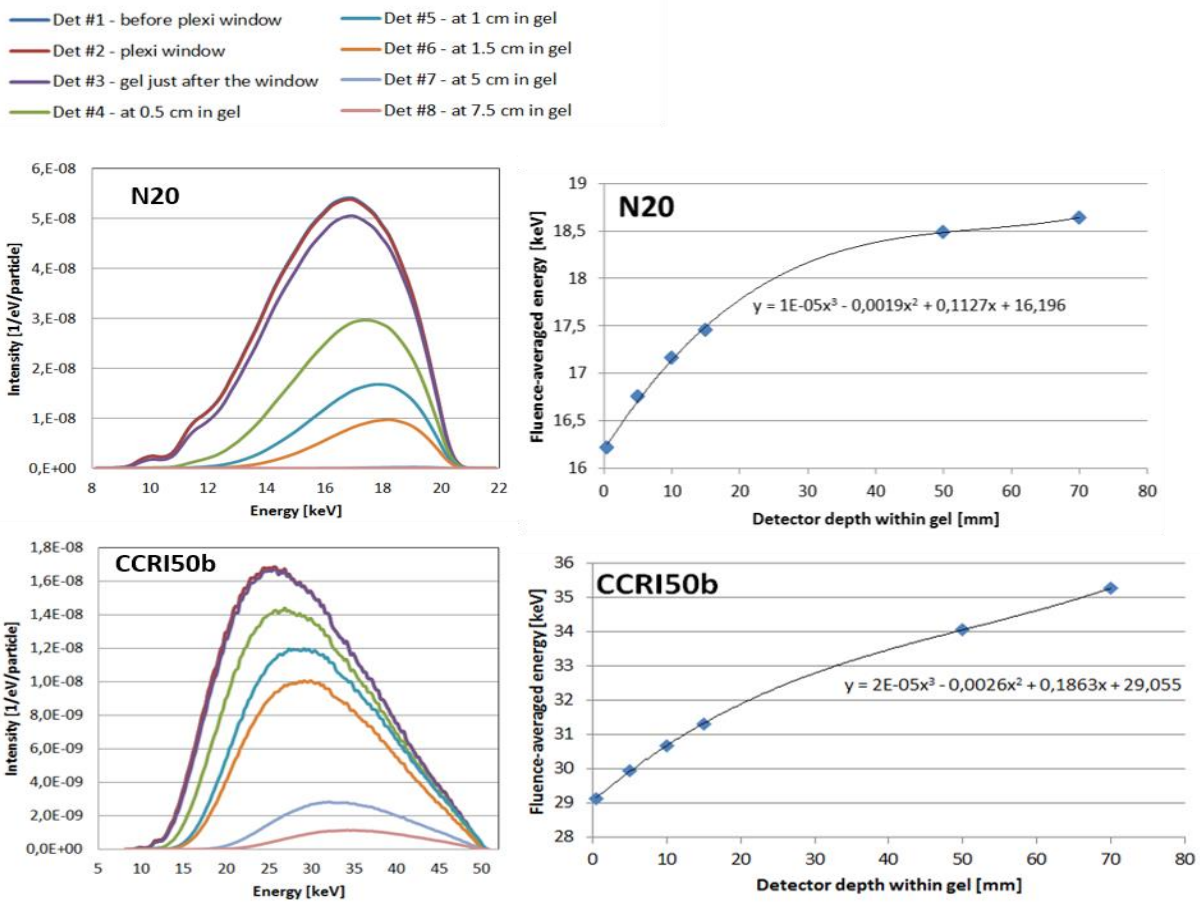

Figure 3.16. Evolution of the two beam qualities, at the eight detectors positions, and their corresponding fluence-averaged photon energy.

The dose distributions (in [eV.g^{-1}.pp^{-1}]) in the gel phantoms were calculated along the beam axis with a higher spatial sampling than for the energy spectra and fluence-averaged energy determination, as seen in Figure 3.17. The calculation volumes had the exact sizes and positions of the ROIs previously selected to assess the gel response along the beam axis, as described in Figure 3.10 (i.e. 0.587 x 8.805 x 4.000 mm^3). To model it, the "GRIDX/Y/Z" option in PENELOPE and the related bin numbers were used.

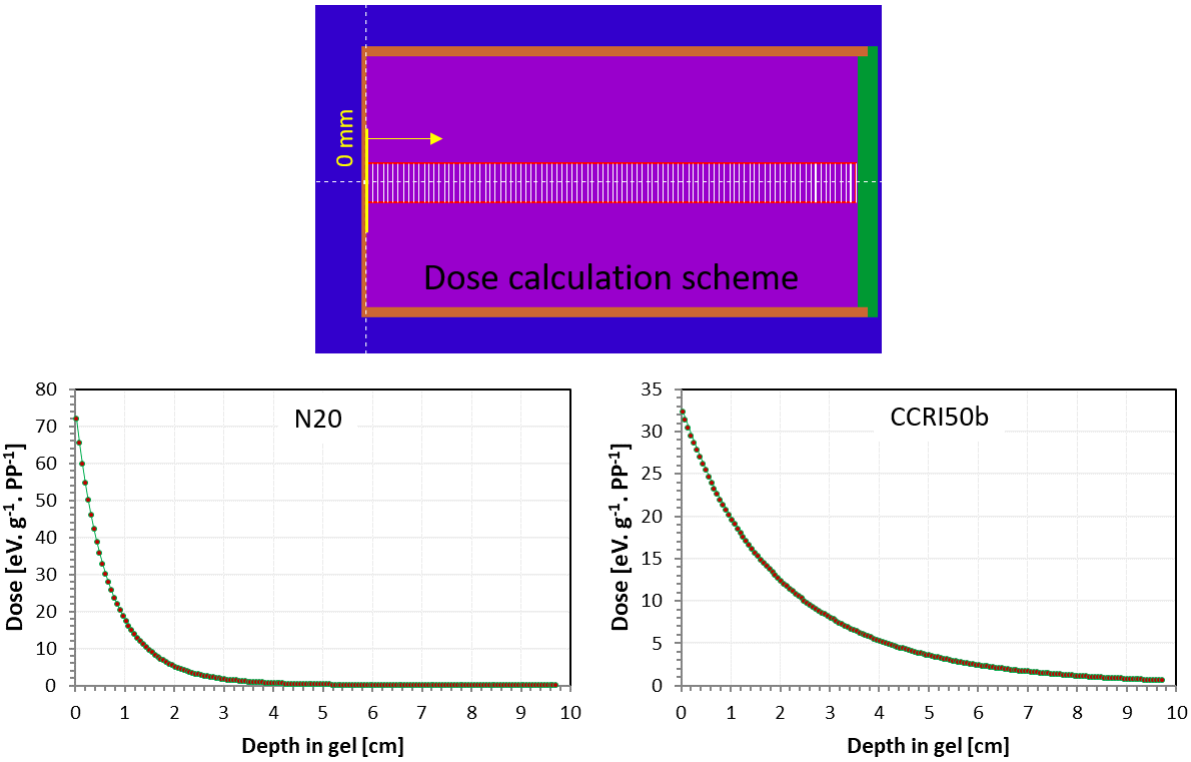

Figure 3.17. Calculated depth dose profiles in gel phantoms under the CCRI50b and N20 beams.

3.1.4.2. MC calculation of $K_{air,MC}$

Air kerma values were calculated relying on the model of the WK07 FAC previously described in section 2.4.1.2. Consequently, the values of the simulation parameters assigned to each material used in the WK07 MC model are identical to the ones presented in Table 3.3. The corresponding air kerma, for each beam quality, was calculated by dividing the transferred energy, in the collection volume of the WK07, by the corresponding air mass. To this end, the same source configurations, as described in the previous part (section 3.1.4.1), were applied. The reference point of the WK07 chamber was placed on the beams axis at 42 cm distance from the source which was collimated to provide an 8.5 cm beam size at this point. The calculated air kerma values of the two considered beams are presented in Table 3.4**Erreur ! Source du renvoi introuvable.**.

Table 3.4. Calculated air kerma, by MC method, for the two beams at a 42 cm reference distance. The relative uncertainty values, $u(K_{air,MC})$, correspond to the statistical uncertainties of the deposited energy values.

Beam Quality	**CCRI50b**	**N20**
transferred energy in the WK07 collection volume E_{dep} [eV.pp^{-1}]	0.01406	0.03717
Air mass density [g. cm^{-3}]	1.20479E-03	
WK07 collection volume V_{coll} [cm^3]	0.4028	
$K_{air,MC}$ [eV.g^{-1}.pp^{-1}]	**28.9805**	**76.5898**
$u(K_{air,MC})$ (%)(k=1)	0.27	0.17

These values are used in the following part, alongside with the dose distributions, to calculate the MC ratio needed to determine the absorbed dose value in each ROI.

3.1.4.3. Determination of $D_{gel}(z)$

The profiles of absorbed dose to gel in the considered ROIs, in all irradiated phantoms are determined in this part. The methodology previously described on the top of Figure 3.3 was used for each ROI to calculate the corresponding absorbed dose value.

For each ROI, the ratio ($D_{gel,MC}/K_{air,MC}$) was calculated according to the values given in the former two parts of this section. Then, this ratio was multiplied by the relevant measured reference air kerma value, $\dot{K}_{air}$ (defined in **Erreur ! Source du renvoi introuvable.**) and irradiation time (defined in Table 3.2) to deduce the dose absorbed in the ROI under study. This calculation was performed for all considered ROIs in the five irradiated phantoms.

The resulting absorbed dose profiles are given in Figure 3.18. The absorbed doses in the first ROI volume of the phantoms irradiated by the CCRI50b beam were of 6.80 Gy, 13.61 Gy, 20.40 Gy and 27.21 Gy for gel phantoms numbered from 1 to 4, respectively. The CCR50b has an exponential dose profile which expands over the phantoms. The beam is almost totally attenuated at the utmost depth in the phantom numbered 1 with the dose value approaching zero.

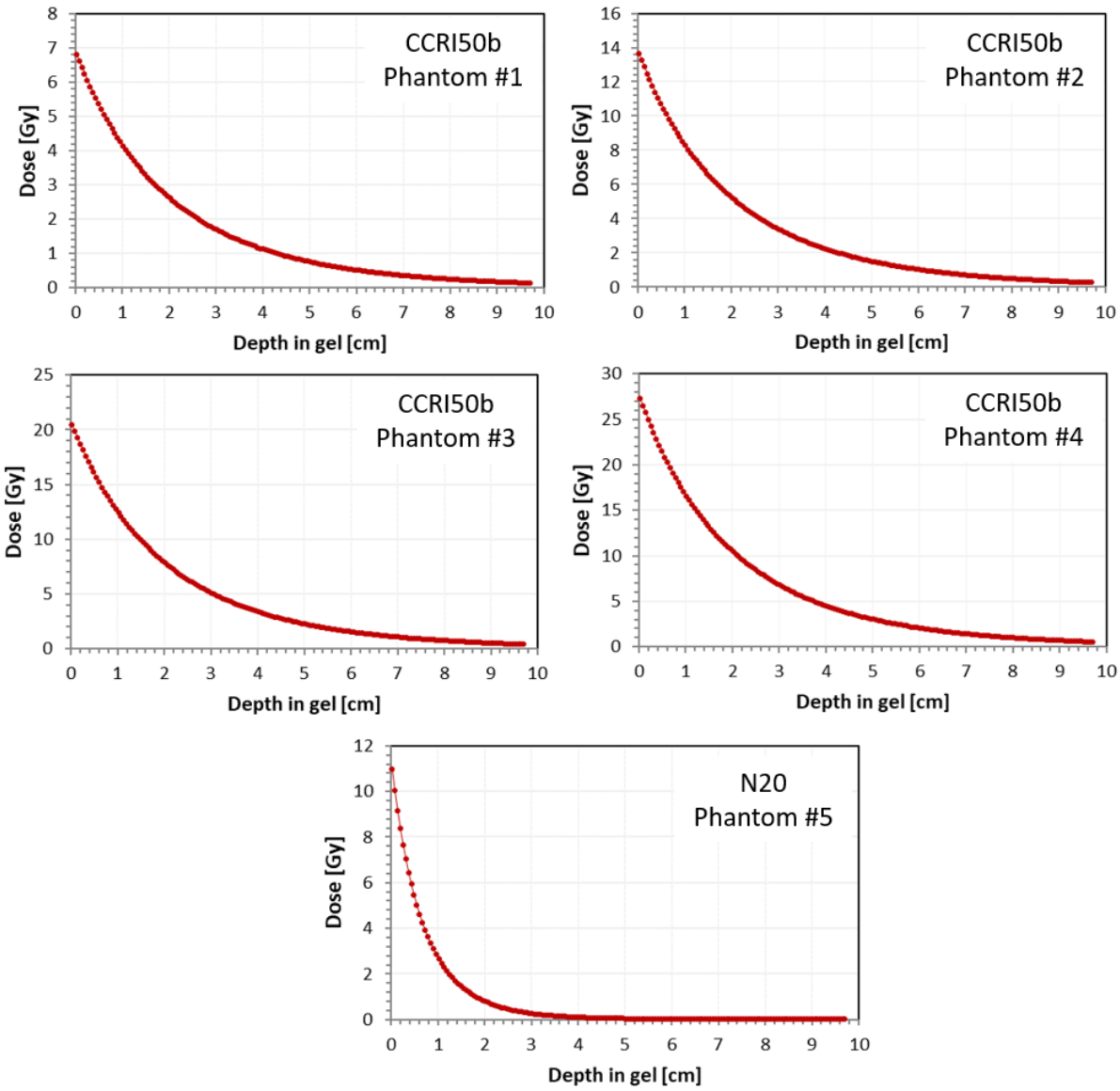

Figure 3.18. Absorbed dose distributions in gel phantoms irradiated with the CCRI50b and N20 beams. The irradiation times for each numbered phantom can be found in Table 4.2.

The delivered absorbed dose, in the first ROI, was of 10.98 Gy for the phantom irradiated by the N20 beam. The corresponding dose profile has a steep gradient and approaches an almost zero dose at 4 cm depth. This distribution behavior is related to the high attenuation coefficients of low-energy photons as discussed earlier. At depths higher than 4 cm, the absorbed dose may be under the gel response threshold. Hence, the data obtained in the N20 profile correspond only to one third of the one deduced from the CCRI50b analysis.

In the next section, the absorbed doses, $D_{gel}(z)$, are used both to calculate the corresponding $R_{2,0}$ values of the five gel phantoms and the $\Delta R_2(z)$ profiles and, *in fine*, to establish the calibration curve of the dosimetric gel.

3.1.5. Establishment of the calibration curve

As explained in section 3.1.1. when describing the calibration methodology, the aim is to establish the calibration curve that relates the variation in gel response, ΔR_2, in a given voxel, at a depth z and with a corresponding average fluence energy of the photon beam incident on it, to the absorbed dose to gel in the same voxel, such that:

$$D_{gel}(z)=f(\Delta R_2(z), \bar{E}(z))$$

Since the $R_{2,0}$ values are still to be obtained in order to calculate the variations in gel response $\Delta\overline{R_2}$, this section starts by calculating the $R_{2,0}$ values for each irradiated gel phantom. Then, these $R_{2,0}$ values are used in the determination of the $\Delta\overline{R_2}(z)$ in each voxel. At last, the resulting $D_{gel}(z)$ values are plotted against the $\Delta\overline{R_2}(z)$ and $\bar{E}(z)$ values.

3.1.5.1. Calculation of $R_{2,0}$ values

The $R_{2,0}$ values were calculated based on fitting curves. In order to define the blank value $R_{2,0}$, the previously obtained $\overline{R_2}$ values (data in Figure 3.12) were plotted against the corresponding absorbed doses determined for each irradiated phantom (data in Figure 3.18). Then, a regression curve was defined over all the values of each phantom. The interception of the regression curve, at the zero-dose point, is hence taken as the $R_{2,0}$ value of the gel phantom under study.

The fitting curves and defined $R_{2,0}$ values for all phantoms are shown in Figure 3.19. Second-order polynomial regression functions ($\overline{R_2} = a.D_{gel}^2 + b.D_{gel} + R_{2,0}$) were found to fit adequately the data of each phantom. $R_{2,0}$ values were found to be different from those obtained for the non-irradiated phantoms, especially for the phantoms irradiated on days 4 and 5. Indeed, as explained in section 3.1.3.2, readings of the gel were undertaken hours after irradiation, and, thus, some oxidation may have changed their value.

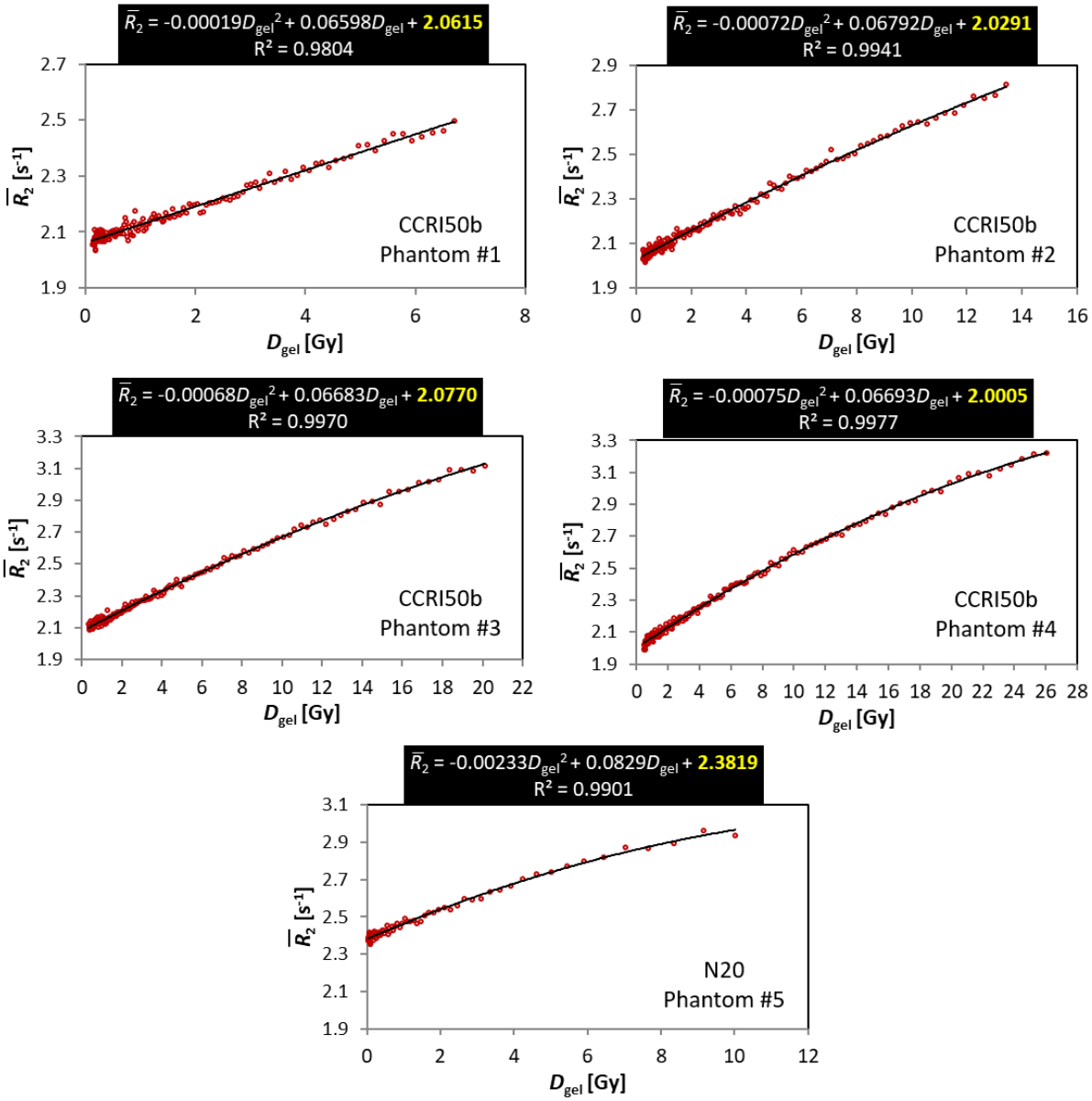

Figure 3.19. Determination of the $R_{2,0}$ values for all phantoms. The yellow-colored value above each curve corresponds to the interception point with the $\overline{R_2}$ axis (zero-dose) taken as the $R_{2,0}$ value.

3.1.5.2. Determination of $\Delta\overline{R_2}(z)$ values and gel calibration

For each selected ROI at depth z in a gel phantom irradiated by a given photon beam quality, $\Delta\overline{R_2}(z)$ was calculated, as stated earlier:

$$\Delta\overline{R_2}(z) = \overline{R_2}(z) - R_{2,0}$$

Since the $\Delta\overline{R_2}$(z) and D_{gel}(z) values had been determined for each z value, it was then possible to plot their relation, considering both the N20 and CCRI50b beam qualities. Plots presented on Figure 3.20 gather the data resulting from both irradiation beams to characterize such relation.

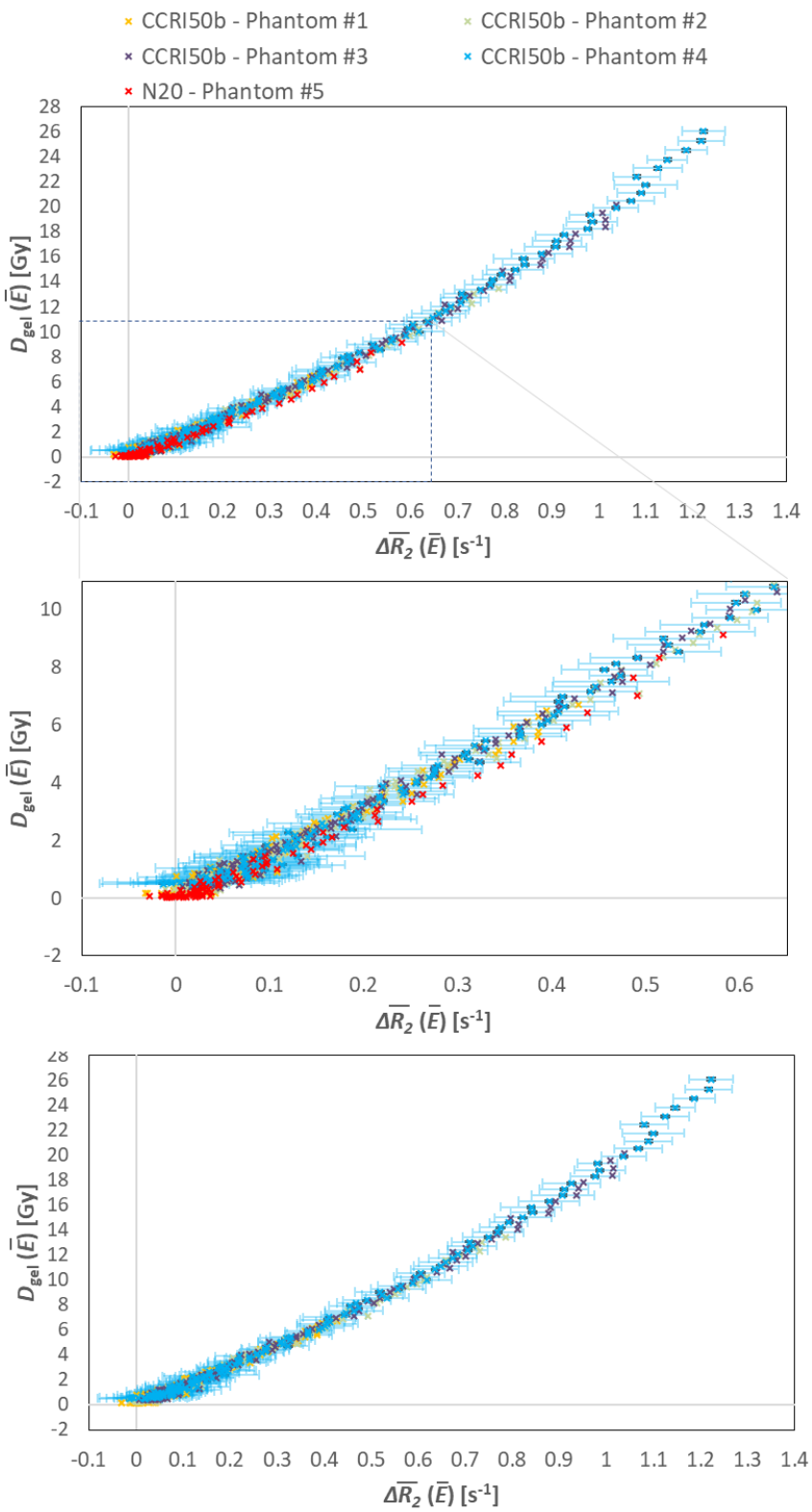

Figure 3.20. Variations of the absorbed dose in gel (D_{gel}) as a function of the gel response ($\Delta\overline{R_2}$), considering at the top (full view) and the middle (zoom in) both the N20 and CCRI50b beams gel phantoms, and at the bottom only the CCRI50b beam.

From the top plot shown on Figure 3.20, it appears that the data obtained from the five irradiation experiments are superposed, with regards to their uncertainties. The superposition

reflects that the variation in gel response exhibits, taking into account the uncertainties, the same dose-response relation for all gel phantoms irradiated whatever the beam.

However, as shown in section 3.1.4.1, the range of the average fluence energy differs between the N20 and CCRI50b beams. As a reminder, this parameter varies from 16 keV to nearly 19 keV for N20 and from 29 keV to almost 35 keV for the CCRI50b. The zoom in on the low $\Delta\overline{R_2}$ range (from 0 up to 0.6 s^{-1}), shown on the middle plot of Figure 3.20, may show that the N20 beam data are slightly lower than the CCRI50b beam ones, this slight divergence may refer to an energy dependence.

Nevertheless, the data obtained with the only CCRI50b beam through the four irradiation experiments with different irradiation times exhibit fluctuations of the same order than the slight difference found between the N20 and CCRI50b data. As a consequence, such inference on energy dependence would require a more rigorous study involving more photon beams with narrower energy distributions. Actually, the average fluence energy, $\bar{E}$, may not be the best suited parameter to perform such energy dependence study. It would worthy hence to conduct experiments, if possible, using monochromatic beams (with energy ranging from 10 to 50 keV).

At the stage of the present study, where it is difficult to infer on a possible energy dependence and, if exist, to account for it, it seemed cautious to restrict the data used to define the relation between D_{gel} and $\Delta\overline{R_2}$ to the CCRI50b ones. This choice is justified due to the similarity of the CCRI50b energy spectrum to the beam on which the calibration curve is to be applied (that is the IB-XRS associated with the 4 cm spherical applicator). As a first approach, without other information provided from a stronger energy dependence study, a flat relation between the variation of relaxation rate and average energy was considered here, and the calibration relation was established, as shown on the bottom plot on Figure 3.20, considering only the data obtained using the CCRI50b.

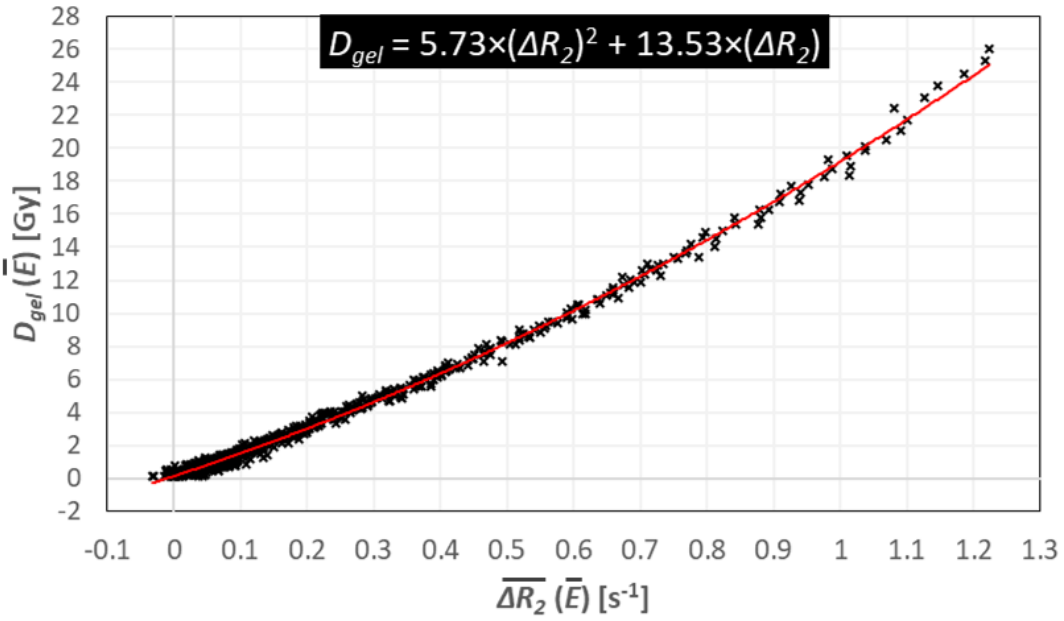

Figure 3.21. The defined calibration curve (polynomial of a 2nd order). Considered data are just taken over the phantoms irradiated with the CCRI50b beam.

Finally, over the studied dose range (below 27 Gy), the absorbed dose to gel exhibits a non-linear relation with the variation of the relaxation rate. A regression curve, in the form of a second-order polynomial function, provided a suitable fit, for all the CCRI50b phantoms data, with a consistent correlation factor R^2 of 0.9967, as follows:

$$D_{\text{gel}} = 5.73 \times (\Delta\overline{R_2})^2 + 13.53 \times (\Delta\overline{R_2})$$

The established calibration curve is represented on Figure 3.21. This curve is limited, for the moment, to dosimetric gels irradiated with a photon beam spectrum similar to that of the CCRI50b and within the dose range considered in this study (< 27 Gy). Any further implementation of this curve, with other photon beam shapes or higher doses, should be accompanied with more examination of the gel response. In any case, this calibration relation is used in the next section to determine the dose profiles around the IB-XR source.

3.2. Absorbed dose profiles in gel around the IB-XRS

The previously calibrated gel was used to determine the absorbed dose profiles in gel along two different axes around the IB-XRS associated with a 4-cm spherical applicator. To do so, a dedicated phantom was designed, then filled with the dosimetric gel before to be irradiated for a given prescribed dose by the INTRABEAM® system. Several slices over the phantom were read by MRI and the gel responses were corrected for the B_1-field inhomogeneity. Finally, the resulting gel response profiles, in terms of $\Delta\overline{R_2}$, were converted into the corresponding absorbed dose profiles, in terms of D_{gel}, in the considered axes.

3.2.1. Phantom design, gel preparation and irradiation

The design, preparation and irradiation of a dosimetric gel phantom, with IB-XRS associated to a 4 cm spherical applicator, are presented in this part.

INTRABEAM® applicators have a fixed metallic ring, a stainless-steel alloy, at the end of their shank to mount them on the IB-XRS. The ring alloy was tested and found to be compatible with MRI machines. However, this stainless-steel alloy still leads to metal induced susceptibility artifacts. Thus, to avoid any signal distortion by the applicator metallic ring, the phantom shown in Figure 3.22 was designed.

The phantom has a cylindrical shape with a pierced and movable cover in which the applicator can be introduced. The phantom size, limited by the MRI head-coil reading field, was chosen to attain abundant gel thickness around the applicator (almost 5 cm in the transverse plane and 7 cm along the probe axis). This gel volume provides a full photon backscattering and enough gel material around the IB-XRS to study the dose profiles in the axial and transverse planes. The polystyrene block, seen on the top of the phantom in Figure 3.22, was added to tight the applicator, in vertical position, along all operation time. To fix the cover position and center the applicator inside the phantom, six guiding screws in Plexiglas were used.

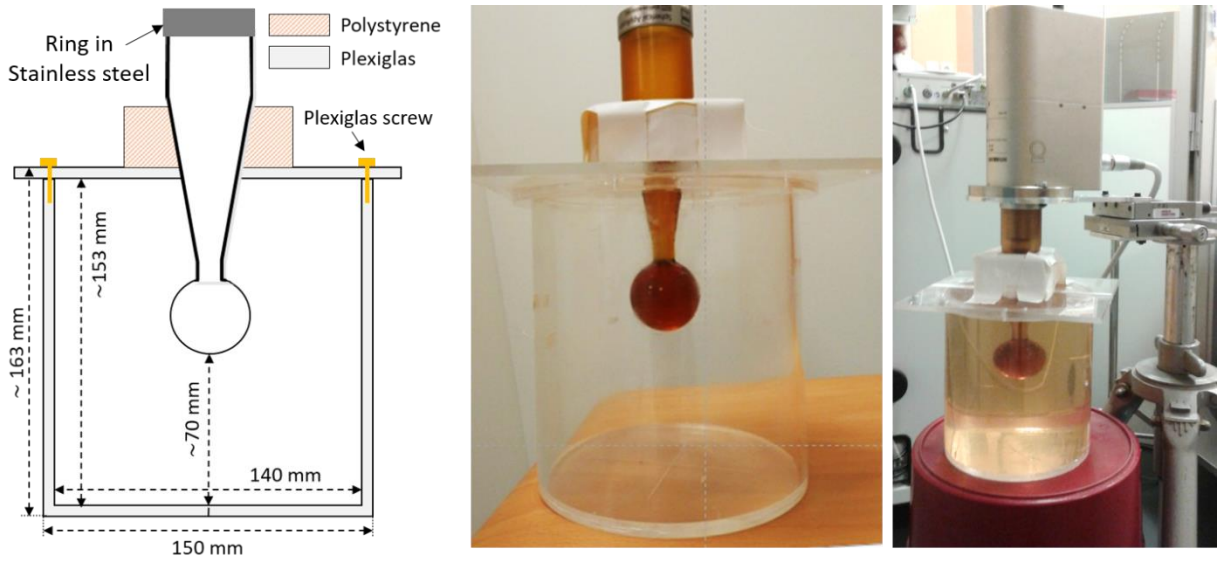

Figure 3.22. Design and irradiation of dosimetric gel phantom with IB-XRS associated to a 4 cm spherical applicator. (Left) Scheme (not to scale) of phantom design with dimensions of the main parts, (middle) the real phantom and (right) the irradiation at Saint-Louis hospital of the phantom filled with dosimetric gel.

The gel phantom was prepared at the same time as the gel vials used for gel calibration, so that the same gel filled all the phantoms. The dosimetric gel was poured into the phantom four days before the irradiation. Once filled, the phantom cover, with the applicator, was fixed in position using the Plexiglas screws. In addition, to eliminate interactions between air and gel, a thin silicone (commercially available) coating was applied all over the interface between the cover and the top of the phantom cylindrical wall. Then, the phantom was left at room temperature, before being moved into the fridge to jellify. The day before irradiation, the phantom was taken out of fridge and transported to the irradiation place, at Saint-Louis hospital in Paris, to stabilize overnight.

The prescribed absorbed dose to water at the applicator surface was 20 Gy. This dose was set relying on ZEISS delivered data for the IB-XRS of 50 kV and 40 µA, with the 4 cm spherical applicator mounted. To reach that dose, the total irradiation time was 25 minutes and 47 seconds.

After irradiation, the gel phantom was read using RMI as presented in the following part.

3.2.2. Gel response reading by RMI

The phantom was transported over about 30 km from Saint-Louis hospital to the SHFJ at Orsay where the MRI reading was performed two hours after the irradiation. As shown in Figure 3.23, the reading was done using the head coil with the positioning tray to control the phantom position inside (as already used in section 3.1.3.2). Moreover, it is also shown in this figure that the metallic ring of the applicator is kept outside the antenna to avoid signal distortion as discussed in the previous section.

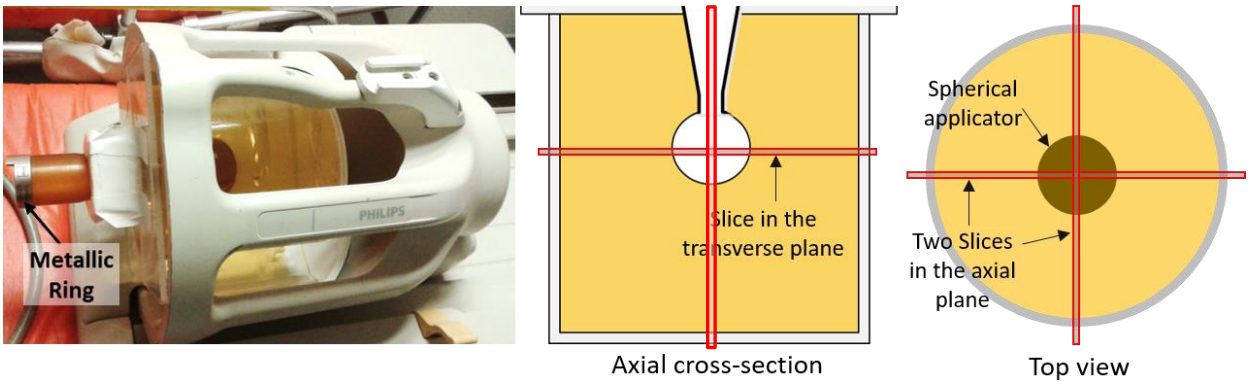

Figure 3.23. Imaging of the gel phantom by MRI: (left) a picture of the phantom analysis in the head-coil and (middle and right) schemes (not to scale) showing the position of the slices analyzed by MRI.

To study the dose distribution along the axial and transverse planes of the IB-XRS probe tip, the corresponding slices were imaged, as demonstrated in Figure 3.23. The sequence parameters used for the MRI machine were those previously presented in section 3.1.3.2. The considered slices were 4 mm thick and covered the whole phantom.

The corresponding data were saved into DICOM images. The actual pixel size, calculated as described in section 3.1.3.2 over the two slices, was of $(0.524 \times 0.524)\ \text{mm}^2$ with an associated relative uncertainty of 0.27 %. These dimensions are compatible with those given for the reconstruction matrix.

DICOM images, obtained for the gel phantom, either irradiated or not, were analyzed. The gel response was calculated using the method described in APPENDIX-D.

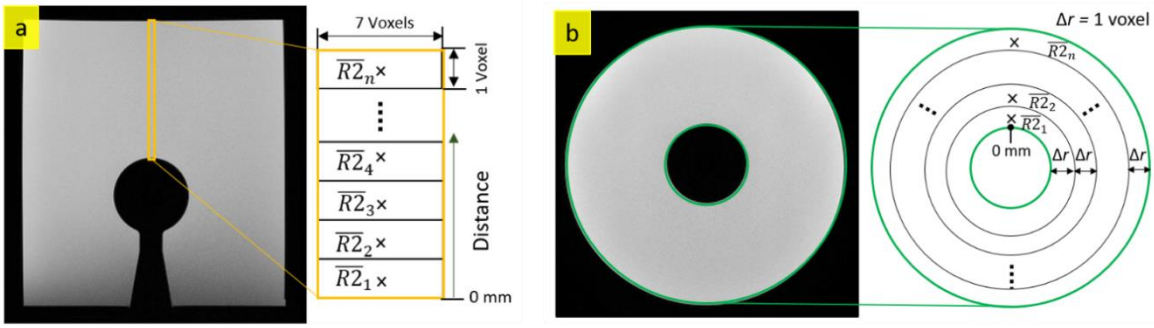

Figure 3.24. Images showing the resulted DICOM images, in ImageJ software, along the axial (a) and transverse (b) planes including the IB-XRS probe tip with the corresponding selected ROIs over each image.

The resulting DICOM images and the studied ROIs are respectively presented in Figure 3.24-a and -b, for slices along the axial and transverse planes. To define the $\overline{R_2}$ distribution of the IB-XRS with the 4-cm applicator along the probe axis, a series of rectangular ROIs were selected over the axial phantom image as demonstrated in Figure 3.24-a. The ROIs, centered along the probe axis, had all a width of seven voxels that is of the order of the probe diameter. Annular ROIs were selected to study the $\overline{R_2}$ distribution in the transverse plane (Figure 3.24-b), to profit from the symmetry around the applicator when the gel is irradiated. The zero-distance points considered in all calculations are at the interface between the gel and the applicator.

The gel phantom being of substantial size within the head coil (as opposed to the calibration gel vials), the homogeneity of the magnetic field over the whole volume occupied by the gel phantom inside the coil was tested, as demonstrated in next sections.

3.2.3. Correction for the B_1-field inhomogeneity

As explained in section 1.3.3.3.3, before the irradiation of the gel phantom, a potential B_1-field spatial inhomogeneity in the head coil was first characterized. This characterization was performed under an image acquisition configuration that perfectly matches the one finally used to read the irradiated gel phantom, notably in terms of the gel phantom position inside the coil. To ensure the position reproducibility of the gel phantom inside the coil, the positioning tray was systematically used when imaging the gel phantom (whatever it was irradiated or not).

The dose distribution being finally required along the axial and transverse planes of the IB-XRS probe tip, the $\overline{R_2}$ spatial profiles obtained when reading the non-irradiated phantom along these two axes were each fitted by a second order polynomial function of the form:

$$\overline{R_2}(x) = a.x^2 + b.x + c$$

where x is the spatial position of the voxel from the center of the coil along the considered axis. The correction factors $k_{B1}(x)$ can then be expressed as:

$$k_{B1}(x) = \frac{c}{a.x^2 + b.x + c}$$

Figure 3.25 shows the fits obtained with the $\overline{R_2}(z)$ values along the transverse and axial directions corresponding to the non-irradiated phantom where $z = x - x_0$, x_0 being the position of the surface of the applicator. The B_1-field inhomogeneity corrections are found both to increase with the distance from the head-coil center. Those corrections are more significant along the transverse plane than the axial one.

The corrected $\overline{R_2}$ profiles, also plotted on the same figure, show flat responses with the distance, as expected for a homogenous gel. However, it can be noticed that the corrected $\overline{R_2}$ profiles along the two orthogonal axes show a discrepancy of 1.2 %. This difference is due to an error in the positioning of the applicator surface with respect to the coil center. As a consequence, since the profile along the axial axis shows very low inhomogeneity with depth, the transverse $\overline{R_2}$ profile was increased for the further application by a factor of 1.012.

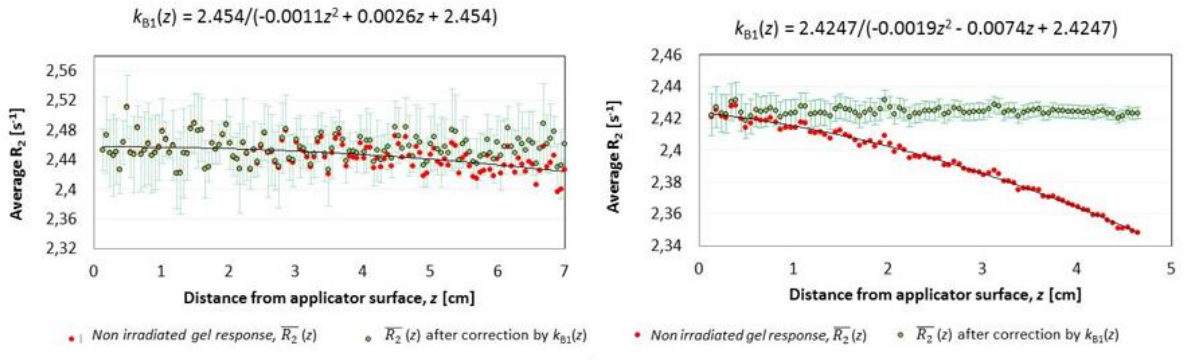

Figure 3.25. $\overline{R_2}$ distributions as a function of depth from applicator surface, corrected or not for inhomogeneity interferences along axial axis (left) and transverse axis (right).

To check if this correction was suitable for the range of $\overline{R_2}$ values that can be attained with the irradiation up to dose saturation, this correction was applied to the analysis of the phantom previously presented filled with the same preparation of dosimetric gel, the only difference being that Fe^{2+} ions were replaced by Fe^{3+} ions, in order to simulate a homogeneously irradiated gel at dose saturation. Figure 3.26 shows that the $\overline{R_2}$ profile in the transverse axis, obtained for the gel phantom whose irradiation was simulated by the addition of Fe^{3+} ions, also tends to decrease when increasing the distance to the center, and regains a flat behavior when corrected for the B_1-field inhomogeneity. Therefore, this correction can be applied to the dose distribution measurements in the gel irradiated by the INTRABEAM® source.

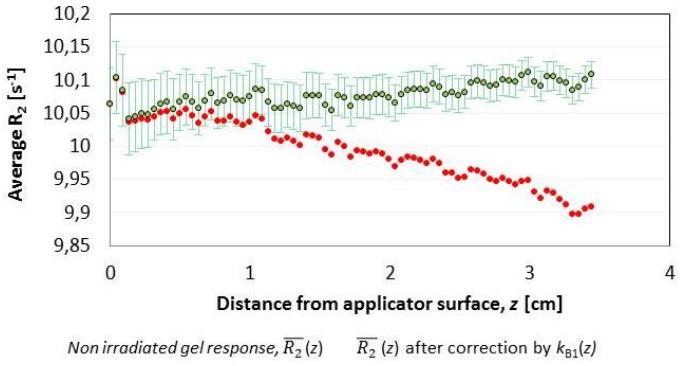

Figure 3.26. $\overline{R_2}$ distributions as a function of depth from applicator surface, corrected or not for inhomogeneity interferences along the transverse axis, using the correction factor function previously defined from non-irradiated gel.

3.2.4. Determination of the absorbed dose profiles in gel

DICOM images, obtained for the gel phantom after irradiation, were analyzed. The relaxation rates, $\overline{R_2}$, were calculated in both axial and transverse planes along the IB-XRS probe tip. Those calculations were done using the previously described ROIs, by applying the method detailed in APPENDIX-D and accounting for the inhomogeneity of the B_1 field. The resulting profiles are shown in the graphs on Figure 3.27, where black and colored curves correspond respectively to the uncorrected and corrected profiles for the gel response inhomogeneity.

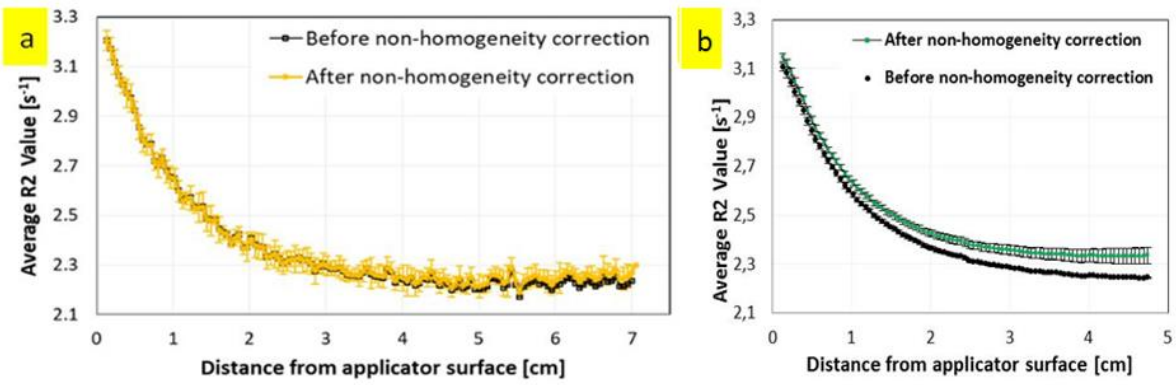

Figure 3.27. Comparison of the calculated average gel response $\overline{R_2}$ before and after inhomogeneity corrections for the axial plane (a) and for the transverse plane (b). Uncertainties are plotted with a coverage factor *k* equal to 1.

The calculation of the variation of the gel relaxation rate, $\Delta\overline{R_2}$, required the intermediate step of determination of the blank value, $R_{2,0}$. For the same reasons as explained before (see section 3.1.3.3), this blank value was not deduced from the non-irradiated gel, but from the fit of the $\overline{R_2}$ values as a function of the MC calculated absorbed dose in gel, D_{gel} (as done in section 3.1.5.1 for the calibration vials). The MC calculations of the absorbed dose in gel, D_{gel}, are presented later on in section 3.3.1. The intermediate results in terms of $\Delta\overline{R_2}$ are further converted in terms of absorbed dose to gel, D_{gel}, using the previously established calibration curve (see section 3.1.5.2). The depth dose profiles in gel, in the two studied axes, are presented and compared in Figure 3.28. The uncertainty bars include the uncertainties on the inhomogeneity correction factors.

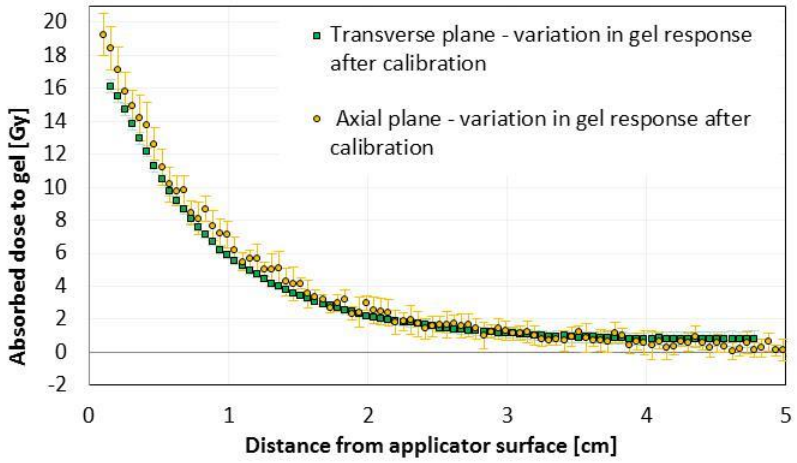

Figure 3.28. Comparison of the absorbed dose to gel profiles in the axial and transverse planes. Uncertainties are plotted with a coverage factor *k* equal to 1.

The absorbed dose to gel profile along the axial direction is higher than the one in the transverse plane in the first few millimeters. This discrepancy can be partly explained by the emission anisotropy of the IB-XRS source, as published by Schneider *et al.* [143], who demonstrated emission intensity differences ranging from about 15 % to 22 % between the axial and transverse planes. This discrepancy could also be partly due to a shift between the center of the spherical applicator and the center of the circular ROIs considered in that study, which would lead, *in fine*, to a shift in the absorbed dose profiles.

The depth dose profiles determined in this section are defined in gel for the IB-XRS with a 4 cm spherical applicator. However, since the depth dose profiles are conventionally given in water, they should be transformed into absorbed dose profiles in water. The next section deals with this issue.

3.3. Absorbed dose profiles in water around the IB-XRS

The absorbed dose to water being the conventional quantity of interest in radiotherapy, MC calculations were implemented to convert the absorbed dose profiles in gel, defined by the dosimetric gel, into absorbed dose profiles in water. While the first part of this section presents the developed MC method and compare the MC calculated dose profiles to the ones obtained using the dosimetric gel, the second one determines the factors to convert the absorbed doses to the gel into absorbed doses to water. At last, the third and final part deal with the absorbed dose profiles obtained in water by application of the resulting conversion factors.

3.3.1. MC calculation of the relative absorbed dose to gel profiles and validation of the calibration procedure

The MC method was used to calculate the dose distributions, in water and gel, around the IB-XRS with a 4 cm spherical applicator, in the two considered planes. The experimental configuration, comprising the phantom and the IB-XRS with a 4 cm spherical applicator (as described in section 3.2.1) was modeled using the PENELOPE code, successively filled with gel and water. The PSF files created in section 2.3.3 were used as source of particles.

To calculate the dose profiles in the axial and transverse planes, several bodies were modeled in those two axes as shown in Figure 3.29 (Top). These body series were meant to match the two series of ROI used to determine the $\Delta\overline{R_2}$ profiles in the irradiated gel (see section 3.2.4). In each configuration, the bodies have the same size, form and position of the corresponding experimental ROI.

The dose calculation in each body was based on the calculation of the deposited energy in the body. The corresponding dose value was calculated by dividing the energy in [eV.pp^{-1}] deposited in each body by its mass in [g]. The simulation parameters assigned for each material of both gel and water phantoms model are as in Table 2.2.3.

Table 3.5. Values of simulation parameters assigned to each material used in the developed MC models.

E_{abs} (1) [eV]	E_{abs} (2) [eV]	E_{abs} (3) [eV]	C_1	C_2	W_{CC} [eV]	W_{CR} [eV]	*DSMAX(KB)*
1.0E+03	1.0E+03	1.0E+03	0.05	0.05	1.0E+03	1.0E+03	1/10th

The MC calculated dose profiles, in the axial and transverse planes, are shown in Figure 3.29 (middle and bottom, respectively). The geometrical center was taken as the reference point of each body, as also considered for all ROIs. In order to compare these two curves to the dose profiles determined by the dosimetric gel, in the corresponding planes, they were all normalized to the dose value at 1 cm depth.

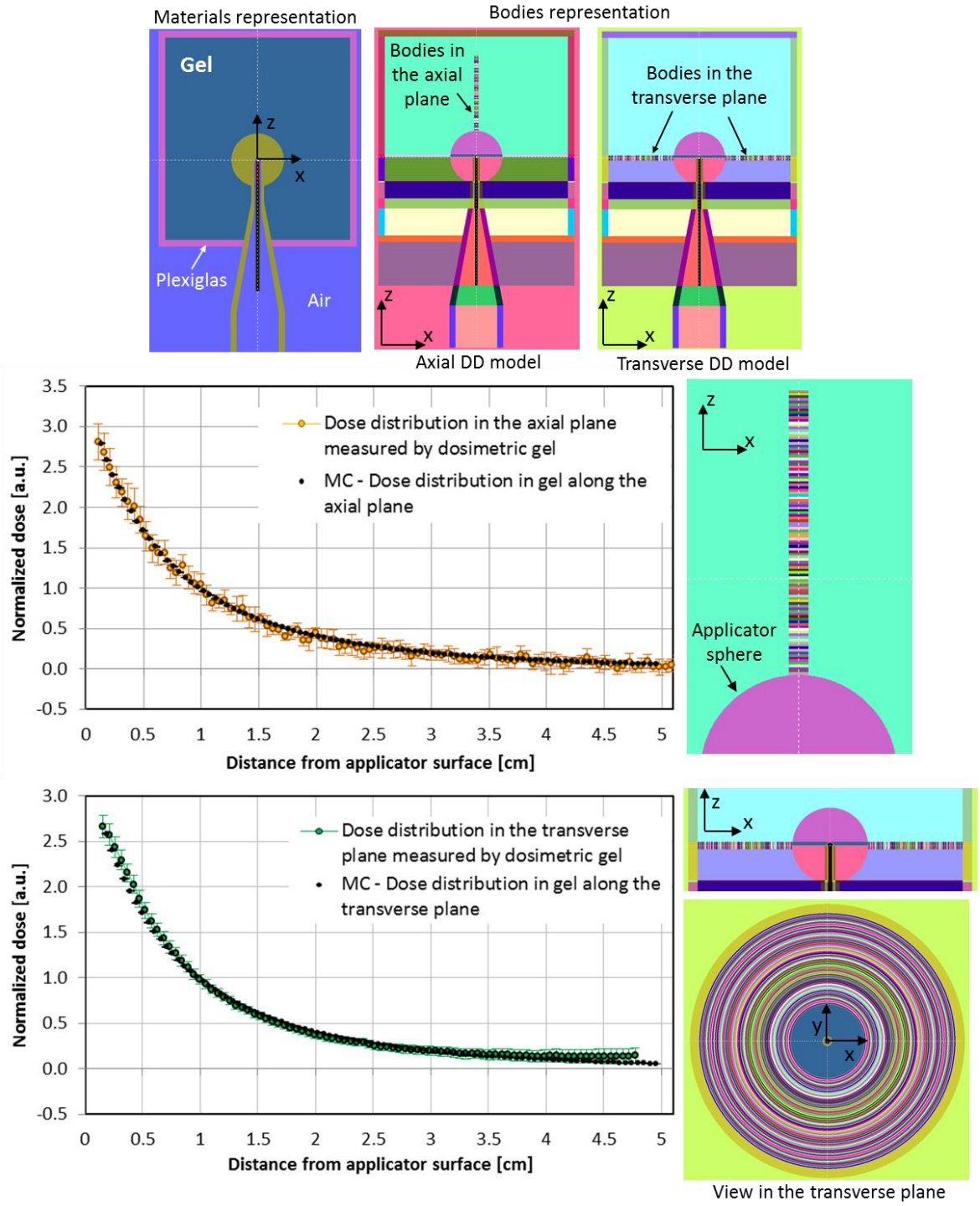

Figure 3.29. (Top) the developed MC models of the irradiated gel phantom with IB-XRS associated to the 4 cm spherical applicator used to calculate the Dose Distributions (DD) in the axial and transverse planes, as viewed in PENELOPE GVIEW2D. (Middle and bottom) Comparison between DD normalized to the dose value at 1 cm calculated by the MC models and those measured by the dosimetric gel in the axial and transverse planes, respectively. The images to the right of the graphs show a zoom-in on the bodies used to calculate the relative DD in the corresponding axis. Uncertainties are presented with a coverage factor *k* equal to 1.

The dose distributions in the two planes, determined by the dosimetric gel and MC method, agree within the uncertainty bars. A better agreement, for doses values at high depths, is found along the axial beam than along the transverse one. Indeed, the importance of the inhomogeneity correction at high depths for the transverse plane might lead to the observed

bias. Nevertheless, these agreements in both planes validate the calibration procedure and, furthermore, the adopted approach consisting in considering no energy dependence of the gel response in the dose and energy ranges under study.

3.3.2. MC calculation of conversion factors to go from gel to water dose profiles

The dose profiles were also calculated in water to determine the conversion factor, from dose in gel to dose in water, at each depth in the two considered planes. The same MC models, bodies configurations and simulation parameters, as detailed above, were used. The only difference was that the gel inside the phantom models was replaced by liquid water (as defined in PENELOPE material pendbase library).

The comparison between the dose distributions in water, D_w, and gel, D_{gel}, is shown on the left of Figure 3.30. The dose distribution in water is slightly higher than the one in gel for low depths (almost by 2 %). The D_w/D_{gel} ratio tends to increase with the distance from the applicator surface, as shown on the right of Figure 3.30. These variations between the two distributions are due to the differences in the photon attenuation and absorption coefficients and mass densities of water and gel.

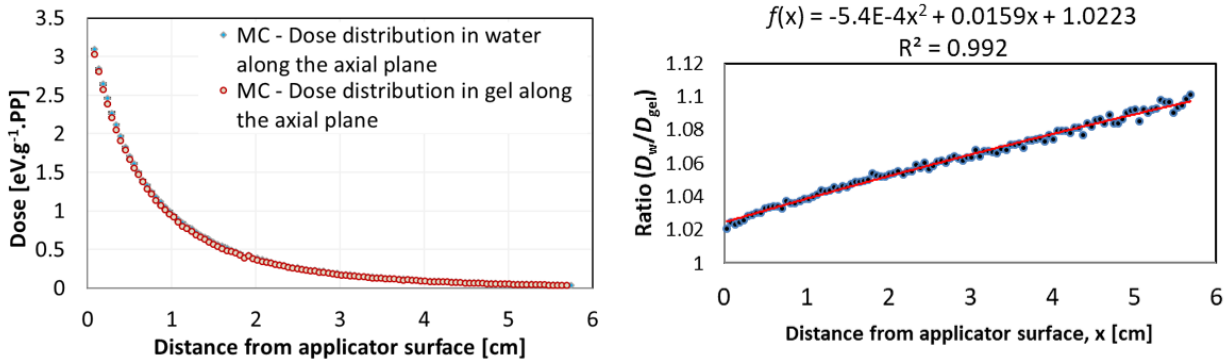

Figure 3.30. (Left) comparison between the dose distributions in water and gel in the axial plane, and (right) the corresponding gel to water dose conversion function $f(x)$, determined over the calculated ratios of (D_w/D_{gel}) at each distance.

The behavior of the D_w/D_{gel} ratio over distance from the applicator was fitted with a polynomial function. This function is used to convert the dose distribution determined in the dosimetric gel into a dose distribution in water, as discussed in the next section. The same study, with similar results, was done in the transverse plane.

3.3.3. Determination of the absorbed dose profiles in water

The absorbed dose distributions in water in the two considered planes for the IB-XRS with the 4 cm spherical applicator were obtained by conversion of the relative absorbed dose distribution in gel using the conversion curves determined in the previous section 3.3.2. The resulting absorbed dose profiles in water are presented on Figure 3.31 and compared to the corresponding data provided by ZEISS.

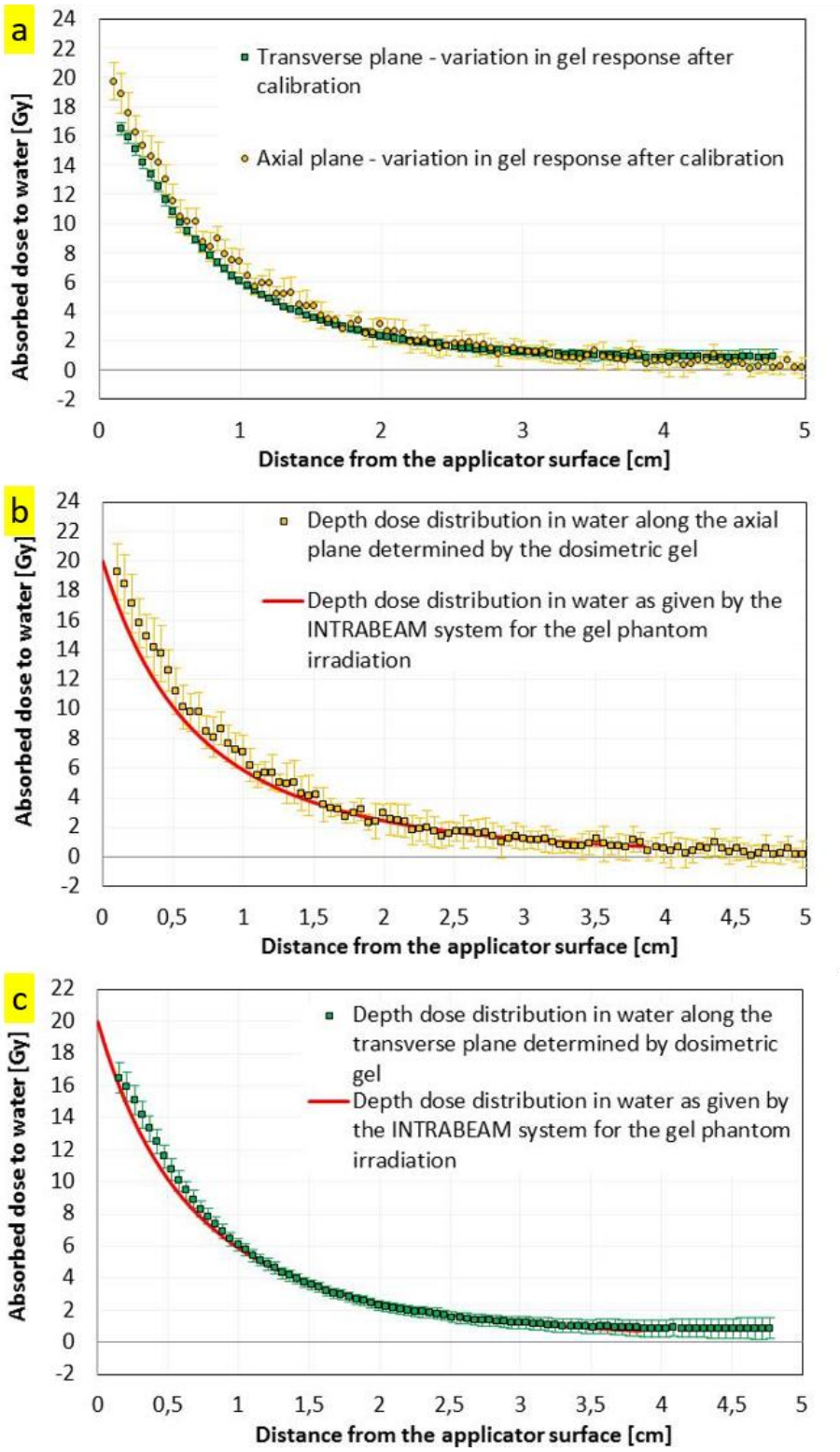

Figure 3.31. Comparison of the two absorbed-dose-to-water distributions obtained using gel dosimetry (a). Plot and comparison to data provided by ZEISS of the absorbed dose to water distributions in the axial (b) and transverse (c) planes along the IB-XRS probe tip associated to a 4 cm spherical applicator. These absorbed-dose-to-water distributions were determined from a dosimetric gel phantom irradiated by the considered source at a prescribed dose at the applicator surface of 20 Gy relying on ZEISS delivered data for the IB-XRS of 50 kV and 40 µA.

Actually, for each treatment (irradiation) by the system INTRABEAM®, the corresponding depth dose profile in water can be accessed. This curve gives the absorbed dose in water expected to be delivered as a function of depth from the surface of the IB-XRS applicator. Thus,

the depth dose profile in water given by the INTRABEAM® system during the irradiation of the gel phantom was retrieved (data are given in APPENDIX-E).

The comments made in section 3.2.4 about the comparison of the absorbed dose to gel profiles are still true when comparing the absorbed-dose-to-water profiles. This was expected since the difference in the two distributions was not attributed to the gel material, but to the anisotropy in terms of emission intensity of the IB-XRS and to a possible center shift in the data treatment. However, the distributions obtained in the two planes are still in agreement within the bars of uncertainty as shown on Figure 3.31-a, at least after a few millimeters depth.

Besides, the comparison between those absorbed-dose-to water profiles obtained from the dosimetric gel with the one given by INTRABEAM system, as shown on Figure 3.31-b et -c, shows that the experimental values are slightly higher than the ones from ZEISS.

Nevertheless, those last conclusions should be handled with some care. Indeed, obtaining accurate results when using of dosimetric gel for absolute doses measurements have proved to be tricky. Actually, whatever the kind of gel and reading method employed, several errors can occur, from the establishment of the calibration curves to the reading of the studied phantom. For example, with MRI readings, the use of a calibration phantom with different shape and volume from the studied one can lead to doses inaccuracies [144]. That is why gel dosimetry is often used as a relative dosimeter rather than an absolute one. Linking to absolute dose is then done with the use of internal or external standards. A comparison, in similar experimental conditions with regards to the phantom shape and to the gel medium, with another dosimeter such as radiochromic films, would have been interesting for the evaluation of the reliability of the method of gel dosimetry for absolute dose distribution assessment [145]. Therefore, as a caution for this study, data obtained from gel dosimetry will be used in chapter 4 to bring relative values to absolute values using the primary measurements obtained in chapter 2.

Thus, Figure 3.32 plots the relative absorbed dose to water profiles. These three curves were respectively measured using gel dosimetry, calculated by MC method and extracted from the ZEISS database. All curves are normalized at a depth of 1 cm. The flawless agreement of those three relative distributions, firstly, participates to validate the relative distribution of the absorbed dose provided by Zeiss, and secondly, comforts the gel dosimetry use, once calibrated using the primary standard developed under the present study, for absolute dose assessment.

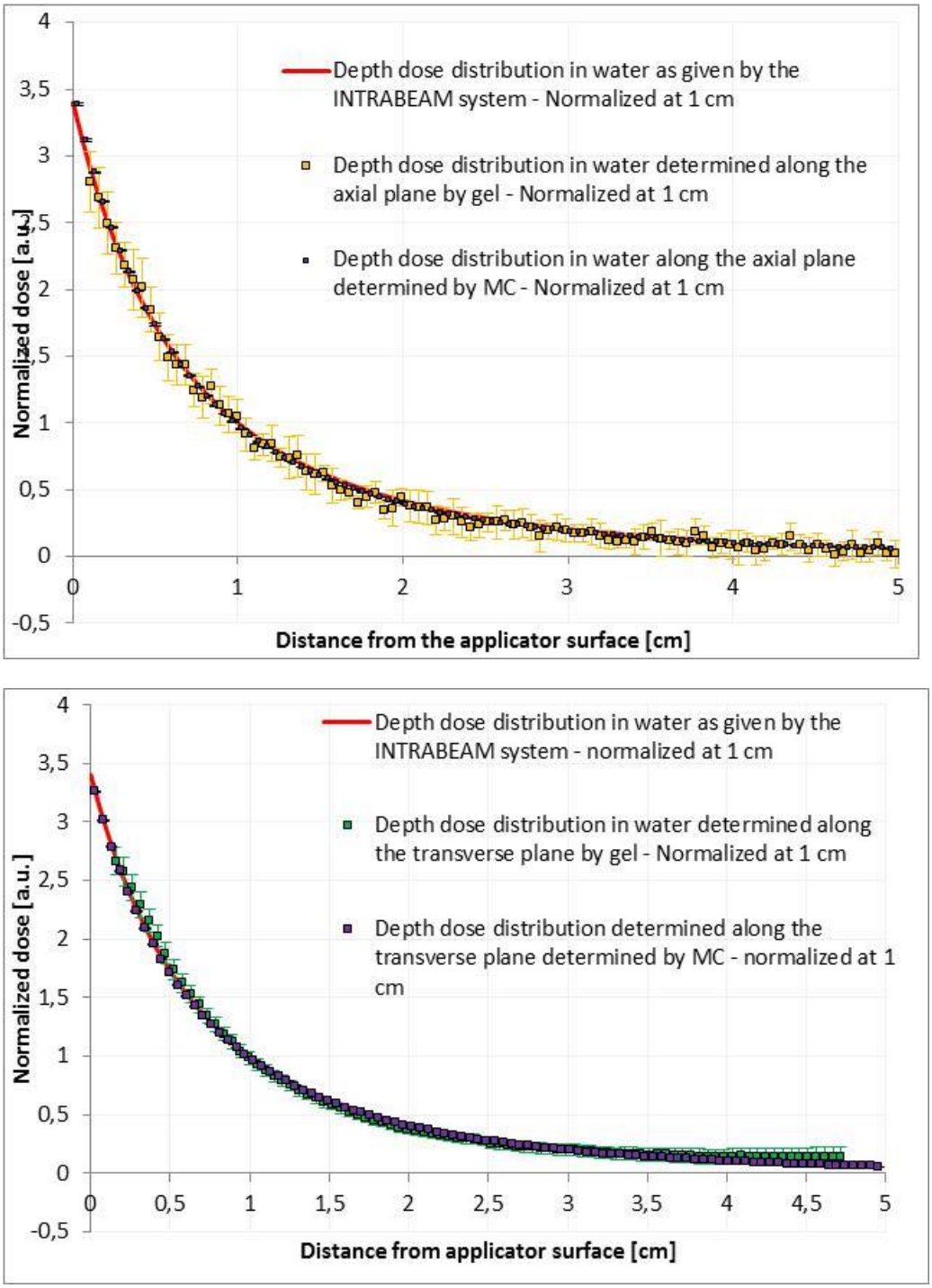

Figure 3.32. Comparison of the relative absorbed dose to water profiles, all normalized at the depth of 1 cm, obtained by gel dosimetry, MC calculation and from the ZEISS database, in the axial (top) and transverse (bottom) axes.

Summary

Gel dosimetry was demonstrated to be a reliable tool to evaluate the relative dose distributions around eBT systems. The dosimetric gel used was characterized for low energy X-Rays (≤ 50 keV). Its dependence on dose and energy was examined. It was found to have a polynomial behavior with the absorbed dose while no solid conclusion could be given about the dependence on energy; indeed, in this study the information was hidden by the statistical uncertainties of the results obtained with the gel.

The relative dose distribution around the IB-XRS associated with 4-cm spherical applicator was determined in the axial and transverse planes of the IB-XRS probe tip. Monte Carlo calculations were implemented to convert these dose distributions measured in gel into dose distributions in water through a gel-to-water conversion function.

The absorbed dose to gel profile along the axial plane was found higher than the one in the transverse plane in the first few millimeters. This discrepancy can be related to several sources such as the emission anisotropy of the IB-XRS source and shift between the center of the spherical applicator and the center of the circular ROIs considered.

The dose profiles, determined by the dosimetric gel and MC method, agree within the uncertainty bars in the two planes. The agreement in both planes validates the calibration procedure and, furthermore, the adopted approach consisting in considering no energy dependence of the gel response in the dose and energy ranges under study.

Despite the fact that the gel analysis in the current study was based on the spin-spin relaxation speed (R_2) due to previous developed expertise, the spin-lattice relaxation speed (R_1) is recommended for further analysis. The R_1 has a better signal-to-noise ratio which is expected to enhance the spatial resolution of the measured doses and to decrease their associated statistical uncertainties.

A comparison, in similar experimental conditions with regards to the phantom shape and to the gel medium, with another dosimeter such as radiochromic films, would be interesting for the evaluation of the reliability of the method of gel dosimetry for absolute dose distribution assessment.

Chapter 4

4. Analysis of the INTRABEAM® dosimetric methods and dose distributions

This chapter is dedicated to the analysis of the dose distributions delivered by Zeiss for the INTRABEAM® system and of the dosimetric procedure that they developed for their assessment.

The reference dose values determined by the primary laboratories, i.e. the LNHB and the PTB (in cooperation with CMI (Czech Republic)), were compared to the absolute dose values delivered by Zeiss for the INTRABEAM® systems studied under equivalent reference conditions. These comparisons are then followed by the analysis of the methods adopted by Zeiss for the INTRABEAM® dosimetry. Finally, the dose distributions in water, obtained in this study by the dosimetric gel, were compared to that delivered by the INTRABEAM® for similar irradiation configurations.

4.1. Comparison of INTRABEAM® doses to the LNHB and the PTB-CMI primary standards

Zeiss provides for each INTRABEAM® system the dose distribution in water, for the bare IB-XRS, and the transfer functions for spherical applicators. These distributions are updated by Zeiss at each calibration period of the IB-XRS. In addition to the regular dose distributions data, based on the initial dosimetry by the TARGIT method, Zeiss started (since 2017) to provide also the dose distributions obtained for the same system by the novel Non-TARGIT method (as presented in section 1.4.2.3). However, no clear statement was given by Zeiss about the methodology that delivers the new "right" dose value.

The LNHB and the PTB primary laboratories have established their primary dosimetric standards in terms of absorbed dose to water for the INTRABEAM® system. Each standard was established for a different INTRABEAM® system under different reference conditions, see section 2.1 and section 1.4.2.3.1 for the reference conditions of the LNHB and PTB dosimetric references, respectively. The reference dose value determined by each laboratory was compared to the values delivered by Zeiss for the two methods (TARGIT and Non-TARGIT) under corresponding conditions, through exercises carried out separately. The comparisons between the values given by Zeiss and those obtained on the one hand, by the LNHB, and on the other hand, by the PTB, for the corresponding IB-XRS and reference conditions, are presented in Table 4.1.

The dosimetric reference of the LNHB, determined in chapter 2, was established for the studied IB-XRS of the Saint-Louis Hospital associated with a 4 cm spherical applicator at 1 cm in water along the probe axis. The $\dot{D}_w$ considered for the comparison is extracted from Table 2.19 presented in section 2.4.5 with the measurements at 13.5 SDD. On the other side, the values considered for Zeiss were extracted from the dose distribution data delivered for the bare IB-XRS under study at 30 mm from the isocenter. The dose rate values were of 3.72 [mGy.s^{-1}] for the TARGIT method and 4.26 [mGy.s^{-1}] for the Non-TARGIT (with a conversion factor of 0.873 between the two methods). Then, the transfer function of the 4 cm spherical applicator

was applied to obtain the dose values at 1 cm distance from the applicator surface; the 4 cm spherical applicator transfer function at this distance has a value of 1.327.

The ratios between the dose rate values determined by LNHB to those provided by Zeiss were calculated ($\dot{D}_{w,LNHB}/\dot{D}_{w,Zeiss}$) and enlightened significant differences between them. The value determined by the LNHB was higher than those provided by Zeiss, by 33 % when compared to the TARGIT method, and by 16 % when compared to the Non-TARGIT method.

The PTB has also published with CMI, in May 2017, a comparison between the $\dot{D}_w$ values they obtained, under the configurations described in section 1.4.2.3.1, and those delivered by Zeiss [146]. All values for the water kerma rate and absorbed dose to water for the bare INTRABEAM® source were determined with an IB-XRS of 50 kV and 40 µA current. The average value obtained for the $\dot{K}_w^{Ph}$ was **71.3 ± 0.006** [µGy.s^{-1}] (at a plate separation zero for specific plate separations x_{i+1}), and the value for the absorbed dose rate at 1 cm SDD from the probe tip was determined equal to **65.4 [mGy s^{-1}]**. However, in the available publication, the PTB result was given without associated uncertainty. They have stated that the uncertainty budget needs further investigations, due to the huge impact of the developed MC model on the result obtained, and a crucial part of the work was the characterization of the source and the design of a detailed MC model.

Table 4.1. Comparison of reference $\dot{D}_w$ determined by LNHB and PTB to that delivered by Zeiss with the two calibration methods under the corresponding reference conditions in each case.

$\dot{D}_w$ values here are determined at 1 cm from the 4 cm spherical applicator surface				
LNHB $\dot{D}_w$ [mGy.s^{-}1] (ref: 13.5 cm SDD)	**Zeiss** $\dot{D}_w$ [mGy.s^{-1}]		$\dot{D}_w$ ratio (LNHB/Zeiss)	
	TARGIT	Non-TARGIT (V4.0)	TARGIT	Non-TARGIT (V4.0)
4.95	3.72	4.26	**1.33**	**1.16**
$\dot{D}_w$ values here are determined at 1 cm from the bare probe tip				
PTB-CMI $\dot{D}_w$ [mGy.s^{-}1]	**Zeiss** $\dot{D}_w$ [mGy.s^{-1}]		$\dot{D}_w$ ratio (PTB-CMI/Zeiss)	
	TARGIT	Non-TARGIT (V4.0)	TARGIT	Non-TARGIT (V4.0)
65.4	40.3	53.6	**1.62**	**1.22**

The comparison between the reference doses determined by the PTB and those relying on the INTRABEAM® data revealed also high differences. The $\dot{D}_w$ determined by the PTB was remarkably higher than the values delivered by Zeiss under the same conditions i.e. at 1 cm distance from the bare probe tip along the probe axis. The PTB value was higher than the one provided by Zeiss, respectively, by 62 % when compared to the TARGIT method, and by 22 % when compared to the Non-TARGIT method.

We can conclude from both comparisons that the values provided by Zeiss are probably significantly underestimated. The higher differences obtained by the PTB can be mainly related

to the closer distance from the probe tip which increases the impact of the uncertainty on the results (this can be also noticed from the correlation factor *f'*(r) value used by Zeiss between the two methods TARGIT and Non-TARGIT, where a correlation factor of 0.75 at 1 cm and 0.87 at 3 cm distances from the probe tip are given, see APPENDIX-A). Zeiss stated in their document [122] an estimation of a minimum error in the determination of the absorbed dose to water, based on the TARGIT method, of (± 4.2 %) at 2 cm distance from the probe and (± 5.3 %) elsewhere. Still, these uncertainties are way far from according Zeiss values with those determined by the LNHB and the PTB laboratories under the considered reference conditions. However, the doses given by the novel Non-TARGIT method are closer than those given by the TARGIT method to the reference dose values determined by the LNHB and PTB.

To carry out a deeper analysis of those results and give more definitive conclusions, a direct comparison between the LNHB and PTB absorbed dose references, and possibly those of other metrology laboratories, would be of high interest. However, due to the apparent bias observed on the Zeiss values that seem systematically too low, their methodologies were examined. The evaluation of these methodologies is presented in the next section.

4.2. Analysis of the absorbed dose to water method, TARGIT, provided by ZEISS

For simplicity, we will consider the TARGIT method in the further analysis, due to a lack of detailed information on the new Non-TARGIT method. The Zeiss approach to determine the absorbed dose to water from a calibration in air kerma is compared to an approach based on a generalized cavity theory formalized at LNHB, which takes into account three different mediums instead of two in conventional theories (Bragg-Gray, Burlin). This approach is presented in the next section.

4.2.1. Expressions of calibration coefficients using the three-medium cavity theory

This cavity theory [147] aims at expressing the relation between the absorbed dose in the medium of interest, in the absence of detector, and the mean absorbed dose in the detection volume (cavity) of the detector. This detector here consists of a cavity surrounded by a wall, the three mediums (cavity, wall, medium of interest) being a priori made of different materials. The absorbed dose in the detection volume results from the interactions in the cavity of charged particles liberated in the three mediums.

This theory can be applied to an ionization chamber with an air-filled cavity. When the medium of interest is water, the absorbed dose to water, D_{wat}, at a reference point, C, in the absence of the chamber, can then be expressed using the following formula:

$$D_{wat}(C) = \bar{D}_{air} \cdot {}_{wall}(\Psi_c)_{wat,wall} \cdot {}_{air}(\Psi_c)_{wat,air} \cdot [(1 - \alpha_{wall} - \alpha_{air})\, s_{wat,air} + \alpha_{wall}\,(\beta\mu_{en}/\rho)_{wat,wall} \cdot s_{wall,air} + \alpha_{air}\,(\beta\mu_{en}/\rho)_{wat,air}]$$

where,

$\bar{D}_{air}$ is the average absorbed dose in the air of the chamber cavity centred on point C, that can be expressed as $\bar{D}_{air} = (\bar{W}/e) \cdot (Q/m)$ with Q the electric charge created in the cavity by ionizing radiation and m the mass of air;

α_{wall} is the fraction of $\bar{D}_{air}$ due to charged particles liberated in the chamber wall;

α_{air} is the fraction of $\bar{D}_{air}$ due to charged particles liberated in the air cavity;

β is the (dose/collision kerma) ratio, in the same medium at the same point, under Transient Charged Particles Equilibrium (TCPE) conditions;

$s_{wat,air}$ is the water-to-air ratio of mean restricted mass collision stopping powers;

$s_{wall,air}$ is the wall-to- air ratio of mean restricted mass collision stopping powers;

$_{wall}(\Psi_c)_{wat,wall}$ is the correction factor for the perturbation in the photon energy fluence, at the detector center, due to the replacement of water by the wall material in the volume occupied by the wall;

$_{air}(\Psi_c)_{wat,air}$ is the correction factor for the perturbation in the photon energy fluence, at the detector center, due to the replacement of water by air in the cavity.

In our case, the absorbed dose to water is determined by using a transfer ionization chamber, PTW 23342, which is characterized by an air cavity of 1 mm thickness (along the beam axis) and an entrance window of 30 µm in polyethylene. These two characteristics, in the studied energy range of (≤ 50) keV, enables:

A- the application of the Bragg-Gray cavity theory [148]: small cavity thickness, compared with the range of incident charged particles in it, and negligible contribution to $\bar{D}_{air}$ of the charged particles liberated in the cavity ($\alpha_{air} \approx 0$);

B- the assumption of TCPE in the material thickness of the PTW 23342 entrance window and negligible contribution to $\bar{D}_{air}$ of the charged particles liberated in the external medium, i.e. water ($\alpha_{wall} = 1$).

Then, <u>the energy deposited in the cavity is only due to charged particles generated in the wall.</u>

Thus, the absorbed-dose-to-water equation presented above, using the PTW 23342 ionization chamber, simply becomes:

$$D_{wat}(C) = Q \frac{\bar{W}}{e} \frac{1}{m} \cdot {}_{wall}(\Psi_c)_{wat,wall} \cdot {}_{air}(\Psi_c)_{wat,air} \cdot (\beta\mu_{en}/\rho)_{wat,wall} \cdot s_{wall,air}$$

This equation can be then used to define the calibration coefficient of the chamber, in terms of absorbed dose to water, as:

$$N_{D,wat}(C) = \frac{D_{wat}(C)}{Q} = \frac{\bar{W}}{e} \frac{1}{m} \cdot {}_{wall}(\Psi_c)_{wat,wall} \cdot {}_{air}(\Psi_c)_{wat,air} \cdot (\beta\mu_{en}/\rho)_{wat,wall} \cdot s_{wall,air}$$

In the same way, the absorbed dose in the air medium in TCPE conditions using the same ionization chamber can be expressed by (we are here in the case of just two mediums instead of three since water is replaced by air, and hence, air(Ψc)air,air = 1),:

$$D_{air}(C) = \bar{D}_{air} \cdot {}_{wall}(\Psi_c)_{air,wall} \cdot (\beta\mu_{en}/\rho)_{air,wall} \cdot s_{wall,air}$$

where, $_{wall}(\Psi_c)_{air,wall}$ is the correction factor for the perturbation in the photon energy fluence, at the detector center, due to the replacement of air by the wall material in the volume occupied by the wall.

From this relation, one gets $K_{air}(C)$ using the relation between $D_{air}(C)$ and $K_{air}(C)$ in the TCPE conditions: $D_{air}(C) = \beta_{air}(1-\bar{g}_{air})K_{air}(C)$, where $\bar{g}_{air}$ is the fraction of the initial kinetic energy of charged particles expended in radiative losses:

$$K_{air}(C) = \bar{D}_{air}\,\frac{1}{1-\bar{g}_{air}}\cdot\frac{1}{\beta_{air}}\cdot {}_{wall}(\Psi_c)_{air,wall}\,(\beta\mu_{en}/\rho)_{air,wall}\cdot s_{wall,air}$$

The corresponding calibration coefficient of the chamber, in terms of air kerma, is then determined by:

$$N_{K,air}(C) = \frac{\bar{W}}{e}\cdot\frac{1}{m}\cdot\frac{1}{1-\bar{g}_{air}}\cdot\frac{1}{\beta_{wall}}\cdot {}_{wall}(\Psi_c)_{air,wall}\,(\mu_{en}/\rho)_{air,wall}\cdot s_{wall,air}$$

In the considered photon energy range ≤ 50 keV, kerma and collision kerma can be considered as equal, with $(1-\bar{g}_{air})$, β_{wall} and β_{wat} equal to one. The ratio of the two calibration coefficients (water to air), can then be theoretically denoted as:

$$\frac{N_{D,wat}(C)}{N_{K,air}(C)} = \frac{{}_{wall}(\Psi_c)_{wat,wall}\cdot {}_{air}(\Psi_c)_{wat,air}\;\;(\mu_{en}/\rho)_{wat,wall}}{{}_{wall}(\Psi_c)_{air,wall}\,(\mu_{en}/\rho)_{air,wall}}$$

$$\left[\frac{N_{D,wat}(C)}{N_{K,air}(C)}\right]_{theo} = \frac{{}_{wall}(\Psi_c)_{wat,wall}\cdot {}_{air}(\Psi_c)_{wat,air}}{{}_{wall}(\Psi_c)_{air,wall}}(\mu_{en}/\rho)_{wat,air} \quad (1)$$

4.2.2. Absorbed dose to water determination by the methods used by Zeiss for the INTRABEAM® dosimetry

The methods followed by Zeiss for INTRABEAM® dosimetry are described in section 1.4.2.3. The calibration coefficients, in terms of absorbed dose to water, are based on the calibration of the ionization chamber, in terms of air kerma (or exposure), using the formula:

$$\left[\frac{N_{D,wat}(C')}{N_{K,air}(C')}\right]_{Zeiss} = (\mu_{en}/\rho)_{wat,air} \quad (2)$$

The reference point C′, is taken in the cavity in contact with the entrance window. Moreover, for the Non-TARGIT method, the conversion factor $\boldsymbol{K_{K_{air}\rightarrow D_w}}$ which has a constant value of 1.036, has to be added to the right side of expression (2)

At this stage, we will omit the problems associated with the use of the chamber holder for measurements in the water phantom while it is not included during calibration in air.

4.2.3. Comparison between the two methods (expressions 1 and 2)

The reference points, C and C', are considered at two different positions. Thus, to use the same reference point, C′, a correction factor ($e^{\mu' x}$) is applied to the numerator and denominator of expression (1) where μ' is the effective attenuation coefficient in water and air, respectively, and *x*, corresponds to the half thickness of the chamber air cavity. This correction factor compensates, for water, the ${}_{air}(\Psi_c)_{wat,air}$ term while it is considered negligible for air (low attenuation in 0.5 mm thickness in air). The change in the photon energy fluence between C and C' due to the different distance from the source, the ($1/r^2$) effect, on expression (1) has no

effect on expression (1) since it is introduced in the numerator as well as in the denominator. So, the comparison between relations (1) and (2) can be written as:

$$\left[\frac{N_{D,wat}(C')}{N_{K,air}(C')}\right]_{theo} \Big/ \left[\frac{N_{D,wat}(C')}{N_{K,air}(C')}\right]_{Zeiss} \approx \frac{{}_{wall}(\Psi_c)_{wat,wall}}{{}_{wall}(\Psi_c)_{air,wall}}$$

The back and lateral walls in plastic of the chamber (surrounding the cavity) are thick (~ 1 cm for the back wall). Therefore, the replacement of air by plastic can provoke a significant rise in the absorbed dose in the air cavity due to the contribution from photons scattered and backscattered in the surrounding walls (back and lateral). The associated correction factor ${}_{wall}(\Psi_c)_{air,wall}$ can hence have a significant value inferior to 1. On the other hand, the perturbation in the photon energy fluence due to the replacement of water by plastic, should have a value remaining close to 1 since the mass densities of the two materials are close, the correction factor ${}_{wall}(\Psi_c)_{wat,wall}$should then have a value close to 1.

These two photon fluence perturbation correction factors ${}_{wall}(\Psi_c)_{air,wall}$ and ${}_{wall}(\Psi_c)_{wat,wall}$ are not present in the relation used by Zeiss, introducing a bias in their method. In view of the above considerations, this should lead for them to a significant underestimation of the calibration coefficient in terms of absorbed dose to water.

4.2.4. Conclusions on the comparison

According to the comparison just discussed above, the $\left[N_{D,wat}(C')/N_{K,air}(C')\right]_{Zeiss}$ value is anticipated to be significantly inferior to $\left[N_{D,wat}(C')/N_{K,air}(C')\right]_{theo}$. Therefore, this will lead to an underestimated absorbed dose to water value by Zeiss; obtained by the application of the calibration coefficient in air kerma (or exposure) for the PTW 23342 ionization chamber. To confirm this conclusion and give an order of magnitude, a MC calculation of the ${}_{wall}(\Psi_c)_{air,wall}$ term was realized, for the PTW 23342 chamber.

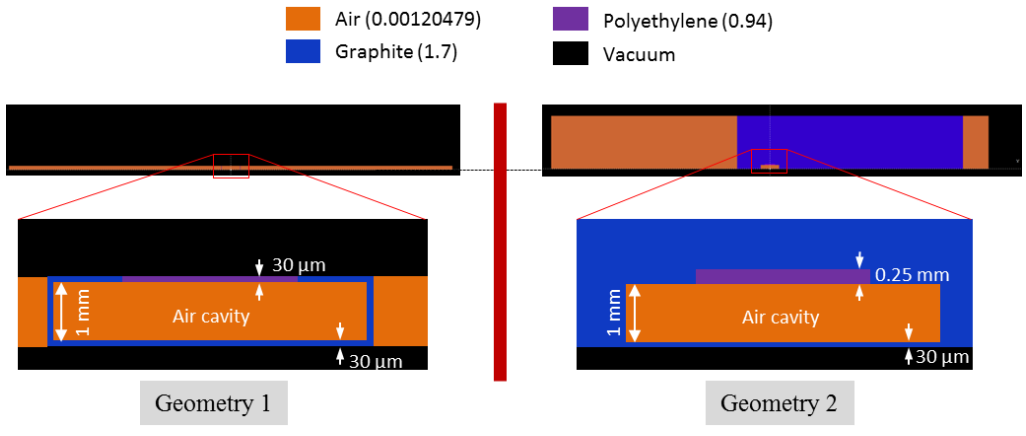

Geometry 1		Geometry 2		${}_{wall}(\Psi_c)_{air,wall} = E_{dep,G1}/E_{dep,G2}$
$E_{dep,G1}$	u (%)	$E_{dep,G2}$	u (%)	0.8734 ± 0.0064
2.3820E-04	0.50	2.7273E-04	0.54	

Figure 4.1.The two considered geometries in the MC calculations with the deposited energy calculated in the corresponding air cavity, the values between brackets beside the materials labels are their corresponding mass densities in [g.cm^{-3}].

The geometries and materials considered in the calculation models are as detailed in Figure 4.1. The term ${}_{\text{wall}}(\Psi_c)_{\text{air,wall}}$ is determined by calculating the ratio of deposited energies, in the air cavities, in the first and second geometries. The first geometry represents the flawless case were the chamber walls surrounding the air cavity are almost eliminated; the 30 µm walls are sufficient to establish the TCPE and their attenuation of the photon energy fluence is negligible. The second geometry represents the real case where the cavity is surrounded by the chamber walls.

The calculated ratio was of 0.8734 ± 0.0064 which indicates a significant difference between the two cases. This ratio means that the chamber walls increases the deposited dose in the cavity by 14.5 % (1/0.8734 = 1.145). Thus, since the ${}_{\text{wall}}(\Psi_c)_{\text{wat,wall}}$ value is estimated close to unity, the absorbed dose to water value estimated by the theoretical method can be expected to be higher, by the same order of magnitude (~ 15 %), than the value obtained by the method adopted by Zeiss as follows:

$$\left[\frac{N_{\text{D,wat}}(C')}{N_{\text{K,air}}(C')}\right]_{\text{theo}} \Big/ \left[\frac{N_{\text{D,wat}}(C')}{N_{\text{K,air}}(C')}\right]_{\text{Zeiss}} \approx \frac{{}_{\text{wall}}(\Psi_c)_{\text{wat,wall}}}{{}_{\text{wall}}(\Psi_c)_{\text{air,wall}}} \approx \frac{1}{0.8734} \approx \mathbf{1.15}$$

Due to the lack of precise knowledge of the geometry of the modeled PTW 23342 ionization chamber, this result gives only an order of magnitude, but it strengthens the first conclusions of the comparisons.

Regarding the Non-TARGIT method, the dose data and information concerning this method was received very recently which limited the time for a thorough analysis. However, the ionization chamber used in this new method, i.e. PTW 34013, has smaller dimensions (width: 10 mm, depth: 8 mm and length: 50 mm) with an air cavity of 0.9 mm, 30 µm polyethylene entrance window (same as for the PTW 23342), and thinner lateral and back walls. Thus, the same effects of the chamber walls around the cavity are expected, but with a decreased quantitative impact.

The previous two sections considered the INTRABEAM® doses at a single point. To extend the comparisons over the whole dose distribution, the relative dose distributions defined by the LNHB using the dosimetric gel, as determined in chapter 3, were compared to the corresponding data delivered by Zeiss as presented in the next section.

4.3.Confrontation of the absolute dose distributions established in the present work with the ones delivered by the Zeiss Company

This section merges the previously obtained results to assess the absolute dose distribution around the IB-XRS associated with a 4 cm spherical applicator. Purposely, the dosimetric reference in terms of absorbed dose to water rate at 1 cm depth in water along the axial plane, as determined in chapter 2, was applied to calibrate the relative dose distributions in water obtained in chapter 3. At last, the absolute dose distributions, obtained in this study, were compared to that delivered by the Zeiss Company, along with the INTRABEAM® system, for the same irradiation conditions.

4.3.1. Determination of absolute dose distributions

In order to turn into absolute absorbed dose distributions in water, the relative ones determined in the axial and transverse planes, around an IB-XRS associated to a 4 cm spherical applicator, the reference absorbed dose value at a 1 cm depth in water $\dot{D}_{\mathrm{w,1cm}}$, determined in chapter 2 for the same IB-XRS and applicator, was used. This $\dot{D}_{\mathrm{w,1cm}}$ was defined at 1 cm in water along the axial plane. Consequently, all the dose values D_{W} (in the two planes) determined using the dosimetry gel were normalized to the dose value at this reference point i.e. the dose value at 1 cm distance from the applicator sphere in the axial plane. However, since this value was not defined, as a specific dose point, on the relative dose distribution, its value was calculated after the definition of the exponential fit curve of the relative dose distribution in the axial plane. Finally, after all relative doses were normalized to the reference relative dose at 1 cm, they were multiplied by the $\dot{D}_{\mathrm{w,1cm}}$ and the total irradiation time in seconds, given in section 3.2.1. The absolute dose D at point located at distance z [cm] is determined using the following equation:

$$D\ (z)\ [Gy] = \frac{D_{relative}(z)}{D_{relative}(1\ \text{cm in axial plane})} \times \dot{D}_{\mathrm{w,1cm}}[Gy.s^{-1}] \times irradiation\ time\ [s]$$

The absolute dose distributions, in the considered axial and transverse planes, are presented and compared, in next section, to the one provided by the INTRABEAM® system in water for the same irradiation conditions.

4.3.2. Comparison of the dose distributions of the current study to the one delivered by ZEISS

The comparisons between the absolute dose distributions determined in the current study, in the two considered planes based on the relative dose distributions determined by the dosimetric gel, to the one delivered by the INTRABEAM® system for the same irradiation conditions are presented in Figure 4.2.

In the two planes, the absolute dose profiles determined in the current study showed a significant difference. This difference tends to increase as approaching the applicator sphere surface. The difference between the dose value delivered by the INTRABEAM® at the applicator surface and the one obtained in this study, attained by exponential extrapolation over the measured points, is in the order of 10 Gy (a factor of 1.5) in the axial plane and 6 Gy in the transverse plane (a factor of 1.3).

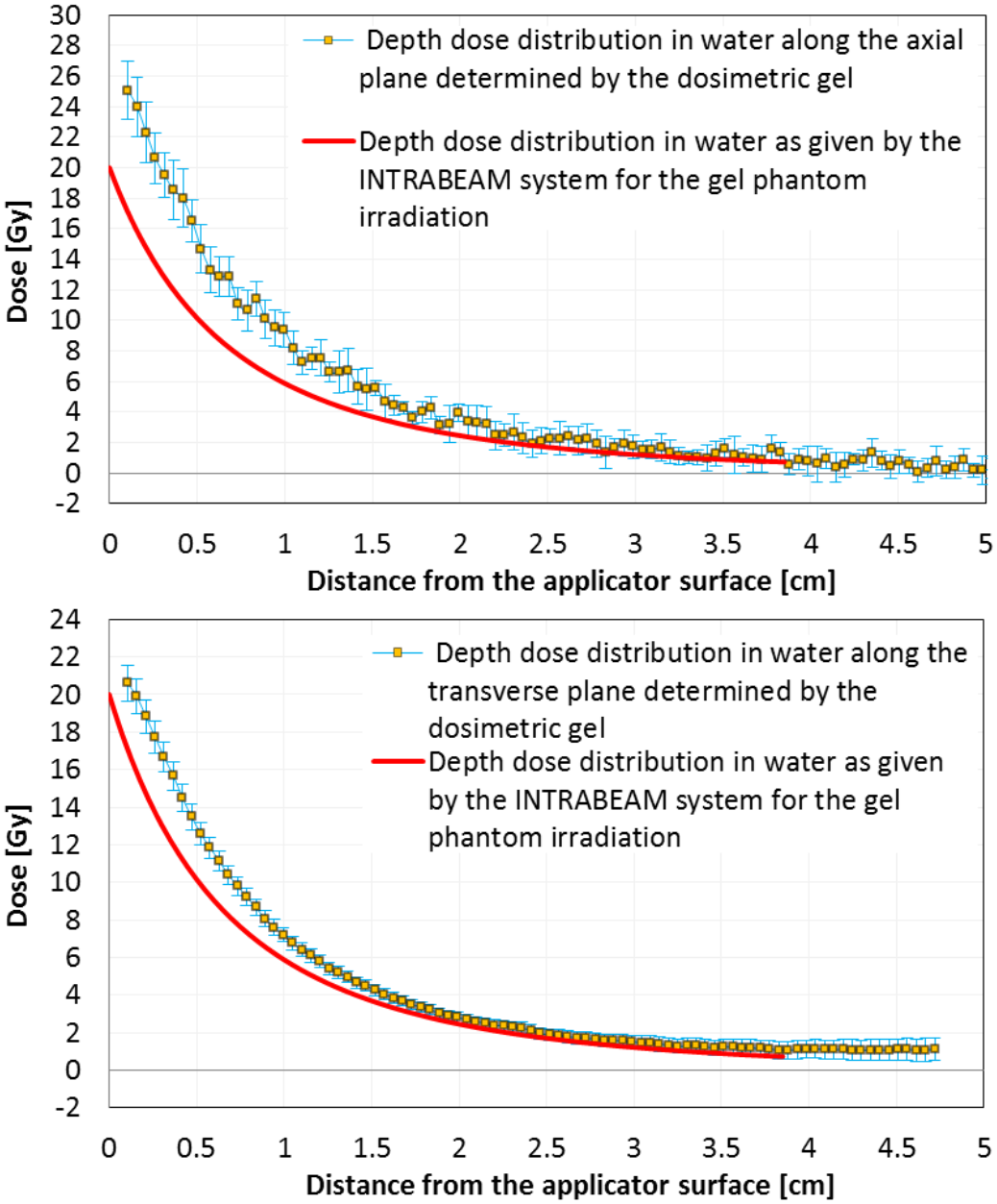

Figure 4.2. The absolute absorbed dose distributions in water, in the axial (top) and transverse (bottom) planes, determined by the dosimetric gel phantom irradiated by the IB-XRS with 4 cm spherical applicator for a dose at the applicator surface of 20 Gy relying on the data provided by ZEISS. Those distributions are compared to the one delivered by the INTRABEAM® for the same irradiation conditions.

Summary

At each calibration period of an INTRABEAM® system, Zeiss updates the dose distribution in water, for the bare IB-XRS. Recently, Zeiss started to provide the dose distributions obtained for the same system by the novel Non-TARGIT method in addition to the original one based on the TARGIT method. However, no clear statement was given by Zeiss about the methodology that delivers the new "right" dose value.

The absorbed dose to water values delivered by Zeiss, for the INTRABEAM® X-Ray source, are probably underestimated. The separate comparisons of the values determined by two primary laboratories, i.e. the LNHB and the PTB, to those delivered by Zeiss for the corresponding INTRABEAM® system under different configurations (i.e. with applicator for the LNHB, and without applicator for the PTB) showed significant dose differences (in the order of 16 % - 62 %). The difference becomes more important when approaching the source due to the steep dose profile and higher impact of the associated uncertainty on the measured source-to-detector distance. However, the doses given by Zeiss based on the novel Non-TARGIT method are closer to the reference dose values determined by the LNHB and PTB when compared to the original TARGIT method.

The Zeiss TARGIT approach to determine the absorbed dose to water, from a calibration in air kerma of a transfer ionization chamber PTW-23342, was evaluated. The evaluation was initiated by a qualitative comparison to an approach based on a generalized cavity theory formalized at LNHB. A significant difference between the two methods was found to be caused by a contribution to the absorbed dose in the chamber cavity of photons scattered in the chamber walls, which is not taken into account by the TARGIT method. This effect was quantified by carrying out Monte Carlo calculations for the PTW-23342 chamber. The estimated absorbed dose–to-water value was found higher by almost 15 % (order of magnitude) than the value obtained by the TARGIT method. This large difference is due to the substantial wall thickness of this chamber. However, due to the lack of precise knowledge of the geometry of the modeled PTW-23342 ionization chamber, this result gives only an order of magnitude, but it still strengthens the first conclusions about the underestimation of Zeiss dose values.

Regarding the Non-TARGIT method, the ionization chamber used in this new method, i.e. PTW 34013, is smaller with thinner walls. Thus, the same effects around the cavity are expected, but with a decreased quantitative impact. Due to the lack of precise information presently available on the Non-TARGIT method, no definitive conclusion can be given on this method, and the origin of the remaining discrepancies are still to be investigated in further studies.

The comparisons between the absolute dose distributions, those determined in the current study to that delivered by the INTRABEAM® system, showed a significant difference. This difference tends to increase as approaching the applicator sphere surface. The difference at the applicator surface is in the order of 10 Gy (a factor of 1.5) in the axial plane and 6 Gy in the transverse plane (a factor of 1.3).

General Conclusion and perspectives

The current study helped to outline several issues concerning the dosimetry in the low energy photon range (≤ 50 keV), and more specifically, with electronic brachytherapy systems (eBT) as the INTRABEAM source manufactured by the Zeiss Company.

A methodology for the primary dosimetry has been proposed in terms of absorbed dose to water at 1 cm depth in water from the eBT source, which is the recommended dosimetric quantity for such systems. This methodology was applied to the INTRABEAM® X-Ray source associated with a 4 cm spherical applicator, for which, the dosimetric reference was established on the source probe axis.

Due to the impossibility to bring together at the same place the INTRABEAM system and the LNHB primary instrument for low-energy photons, a six-step methodology was developed to establish and transfer a dosimetric reference in terms of absorbed dose to water at 1 cm in water. The two first steps consisted in the characterization of the photon energy spectrum of the considered IB-XRS configuration and in the demonstration of the possibility to reproduce it at LNHB using a conventional X-Ray generator with appropriate filtrations. Throughout the third step, the reproduced photon beam was characterized in terms of air kerma rate using a primary standard free-air ionization chamber, developed at LNHB in a previous work and dedicated to the considered energy range. The use of this primary standard required to determine the appropriate factor correcting for the presence of the chamber, instead of air, in the reference beam. This was done by two methods leading to compatible results: A conventional method based on measurements and calculations of separate factors, the second method is based on MC calculation of a single global factor. The reproduced beam, once characterized in air kerma rate, was employed in the fourth step to calibrate a PTW 23342 cavity ionization chamber. Subsequently, this chamber was used as a transfer instrument, during the fifth step, to calibrate the IB system at the Saint-Louis hospital in Paris associated with a 4 cm spherical applicator. In the sixth and last step, an equivalent MC model of the IB-XRS configuration under study was performed in order to calculate a conversion factor, from air kerma to absorbed dose to water at 1 cm distance from the considered IB spherical applicator surface along the IB-XRS probe axis.

Once a dosimetric standard was established to determine the absolute absorbed dose rate to water at a point in water around the IB-XRS for a given configuration, a relative measurement of the 3D absorbed–dose-to-water distribution was still required to finally deduce the dose spatial distribution around the IB-XRS under the considered configurations. This was achieved using gel dosimetry since it is the only dosimeter capable of providing dose distribution in the three dimensions without data inter- or extra-polation. The dosimetric gel system used was a Fricke-based hydrogel read by Magnetic Resonance Imaging (MRI). The MRI was chosen as the associated readout system due to its availability for this study. A methodology was proposed to calibrate the MRI response of the gel dosimeter in the considered energy and dose ranges. This was then applied to determine the relative profiles of absorbed dose to gel around the considered INTRABEAM® system configuration in the axial and transverse planes including its probe tip. Prior to any analysis of irradiated gel, the homogeneity of the gel response in the used coil (namely the head coil of the radiology service of the SHFJ hospital in Orsay) was characterized and correction factors were established when necessary.

The dependence on dose and energy of the MRI response of the used dosimetric gel was examined in the low-energy X-ray range (≤ 50 keV) using both the N20 and CCRI50b photon beams. Indeed, these two RX standard beams were the only available and suitable in terms of energy range and dose rate range; to avoid ionic diffusion within the gel. Even though no solid conclusion could be given on the energy dependence because of high associated statistical uncertainties on the obtained results, there were sufficient data to show that an independent energy relation between the absorbed dose to gel and the variation of the relaxation rate could be considered as a first approach. Furthermore, as a precaution, the calibration function was derived only from data related to the CCRI50b beam since its energy distribution is very close to the one of the considered IB-XRS configuration. Doing so, a polynomial calibration relation was obtained for the gel response as a function of the absorbed dose. The calibrated dosimetric gel was then used to determine the profiles of absorbed dose to gel around the considered INTRABEAM® system configuration in the axial and transverse axes. The comparison of the resulting relative dose profiles with the MC calculated ones showed a good agreement, thus comforting the overall adopted methodology. The profiles of absorbed dose to gel were then converted into profiles of absorbed dose to water using MC calculations; since it is the conventional quantity of interest in radiotherapy. At last, the good agreement between the relative profiles of absorbed dose to water assessed in the two axes of the IB-XRS configuration and those calculated by MC demonstrated that dosimetric gels, calibrated in this way, were reliable tools to evaluate the relative dose distributions around eBT systems. Those relative dose distribution have, thus, been combined with the absorbed dose reference value at 1 cm depth, to calculate the absolute spatial distribution of absorbed dose to water.

All the dosimetric data obtained by LNHB for the IB-XRS of the Saint-Louis hospital, associated to a 4 cm spherical applicator, were compared to those provided by Zeiss for the same system. At this point, it has to be noticed that the data provided by Zeiss were recently changed. Actually, in addition to their regular dose distribution data based on the initial dosimetry with the TARGIT method, Zeiss started very recently (since 2017) to provide also the dose distributions obtained for the same system by the novel Non-TARGIT method. Now, in both cases, it turns out that the data provided by Zeiss are significantly lower than those obtained through the present study. While there is a good agreement between the relative absorbed dose profiles obtained by LNHB and those delivered by the INTRABEAM® TARGIT method, the difference lies in the absolute values. For example, at the applicator's surface, the ratios of LNHB to the TARGIT method values are of about 1.5 and 1.3 in the axial and transverse axes, respectively. Explicitly, considering the IB-XRS with a 4 cm spherical applicator, the absolute absorbed dose to water rate value provided by LNHB show differences in the order of 33 % and 16 % to those delivered by Zeiss through the TARGIT and non-TARGIT methods, respectively, under the same reference conditions (at 1 cm depth in water). Since no clear statement was communicated, so far, by Zeiss about the methodology that delivers the new "right" dose value, one can however notice that the doses given by Zeiss based on the novel Non-TARGIT method are closer to the reference dose value determined by the LNHB. Consistent observations and conclusions can be also drawn from a separate comparison performed by the PTB laboratory with data provided by Zeiss under a different configuration; INTRABEAM® system without any applicator. In this latter comparison, the PTB and the Zeiss dosimetric data show differences in the order of 62 % to 22 % with the TARGIT and non-TARGIT values, respectively. Since differences in absorbed dose to water values are expected to become more important when approaching the source due to both the steep dose profile and

higher impact of the associated uncertainty on the measured source-to-detector distance, it is not surprising that the INTRABEAM® configuration considered by the PTB leads to higher differences than the one studied by the LNHB. In both cases, the independent comparisons demonstrate that the absorbed dose to water values delivered by Zeiss are probably underestimated. In addition, the Zeiss TARGIT approach, based on the derivation of the absorbed dose to water from measurements performed in water, with a transfer ionization chamber PTW-23342 calibrated in terms of air kerma, was analyzed in the present study. The analysis consisted first in a qualitative comparison to an approach based on a generalized cavity theory formalized at LNHB. It was found that the contribution of photons scattered in the chamber walls, to the absorbed dose in the chamber cavity, was not taken into account by the TARGIT method. This default was quantified, in this study, by carrying out Monte Carlo calculations for the PTW 23342 chamber. The estimated absorbed dose–to-water value was found higher by almost 15 % (order of magnitude) than the value obtained by the TARGIT method. This large difference results from the substantial wall thickness of this chamber. However, due to the lack of precise knowledge of the geometry of the modeled PTW 23342 ionization chamber, this result gives only an order of magnitude, yet it still strengthens the first conclusions about the underestimation of Zeiss dose values. Regarding the Non-TARGIT method, the ionization chamber used, i.e. PTW 34013, is smaller with thinner walls. Thus, although the same effect is expected, its quantitative impact should be smaller. Due to the lack of precise information presently available on the Non-TARGIT method, no definitive conclusion can be given on this method, and the origins of the remaining discrepancies are still to be investigated in further studies.

In the course of this study, several issues and error sources concerning the dosimetry of eBT systems were revealed, in addition to some proposed eventual solutions. Even if the work presented here does not lead yet to possibilities of transferring the dosimetric reference to the users of eBT systems, it strongly participated to evaluate the data provided by the Zeiss Company throughout the performed comparisons. This work was part of a project funded by the Laboratoire National de Métrologie et d'Essais (LNE) that will be carried on. The LNHB laboratory will take benefit of this ongoing study to confirm the present results and consolidate their uncertainty budget. Nevertheless, the transfer of the developed reference to hospital users will require addressing several issues. Among others, the absolute dose distribution measurements obtained here will have to be compared with other methods, i.e using radiochromic films calibrated according to a proper procedure in LNHB reference beams. A comparison between primary standards of several national metrology laboratories would be necessary to ensure the international traceability of these new standards. As the German PTB laboratory has been working on the establishment of a primary standard for the bare IB-XRS probe since 2012 through the European Project EURAMET MetrExtRT", it stands, with LNHB, among the European national metrology laboratories likely to work on this comparison. To proceed with the investigations conducted by the LNHB on the causes of discrepancies of the two methods of the manufacturer (TARGIT and non-TARGIT), it would be worthy to encourage the PTW Company to communicate the precise composition and design of their two ionization cavity chambers PTW 23342 and PTW 34013 for improving the precision of MC calculations. Once the final dosimetric reference established and consolidated through international comparisons, the transfer method to users will be planned. For this purpose, the help of medical physicists will be required to define adapted transfer conditions, for providing a calibration service to eBT users in radiotherapy services.

References

1. E. B. Podgorsak, "Radiation oncology physics," Handb. Teach. Stud. Podgorsak–Vienna Int. At. Energy Agency **657**, (2005).
2. L. L. Gunderson, C. G. Willett, L. B. Harrison, and F. A. Calvo, *Intraoperative Irradiation: Techniques and Results* (Springer Science & Business Media, 1999).
3. C. C. Park, S. S. Yom, M. B. Podgorsak, E. Harris, R. A. Price Jr., A. Bevan, J. Pouliot, A. A. Konski, and P. E. Wallner, "American Society for Therapeutic Radiology and Oncology (ASTRO) Emerging Technology Committee Report on Electronic Brachytherapy," Int. J. Radiat. Oncol. **76**, 963–972 (2010).
4. J. S. Vaidya, D. J. Joseph, J. S. Tobias, M. Bulsara, F. Wenz, C. Saunders, M. Alvarado, H. L. Flyger, S. Massarut, W. Eiermann, M. Keshtgar, J. Dewar, U. Kraus-Tiefenbacher, M. Sütterlin, L. Esserman, H. M. Holtveg, M. Roncadin, S. Pigorsch, M. Metaxas, M. Falzon, A. Matthews, T. Corica, N. R. Williams, and M. Baum, "Targeted intraoperative radiotherapy versus whole breast radiotherapy for breast cancer (TARGIT-A trial): an international, prospective, randomised, non-inferiority phase 3 trial," The Lancet **376**, 91–102 (2010).
5. U. Kraus-Tiefenbacher, L. Bauer, T. Kehrer, B. Hermann, F. Melchert, and F. Wenz, "Intraoperative Radiotherapy (IORT) as a Boost in Patients with Early-Stage Breast Cancer – Acute Toxicity," Oncol. Res. Treat. **29**, 77–82 (2006).
6. Haute Autorité de Santé, *Radiothérapie de contact - rapport d'évaluation technologique.* (HAS, 2008).
7. G. Lofts, *Jacaranda Physics 1, 2nd Edition*, John Wiley & Sons Australia Ltd (2003).
8. J. A. Seibert, "X-Ray Imaging Physics for Nuclear Medicine Technologists. Part 1: Basic Principles of X-Ray Production," J. Nucl. Med. Technol. **32**, 139–147 (2004).
9. V. Filip, L. D. Filip, and F. Okuyama, "Miniature x-ray tubes: current state and future prospects," J. Instrum. **8**, T03005 (2013).
10. N. de Jonge and J.-M. Bonard, "Carbon nanotube electron sources and applications," Philos. Trans. R. Soc. Lond. Math. Phys. Eng. Sci. **362**, 2239–2266 (2004).
11. D. J. Eaton, "Electronic brachytherapy—current status and future directions," Br. J. Radiol. **88**, 20150002 (2015).
12. S. Richardson, J. Garcia-Ramirez, W. Lu, R. J. Myerson, and P. Parikh, "Design and dosimetric characteristics of a new endocavitary contact radiotherapy system using an electronic brachytherapy source," Med. Phys. **39**, 6838–6846 (2012).
13. Y. Rong and J. S. Welsh, "Surface applicator calibration and commissioning of an electronic brachytherapy system for nonmelanoma skin cancer treatmenta)," Med. Phys. **37**, 5509–5517 (2010).
14. A. Dickler, M. C. Kirk, A. Coon, D. Bernard, T. Zusag, J. Rotmensch, and D. E. Wazer, "A dosimetric comparison of Xoft Axxent Electronic Brachytherapy and iridium-192 high-dose-rate brachytherapy in the treatment of endometrial cancer," Brachytherapy **7**, 351–354 (2008).
15. T. Garcia-Martinez, J.-P. Chan, J. Perez-Calatayud, and F. Ballester, "Original paperDosimetric characteristics of a new unit for electronic skin brachytherapy," J. Contemp. Brachytherapy **6**, 45–53 (2014).
16. R. M. Douglas, J. Beatty, K. Gall, R. F. Valenzuela, P. Biggs, P. Okunieff, and F. S. Pardo, "Dosimetric results from a feasibility study of a novel radiosurgical source for irradiation of intracranial metastases," Int. J. Radiat. Oncol. Biol. Phys. **36**, 443–450 (1996).
17. D. J. Eaton, "Quality assurance and independent dosimetry for an intraoperative x-ray device," Med. Phys. **39**, 6908–6920 (2012).
18. S. Potemin, I. Uvarov, and I. Vasilenko, "Intraoperative radiotherapy in locally-advanced and recurrent rectal cancer: retrospective review of 68 cases," Transl. Cancer Res. **4**, 189–195 (2015).

19. F. Wenz, F. Schneider, C. Neumaier, U. Kraus-Tiefenbacher, T. Reis, R. Schmidt, and U. Obertacke, "Kypho-IORT - a novel approach of intraoperative radiotherapy during kyphoplasty for vertebral metastases," Radiat. Oncol. Lond. Engl. **5**, 11 (2010).
20. F. Schneider, S. Clausen, J. Thölking, F. Wenz, and Y. Abo-Madyan, "A novel approach for superficial intraoperative radiotherapy (IORT) using a 50 kV X-ray source: a technical and case report," J. Appl. Clin. Med. Phys. **15**, 167–176 (2014).
21. A. B. Cognetta, B. M. Howard, H. P. Heaton, E. R. Stoddard, H. G. Hong, and W. H. Green, "Superficial x-ray in the treatment of basal and squamous cell carcinomas: A viable option in select patients," J. Am. Acad. Dermatol. **67**, 1235–1241 (2012).
22. K. R. Muralidhar, B. K. Rout, A. Mallikarjuna, A. Poornima, and P. N. Murthy, "Commissioning and quality assurances of the Intrabeam Intra-Operative radiotherapy unit," Int. J. Cancer Ther. Oncol. **2**, (2014).
23. P. M. Härtl, B. Dobler, O. Kölbl, and M. Treutwein, "[Practical dosimetry and constancy check at introduction of intraoperative radiotherapy with Intrabeam (Zeiss)]," Z. Med. Phys. **19**, 288–293 (2009).
24. U. Kraus-Tiefenbacher, A. Scheda, V. Steil, B. Hermann, T. Kehrer, L. Bauer, F. Melchert, and F. Wenz, "Intraoperative radiotherapy (IORT) for breast cancer using the intrabeam™ system," Tumori **91**, 339 (2005).
25. Carl ZEISS, "Document: INTRABEAM® Spherical Applicators Version 11.0," (2015).
26. D. J. Eaton and S. Duck, "Dosimetry measurements with an intra-operative x-ray device," Phys. Med. Biol. **55**, N359 (2010).
27. D. J. Thomas, "ICRU report 85: fundamental quantities and units for ionizing radiation," Radiat. Prot. Dosimetry **150**, 550–552 (2012).
28. M. Boutillon and A. M. Perroche-Roux, "Re-evaluation of the W value for electrons in dry air," Phys. Med. Biol. **32**, 213 (1987).
29. D. W. O. Rogers, "Introduction to Radiological Physics and Radiation Dosimetry by F. H. Attix," Med. Phys. **14**, 692–692 (1987).
30. P. Andreo, D. Burns, K. Hohlfeld, M. S. Huq, T. Kanai, F. Laitano, V. Smyth, and S. Vynckier, "Absorbed dose determination in external beam radiotherapy: an international code of practice for dosimetry based on standards of absorbed dose to water," IAEA TRS **398**, (2000).
31. E. B. Podgorsak, *Radiation Physics for Medical Physicists* (Springer, 2016).
32. Netherlands Commission on Radiation Dosimetry, "Dosimetry of low and medium energy x-rays A code of practice for use in radiotherapy and radiobiology - Report 10 on radiation dosimetry," http://radiationdosimetry.org/files/documents/0000033/79-ncs-rapport-10-dosimetry-of-low-and-medium-energy-xrays.pdf.
33. J. R. Greening, *Fundamentals of Radiation Dosimetry, Second Edition* (CRC Press, 1985).
34. G. Alm-Carlsson, D. Dance, L. DeWerd, H. Kramer, K. Ng, F. Pernicka, and P. Ortiz-Lopez, "Dosimetry in diagnostic radiology: an International code of practice," Int. At. Energy Agency Tech. Rep. Ser. (2007).
35. D. T. Burns and L. Büermann, "Free-air ionization chambers," Metrologia **46**, S9 (2009).
36. W. Ksouri, *Manuscrit de Thése, Étude et Réalisation Des Références Dosimétriques Nationales En Termes de Kerma Dans l'air Pour Les Faisceaux de Rayons X de Basses et Moyennes Énergies* (Nice, 2008).
37. T. Sander, "Air kerma and absorbed dose standards for reference dosimetry in brachytherapy," Br. J. Radiol. **87**, (2014).
38. C. K. Ross and N. V. Klassen, "Water calorimetry for radiation dosimetry," Phys. Med. Biol. **41**, 1 (1996).
39. B. Rapp, N. Perichon, M. Denoziere, J. Daures, A. Ostrowsky, and J.-M. Bordy, "The LNE-LNHB water calorimeter for primary measurement of absorbed dose at low depth in water: application to medium-energy x-rays," Phys. Med. Biol. **58**, 2769 (2013).

40. A. Krauss, L. Büermann, H.-M. Kramer, and H.-J. Selbach, "Calorimetric determination of the absorbed dose to water for medium-energy x-rays with generating voltages from 70 to 280 kV," Phys. Med. Biol. **57**, 6245 (2012).
41. PTW 23342 0.02cc Soft X-Ray Chamber - Radiation Products Design, Inc., "PTW 23342 0.02cc Soft X-Ray Chamber - Radiation Products Design, Inc.," http://www.rpdinc.com/ptw-23342-002cc-soft-x-ray-chamber-964.html.
42. "PTW User Manual. Soft-X-Ray Chambers Type 34013, Type 23342 and Type 23344. D564.131.00/03.," (2009).
43. O. Ávila, E. Ramírez-Barbosa, and I. Gamboa-deBuen, "Energy dependence of TLD-900 dosimeters exposed to low energy X-rays," Radiat. Meas. **71**, 127–132 (2014).
44. A. A. Nunn, S. D. Davis, J. A. Micka, and L. A. DeWerd, "LiF:Mg,Ti TLD response as a function of photon energy for moderately filtered x-ray spectra in the range of 20–250 kVp relative to C60o," Med. Phys. **35**, 1859–1869 (2008).
45. G. H. Hartmann, W. Schlegel, and H. Scharfenberg, "The three-dimensional dose distribution of 125I seeds in tissue," Phys. Med. Biol. **28**, 693 (1983).
46. R. Hill, B. Healy, L. Holloway, Z. Kuncic, D. Thwaites, and C. Baldock, "Advances in kilovoltage x-ray beam dosimetry," Phys. Med. Biol. **59**, R183 (2014).
47. V. K. Nelson and R. F. Hill, "Backscatter factor measurements for kilovoltage X-ray beams using thermoluminescent dosimeters (TLDs)," Radiat. Meas. **46**, 2097–2099 (2011).
48. S. Devic, "Radiochromic film dosimetry: Past, present, and future," Phys. Med. **27**, 122–134 (2011).
49. Azam Niroomand-Rad, Charles R. Blackwell, Bert M. Coursey, Kenneth P. Gall, James M. Galvin, William L. McLaughlin, Ali S. Meigooni, Ravinder Nath, James E. Rodgers, and Christopher G. Soares, "AAPM Report No. 63 Radiochromic Film Dosimetry," https://www.aapm.org/pubs/reports/rpt_63.pdf.
50. M. A. Ebert, A. H. Asad, and S. A. Siddiqui, "Suitability of radiochromic films for dosimetry of low energy X-rays," J. Appl. Clin. Med. Phys. **10**, 232–240 (2009).
51. K. Armoogum and C. Watson, "A dosimetry intercomparison phantom for intraoperative radiotherapy," Z. Für Med. Phys. **18**, 120–127 (2008).
52. S.-T. Chiu-Tsao, Y. Ho, R. Shankar, L. Wang, and L. B. Harrison, "Energy dependence of response of new high sensitivity radiochromic films for megavoltage and kilovoltage radiation energies," Med. Phys. **32**, 3350–3354 (2005).
53. O. Croce, S. Hachem, E. Franchisseur, S. Marcié, J.-P. Gérard, and J.-M. Bordy, "Contact radiotherapy using a 50 kV X-ray system: Evaluation of relative dose distribution with the Monte Carlo code PENELOPE and comparison with measurements," Radiat. Phys. Chem. **81**, 609–617 (2012).
54. T. Bortfeld, A. L. Boyer, W. Schlegel, D. L. Kahler, and T. J. Waldron, "Realization and verification of three-dimensional conformal radiotherapy with modulated fields," Int. J. Radiat. Oncol. Biol. Phys. **30**, 899–908 (1994).
55. T. Bortfeld, "IMRT: a review and preview," Phys. Med. Biol. **51**, R363 (2006).
56. L. Schreiner and T. Olding, "Gel dosimetry AAPM Medical Physics Monograph No. 34: Clinical Dosimetry Measurements in Radiotherapy ed DW Rogers and JE Cygler (Madison, WI," (2009).
57. B. Winey, "Advances in Medical Physics," Med. Phys. **43**, 1583–1583 (2016).
58. L. J. Schreiner, "True 3D chemical dosimetry (gels, plastics): Development and clinical role," J. Phys. Conf. Ser. **573**, 012003 (2015).
59. M. Oldham, D. Godfrey, S. Das, and A. Wolbarst, "Advances in Medical Physics," (2014).
60. C. Baldock, Y. De Deene, S. Doran, G. Ibbott, A. Jirasek, M. Lepage, K. B. McAuley, M. Oldham, and L. J. Schreiner, "Topical Review: Polymer gel dosimetry," Phys. Med. Biol. **55**, R1–R63 (2010).
61. J. Gore, Y. Kang, and R. Schulz, "Measurement of radiation dose distributions by NMR imaging," Magn. Reson. Imaging **2**, 244 (1984).

62. A. Appleby, E. Christman, and A. Leghrouz, "Imaging of spatial radiation dose distribution in agarose gels using magnetic resonance," Med. Phys. **14**, 382–384 (1987).
63. K. Chu, K. Jordan, J. Battista, J. Van Dyk, and B. Rutt, "Polyvinyl alcohol-Fricke hydrogel and cryogel: two new gel dosimetry systems with low Fe3+ diffusion," Phys. Med. Biol. **45**, 955 (2000).
64. Y. Tseng, W. Chu, W. Chung, W. Guo, Y.-H. Kao, J. Wang, and S.-C. Huang, "The role of dose distribution gradient in the observed ferric ion diffusion time scale in MRI-Fricke-infused gel dosimetry," Magn. Reson. Imaging **20**, 495–502 (2002).
65. B. Gupta, U. Kini, R. Bhat, and U. Madhvanath, "Use of the FBX dosemeter for the calibration of cobalt-60 and high-energy teletherapy machines," Phys. Med. Biol. **27**, 235 (1982).
66. R. Kelly, K. Jordan, and J. Battista, "Optical CT reconstruction of 3D dose distributions using the ferrous–benzoic–xylenol (FBX) gel dosimeter," Med. Phys. **25**, 1741–1750 (1998).
67. F. Cavalcante, L. de Oliveira, A. de Almeida, and M. M. Vasques, "Fe+ 3 diffusion coefficient in Fricke xylenol gel through shielding half of a 6 MV photon beam field size," International Nuclear Atlantic Conference - INAC 2009 (2009).
68. M. Oldham, V. Khoo, C. Rowbottom, J. Bedford, and S. Webb, "A case study comparing the relative benefit of optimizing beam weights, wedge angles, beam orientations and tomotherapy in stereotactic radiotherapy of the brain," Phys. Med. Biol. **43**, 2123 (1998).
69. M. Lepage and K. Jordan, "3D dosimetry fundamentals: gels and plastics," J. Phys. Conf. Ser. **250**, 012055 (2010).
70. L. J. Schreiner, "Review of Fricke gel dosimeters," J. Phys. Conf. Ser. **3**, 9 (2004).
71. M. J. Maryanski, J. C. Gore, R. P. Kennan, and R. J. Schulz, "NMR relaxation enhancement in gels polymerized and cross-linked by ionizing radiation: a new approach to 3D dosimetry by MRI," Magn. Reson. Imaging **11**, 253–258 (1993).
72. C. Baldock, "Historical overview of the development of gel dosimetry: Another personal perspective," J. Phys. Conf. Ser. **164**, 012002 (2009).
73. P. M. Fong, D. C. Keil, M. D. Does, and J. C. Gore, "Polymer gels for magnetic resonance imaging of radiation dose distributions at normal room atmosphere," Phys. Med. Biol. **46**, 3105 (2001).
74. R. Senden, P. De Jean, K. McAuley, and L. Schreiner, "Polymer gel dosimeters with reduced toxicity: a preliminary investigation of the NMR and optical dose–response using different monomers," Phys. Med. Biol. **51**, 3301 (2006).
75. M. Lepage, P. M. Jayasakera, S. Å. J. Bäck, and C. Baldock, "Dose resolution optimization of polymer gel dosimeters using different monomers," Phys. Med. Biol. **46**, 2665 (2001).
76. L. J. Schreiner, T. Olding, and K. B. McAuley, "Polymer gel dosimetry," J. Phys. Conf. Ser. **250**, 012014 (2010).
77. J. Adamovics and M. J. Maryanski, "Characterisation of PRESAGE^{TM}: A new 3-D radiochromic solid polymer dosemeter for ionising radiation," Radiat. Prot. Dosimetry **120**, 107–112 (2006).
78. K. Jordan and N. Avvakumov, "Radiochromic leuco dye micelle hydrogels: I. Initial investigation," Phys. Med. Biol. **54**, 6773 (2009).
79. S. Babic, J. Battista, and K. Jordan, "Radiochromic leuco dye micelle hydrogels: II. Low diffusion rate leuco crystal violet gel," Phys. Med. Biol. **54**, 6791 (2009).
80. J. Vandecasteele, S. Ghysel, S. H. Baete, and Y. D. Deene, "Radio-physical properties of micelle leucodye 3D integrating gel dosimeters," Phys. Med. Biol. **56**, 627 (2011).
81. S. J. Doran, "The history and principles of optical computed tomography for scanning 3-D radiation dosimeters: 2008 update," J. Phys. Conf. Ser. **164**, 012020 (2009).
82. S. J. Doran and N. Krstajić, "The history and principles of optical computed tomography for scanning 3-D radiation dosimeters," J. Phys. Conf. Ser. **56**, 45 (2006).
83. M. Oldham, J. H. Siewerdsen, A. Shetty, and D. A. Jaffray, "High resolution gel-dosimetry by optical-CT and MR scanning," Med. Phys. **28**, 1436–1445 (2001).
84. M. Oldham, J. H. Siewerdsen, S. Kumar, J. Wong, and D. A. Jaffray, "Optical-CT gel-dosimetry I: Basic investigations," Med. Phys. **30**, 623–634 (2003).

85. M. Oldham and L. Kim, "Optical-CT gel-dosimetry II: Optical artifacts and geometrical distortion," Med. Phys. **31**, 1093–1104 (2004).
86. J. Vandecasteele and Y. D. Deene, "On the validity of 3D polymer gel dosimetry: III. MRI-related error sources," Phys. Med. Biol. **58**, 63 (2013).
87. Y. D. Deene, "How to scan polymer gels with MRI?," J. Phys. Conf. Ser. **250**, 012015 (2010).
88. C. Stien, "NT 14-41 (LNHB 2014/41): Dosimetric characteristics of a new gel dosimeter," (2014).
89. M. R. Pérez Cerquera, "Massively parallel method of moments for fast and reliable electromagnetic simulations for dielectric bodies and metals | banrepcultural.org," http://www.banrepcultural.org/blaavirtual/tesis/colfuturo/massively-parallel-method-of-moments-for-fast-and-reliable.
90. I. Aubineau-Lanièce, B. Chauvenet, D. Cutarella, J. Gouriou, J. Plagnard, and P. A. Lucas, "LNE–LNHB air-kerma and absorbed dose to water primary standards for low dose-rate 125 I brachytherapy sources," Metrologia **49**, S189 (2012).
91. J. Plagnard, "Comparison of measured and calculated spectra emitted by the X-ray tube used at the Gustave Roussy radiobiological service," X-Ray Spectrom. **43**, 298–304 (2014).
92. S. Deloule, *Ph.D. Thesis, Développement d'une Méthode de Caractérisation Spectrale Des Faisceaux de Photons d'énergies Inférieures à 150 KeV Utilisés En Dosimétrie* (Paris 11, 2014).
93. P Mayles, A Nahum, and J.C Rosenwald, "Handbook of Radiotherapy Physics: Theory and Practice," https://www.crcpress.com/Handbook-of-Radiotherapy-Physics-Theory-and-Practice/Mayles-Nahum-Rosenwald/p/book/9780750308601.
94. A. F. Bielajew, "Fundamentals of the Monte Carlo method for neutral and charged particle transport," Univ. Mich. (2001).
95. I. Kawrakow and D. Rogers, "The EGSnrc code system: Monte Carlo simulation of electron and photon transport," (2000).
96. S. Agostinelli, J. Allison, K. al Amako, J. Apostolakis, H. Araujo, P. Arce, M. Asai, D. Axen, S. Banerjee, and G. Barrand, "GEANT4—a simulation toolkit," Nucl. Instrum. Methods Phys. Res. Sect. Accel. Spectrometers Detect. Assoc. Equip. **506**, 250–303 (2003).
97. Los Alamos National Laboratory, "Monte Carlo N-Particle Transport Code System for Multiparticle and High Energy Applications, RSICC Computer Code, Collection Report CCC-715, LANL," http://www.mcnp.ir/admin/imgs/1354175991.C715.PDF.
98. Francesc Salvat, José M. Fernández-Varea, and Josep Sempau, "PENELOPE-2006: A Code System for Monte Carlo Simulation of Electron and Photon Transport, NEA-OCED," https://www.oecd-nea.org/science/pubs/2006/nea6222-penelope.pdf.
99. J. F. Almansa, R. Guerrero, F. M. O. Al-Dweri, M. Anguiano, and A. M. Lallena, "Dose distribution in water for monoenergetic photon point sources in the energy range of interest in brachytherapy: Monte Carlo simulations with PENELOPE and GEANT4," Radiat. Phys. Chem. **76**, 766–773 (2007).
100. B. Reniers, F. Verhaegen, and S. Vynckier, "The radial dose function of low-energy brachytherapy seeds in different solid phantoms: comparison between calculations with the EGSnrc and MCNP4C Monte Carlo codes and measurements," Phys. Med. Biol. **49**, 1569 (2004).
101. U. Chica, M. Anguiano, and A. M. Lallena, "Benchmark of penelope for low and medium energy X-rays," Phys. Med. **25**, 51–57 (2009).
102. X. Llovet L. Sorbier, C. S. Campos, E. Acosta, and F. Salvat, "Monte Carlo simulation of x-ray spectra generated by kilo-electron-volt electrons," J. Appl. Phys. **93**, 3844–3851 (2003).
103. D. Bote, X. Llovet, and F. Salvat, "Monte Carlo simulation of characteristic x-ray emission from thick samples bombarded by kiloelectronvolt electrons," J. Phys. Appl. Phys. **41**, 105304 (2008).
104. F. Tola, B. Poumarede, M. Gmar, and B. Habib, "Optimization of Monte Carlo codes PENELOPE 2006 and PENFAST by parallelization and reduction variance implementation," in (2009).

105. I. BIPM, I. IFCC, I. IUPAC, and O. ISO, "The international vocabulary of metrology—basic and general concepts and associated terms (VIM), 3rd edn. JCGM 200: 2012," JCGM Jt. Comm. Guid. Metrol. (2008).
106. T. Quinn, "The Metre Convention and world-wide comparability of measurement results," Accreditation Qual. Assur. **9**, 533–538 (2004).
107. P. J. Allisy, D. T. Burns, and P. Andreo, "International framework of traceability for radiation dosimetry quantities," Metrologia **46**, S1 (2009).
108. T. IAEA, "No. 277," Absorbed Dose Determ. Photon Electron Beams Int. Code Pract. Second Ed. Vienna IAEA (1997).
109. C.-M. Ma, C. W. Coffey, L. A. DeWerd, C. Liu, R. Nath, S. M. Seltzer, and J. P. Seuntjens, "AAPM protocol for 40–300 kV x-ray beam dosimetry in radiotherapy and radiobiology," Med. Phys. **28**, 868–893 (2001).
110. M. J. Rivard, B. M. Coursey, L. A. DeWerd, W. F. Hanson, M. Saiful Huq, G. S. Ibbott, M. G. Mitch, R. Nath, and J. F. Williamson, "Update of AAPM Task Group No. 43 Report: A revised AAPM protocol for brachytherapy dose calculations," Med. Phys. **31**, 633–674 (2004).
111. M. J. Rivard, W. M. Butler, L. A. DeWerd, M. S. Huq, G. S. Ibbott, A. S. Meigooni, C. S. Melhus, M. G. Mitch, R. Nath, and J. F. Williamson, "Supplement to the 2004 update of the AAPM Task Group No. 43 Report," Med. Phys. **34**, 2187–2205 (2007).
112. International Commission on Radiation Units, *Fundamental Quantities and Units for Ionizing Radiation* (International Commission on Radiation, 1998), Vol. 60.
113. A. Henson, M. Kühne, and L. Erard, "The European metrology research programme in action," NCSLI Meas. **4**, 26–33 (2009).
114. J. Solc, U. Ankerhold, L. Burianova, and M. Meier, "Full 3D dose distribution around electronic brachytherapy X-ray tube INTRABEAM® determined by radiochromic gel dosimeters," Phys. Medica Eur. J. Med. Phys. **31**, e51–e52 (2015).
115. J. Šolc and V. Sochor, "Feasibility of radiochromic gels for 3D dosimetry of brachytherapy sources," Metrologia **49**, S231 (2012).
116. T. Schneider, D. Radeck, and J. Šolc, "Development of a New Primary Standard for the Realization of the Absorbed Dose to Water for Electronic Brachytherapy X-ray Sources," Brachytherapy **15**, S27–S28 (2016).
117. T. Schneider, "The PTB primary standard for the absorbed-dose to water for I-125 interstitial brachytherapy sources," Metrologia **49**, S198 (2012).
118. T. Schneider, "A method to determine the water kerma in a phantom for x-rays with energies up to 40 keV," Metrologia **46**, 95 (2009).
119. S. M. Seltzer, M. O'Brien, and M. G. Mitch, "New National Air-Kerma Standard for Low-Energy Electronic Brachytherapy Sources," J. Res. Natl. Inst. Stand. Technol. **119**, 554–574 (2014).
120. P. Lamperti and H. Wyckoff, "NBS free-air chamber for measurement of 10 to 60 kV x rays," J. Res. Natl. Bur. Stand. Sect. C-Eng. Instrum. **100**, 39–+ (1965).
121. "INTRABEAM - breast cancer - Oncology - Medical Technology | ZEISS United States," https://www.zeiss.com/meditec/us/products/intraoperative-radiotherapy/intrabeam-for-breast-cancer/intrabeam.html.
122. Carl Zeiss Meditec AG, "INTRABEAM® Dosimetry, document reference: EN_30_010_155II," (2011).
123. Carl Zeiss Surgical GmbH, "INTRABEAM® Product Specifications," (2010).
124. International Commission on Radiation Units, *Radiation Dosimetry: X Rays Generated at Potentials of 5 to 150 KV.* (International Commission on Radiation Units and Measurements, 1970), Vol. 17.
125. "PTW 34013 0.005cc Soft X-Ray Chamber - Radiation Products Design, Inc.," https://www.rpdinc.com/ptw-34013-0005cc-soft-x-ray-chamber-968.html.
126. Haute Autorité de Santé (HAS), "Evaluation de la radiothérapie peropératoire dans le cancer du sein," (2016).
127. D. Swinehart, "The beer-lambert law," J Chem Educ **39**, 333 (1962).

128. R. Nowotny, "NUCLEAR DATA SERVICES," (1998).
129. D. C. Jiles, *Introduction to Magnetism and Magnetic Materials, Second Edition* (CRC Press, 1998).
130. M. Dinsmore, K. J. Harte, A. P. Sliski, D. O. Smith, P. M. Nomikos, M. J. Dalterio, A. J. Boom, W. F. Leonard, P. E. Oettinger, and J. C. Yanch, "A new miniature x-ray source for interstitial radiosurgery: Device description," Med. Phys. **23**, 45–52 (1996).
131. J. Beatty, P. J. Biggs, K. Gall, P. Okunieff, F. S. Pardo, K. J. Harte, M. J. Dalterio, and A. P. Sliski, "A new miniature x-ray device for interstitial radiosurgery: Dosimetry," Med. Phys. **23**, 53–62 (1996).
132. F. Schneider, F. Greineck, S. Clausen, S. Mai, U. Obertacke, T. Reis, and F. Wenz, "Development of a Novel Method for Intraoperative Radiotherapy During Kyphoplasty for Spinal Metastases (Kypho-IORT)," Int. J. Radiat. Oncol. **81**, 1114–1119 (2011).
133. J. C. Yanch and K. J. Harte, "Monte Carlo simulation of a miniature, radiosurgery x-ray tube using the ITS 3.0 coupled electron-photon transport code," Med. Phys. **23**, 1551–1558 (1996).
134. O. Nwankwo, S. Clausen, F. Schneider, and F. Wenz, "A virtual source model of a kilo-voltage radiotherapy device," Phys. Med. Biol. **58**, 2363 (2013).
135. P. Sievers, T. Schneider, T. Michel, and G. Anton, "X-ray spectroscopy with photon counting imaging detectors such as Timepix," in *2011 IEEE Nuclear Science Symposium Conference Record* (2011), pp. 1826–1828.
136. J. GOURIOU, "Détermination du facteur de correction lié à la présence d'un diaphragme localisé à l'entrée des chambres à parois d'air du LNE-LNHB pour les rayons X de basses et moyennes énergies," (2013).
137. "max4000.pdf," (n.d.).
138. K. Tw, L. U, P. F, L. J, M. U, L. W, B. Kh, N. F, and B. M, "[Physical and technical quality assurance and radiation protection in transperineal interstitial permanent prostate brachytherapy with 125-iodine seeds].," Strahlenther. Onkol. Organ Dtsch. Rontgengesellschaft Al **178**, 667–675 (2002).
139. D. Granero, J. Pérez-Calatayud, J. Gimeno, F. Ballester, E. Casal, V. Crispín, and R. van der Laarse, "Design and evaluation of a HDR skin applicator with flattening filter," Med. Phys. **35**, 495–503 (2008).
140. J. Hiatt, G. Cardarelli, J. Hepel, D. Wazer, and E. Sternick, "A commissioning procedure for breast intracavitary electronic brachytherapy systems," J. Appl. Clin. Med. Phys. **9**, 58–68 (2008).
141. M. Berger and J. Hubbell, "XCOM: Photon Cross Sections on a Personal Computer, NBSIR 87–3597, National Bureau of Standards (former name of NIST), Gaithersburg, MD," (1987).
142. M. D. Abramoff, P. J. Magalhães, and S. J. Ram, "Image processing with ImageJ," http://dspace.library.uu.nl/handle/1874/204900.
143. T. Schneider, M. Rouija, and H.-J. elbac, "Absolute Dosimetry for Brachytherapy with the INTRABEAM® miniature x-ray devices," ESTRO 29 (2010).
144. Y. De Deene and A. Jirasek, "Uncertainty in 3D gel dosimetry," in *Journal of Physics: Conference Series* (IOP Publishing, 2015), Vol. 573, p. 012008.
145. Y. De Deene, "Fundamentals of MRI measurements for gel dosimetry," in *Journal of Physics: Conference Series* (IOP Publishing, 2004), Vol. 3, p. 87.
146. Thorsten Schneider, "Towards reference dosimetry of electronic brachytherapy sources, WG 6.34 Dosimetry for Brachytherapy and Beta Radiation Protection," (May 2017).
147. B. Chauvenet, D. Baltes, and F. Delaunay, "Transfert de la dose absorbée dans le graphite à la dose absorbée dans l'eau pour les photons de haute énergie au BNM-LPRI : cas du Cobalt 60," Bull. Bur. Natl. Métrologie 9–18 (1996).
148. C. Ma and A. E. Nahum, "Bragg-Gray theory and ion chamber dosimetry for photon beams," Phys. Med. Biol. **36**, 413 (1991).

APPENDIX-A

Information about INTRABEAM® dose rate values:

The following information is recently delivered by Zeiss concerning the INTRABEAM® system dosimetry:

The following information about the dose rate values is based on the measuring method "Measured according to TARGIT" (INTRABEAM SW 2.2) and the "NON-TARGIT method" (for INTRABEAM Water Phantom, among others).

The INTRABEAM system with its special feature of low-energy X-ray radiotherapy and the associated challenge to dosimetry has existed since 1990. With the water phantom particularly developed to measure the low-energy X-ray source of the INTRABEAM system, an additional quality assurance accessory is provided to the customer. At the same time, this also satisfies the customer's request to have the required measuring procedure for precise positioning of the X-ray source relative to the new ionization chamber PTW 34013 with a smaller input window. Another justified customer request is the adaptation of the algorithm for the calculation of the water energy dose to international standards (AAPM TG61 or IAEA TRS 398). These two requests have been discussed and implemented with the close involvement of the TARGIT Physics Group made up of international physicists.

Because of these changes to the measurement of the depth dose curve and the calculation of the water energy dose, the depth dose has changed compared to the SW2.2 data. As the prescribed dosage for tumor bed radiotherapy of the breast determined by the international TARGIT study should not be changed, the process (method) of defining the depth dose rate cannot be changed. For this reason, there is a difference between the depth dose curve supplied with the XRS for the SW2.2 (TARGIT) and the values measured for the needle and flat/surface applicators using the INTRABEAM water phantom method (NON-TARGIT).

TARGIT measuring method

This measuring method is based on the use of a PTW TN23342 ionization chamber calibrated by means of a standard ion dose. This chamber is located in a specially designed watertight holder that is applied inside a gold standard water phantom. To convert the measured standard ion dose to a water energy dose, a roentgen-to-gray conversion factor of 8.81 mGy/R was used (taken from ICRU Report No.17).

NON-TARGIT measuring method

This process is described in detail in the Instructions for Use of the INTRABEAM Water Phantom. This measuring method is based on the use of an air kerma-calibrated PTW TN34013 ionization chamber. This chamber is located in a specially designed watertight holder that is applied inside a gold standard water phantom. To convert the measured air kerma to a water energy dose, a $\boldsymbol{K}_{\boldsymbol{K_{air \rightarrow D_w}}}$ conversion factor that is determined there by the manufacturer of the ionization chamber (PTW) during the calibration of the ionization chamber is used in each case.

The correlation between the depth dose curve supplied with the XRS and the values measured with the water phantom is defined by the following formula:

$$\dot{D}_{w,TARGIT}(r) = f'(r) \times \dot{D}_{w,NON-TARGIT}(r)$$

Here, $f'(r)$ stands for the conversion factor. It has a standard error of max. 5.1%. The values for the conversion function itself can be taken from the calibration documents of the XRS. Altogether, the conversion factor consists of 3 different parts:

1) Use of two different ionization chamber models (PTW TN34013 vs.TN23342) in the water phantom. The diameter of the chamber entrance foil of the active volume of TN23342 is approx. 5.2 mm as opposed to only 2.9 mm for TN34013. This produces different angular resolutions and different "real" r distances (typical geometric and absorption problem for point sources). Therefore, the errors between the two depth dose curves are greater, the smaller the r distance becomes.
2) Use of two different designs for the ionization chamber holder. This produces different measured dose rates, which is particularly noticeable with small r distances.
3) Use of two different algorithms to calculate the water energy dose rate (standard ion dose rate with a roentgen-to-gray conversion factor of 8.81 mGy/R as opposed to air kerma with a conversion factor by PTW, which produces a constant offset in the entire measuring range.

The conversion function was determined by calibrating many XRS in both calibration methods, calculating the conversion functions for every XRS and averaging the functions. The resulted values are presented in Figure A.1.

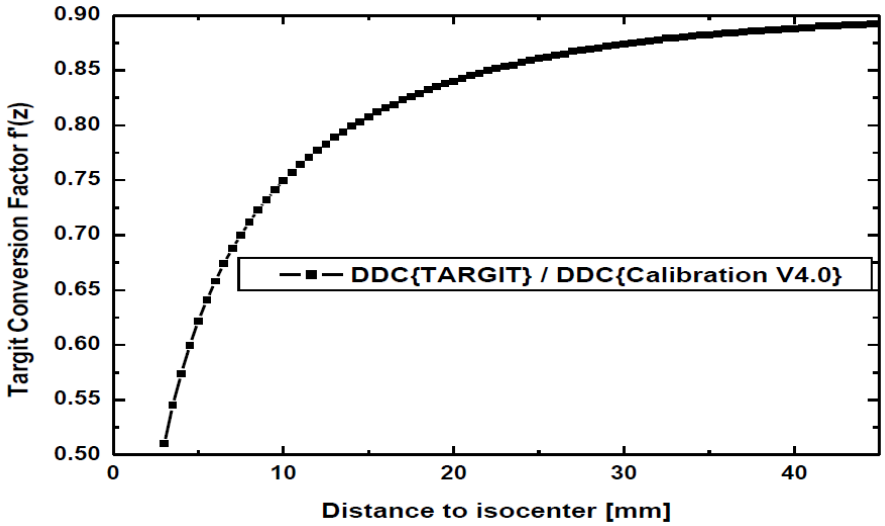

Figure A.1. TARGIT to Non TARGIT Conversion Factor $f'(r)$ as a function of distance to isocenter.

APPENDIX-B

IB photon Spectra after different depths in water:

All the measured photon spectra, of IB-XRS with 4 cm spherical applicator along the probe axis, using the second measurement setup, described in section 2.2.1.1, are given in Figure B.1. The spectra were measured at the different equivalent depths in water using the aluminum filters configurations. The spectra were all normalized over the corresponding total photon fluence for comparison. The corresponding filter thickness and fluence average energy are summarized in the table just below the figure showing the normalized photon spectra.

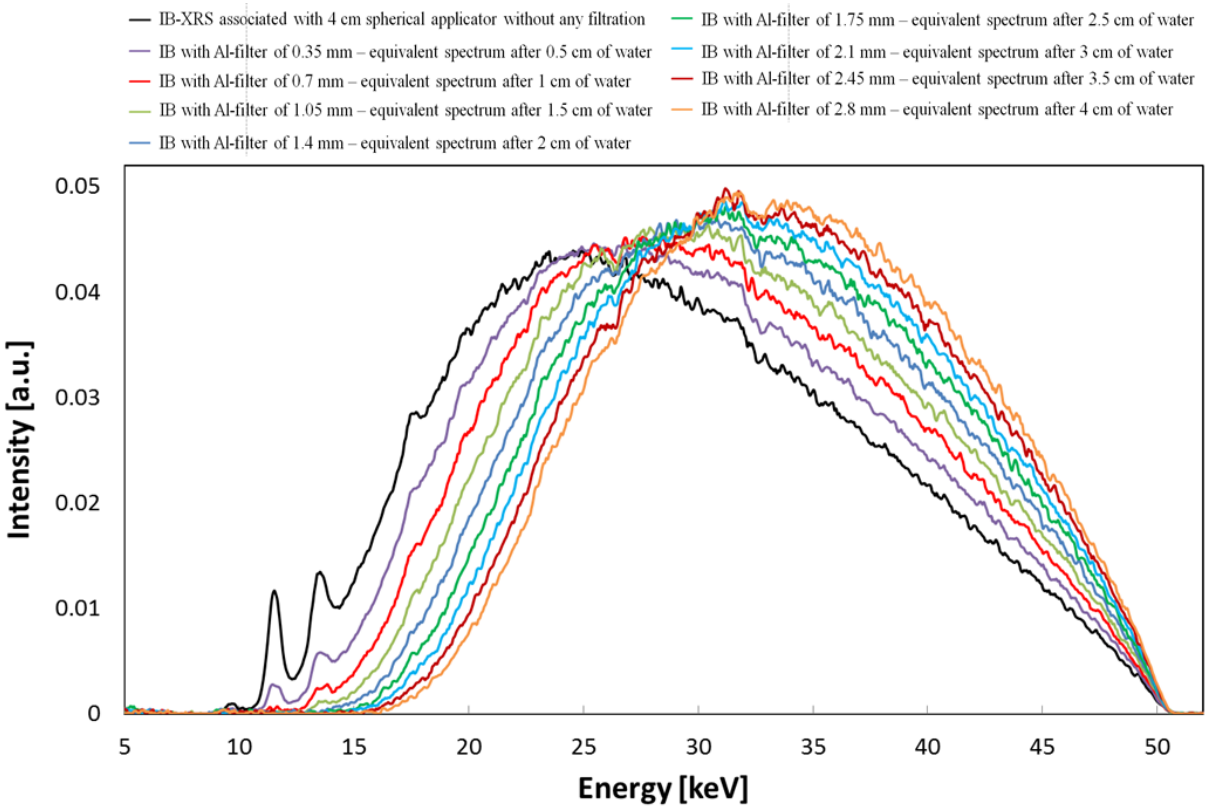

Equivalent depth in water [cm]	0.5	1	1.5	2	2.5	3	3.5	4
Filter thickness [mm – Al]	0.35	0.7	1.05	1.4	1.75	2.1	2.45	2.8
Fluence average energy [keV]	30.00	30.89	31.63	32.25	32.80	33.27	33.71	34.14

Figure B.1. Normalized photon energy spectra of IB-XRS with 4 cm spherical applicator measured at the different depths in water using aluminum filtrations. The table below the graph shows the corresponding parameters of the measured spectra.

APPENDIX-C

Simulation parameters in PENELOPE

The simulation of electron and positron transport is much more difficult than that of photons mainly due to very small average energy loss in a single interaction (of the order of a few tens of eV). As a consequence, high-energy electrons suffer a large number of interactions before being effectively absorbed in the medium. In practice, detailed simulation is feasible only when the average number of collisions per track is not too large (say, up to a few hundred). Therefore, multiple-scattering theories, which allow the simulation of the global effect (referred to as condensed) of a large number of events in a track segment of a given length (step), are implemented in the simulation code to accelerate the calculations.

In PENELOPE, photon transport is simulated by means of the conventional detailed method. However, the simulation of electron and positron transport is performed by means of a mixed procedure. Hard interactions, with energy loss greater than pre-selected cutoff values are simulated in detail. Soft interactions, with scattering angle or energy loss less than the corresponding cutoffs, are described by means of multiple-scattering approaches.

Four parameters can be varied to adjust the mixed procedure electron tracking i.e., W_{CC}, W_{CR}, C_1 and C_2. The cutoff energies of inelastic collisions and bremsstrahlung emission are designated by the W_{CC}, W_{CR} parameters, respectively. The cutoff energies W_{CC} and W_{CR} mainly influence the energy distributions, and hence, their values should be less than the energy bin (channel) used to tally the energy distributions. In addition, the calculations are faster when their value is higher. The parameter C_1 determines the mean free path between hard elastic events; it should be small enough to ensure reliable simulation results, while C_2 gives the maximum average fractional energy loss in a single step. PENELOPE admits values of C_1 and C_2 from 0 (detailed simulation) up to 0.2, with a recommendation of 0.05 value for each parameter.

Absorption energy parameters, E_{abs}, are also designated in each material for all particle types, KPAR (1: electrons, 2: photons, 3: positrons). These parameters define the energy threshold, below which particle tracking in the material is stopped and the particle is absorbed. Finally, the DSMAX(KB) parameter, which controls the maximum step length (in cm) of electrons and positrons in a body KB, is recommended to be given a value of the order of one tenth of the corresponding body thickness.

To extract information about particle fluxes within the geometrical structure, the user can define impact detectors. Each impact detector consists of a set of active (non-void) bodies, which must have been defined as parts of the geometry.

Impact detectors calculate, for a certain type of particles and within a given energy range (window), the probability density, per primary particle and energy, for a particle to be detected in the detector volume. The energy window of impact detectors can be divided into a specific number of energy bins, and hence, the photon energy distribution of the detected particles in the impact detector volume can be recorded.

Optionally, for each impact detector, the program can generate a Phase-Space File (PSF) where the state variables of particles at the detector entrance are recorded. PSF files contain the initial state of particles. For each particle detected, they save the information about its type, energy, position, direction, weight as well as a set of indices on how the particle was generated.

The use of PSF files as a source model reduces significantly the calculation by storing the histories of particles at certain position and enabling further manipulations of these data. However, this method still has some disadvantages mainly in the flexibility of further modifications on the initial parameters and geometry.

APPENDIX-D

R_2 calculations and treatment:

The calculation of R_2 is realized using the ImageJ and Excel® Visual Basic software. ImageJ is mainly used to transform the DICOM images, obtained for considered slices, into numeric data matrices. These data matrices are then manipulated based on the method described in section 1.3.3.3.3, using a home-made program developed in Excel® Visual Basic. The program calculates the R2 value for each voxel in the studied slice, as shown in Figure D.1, and returns a full R_2 matrix in an Excel sheet. The corresponding calculation time is in the order of tens of seconds up to a couple of minutes.

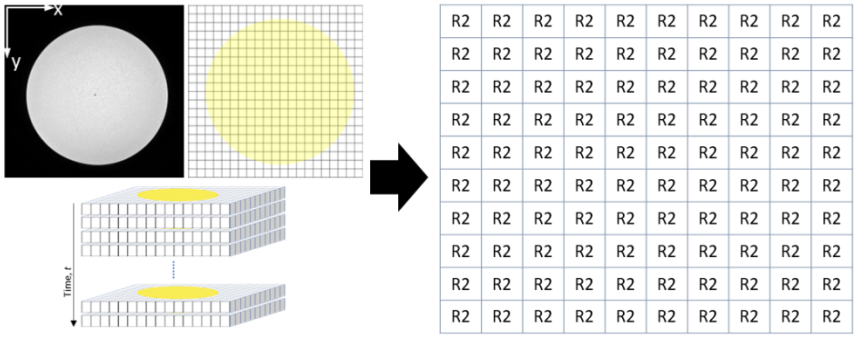

Figure D.1. R_2 matrix creation by calculations of the R_2 value of each voxel.

Gel response profiles or cartographies can be created by considering one or several Regions-Of-Interest (ROI). ROIs are regions, of any shape, that cover single or multiple voxels partially or totally. These regions are defined to decrease the associated uncertainty of R_2 resulting from measurement variations, by considering the average R_2 over the selected ROI and, thus, increasing statistical information. In addition, the experimental standard deviation of the average R_2 value, $\overline{R_2}$, over the chosen ROI is calculated to assess the uncertainty on the R_2 value. However, in the course of this study, regarding the type of beam used, only rectangular and circular ROIs were considered. The process to manipulate these two types of ROI is presented in the two following parts.

D.1. Rectangular ROI

The rectangular ROIs are selected directly on the returned R_2 matrix in Excel® and cover several voxels of the same gel response. However, only ROIs with entire voxels are accessible, as shown in Figure D.2. The average R_2 value ($\overline{R_2}$) in a ROI is calculated using the average-function in Excel®. This function returns the arithmetic mean of all the R_2 values inside the selection, as follows:

$$\overline{R_2} = \sqrt{\frac{\sum_{j=1}^{n} R_{2_j}}{n}}$$

The corresponding statistical uncertainty (standard deviation) of the $\overline{R_2}$ value is calculated using the STDEV-function in excel for a ROI with n covered voxels, using the following equation:

$$u(\overline{R_2}) = \sqrt{\frac{\sum_{j=1}^{n}\left(R_{2_j} - \overline{R_2}\right)^2}{(n-1)}}$$

Finally, the gel response cartography or a profile can be generated by tracing the calculated $\overline{R_2}$ in each ROI with their corresponding position in the R_2 matrix. The ROI reference position is considered to be the average spatial center of all its voxels, as demonstrated in Figure D.2. Moreover, the rectangular ROI is convenient to be used for gel response irradiated with parallel or collimated photon beams; over the gel regions with uniform irradiation along the beam axis.

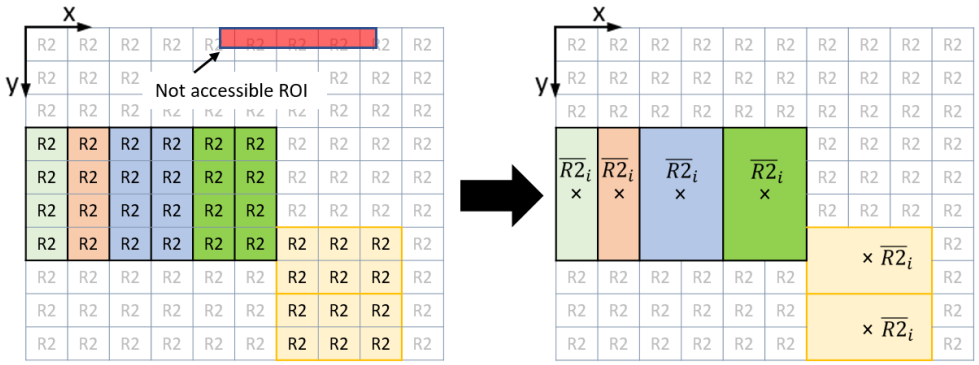

Figure D.2. Scheme of (left) selection of rectangular ROIs and (right) the calculation of the averaged R_2 ($\overline{R_{2_i}}$) values over each ith selected ROI. The cross signs represent the ROI center positions.

D.2. Annular ROI

Annular selection is another efficient form of ROI to increase R_2 statistical information. It provides a powerful tool to calculate the average R_2 value for circular isotropic zones. The annular ROI can be used to average the gel response either around isotropic point sources or around sources emitting under 4π when considering their corresponding isotropic emission plane, or to study a beam profile around a collimated beam axis.

However, the results obtained from the ImageJ Oval ROI selection tool were not reliable as they do not provide an exact selection of the annular region as shown in Figure D.3. Then, a second program was developed for this purpose.

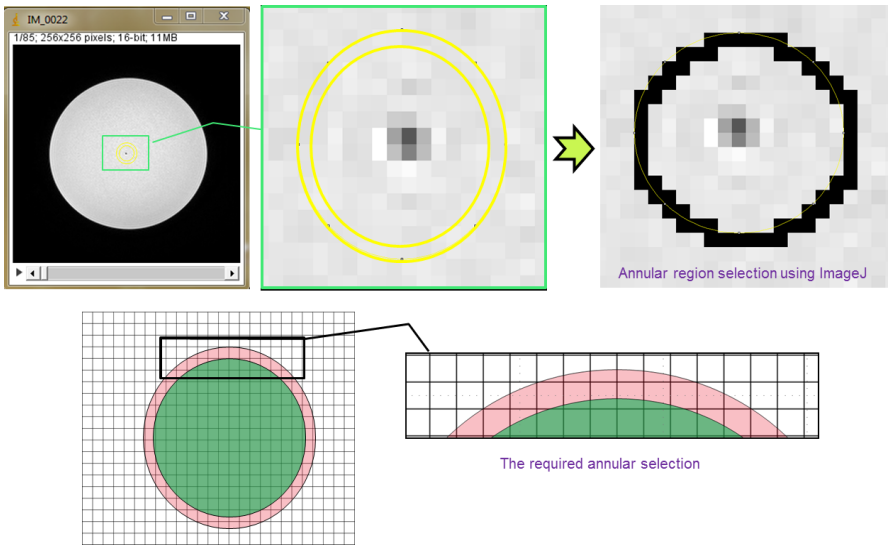

Figure D.3. The problem of annular region selection using Oval ROI selection tool in ImageJ: the resulting annular ROI in ImageJ (top) compared to the intended annular region (bottom).

This second program precisely selects the intended annular ROIs, and then, calculates the corresponding $\overline{R_2}$ values. The program is written in Excel® Visual Basic. It is based on the previously described program with an updated calculation algorithm. This algorithm calculates the area of each voxel covered by the ROI; this area might be the partial or total voxel area. Then, the R_2 value of the covered area of a voxel is calculated by multiplying the voxel R_2 value by its covered area. Finally, the $\overline{R_2}$ value of a ROI is calculated by averaging these values on the total area covered by the ROI.

The calculations of $\overline{R_2}$ value and the corresponding statistical uncertainty for annular ROIs are as follows; the grid, shown on Figure D.4, represents the R_2 values matrix for a slice of a certain phantom. This phantom was irradiated with an isotropic source, S, placed at a certain position inside. The assumption made, as dealing with isotropic source, is that the signals obtained by MRI are considered to be symmetrically distributed around the source center, and hence, the calculated value of R_2 should be of the same value in all grid elements located at the same distance, r, from the source.

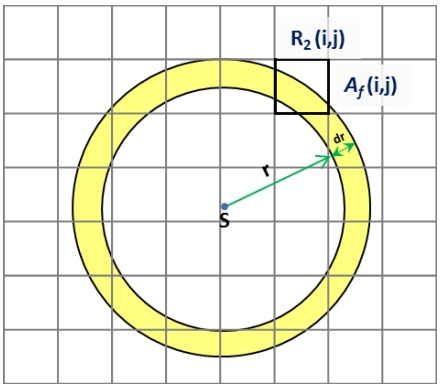

Figure D.4. Scheme of an annular ROI around an isotropic photon source S.

Let us consider an annular region of thickness, dr, located at distance, r, from the source. Then, the total R_2 value in this annular region is calculated using the following equation:

$$R_{2_{total}}(r) = \sum_1^N R_2(i,j) \times A_f(i,j),$$

where $R_2(i,j)$ and $A_f(i,j)$ are the R_2 value and the area fraction, respectively, of the voxel at the (i, j) positions on the grid. Then, the average value of R_2 in the annular region at a distance $\left[\left(r + \frac{dr}{2}\right) \pm \frac{dr}{2}\right]$ from the center, S, can be calculated as the following:

$$\overline{R_2}(r) = \frac{\sum_1^N R_2(i,j) \times A_f(i,j)}{\sum_1^N A_f(i,j)},$$

The associated uncertainties $u\big(R_2(i,j)\big)$ and $u\big(\bar{R}_2(r)\big)$ are calculated as the following with N, the total number of grid elements covered totally or partially by the annular region:

$$u\big(R_2(i,j)\big) = \sqrt{\frac{\sum_{(i,j)}(\bar{R}_2(r) - R_2(i,j))^2}{N-1}}$$

$$u\big(\overline{R_2}(r)\big) = \frac{u(R_2(i,j))}{\sqrt{N}}$$

Moreover, the program provides also the possibility to calculate the gel response over several concentric annular regions of different sizes as shown in Figure D.5.

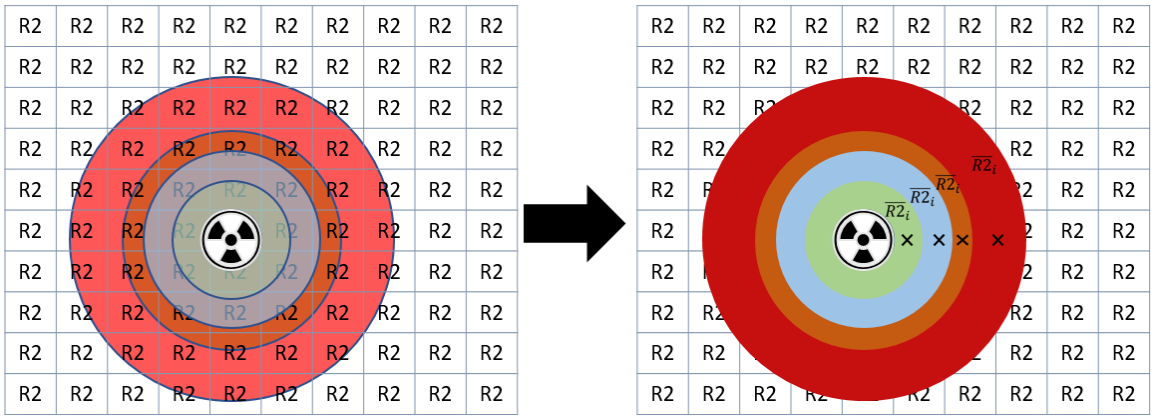

Figure D.5. Schemes of (left) the selection of annular ROI around an isotropic source and (right) the calculations of averaged R_2 ($\overline{R_{2_i}}$) values over the selected ROI.

APPENDIX-E

Total delivered doses, in water, retrieved from the treatment protocol, supplied by the INTRABEAM® system after the irradiation of the gel phantom, with the IB-XRS with 4 cm spherical applicator, for 25 minutes and 47 seconds of total irradiation time.

Prescribed Depth [mm]	Delivered Dose [Gy]		Prescribed Depth [mm]	Delivered Dose [Gy]
0	20		19.5	2.554
0.5	18.534		20	2.457
1	17.213		20.5	2.365
1.5	16.019		21	2.277
2	14.936		21.5	2.193
2.5	13.951		22	2.112
3	13.052		22.5	2.036
3.5	12.232		23	1.963
4	11.48		23.5	1.893
4.5	10.789		24	1.827
5	10.154		24.5	1.763
5.5	9.568		25	1.702
6	9.027		25.5	1.644
6.5	8.526		26	1.588
7	8.062		26.5	1.534
7.5	7.631		27	1.483
8	7.231		27.5	1.434
8.5	6.858		28	1.387
9	6.51		28.5	1.341
9.5	6.185		29	1.298
10	5.881		29.5	1.256
10.5	5.597		30	1.216
11	5.33		30.5	1.178
11.5	5.08		31	1.141
12	4.845		31.5	1.105
12.5	4.624		32	1.071
13	4.416		32.5	1.038
13.5	4.22		33	1.007
14	4.036		33.5	0.976
14.5	3.861		34	0.947
15	3.697		34.5	0.919
15.5	3.541		35	0.891
16	3.393		35.5	0.865
16.5	3.254		36	0.84
17	3.122		36.5	0.815
17.5	2.996		37	0.792
18	2.877		37.5	0.769
18.5	2.764		38	0.747
19	2.657		38.5	0.726

Développement d'une référence métrologique pour les faisceaux X de basse énergie utilisés en radiothérapie de contact

La curiethérapie électronique, également appelée radiothérapie de contact, est une technique de traitement du cancer utilisant des rayons X de faible énergie (≤ 50 keV) générés par des tubes à rayons X miniaturisés et positionnés au contact des tissus à irradier. La miniaturisation des générateurs à rayons X a conduit au développement de nouveaux systèmes de traitement, dont le plus répandu dans le monde et le seul utilisé en France est le système INTRABEAM® commercialisé par la société Zeiss. Au-delà du bénéfice médical, les avantages potentiels de la curiethérapie électronique sont une diminution drastique de l'inconfort du patient combinée à un moindre coût de traitement. Ainsi, dans le cadre du cancer du sein qui correspond à l'application principale de l'INTRABEAM, cette technique remplace la trentaine de séances de radiothérapie externe classiquement prescrite suite à l'exérèse du volume tumoral par une seule et unique séance délivrée en 20 à 50 minutes au bloc opératoire directement après l'acte chirurgical alors que la patiente est encore sous anesthésie. Cette radiothérapie peropératoire (RTPO) associe au mini générateur de rayons X des applicateurs qui, en sénologie, correspondent à des sphères de différents diamètres conçues pour épouser au mieux la cavité tumorale résultant de l'exérèse, voir Figure 1. La dose délivrée en RTPO est classiquement de l'ordre de 20 Gy en surface du lit tumoral et diminue rapidement avec la profondeur afin de préserver les tissus sains voisins (< 1 Gy après quelques cm). En France, le 1er traitement par RTPO a eu lieu à Nantes fin 2011. Aujourd'hui, une dizaine de centres hospitaliers français propose des traitements par RTPO au moyen de la technique INTRABEAM®. Très rapidement, plusieurs physiciens médicaux ont exprimé au laboratoire français de métrologie de la dose (LNHB), leur besoin de raccordement dosimétrique à une référence indépendante du constructeur. Ce besoin a été réaffirmé par la Haute Autorité de Santé (HAS) dans un rapport sur l'évaluation de la RTPO dans le cancer du sein, édité en avril 2016.

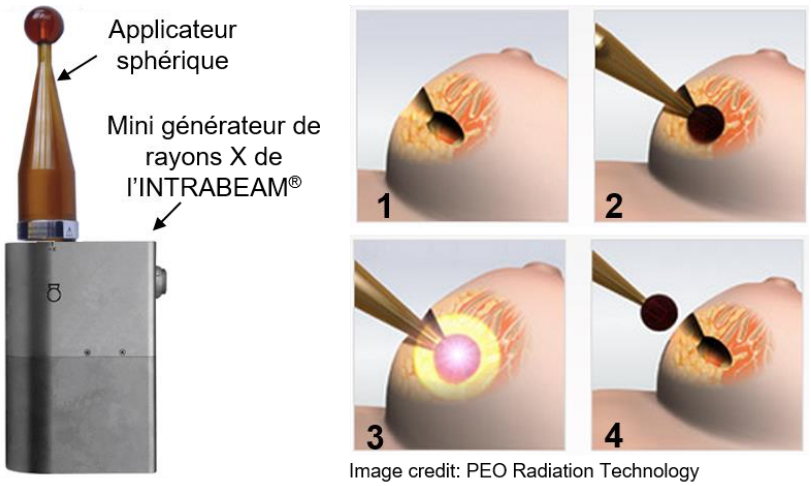

Image credit: PEO Radiation Technology

Figure 1: L'INTRABEAM dans le cadre du traitement du cancer du sein : 1. Tumeur retirée chirurgicalement au bloc, 2. Insertion dans la cavité tumorale de l'applicateur sphérique de l'INTRABEAM, 3. Irradiation du lit tumoral au bloc et 4. L'applicateur est retiré puis l'incision est fermée

Le présent travail vise à renforcer la sécurité d'emploi d'appareils de RTPO par rayons X de basse énergie (< 50 keV). Cependant, afin de répondre aux physiciens médicaux français et du fait de contraintes temporelles, l'étude est ici limitée au système INTRABEAM® associé au seul applicateur sphérique de 4 cm de diamètre. Ce travail a été réalisé au Laboratoire National Henri Becquerel (LNHB) du CEA Saclay en collaboration avec l'hôpital Saint Louis et le Service Hospitalier Frédéric Joliot Curie (SHFJ).

Ce document est un résumé du mémoire de recherche rédigé en anglais, articulé autour de quatre chapitres en répondant à trois objectifs principaux.

Le premier chapitre fait un état de l'art du sujet à différents niveaux : technique, métrologie, protocole et il introduit les outils utilisés dans les travaux (système expérimental, simulation Monte-Carlo avec le code PENELOPE). Il commence par une présentation de la technique de la radiothérapie de contact par rayons X, son principe et les différents dispositifs existants sur le marché où le système INTRABEAM qui fait l'objet de l'étude est particulièrement détaillé. Puis, les principales quantités dosimétriques, i.e. la dose absorbée dans l'eau et le kerma dans l'air, avec leur formulation sont rappelées en lien avec la spécificité de la dosimétrie des rayons X et la chaîne métrologique garantissant la traçabilité des quantités dosimétriques. Différents protocoles basés sur des méthodes directes ou indirectes sont ainsi présentés (IAEA, AAPM, NIST, etc.) Ce chapitre expose également les différents détecteurs utilisés en métrologie et plus particulièrement les dosimètres chimiques avec leur système de lecture, capables de donner une information véritablement 3D, c'est-à-dire non reconstruite mathématiquement. On citera notamment les gels de Fricke, les gels polymères et les gels radiochromiques. Les principes des gels de Fricke et leur méthode de lecture associée par RMN sont plus particulièrement développés, car ils seront utilisés dans ces travaux.

Le second chapitre répond au premier objectif de l'étude que concerne l'établissement et le transfert d'une référence dosimétrique en termes de la dose absorbée dans l'eau à 1 cm de la source, qui est la quantité dosimétrique recommandée pour la curiethérapie électronique. Pour établir cette référence, il a été nécessaire d'adapter le protocole, car le LNHB ne disposait que d'un générateur de rayons X (GRX) conventionnel et le système INTRABEAM n'était disponible à l'hôpital Saint Louis qu'en-dehors des séances de traitement. La méthode développée se base tout d'abord sur la caractérisation du spectre photonique du système INTRABEAM® de l'hôpital Saint-Louis, en particulier pour un applicateur sphérique de 4 cm de diamètre, à l'aide d'un détecteur CdTe puis la production d'un spectre équivalent par un générateur X conventionnel (Gulmay 160) disponible au LNHB. Le débit de kerma dans l'air a ensuite été établi en utilisant une chambre d'ionisation à parois d'air WK07 au LNHB. Les facteurs de correction à appliquer, liés au détecteur primaire, ont été déterminés par deux méthodes différentes, associant mesures expérimentales et simulations Monte-Carlo. Puis, la mesure du débit de kerma dans l'air pour le système INTRABEAM® a été réalisée à l'hôpital Saint Louis avec un détecteur de transfert (PTW-23342), dont le coefficient d'étalonnage avait été établi au LNHB au préalable à partir du faisceau reproduisant le spectre étudié. Pour optimiser la fiabilité de ces

mesures, un dispositif spécifique a été mis en place, permettant notamment un alignement optimal du détecteur avec l'axe de la source. Enfin, la détermination du coefficient de conversion du kerma dans l'air en dose absorbée dans l'eau à 1 cm de profondeur a été effectuée par calculs Monte Carlo.

La méthodologie adoptée, a été ainsi, décomposée dans les étapes suivantes :

1) Reproduction, par le GRX du LNHB, du faisceau INTRABEAM® sous 1 cm d'eau

2) Etablissement de la réf. primaire en $\dot{K}_{\mathrm{air,\,ref}}$ de ce faisceau à l'aide de la chambre à parois d'air étalon du LNHB (incluant la détermination des facteurs correctifs)

$$\dot{K}_{\mathrm{air,\,ref}} = I_{\mathrm{ref}} \cdot \frac{1}{V.\rho_{\mathrm{air}}} \cdot \frac{\bar{W}_{\mathrm{air}}}{e} \cdot \left(\frac{1}{1-g} \cdot \prod_{\mathrm{i}} k_{\mathrm{i}}\right)_{conv.\ ou\ MC}$$

3) Etalonnage en $\dot{K}_{\mathrm{air,\,ref}}$ d'une chambre d'ionisation de transfert dans ce faisceau

$$N_K = \frac{\dot{K}_{\mathrm{air,ref}}}{I_{\mathrm{TC,ref}}}$$

4) Mesure du $\dot{K}_{\mathrm{air,\,IB}}$ dans le faisceau INTRABEAM considéré entouré d'1 cm d'eau

$$\dot{K}_{\mathrm{air,\,IB}} = N_K \cdot I_{\mathrm{TC,\,IB}}$$

5) Calcul MC du facteur de passage du $\dot{K}_{\mathrm{air,\,IB}}$ à la $\dot{\boldsymbol{D}}_{\mathbf{w,\,1\,cm}}$ dans les conditions de réf.

$$\dot{\boldsymbol{D}}_{\mathbf{w,\,1\,cm}} = \dot{K}_{\mathrm{air,\,IB}} \cdot F_{\dot{K}_{\mathrm{air,\,IB}} \text{ à } \dot{\boldsymbol{D}}_{\mathbf{w,\,1\,cm}}}$$

Le faisceau de photons délivré par l'INTRABEAM a été caractérisé par mesures expérimentales en optimisant le dispositif (influence du de la filtration) et puis corrigé des artéfacts des mesures par des algorithmes déjà développées au LNHB. Un travail important a ensuite été réalisé (principalement liée au matériau de l'anode et la filtration) sur le générateur X du LNHB pour reproduire le spectre mesuré.

Les calculs avec le code PENELOPE ont permis, après validation du modèle MC de la source de GRX du LNHB avec les données expérimentales, de comparer les deux méthodes de détermination des facteurs de correction (méthode globale ou conventionnelle). Les résultats obtenus par les deux méthodes sont montrés un bon accord avec un rapport (méthode Globale/méthode conventionnelle) de $\mathbf{1,003}(2)$.

La partie de la détermination du coefficient de conversion met en évidence les limites de la simulation : temps de calcul, stockage, difficulté à obtenir les données du constructeur pour modéliser correctement les systèmes. Elle attire notamment l'attention sur l'influence des paramètres physiques et dimensionnels sur les résultats, particulièrement importante dans ce domaine des basses énergies. Ainsi, pour réduire

les temps de calcul, des fichiers d'espace des phases ont été générés au niveau de la surface de l'applicateur et utilisés pour la détermination de la dose absorbée dans l'eau à 1 cm. Une méthode analytique a été préférée pour le calcul des valeurs du kerma dans l'air à partir des distributions de la fluence en énergie des photons.

Enfin, l'ensemble des résultats obtenues dans ce chapitre, voir Tableau 1, a permis d'évaluer le débit de dose absorbée dans l'eau $\dot{D}_{\mathbf{eau,\,1\,cm}}$ dans les conditions de référence avec les incertitudes associées, pour le système INTRABEAM® avec un applicateur sphérique de 4 cm.

Tableau 1: les valeurs des paramètres calculés, mesurés ou utilisés pour obtenir la valeur de référence $\dot{D}_{eau,\,1\,cm}$

$\dot{D}_{\mathrm{eau,\,1\,cm}} = \frac{I_{\mathrm{FAC}}}{\rho_{\mathrm{air}}} \cdot \frac{\overline{W}_{\mathrm{air}}}{e} \cdot \frac{1}{V_{\mathrm{ref,MC}}} \cdot \frac{E_{\mathrm{tr}}}{E_{\mathrm{dep}}} \cdot \frac{I_{\mathrm{TC,IB}}}{I_{\mathrm{TC,ref}}} \cdot \frac{D_{\mathrm{eau,1cm}}}{K^{\mathrm{MC}}_{\mathrm{air,IB}}}$				
Paramètres	**Symbole**	**Unité**	**Valeur**	***u* (%) (*k*=1)**
Courant mesuré net WK07 (corrigé de k_T, k_P, k_h, k_s k_{pol}, k_d et MP)	I_{FAC}	A	**4,784E-11**	**0,24**
Masse volumique de l'air (20 °C, 1013.25 hPa)	ρ_{air}	kg.m^{-3}	**1,20479**	**0,01**
Energie moyenne nécessaire pour créer 1 paire d'ions	$\frac{\overline{W}_{air}}{e}$	J.C^{-1}	**33,97**	**0,35**
Volume de référence	$V_{ref,MC}$	m^{-3}	**1,576E-07**	**0,05**
Energie transérée dans $V_{ref,MC}$	E_{tr}	eV. pp^{-1}	**0,06321**	**1,00**
Energie déposée dans V_{col}	E_{dep}	eV. pp^{-1}	**0,16135**	**1,00**
Courant net mesuré par la CT au LNHB avec GRX	$I_{TC,ref}$	A	**2,424E-12**	**0,16**
Dose absorbée dans l'eau dans les conditions de réf.	$D^{MC}_{eau,1cm}$	eV. g^{-1} pp^{-1}	**9,7E-02**	**1,42**
Kerma dans l'air calculé dans les conditions de mesure	$K^{MC}_{air,IB}$	eV. g^{-1} pp^{-1}	**0,002585**	1,28
Courant net mesuré par la CT pour l'INTRABEAM®	$I_{TC,\,IB}$	A	**9,507E-14**	0,29
Débit de dose absorbée dans l'eau dans les conditions de réf.	$\dot{D}_{eau,\,1\,cm}$	Gy. s^{-1}	**4,951E-03**	**2,45**

Le troisième chapitre porte sur la détermination de la distribution spatiale de dose autour de la source considérée par l'utilisation de gels dosimétriques et par calcul de type Monte Carlo. L'hydrogel à base de Fricke, utilisé ici, est lu par imagerie par résonance magnétique (IRM). Ce gel a été étalonné en dose pour des photons d'énergie inférieure à 50 keV puis utilisé pour déterminer les profils de doses autour de la source INTRABEAM® associée à l'applicateur sphérique de 4 cm de diamètre dans les plans axial et transverse incluant le centre de la source INTRABEAM®.

Dans un premier temps, la méthode de l'étalonnage, le choix de la qualité des faisceaux pour évaluer la réponse du gel dans ce domaine des faibles énergies, la conception des fantômes ainsi que la méthode de lecture par RMN ont été présentés. En effet, cinq fantômes physiques de gel ont été élaborés puis irradiés sous les deux types de faisceaux de qualité choisis pendant des périodes du temps variées. Les modifications induites dans le gel ont ensuite été mesurées par IRM en collaboration avec le SHFJ. Pour analyser au mieux les résultats issus des images DICOM et déterminer la réponse du gel en fonction de la profondeur, deux programmes sous Visual Basic ont été développés. Ensuite, afin de déterminer la courbe d'étalonnage reliant les variations de la réponse du gel obtenues par IRM à la dose absorbée, des modélisations MC ont été réalisées sous PENELOPE. D'après les résultats obtenus, la relation entre les variations de la dose absorbée dans le gel et la réponse du gel semble valable pour tous les fantômes de gel irradiés et les deux types de faisceaux de qualité éventuellement choisi en prenant en compte les incertitudes associés. On précise néanmoins qu'une étude plus poussée serait nécessaire pour établir une possible dépendance en énergie.

L'homogénéité de la réponse du taux de relaxation R_2 a particulièrement été étudiée. Une attention particulière a été apportée à la fabrication des gels, au temps de latence entre les différentes étapes allant de la fabrication à la lecture pour optimiser la réponse des gels tout en tenant compte des paramètres intrinsèques tels que la diffusion.

Après l'étalonnage du gel, un protocole expérimental a été mis en place afin de déterminer les variations de la réponse du gel pour le système INTRABEAM® et donc les profils de doses correspondants après étalonnage. Les distributions de doses absorbées dans le gel sont obtenues dans deux axes, les plans transverse et axial autour de la source INTRABEAM®. Enfin, des calculs Monte-Carlo ont ensuite permis de calculer les coefficients pour passer de la dose absorbée dans le gel à la dose absorbée dans l'eau ; grandeur de référence en radiothérapie.

A ce niveau, il peut d'ailleurs être souligné que la comparaison entre les distributions relatives de doses déterminées par les gels dosimétriques et les simulations Monte Carlo normalisées à la dose à 1 cm de profondeur sont en très bon accord. Les doses absorbées dans l'eau en fonction de la distance depuis la surface de l'applicateur selon les plans axial et transverse sont finalement comparées avec les valeurs données par la société ZEISS et les valeurs obtenues par simulation Monte Carlo ; toutes normalisées à la profondeur de 1 cm. Les 3 courbes présentent un parfait accord, voir

Figure 2. Néanmoins, des limitations de l'utilisation des gels dosimétriques pour une quantification absolue de la dose sont brièvement discutés.

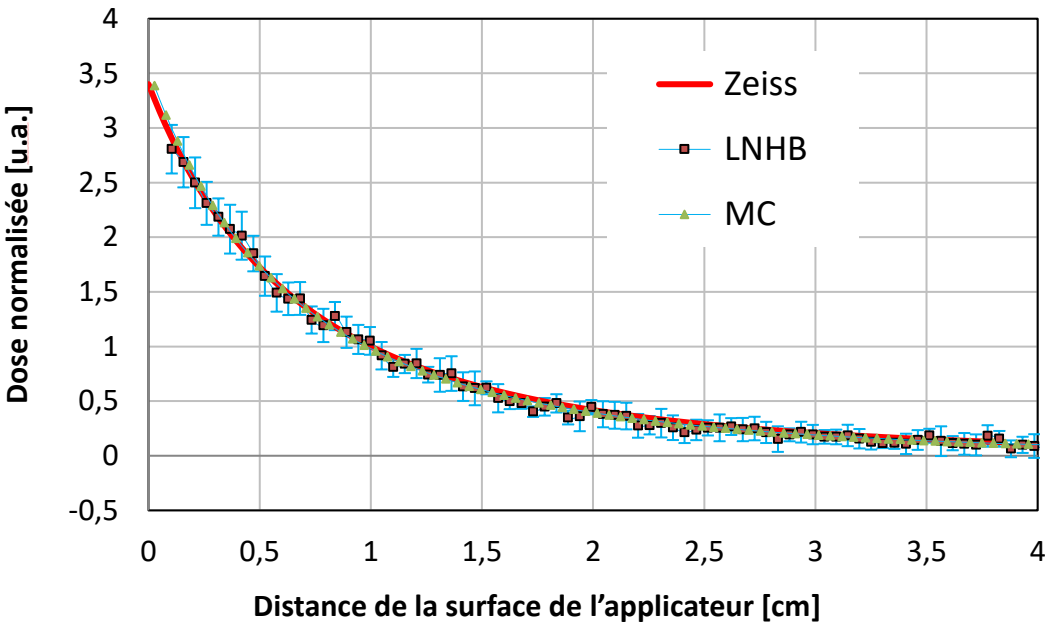

Figure 2: Comparaisons des distributions relatives des doses absorbées dans l'eau en fonction de la distance depuis la surface de l'applicateur selon le plan axial avec celles données par la société ZEISS et les valeurs obtenues par simulation Monte Carlo (MC), tous normalisées à la dose à la profondeur de 1 cm

Quant au dernier chapitre, chapitre quatre, il s'est agi de confronter des données dosimétriques en absolu fournies par la société Zeiss, concernant l'INTRABEAM® en utilisation à l'hôpital St-Louis à Paris, à celles obtenues au cours de la présente étude pour le même système. La société ZEISS fournit les distributions de dose dans l'eau pour le système nu et les fonctions de transfert pour tenir compte des applicateurs sphériques. Deux méthodes dosimétriques sont actuellement disponibles par Zeiss (TARGIT et non-TARGIT). Des différences significatives ont été trouvées entre les doses délivrées par Zeiss et celles obtenues dans la présente étude. Les valeurs de débit de dose absolue dans l'eau déterminés dans le cadre de ce travail étaient supérieures de 33% et 16% à ceux donnés selon les méthodes "TARGIT" et "Non-TARGIT" de la société Zeiss, respectivement. Ces résultats vont dans le même sens que ceux obtenus par l'institut national de métrologie allemand (PTB) pour la configuration sans applicateur du système INTRABEAM®, voir Tableau 2.

Tableau 2 : Comparaison des débits de dose absolus dans l'eau obtenues par différents laboratoires primaires (LNHB et PTB) aux celles du fabricant du système INTRABEAM®, la société ZEISS.

$\dot{D}_{eau,\,1\,cm}$ définis de la surface de l'applicateur				
LNHB $\dot{D}_{eau,\,1\,cm}$ [mGy.s-1]	**Zeiss** $\dot{D}_{eau,\,1\,cm}$ [mGy.s^{-1}]		Rapport $\dot{D}_{eau,\,1\,cm}$ (LNHB/Zeiss)	
	TARGIT	Non-TARGIT (V4.0)	TARGIT	Non-TARGIT (V4.0)
4,95	3,72	4,26	**1,33**	**1,16**
$\dot{D}_{eau,\,1\,cm}$ définis de la surface de l'aiguille de SRX-IB				
PTB-CMI $\dot{D}_{eau,\,1\,cm}$ [mGy.s-1]	**Zeiss** $\dot{D}_{eau,\,1\,cm}$[mGy.s^{-1}]		Rapport $\dot{D}_{eau,\,1\,cm}$ (PTB-CMI/Zeiss)	
	TARGIT	Non-TARGIT (V4.0)	TARGIT	Non-TARGIT (V4.0)
65,4	40,3	53,6	**1,62**	**1,22**

Par ailleurs, la comparaison de la distribution de dose absolus, déterminées par les distributions relatives dans le gel normalisées par la valeur de débit de dose de référence $\dot{D}_{eau,\,1\,cm}$, avec celle de Zeiss a montré des différences significatives de l'ordre de 10 Gy dans le plan axial et de 6 Gy dans le plan transverse au niveau de la dose en surface, voir Figure 3. Il sera donc pertinent à l'avenir de poursuivre les investigations afin de définir des conditions de transfert adaptées et indépendantes du constructeur aux utilisateurs des systèmes de radiothérapie de contact.

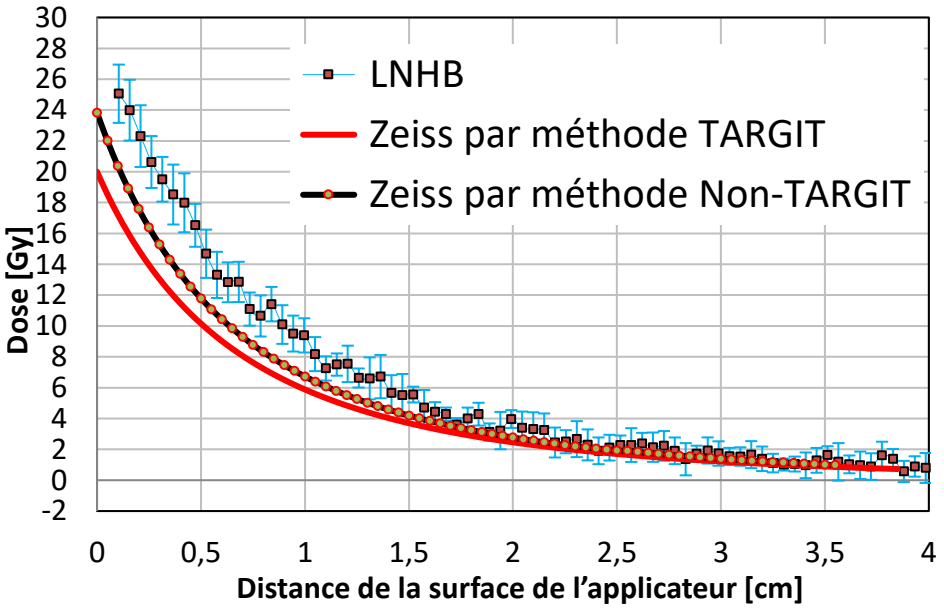

Figure 3 : la comparaison de la distribution de dose absolus obtenue dans la présente étude, dans le plan axial de l'applicateur de 4 cm de diamètre, avec celles de Zeiss sous la même configuration.

Liste de communications:

- Orale - 18e Congrès International de Métrologie (CIM), (Sep. 2017), "Étalonnage en dose absorbée dans l'eau pour des sources basses énergie de rayons X pour la radiothérapie", **A. Abudra'a**, J. Gouriou, M. Denozière, J. Plagnard, R. Itti, I. Aubineau-Lanièce

- Poster - PTB workshop (Mai 2017), "Metrology for brachytherapy: state-of-the-art and beyond", I. I. Aubineau-Lanièce, **A. Abudra'a**, B. Chauvenet, D. Cutarella, J. Gouriou, J. Plagnard, R. Itti, C. Stien

- Orale - 55éme journée scientifique de la SFPM (Juin 2016), "Reproduction de spectres INTRABEAM® à l'aide d'un générateur de rayon x de référence", **A. Abudra'a** , M. Denozière, J. Plagnard, J. Gouriou, R. Itti, I. Aubineau-Lanièce

- Poster - 55éme journée scientifique de la SFPM (Juin 2016), "Détermination par gel dosimétrique de la distribution de dose autour d'un grain d'^{125}I de curiethérapie", **A. Abudra'a**, C. Stien, D. Cutarella, M. Denozière, I. Aubineau-Lanièce

- Oraux (2015, 2016 et 2017) aux journées des thèses du CEA/LIST/DM2I.

- Poster (2015) et Orale (2016) aux journées des doctorants à l'école doctorale.